Shape-Memory Polymers for Bioinspired, Tunable Photonic Structures

Zur Erlangung des akademischen Grades
Doktor der Ingenieurwissenschaften
der Fakultät für Maschinenbau
Karlsruher Institut für Technologie (KIT)

genehmigte
Dissertation
von

Dipl.-Ing. Senta Rebecca Schauer

Tag der mündlichen Prüfung:	15. September 2017
Referent:	PD. Dr. Hendrik Hölscher
Korreferenten:	Prof. Dr. Manfred Kohl
	Prof. Dr. Aránzazu del Campo Bécares

Abstract

Structural colors fulfill an overwhelming multitude of functions in nature and their occurrence is manifold both in species and in shapes. The color producing mechanisms rely on often sophisticated, hierarchical structures with structure features in the range of the wavelength of light. Due to their complexity, mimicking those structures is still a challenge for engineers as they are often beyond the limits of established microfabrication technologies. However, color yielding structures are of great interest, since the color generation is neither based on pigments (that fade with time) nor emission of light (that permanently consume energy). Furthermore, with smallest changes of structure dimensions, the induced structural color changes.

My approach to design tunable structural colors comprises the utilization of shape-memory polymers. This class of polymers is able to remember a predefined shape and recover it even after extensive mechanical deformations when triggered with a suitable stimulus like heat. Although shape-memory polymers are a new material to optics their applicability has been proven in the realization of tunable diffractive optical elements. In the course of this thesis I adapted the same concept of embossing a grating on the surface of a shape-memory polymer substrate and attaining a temporary period change by stretching, and scaled it down to sub-micron structures. The in this way produced tunable Bragg grating was applied as a resonator for an organic distributed feedback laser with an over a wide range tunable emission wavelength.

Furthermore, I explored the potential of shape-memory polymers not only to produce bioinspired light-modulating structures but also to tune structure features in a way that their optical properties are affected. Based on the color creating principles found in squids, flowers, and opals three corresponding artificial counterparts were developed.

First, a procedure was engineered to generate a polymer thin film with tunable thickness due to the film's shape-memory effect inspired by the color changing principles in some cephalopod species. With the enhancement of two reflective silver layers framing the

shape-memory polymer film I designed a tunable, highly wavelength selectivly filtering Fabry-Pérot interferometer.

Secondly, I advanced a self-assembly method to produce plain and hierarchical surface wrinkles that show strong iridescence mimicking multifarious petal structures. Thorough investigation of the influence of the fabrication parameters enables us to adjust the resulting structure period from few hundred nanometers up to several microns. In addition, various combinations of wrinkling of embossed films or wrinkling on prestructured substrates offer a wealth of feasible structure geometries. Furthermore, due to their dimension and the small, inherent structure disorder, the plain wrinkle structures possess not only diffractive behavior but also anti-reflective properties. Hence, we successfully applied them as beneficial light in-coupling coatings to increase the efficiency of solar cells.

Lastly, small polymer spheres were aligned to an opalescent 3D photonic crystal in an elastomer and a specific amount of shape-memory polymer was added to develop a material with an on-demand color change ability. Before required external forces to maintain the deformation for stretch-tuning of the color are now implemented in the composite by the shape-memory polymer. Hence, these shape-memory polymer opals allow not only to tune the reflected color by stretching but also by compressing the composite which enables us to imprint shape-coupled color changes.

Kurzfassung

Strukturelle Farben erfüllen eine enorme Vielzahl von Funktionen in der Natur und ihr Vorkommen ist vielfältig sowohl in Arten als auch in Formen. Die farbproduzierenden Mechanismen basieren auf oft filigranen und hierarchischen Strukturen mit Strukturabmessungen in der Größenordnung der Wellenlänge des Lichtes. Aufgrund ihrer Komplexität ist das Nachahmen solcher Strukturen immer noch eine große Herausforderung für Ingenieure. Die Größen der Strukturdetails sind an oder unter der Grenze der heutzutage etablierten Herstellungsverfahren. Nichtsdestotrotz sind diese farbgebenden Strukturen von großem Interesse da sie im Gegensatz zu Pigmenten oder emissionsbasierten Farbquellen weder mit der Zeit verblassen noch konstanten Energieverbrauch aufweisen. Darüber hinaus sind kleinste Strukturänderungen ausreichend um die erzeugte Farbe zu verändern.

Unser Ansatz zur Gestaltung von farbwechselnden Strukturen basiert auf der Nutzung von Formgedächtnispolymeren. Diese Klasse von Polymeren kann sich eine zuvor definierte Form merken und in diese selbst nach großen, mechanischen Deformierungen zurückkehren wenn sie mit einem passenden Stimulus wie beispielsweise Hitze angeregt werden. Obwohl Formgedächtnispolymere für die Optik neue Materialien sind, wurde ihre Einsetzbarkeit bereits bei diffraktiven optischen Elementen bewiesen. Im Rahmen meiner Dissertation habe ich das Konzept vom Heißprägen eines Gitters in die Oberfläche eines Formgedächtnispolymersubstrates und Erreichen einer Vergrößerung der Gitterperiode durch Strecken adaptiert und es auf unter Mikrometergröße skaliert. Auf diese Weise konnte ein veränderbares Bragg-Gitter hergestellt und erfolgreich als Resonator für einen organischen DFB-Laser angewendet werden. Durch die durch den Formgedächtniseffekt gegebene Durchstimmbarkeit der Resonatorperiode ist die Emissionswellenlänge über einen großen Bereich einstellbar.

Des Weiteren habe ich das Potential von Formgedächtnispolymeren bezüglich einerseits der Herstellung und andererseits der Durchstimmbarkeit von aus der Natur inspirierten, mit Licht wechselwirkenden Strukturen untersucht. Basierend auf den farberzeu-

genden Mechanismen in Tintenfischen, Blütenblättern und Opalen sind drei Ansätze zur Realisierung der entsprechenden künstlichen Pendants entstanden.

Als Erstes konzipierte ich eine Methode um eine Polymerdünnschicht mit Formgedächtniseffekt herzustellen, die es erlaubt die Schichtdicke, und damit einhergehend die Interferenzeigenschaften, zu verändern wie es in manchen Tintenfischarten zu beobachten ist. Mit der Verstärkung des Phänomens durch zwei reflektierende, die Dünnschicht einrahmenden Silberschichten entstand ein stark wellenlängenselektives, durchstimmbares Fabry-Pérot-Interferometer.

Im zweiten Ansatz entwickelte ich ein Verfahren zur selbstorganisierten Herstellung von Oberflächenfaltungen weiter, um sowohl einfache als auch hierarchische Strukturen, wie sie auf vielen Blütenblättern zu finden sind, herzustellen. Die sorgfältige Untersuchung des Einflusses der Fabrikationsparameter erlaubt ein gezieltes Einstellen der resultierenden Strukturgröße von wenigen hundert Nanometern bis zu mehreren Mikrometern. Zusätzlich ermöglichen diverse Kombinationen aus Faltenbildung von zuvor strukturierten Filmen oder auf vorgeformten Formgedächtnispolymersubstraten eine Vielzahl weiterer hierarchischer Topographien. Auf Grund der Dimensionen der Strukturen und der kleinen, inhärenten Unregelmäßigkeit führen die entwickelten einfachen Strukturen nicht nur zur Beugung von einfallendem Licht sondern weisen auch Anti-Reflex-Eigenschaften auf. Mit meiner Struktur versehene Solarzellen führten deshalb zu verbesserter Lichteinkopplung und folglich zu einer Steigerung der Effizienz der Solarzelle.

Der letzte der vorgestellten Ansätze beinhaltet die Zusammenführung von in einer Elastomer-Matrix eingebetteten Polymerkügelchen und unserem Formgedächtnispolymer zu einem opalisierenden, dreidimensionalen, photonischen Kristall. Zuvor zur Aufrechterhaltung einer Form- und damit Farbänderung notwendige externe Kräfte sind durch das Formgedächtnispolymer in den Verbundstoff integriert. Demnach ist eine Farbdurchstimmung nicht mehr nur durch Verstreckend es Materials möglich sondern zudem auch durch Kompression wodurch das Einprägen von formgekoppelten Farbänderungen ermöglicht wird.

Contents

1 Introduction **1**

2 Theoretical Background **5**

2.1 Shape-Memory Polymers 5

2.1.1 Shape-Memory Effect 6

2.1.2 Applications of Shape-Memory-Polymers 11

2.2 Light Modulation by Periodic Structures 12

2.2.1 Reflection, Refraction, Diffraction, and Interference 12

2.2.2 Diffraction Gratings 14

2.2.3 Photonic Crystals 15

2.3 Materials and Methods 20

2.3.1 Materials 20

2.3.2 Fabrication Tools and Techniques 22

2.3.3 Dynamic Mechanical Analysis 32

2.3.4 Microscopic and Surface Analytic Tools 32

2.3.5 Optical Spectroscopic Methods 35

2.4 State-of-the-Art: SMPs in Optics 36

3 Tunable Organic Distributed Feedback Lasers **43**

3.1 Motivation and Background 43

3.2 Fabrication 46

3.3 Results and Discussion 49

3.4 Conclusion and Outlook 52

4 Tunable Fabry-Pérot Interferometer **55**

4.1 Motivation and Background 55

4.2 Fabrication 58

4.3 Results and Discussion 61

4.4 Conclusion and Outlook 66

5 Surface Wrinkles . . . 69
5.1 Motivation and Background . . . 69
5.2 Linear Wrinkles on Shape-Memory Polymers . . . 75
5.2.1 Adjustable Structure Size . . . 77
5.2.2 Parametric Study . . . 80
5.2.3 Cracking . . . 84
5.3 Hierarchical Surface Wrinkles . . . 85
5.3.1 Wrinkling Combined with Hot Embossing . . . 85
5.3.2 Hot Embossing Combined with Wrinkling . . . 89
5.3.3 Hot Pulling Combined with Wrinkling . . . 94
5.4 Wetting Properties . . . 100
5.5 Optical Characterization . . . 102
5.5.1 Diffractive Properties . . . 102
5.5.2 Anti-Reflective Behaviour . . . 105
5.5.3 Application on Solar Cells . . . 107
5.6 Conclusion and Outlook . . . 111

6 Shape-Memory Polymer Opals . . . 115
6.1 Motivation and Background . . . 115
6.2 Fabrication . . . 122
6.2.1 Emulsion Polymerization of CIS-Spheres . . . 122
6.2.2 Extrusion and Ordering . . . 123
6.3 Results and Discussion . . . 126
6.3.1 Analysis of the SMPO Composite Structure . . . 126
6.3.2 Shape-Memory Ability of SMPOs . . . 129
6.3.3 Compression Induced Color Change on Demand . . . 133
6.4 Conclusion and Outlook . . . 135

7 Summary and Outlook . . . 139

Acknowledgement . . . 143

List of Publications . . . 145

List of Figures

1.1 Outline of work on bioinspired structural colors. 4

2.1 Demonstration of the shape-memory effect of two polymers. 6
2.2 Molecular mechanism of the thermally triggered, one-way SME. 8
2.3 Rheological model for the shape recovery process. 9
2.4 Reflection, refraction and interference at a thin film. 13
2.5 Diffraction grating. 14
2.6 Types of photonic crystals. 15
2.7 Interference effects at thin films. 16
2.8 Interference at multilayer structures and Bragg grating. 18
2.9 Molecular formula of the repeating unit of Tecoflex®EG 72D. 20
2.10 Transmission, absorption, and reflection spectra of Tecoflex®EG 72D. 21
2.11 Molecular formula of the repeating unit of PMMA. 22
2.12 Illustration of the hot embossing process. 23
2.13 Exemplary force and temperature profiles for hot embossing. 24
2.14 Shear modulus as f(T) and displacement as f(t) 25
2.15 Preparation of the mold negative. 27
2.16 Fabrication of the mold and replication. 28
2.17 Structure of the finished mold. 29
2.18 Illustration of the extruding process. 29
2.19 Illustration of the spin coating process. 30
2.20 Exemplary stress-strain curve of a TFX sample. 31
2.21 Set-up and force-distance curve for atomic force microscopy. 34
2.22 Illustration of the set-up to measure AOI resolved reflection. 36
2.23 Tuning of the focal point of a convex lens. 36
2.24 Fabrication of tunable diffractive optical elements made from SMPs. 37
2.25 Demonstration of tunable SMP diffractive optical elements. 38
2.26 Long term stability and time dependent recovery rate. 39

3.1 Organic laser active material Alq_3:DCM. 46

3.2 Schematic of the organic DFB laser device based on a tunable SMP resonator. 46
3.3 Exemplary permanent and temporary shape. 47
3.4 Experimental set-up for device fabrication and optical characterization. 48
3.5 Lasing threshold and life span of the SMP resonator based organic DFB laser. 49
3.6 Tuning of the emission wavelength. 50
3.7 Adjusting of the emission wavelength. 51

4.1 Color production in cephalopods. 56
4.2 Schematic illustration of the tri-layer fabrication. 58
4.3 Different TFX layer thicknesses result in different colors. 59
4.4 Schematic illustration of the programming and tuning procedure. 60
4.5 Tunable color in the programming and recovery steps. 62
4.6 Topography and thickness of the three states of a sample measured with AFM. 63
4.7 Measured and calculated reflection of the three sample states. 64
4.8 Outlook on advancement of our current device. 66

5.1 Examples of hierarchically wrinkled flower petals. 71
5.2 Optical measurements performed on original *Queen of the Night* structures. . 73
5.3 Schematic of the surface wrinkles fabrication process. 75
5.4 Model to describe wrinkle evolution. 76
5.5 Overview of surface wrinkle structures and their adjustability. 78
5.6 Adjustability of wrinkle size through fabrication parameters. 81
5.7 Temperature dependence of the wrinkle formation. 83
5.8 Comparison regarding cracking behavior 85
5.9 Schematical depiction of wrinkling of structured polymer coatings. 86
5.10 Hierarchical, artificial wrinkles mimicking the tulip structure. 87
5.11 Hierarchical, artificial wrinkles mimicking the daisy structure. 88
5.12 Schematic of wrinkling on structured surfaces. 90
5.13 Hierarchical, artificial wrinkles mimicking the treasure flower structure. . . . 91
5.14 Photographic documentation of the fabrication steps. 92
5.15 Influence of Ag film thickness on structure topography. 93
5.16 Schematic of the hot pulling process and wrinkling on pillars. 94
5.17 Exemplary influence of process parameters on the hot pulling success. 96
5.18 Recoverable strain of temporarily hot pulled pillars. 98
5.19 Documentation of the process from stretching to wrinkling. 99
5.20 Pillar structures with wrinkled, vertical side walls. 100

5.21 Wetting behavior of non-hierarchical and hierarchical surface wrinkles. 101
5.22 Transmission and reflection on wrinkled samples and references. 103
5.23 Iridescence on wrinkle structures. 105
5.24 Comparison of the reflectivity of diverse wrinkle structures. 107
5.25 Schematic of the replication process. 108
5.26 Back side reflection of replicated wrinkle and grating structures. 109
5.27 Anti-glaring and light-harvesting properties of wrinkle structures. 110
5.28 Concept of a *Morpho* inspired color tunable device. 112

6.1 Light modulation by a natural opal. 116
6.2 Concepts for color tuning of opals. 119
6.3 State-of-the-art examples of polymer opals. 120
6.4 Schematic of the fabrication of CIS-particles by emulsion polymerization. . . 122
6.5 Different PO particle sizes yield different SMPO colors. 124
6.6 Schematic of the SMPO extrusion process, shearing, and color change. 125
6.7 Materials and products at different stages of the fabrication process. 126
6.8 Influence of PO:SMP ratio on optical appearance. 127
6.9 PeakForce QNM of PO and SMPO samples. 128
6.10 Programming and recovery cycle to determine R_f and R_r. 130
6.11 Demonstration of the color change coupled with programming and recovery. . 131
6.12 DMA of the shape memory abilities of various SMPO composites. 132
6.13 Color change on demand of temporarily imprinted structures. 134
6.14 Spatially resolved recovery due to light absorption. 136

List of Tables

4.1 Height of film and pillars in the three sample states. 63

5.1 Correlation between solution concentration, coating thickness, and period. . . 80
5.2 Correlation between temperature, wrinkle period, height, and recovery rate. . 84
5.3 Process parameters for successful, temporary hot pulling. 97

6.1 Shape fixity ratio and shape recovery ratio for various SMP:PO ratios. 133

List of Abbreviations

1,4-BD	1,4-butanediol
AFM	atomic force microscope
ALMA	allyl methacrylate
Alq_3	tris-(8-hydroxyquinoline)aluminium
AOI	angle of incidence
AR	aspect ratio
BIOS	bending-induced oscillatory shear
CA	contact angle
CB	carbon black
CIS	core-interlayer-shell
c-Si	crystalline silicon
CVD	chemical vapour deposition
DBR	distributed bragg reflector
DCM	4-(Dicyanomethylen)-2-methyl-6-(p-dimethylamino styryl)-4H-pyran
DFB	distributed feedback
DKZ	Deutsches Kunststoffzentrum
DMA	dynamic mechanical analysis
DOE	diffractive optical element
EQE	external quantum efficiency
fcc	face centered cubic
FDTD	finite difference time domain
H_{12}MDI	1-isocyanato-4-[(4-isocyanatocyclohexyl)methyl] cyclohexane
IMT	Institute of Microstructure Technology
IR	infrared
ITO	indium tin oxide
KIT	Karlsruhe Institute of Technology

LCD	liquid crystal display
LED	light emitting diode
LTI	Light Technology Institute
MMA	methyl methacrylate
NIR	near infrared
NOA	Norland Optical Adhesives
OPD	optical path difference
PC	polycarbonate
PDMS	polydimethylsiloxane
PEA	poly(ethyl acrylate)
perm	permanent shape
PET	poly(ethylene terephthalate)
PMMA	poly(methyl methacrylate)
pNIPAm	poly (N-isopropylacrylamide)
PO	polymer opal
PS	polystyrene
PSD	position sensitive photo detector
PTMEG	poly(tetramethylene ether) glycol
QNM	quantitative nanomechanical mapping
R	reflection
rec	recovered shape
SCP	shape-changing polymer
SEM	scanning electron microscope
SMA	shape-memory alloy
SME	shape-memory effect
SMP	shape-memory poylmer
SMPO	shape-memory polymer opal
SW	surface wrinkles
T	transmission
temp	temporary shape
TFX	Tecoflex®EG 72D
UV	ultraviolet
VIS	visible spectrum
VSI	vertical scanning interferometer

A	height
c	velocity
d, h	thin film thickness
ε	strain
E	Young's modulus
F	Force
G	shear modulus
λ	wavelength
Λ	period
m	integer
ν	Poisson's ratio
n	refractive index
ϕ	phase difference
σ	stress, standard deviation
τ	relaxation time
t	time
T	temperature
θ	angle of incidence/reflection

1 Introduction

Nature has ever been captivating and an infinite source of inspiration for researchers and engineers that seek to understand observed phenomena and find answers to existing problems. Survival of the fittest has lead to the evolution of highly diverse, perfectly optimized life forms in every habitat since the beginning of life on earth 3.8 billion years ago. Adaptation to environmental conditions, nourishment and mating are the driving forces to nature's development of most efficient solutions in terms of energy and material consumption.

With the advancements in microscope technologies and the invention of the transmission and scanning electron microscope in the first decades of the 20^{th} century scientists have been able to link macroscopically observed phenomena to the responsible micro- and nano-structures.[1,2] Properties such as the famous self-cleaning properties of the lotus leaf can now be explained by the hierarchical microstructure coated in wax crystals covering the leaves' surfaces.[3] The sublime adhesion of geckos on nearly every surface is now understood to be caused by attractive forces on the atomic scale between the respective surface and the nanosized tips of hierarchical hairs on the gecko's toes.[4]

The newly gained resolution with those microscopes also allowed to fathom the cause of some of the most vivid and brilliant colors witnessed in nature: structural colors. Not only their striking intensity fascinates but also the viewing-angle dependent hue. Those colors are caused by diverse interactions of light with sophisticated nanostructures generated by the respective species. Color generating structures range from structures as simple as a single thin film to complex, three-dimensional architectures. Wavelength-dependent phenomena such as interference, diffraction, and scattering and often combinations of them modulate the propagation of light and give rise to the marvelous colors.[2]

Among the most popular examples for structural coloration are the shining blue-green feathers of male peacocks. Less than 200 nm thick melanin rods arrange to a regular, 2D photonic crystal-like structure.[5] As well as the peacock feathers, nacre has been used for decorative purposes since centuries because of its colorful, pearly luster. Nacre consists of stacks of around half a micron thick aragonite platelets that cause the often in shells observed multicolored iridescence through interference effects.[6] The most multifaceted

occurrence of structural colors is probably found among insects with the magnificent blue of the *Morpho rhetenor* butterfly as the most prominent example. In the scales of this butterfly species' wings a Christmas-tree like architecture causes multilayer interference and therefore, reflects the incident light highly wavelength selective.[7] Besides being bright and brilliant, structural colors are extremely long-lasting. More than 200 years old beetle exosceletons are today as intensely colorful as fresh specimen.[8] Structural colors occur due to purely physical interaction of light and matter that reflect certain wavelengths to the observer. Hence, they are highly energy efficient.[2] Pigmentary colors, however, are not nearly as long-lasting. In pigments, the color is produced by selective absorption of a small wavelength range of light. The chemical structure of pigments define how much energy, i.e. which wavelength, is consumed to excite electrons to a higher state. Radiation with high photon energy such as UV light can destroy the molecules with time and the colors fade.[2,9] Those pigmentary colors are one of two ways that dominate the color producing mechanisms in our daily lives. They are used to dye anything from fabrics to paint to plastics. Besides the drawback of fading, the synthesis of pigments often involves highly toxic chemicals and leads to serious pollution and environmental issues. The second way to make our lives colorful are colors produced by emission such as in, amongst others, LEDs (light emitting diode) and LCDs (liquid crystal display). In LEDs a high-energy electron combines with a low-energy hole and the energy difference is released as a photon of respective energy, hence, color.[10] In LCDs color is produced by changing the transmission of the respective color generated by fluorescent or phosphorescent light sources.[11] In all cases, constant energy supply is needed. Structural colors neither fade, are toxic, nor constantly consume energy. Furthermore, they feature another interesting asset. Since the formation colors relies on the interaction of light with structure features of few hundred nanometers, smallest changes in the size of those structures yield significant color changes. Together with the previously listed benefits, the realization of tunability in structural colors makes them extraordinarily promising candidates for electronic paper applications.

The objective of this work comprises the development of concepts to accomplish the realization of those structures and address the necessary structure changes required for tunable colors by utilizing smart materials, in this case shape-memory polymers.

Smart materials comprise a class of materials, that react independently and in a defined way to specific stimuli to serve a particular purpose. Shape-memory polymers are among this class of materials. Due to their specific molecular structure shape-memory

polymers can remember a predefined shape and recover it even after strong mechanical deformations. This recovering process is triggered by a proper stimulus like heat or light.

Shape-memory polymers are novel materials for optical applications but their assets such as transparency, thermoplasticity, and shape-changing ability suggest them as very promising candidates for tunable optics.[12] Common fabrication techniques for micro- or nanostructured optical components such as diffraction gratings allow high precision production. However, in practically all cases the structure is fixed at the end of the fabrication process. Demanded structure changes require the cost- and time-consuming manufacturing of new structures and hence, tuning is only possible in successive steps. If elastic materials are utilized, changing of structure features by stretching might be feasible but a mechanical framework to impose and sustain the strain is needed.

Light modulating structures made from shape-memory polymers have been proven to overcome those drawbacks in previous work of our group.[12] Tunability of optical features of a structure is effectuated by programming and on demand recalling shape changes of the shape-memory polymer material. First, the effect was demonstrated macroscopically with a shape-memory polymer lens that allows continuous tuning of the focal length. Subsequently, the principle was transferred to the micrometer scale and the shape-memory effect was utilized to tune the crucial structure features of diffractive optical elements. The basic findings of this work are recapitulated in the state-of-the-art section of **Chapter 2**. In addition, this chapter provides the theoretical background for this thesis regarding shape-memory polymers, fundamentals of light modulation at periodic structures, and the applied fabrication techniques as well as analytic methods.

Chapter 3 introduces my advancements on the fabrication on tunable shape-memory polymer structures. Compared to the diffractive optical elements, the feature size was further scaled down to nanometer dimensions and the results on the application of those structures as tunable resonators for organic distributed feedback lasers are presented.

In the next three chapters I introduce several bioinspired approaches for using shape-memory polymers to either fabricate or tune micro-and nanostructures that cause structural coloration. Leaving behind the simple structures of diffractive gratings, the potential of shape-memory polymers to realize - with each chapter - increasingly complex architectures as observed in the biological role models is explored as graphically summarized in **Figure 1.1**. Every chapter presents the respective inspiration for my work and provides background information. Additionally, the developed fabrication methods and tuning strategies are explained and the results summarized and discussed.

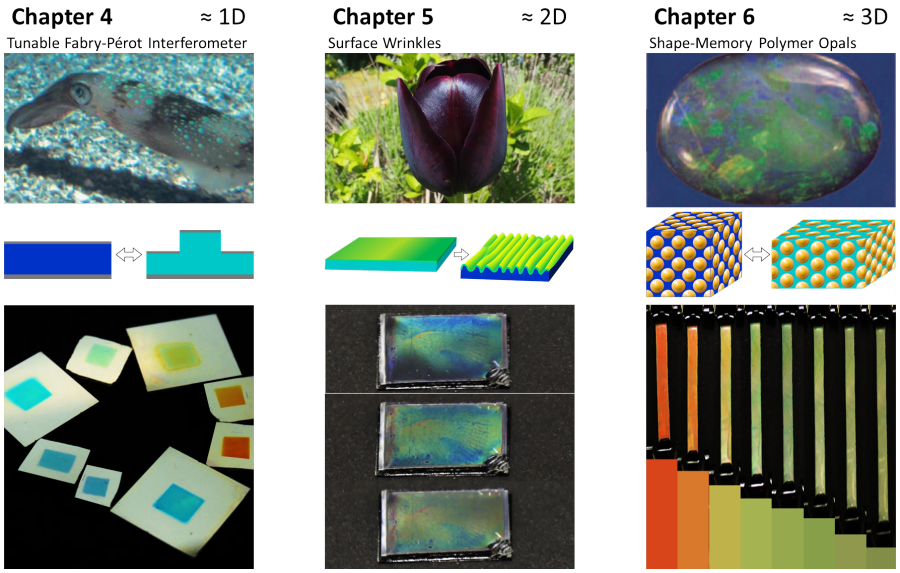

Figure 1.1: **Outline of my work on bioinspired concepts for using shape-memory polymers to either fabricate or tune micro-and nanostructures that cause structural coloration.** Photograph of squid (top left) adapted from [13], photograph of opal (top right) adapted from [14].

Chapter 4 contains my approach to mimic tunable thin film interference as exhibited in some cephalopod species in an artificial structure. Here, the development of a tunable Fabry-Pérot interferometer based on an in thickness variable, one-dimensional shape-memory polymer thin film is shown.

Illustrated in **Chapter 5** is the benefit of shape-memory polymers to enable mechanically directed self-assembly of disordered diffraction gratings. Diverse advancements of the developed full-polymer wrinkling method to resemble the two-dimensional, hierarchical structures found on petals are developed and the respective results presented. The study is completed by an in-depth optical characterization of the basic structure and a proof-of-concept of their application on photovoltaic devices.

In **Chapter 6** a material is introduced that mimics the striking optical appearance caused by the three-dimensional photonic crystal structure in opals but features in addition a broad tunability of its structural color. My concept to implement otherwise needed external forces into the material by adding a shape-memory polymer is presented and the resulting material is characterized.

Finally, in **Chapter 7** a summary and an outlook on possible future developments are given.

2 Theoretical Background

For the development of novel devices that, in some way, modify the propagation of light with micro- and nanostructured shape-memory polymers, an understanding of the nature of those polymers and their interaction with light is necessary. Therefore, this chapter gives an introduction to the molecular mechanism of the shape-memory effect as well as shape-memory polymers in general and the modulation of light by periodic structures, specifically for wavelength selective reflection, is discussed. Additionally, the for my work relevant basic techniques and materials used to fabricate my structures are presented and the important analytic methods are described. And finally, a state-of-the-art summary highlights pioneering work on the implementation of shape-memory polymers in tunable optical devices.

2.1 Shape-Memory Polymers

Since a few decades, one of the main focuses of material scientists is the development of smart materials.[15–20] In a loose definition, this class of materials comprises materials that react independently and in a defined way to specific stimuli to serve a particular purpose. Shape-memory polymers along with, e.g., shape-memory alloys and self-repairing materials have been at the forefront of research interest in this material class. Especially designing multifunctional materials with an unexpected combination of functionalities, i.e., biocompatibility, biodegradability, specific mechanical properties, thermo-, electric- or optical responses, and shape-memory effect (SME) is of interest. In general, shape-memory polymers (SMPs) are polymers that respond to an appropriate stimulus with a previously defined shape change. As a result of their special molecular structure and a certain programming cycle, the basic SME is characterized by the SMP's ability to retain a second, so-called temporary shape while remembering an original, permanent shape and to recover this shape on demand. The permanent shape is defined while synthesizing or, regarding thermoplastic SMPs, by melt processing. Mechanical deformation of the permanent shape into any arbitrary shape at the individual SMP's specific conditions programs the temporary shape into the polymer. When the SMP is subsequently exposed to a suitable trigger such as heat, electrostatic or magnetic field, solvent, or light, the SMP re-

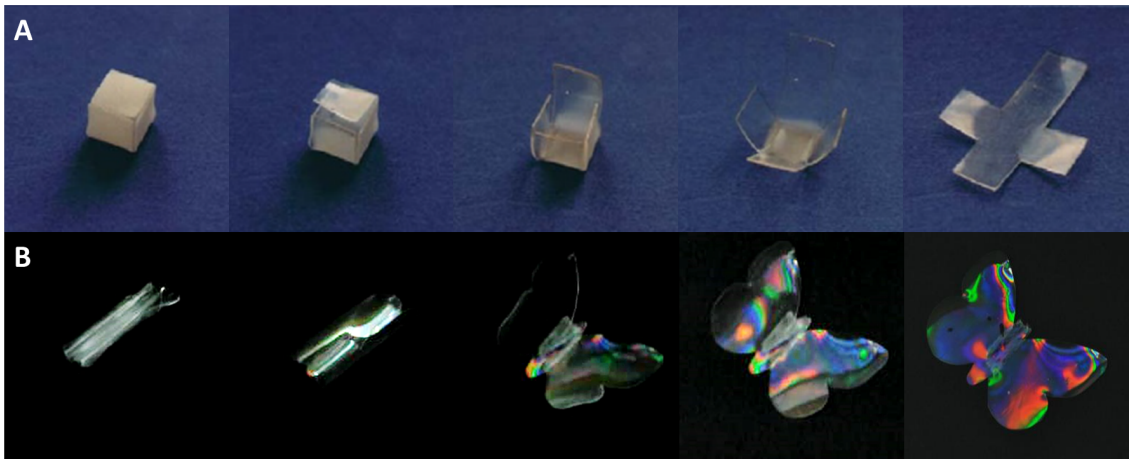

Figure 2.1: **Demonstration of the shape-memory effect of two polymers.** The photo-sequences demonstrate the shape recovery process of temporarily deformed SMP samples (left) back to their original, permanent shapes (right). **A** For the temporary shape, a covalently cross-linked polymer network was folded into a cube. Upon heating it to 70 °C the sample recovers its original flat shape. **B** A butterfly shaped cut-out of a microstructured polyurethane SMP foil unfolds its wings in the recovery process. The recovered flat shape appears colorful due to diffraction of light at the imprinted microstructure. Adapted from [21].

covers its original shape. Two exemplary shape changing cycles from the permanent to the temporary and back to the permanent shapes are reported in **Figure 2.1**. The facile synthesis, processing, and programming of SMPs recommend their utilization as an inexpensive alternative for some applications of well-established shape-memory alloys (SMA). Usually, SMPs surpass their metallic alloy counterparts by far in terms of strain recoverability. Reportedly, SMAs allow a displacement in the range of 8 % of the material dimensions, while SMPs show significantly higher shape-changing capabilities.[15,22,23] To give some examples, chemically crosslinked, acrylate based SMPs can have recoverable strains of $\varepsilon_{rec} > 800\,\%$, shape-memory natural rubbers with $\varepsilon_{rec} = 1000\,\%$, and $\varepsilon_{rec} \approx 1500\,\%$ for polyethylene blend materials have been reported.[24–26]

2.1.1 Shape-Memory Effect

In its most common and plain form the SME constitutes of a thermally triggered, one-way transition between two shapes. Each of those characteristics can be used to classify SMPs. The basic principle needed to obtain a shape-memory effect is the existence of two (or more), individually addressable domains in the polymer. These can be present in the form of, e.g., functional groups, crystalline and amorphous phases, or differing glass transition temperatures in the segments of block co-polymers. The molecular mechanisms

yielding the shape-memory ability in each of those examples are highly diverse and will be discussed in a few examples in the following.

One-Way SMPs

In a typical one-way SMP, the molecule chains build a network held together by two different or differently strong molecular interactions. In this structure, so-called netpoints (the segments with the stronger interactions) are linked with each other by the softer, switching segments (the segments with weaker interactions or otherwise stimulus-sensitive bonds).[15–21,27] When an external, mechanical force is applied, the strain is first compensated by a deformation of only the softer segments since in those segments the resistance to rotational and translational motion is lower than in the netpoints. To effect a quasi-plastic deformation, a trigger-specific shape-fixing treatment is applied. An exposure to the proper stimulus at any time afterwards, releases the interactions between the switching segments and they relax to their initial conformation. This motion is guided by the netpoints. The polymer used for this study is an amorphous block co-polymer with a thermally triggered one-way SME. On account of this, this particular molecular mechanism is discussed in detail. The in the previous section mentioned cycle, consisting of a permanent shape that is programmed into a temporary shape by mechanical deformation and subsequent recovery upon triggering, is schematically illustrated in **Figure 2.2** for a thermoplastic, thermally activated, one-way SMP. In the given example of a thermorheological simple polymer, the netpoints as well as the switching segments both consist of amorphous segments of the different blocks of the block co-polymer that arrange phase-segregated. As those blocks are composed of dissimilar monomers, the molecular interaction forces differ in strength which results in two unequal glass transition temperatures of those domains. A lower glass transition temperature T_{switch} correlates with the weak interactions in the switching segments and a higher glass transition temperature T_{perm} refers to the netpoints' softening range. If the thermoplast is heated above T_{perm}, both segments are in a melt state and the chain motion is barely constricted, hence, low forces are sufficient to form the polymer into any arbitrary shape. While cooling down, the blocks separate again into the two domains of netpoints and switching segments with the individual switching segment chain blocks being in their relaxed, highest entropy state. To program a temporary shape, the SMP is deformed at a temperature well below T_{perm}, typically in the range of T_{switch} or slightly below. At this temperature, the netpoints are still frozen in their energy elastic state with therefore high resistance to distorting external forces. Simultaneously, the polymer chain domains in the switching segments are in

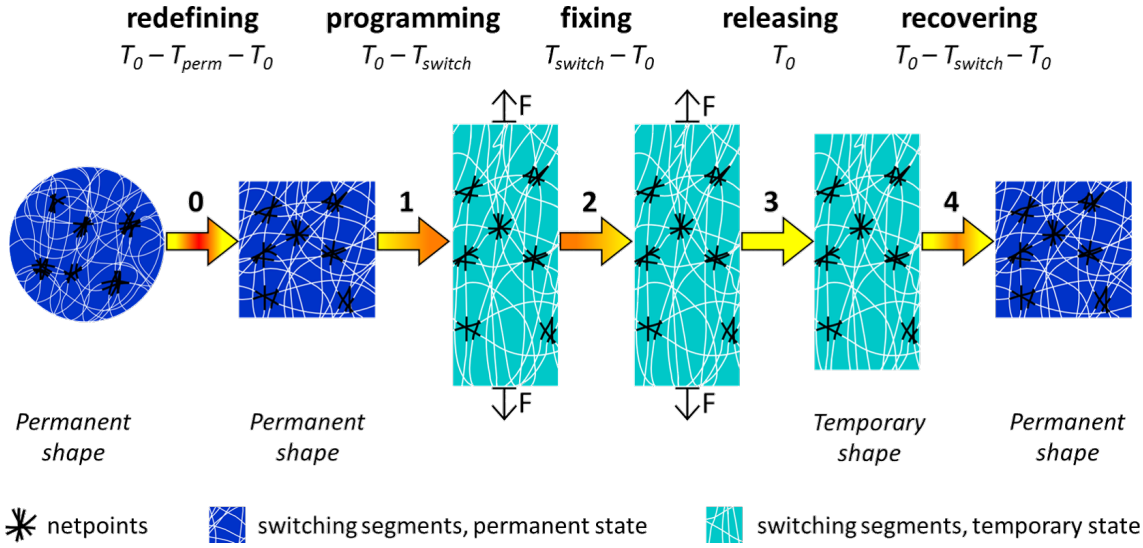

Figure 2.2: **Molecular mechanism of the thermally triggered, one-way shape-memory effect.** **Step 0** The permanent shape can be redefined by deformation of the SMP above T_{perm}. **Step 1** For programming the temporary shape the sample is first deformed (in this example stretched) at a temperature not exceeding T_{switch}. **Step 2** Fixing of this shape takes place by cooling the sample under constant load. **Step 3** Releasing the load afterwards yields a small contraction due to the elastic part of the deformation. **Step 4** Subsequent heating of the sample above T_{switch} triggeres the recovery process and the sample morphs back to its original, permanent shape.

their entropy-elastic state with higher chain mobility. The latter compensate the imposed deformation first by an elastic rotational motion of the molecular bonds and then by disentangling and flow. This leads to a displacement of the chains, i.e., viscous flow, to the extent the matrix of netpoints allows displacement. When cooled down under constant load, the motion of the switching segments chain blocks is suppressed and they freeze in their momentary conformation. At this low temperature T_0 the molecular interaction forces in SMPs exceed the restoring forces arising from the non-equilibrium, tensed conformation of the switching segments. Hence, the polymer keeps this imposed, temporary shape even after the external load is detached. However, after releasing the force, an elastic part of the deformation of the switching segments causes a small, proportionate reversion of the deformation. If now the temperature of the polymer is raised to T_{switch} to trigger the shape-memory effect, motion of the switching segment chain blocks is enabled again as the chain mobility drastically increases around the glass transition temperature. In absence of an external force, the molecule chains aim for the conformation with their equilibrium state of highest entropy and therefore lowest energy. Still connected by the matrix of netpoints, the only way all of the switching segments can recover this state is to restore the conformation they had in the shape that was defined from melt previously. In

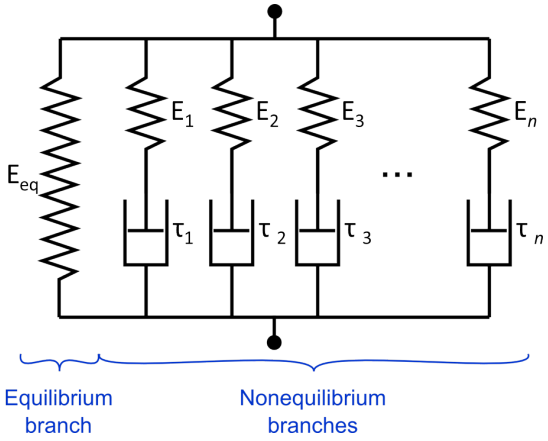

Figure 2.3: **Rheological model for the shape recovery process.** The recovery dynamics are described by the combination of an elastic spring (equilibrium branches) and multiple thermo-viscoelastic Maxwell elements (non-equilibrium branches).

order to recover this conformation, the switching segments pull or push the netpoints into a spatial arrangement equal to the one of the initial shape, which, macroscopically, results in the recovery of the original, permanent shape. Alternatively to the shape transformation in free recovery conditions, the SMP can provide recovery stresses if it is spatialy constrained during the recovery step.

The recovery can be described by the well-known multi-branch rheological model consisting of one equilibrium branch and, to give consideration to the multiple relaxation processes, several thermo-viscoelastic non-equilibrium branches.[28,29] The equilibrium branch, and thereby the elastic response, is represented by a single spring. The viscoelastic behavior of a polymer is represented by a Maxwell element (non-equilibrium branch) consisting of a Hookean spring and a Newtonian dashpot in series. The dashpot describes the viscosity and the relaxation time as strongly temperature dependent mechanical characteristics of the polymer. The total stress $\sigma(t)$ in dependence of time described by this model results from the Boltzmann's superposition principle to:

$$\sigma(t) = E_{\mathrm{eq}} e_m(t) + \sum_{i=1}^{n} E_i e_i^e \tag{2.1}$$

with

$$e_i^e = \int_0^t \frac{de_m(s)}{dt} \exp\Big(- \int_{\mathrm{s}}^{\mathrm{t}} \frac{\mathrm{dt}'}{\tau_{\mathrm{i}}(\mathrm{T},\mathrm{t}')} \Big) \mathrm{ds} \tag{2.2}$$

where E_{eq} and E_i are the elastic moduli of the equilibrium (eq) and non-equilibrium ($i = 1$, ..., n; n = number of branches) branches, respectively. The total strain is given by $e_m(t)$ and e_i^e describes the elastic strain evolution in each of the non-equilibrium branches as a

function of $\tau_i(T)$, the relaxation time in dependence of the temperature T in the dashpots. A more detailed discussions on the thermo-rheological behavior of polymers can be found in references [30–32].

The extent, to which a polymer is able to retain a temporary shape and recover its permanent shape, is not only determined by its molecular structure but also affected by the thermo-temporal conditions during programming and recovery. [29] Programming temperature, deformation rate, and holding time as well as recovery temperature, heating rate, and time have a strong influence on the SMP's performance. Netpoints can also be built by crystalline physical crosslinks or chemical crosslinks such as covalent bonds instead of amorphous hard segements. [16–20,23,27,33–37] In the case of covalent bonds, the thermoplasticity of the material is lost and the permanent shape has to be defined during synthesis. The diversity of switching mechanisms and stimuli is at least as diverse as the variety of netpoints. Semi-crystalline domains respond very similar to the discussed amorphous switching segments and constitute the second type of thermally triggered SME. However, the shape fixation and relaxation can also be effected by building and breaking of bonds such as for instance covalent bonds, hydrogen bonds, and ionic assemblies. With this diversity, the SME can be tailored by implementing molecular switches that are sensitive to light, radiation, moisture, pH level, solvent, and many other triggers. [21]

Multi-Shape SMPs

The principles of one-way SMPs that are able of one self-acting shape change that is defined by the permanent shape and one temporary shape, were recently advanced to design SMPs that feature more than one temporary shape. Additional temporary shapes are achieved by incorporating a second switching mechanism into the molecular structure. As a result the SMP responds for example with two distinct shape changes to two different temperatures in the case of a fully thermally triggered polymer or one of the above mentioned triggers is implemented to enhance the functionality of the SMP. [27,28,38–42]

Two-Way SMPs

The as yet described SMPs offer the possibility of a singular autonomous shape change but need to be reprogrammed by external forces for further usage. This drawback is overcome by two-way SMPs which are capable of a repeatedly reversible shape change. Their SMEs are caused by a slightly different molecular mechanism. Based on the respective molecular mechanism, such polymers can be divided into shape-changing polymers (SCPs), that feature a shape change of one spatial dimension between two fixed equilibrium states, and

two-way SMPs with their capability of switching reversibly between two programmable temporary shapes.[19] An example for SCPs are liquid crystalline elastomers. The crystalline domains loose their configuration when a critical temperature is exceeded which yields a contraction of the according polymer chains. If this effect is concentrated in one direction by primarily biasing the polymer, the superposition of all those contractions results in a macroscopically noticeable shape change. The process is reversible by decreasing the temperature again. Thus, switching between two distinct sample lengths, the high temperature length and the low temperature length, is possible.[19,43–49] Crystallization and decrystallization in response to a lower and an elevated temperature also give rise to a shape change in semi-crystalline networks. To accumulate those, on molecular level occurring, chain length changes, a constant load is necessary to align the chains unidirectionally.[19,50,51] Therefore, these polymers are suitable rather for providing recovery stress than for actual shape-changing applications. True two-way SMPs, that overcome the one-way limitation and the restriction to two constant temperatures and preload required by SCPs, have been reported. The two-way effect is achieved by providing two different crystalline phases in the switching segments of one polymer.[52–55] The key to this concept is to separate the tasks of shape fixation and entropy driven relaxation to two different domains and thereby implementing the for one-way SMPs needed external force for reprogramming into one polymer network. However, since this two-way effect relies on crystalline domains, their applicability for optical components is limited due to the lack of transparency.

2.1.2 Applications of Shape-Memory-Polymers

The wealth of potential applications of SMPs is enormous in various areas of our daily lives: From self-repairing car bodies to kitchen utensils, from airplanes to satellites, from switches to senors, from intelligent packaging to tools to toys. The first commercially relevant SMP was covalently cross-linked polyethylene that has found excessive use predominantly as packing films and insulating shrink wraps since the 1960s.[56–59] Around the same time numerous heat-shrinkable polymers such as cross-linked polyvinylchloride, polyolefines, polyamides, or polytetrafluoroethylene, and silicone rubbers have been developed and are nowadays mainly used for packaging. The specific development and utilization of polymers with SME was pioneered by thermoplastic polyurethane-based SMPs that found applications in automatic chokes for combustion engines, protection cover for auto assembly lines, damping materials, smart textile products for outdoor and sports clothing, and various toys for children.[60,61] Two of the most profoundly studied fields

for future SMP applications are aerospace and medical devices. Under intense investigation is the benefit of SMPs for the realization of self-unfolding screens for satellites and hinge structures in aerospace devices due to their light weight and smart actuation.[62–66] For medical engineering, the special properties and multifunctionalities of SMPs have been explored and applied for polymer stents with implemented drug delivery systems, orthodontic wires, softening intravenous canula, micro-actuators for treating strokes, and smart surgical sutures.[23,67–71] Recently, with the advancements in micro and nanostructuring technologies, using the shape-memory effect of polymers for actuation on such small length scales came to the fore.[19,72–79] In those reports, the SME was either used to provide surface structures with tunable properties such as for example wetting behavior, dry adhesion, or interaction with light, or to create micron and sub-micron sized structures with methods that overcome the current limitations of microstructuring technologies. The majority of those mentioned applications require specially designed, multifunctional and high performance SMPs. Material research is at the beginning of this mission propelled by the massive economical prospects.

2.2 Light Modulation by Periodic Structures

To predict the behavior of light in reaction to an object that is much larger than the wavelength λ, ray optics can be sufficient. However, in order to understand the interaction of light with micro and especially nanostructures it is necessary to understand the wave character of light. Defined as light is a certain range of the spectrum of electromagnetic waves. Furthermore, only a part of this range is the spectrum visible for humans. This visible light (VIS) ranges from violet (390 nm wavelength) to red (760 nm) framed by the ultraviolet (UV, 10 nm to 390 nm) and the infrared (IR, 760 nm to 300 μm).[80] This section gives a brief and basic introduction to the interaction of light with periodic structures. For detailed discussions on the topic I like to refer to relevant literature.[80–84]

2.2.1 Reflection, Refraction, Diffraction, and Interference

Light travels as a wave with a velocity of $c_0 \approx 3.0 \times 10^8\,\mathrm{ms}^{-1}$ in vacuum.[80–83] In a homogeneous medium, the electromagnetic wave has a decreased velocity c and its relation to c_0 is determined by a medium characteristic constant, the refractive index n of the medium, according to

$$c = \frac{c_0}{n}. \tag{2.3}$$

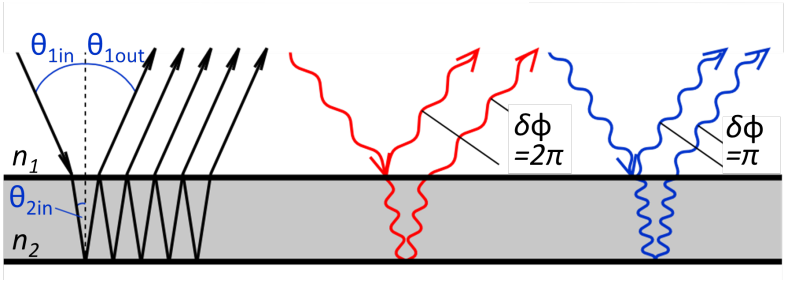

Figure 2.4: **Reflection, refraction and interference at a thin film.** The angle of the reflected light beam is the same as the angle of incidence (black). The refractive index of the medium influences the light propagation: depending on the wavelength, the light path is refracted to differing angles. Reflected waves interfere constructively, if the phase difference is 2π (red) and destructively, if the phase difference is π (blue).

If a wave with an angle of incidence of θ_1 is reflected on a flat mirror, a reflected wave at an angle of θ_2 occurs. At the surface of the mirror ($z = 0$), the exact same conditions apply to incident and reflected wave. Hence, angle of incidence and the angle of the reflected light must always be equal:

$$\theta_{1\text{in}} = \theta_{1\text{out}} \tag{2.4}$$

In the case that the wave is only partially reflected at the interface of two mediums with different refractive indices n_1 and n_2, a part of the beam travels through the second medium. Again, at $z = 0$ all three waves are subject to the same conditions and are equal. This correlation is known as the Snells' law:

$$n_1 \sin(\theta_1) = \mathrm{n}_2 \sin(\theta_2) \tag{2.5}$$

When light propagates from one medium with n_1 with an angle of incidence θ_1 to a second medium with n_2, the waves change their propagation direction to θ_2, the angle of refraction. The change of medium results in a change of phase velocity but the frequency remains constant, hence, for the wavelength applies $\lambda_2 < \lambda_1$ for $n_2 > n_1$. If the medium with n_2 is a slab with a finite thickness of d, a part of the wave is reflected at the bottom interface and thereafter exits the slab at the upper interface as depicted in **Figure 2.4** on the left side. At this interface, the wave is refracted a second time. Although this wave travels with the same direction, wavelength, and frequency as the first reflected wave, there is a phase difference depending on the slab's thickness d.

$$\delta\phi = \frac{2\pi}{\lambda} d \sin(\theta_1) \tag{2.6}$$

To understand the diffraction of light as it occurs in diffraction gratings, the Huygens-Fresnel principle has to be considered. This principle says, that every point of a wave front is a point source of a spherical wave. The superposition of those secondary waves builds a new wave front. Whenever two or more waves exist, their electric fields superimpose. In this so-called interference effect, the individual amplitudes combine to a resultant amplitude. Constructive interference occurs when the phase difference between the waves is 0 or an integer multiple of 2π: the waves are in-phase and the resultant amplitude is equal to the sum of all waves' amplitudes. Differs the phase by an odd integer multiple of π, the waves are anti-phase and the sum of the amplitudes is zero. Destructive interference occurs. Phase differences between those two extremes lead to amplitudes between the two described maxima.

2.2.2 Diffraction Gratings

The light modulating properties of diffractive gratings are caused by their periodic microstructure. The optical path difference (OPD) experienced by light propagating through this grating is alternated perpendicularly to the light's direction with structure features in the same range as the wavelength.[81,82] Waves exiting the grating at a cavity interfere with the waves exiting the adjacent bar. Those two types of waves differ in phase due to the different OPDs and, as explained by the Huygens-Fresnel principle, the incident beam is diffracted. Constructive interference always occurs when $OPD = m\lambda$ is satis-

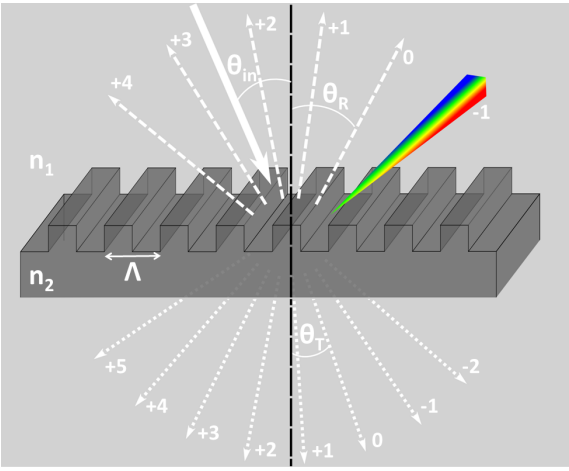

Figure 2.5: **Diffraction grating.** The incident beam is split into various diffraction orders in reflection (dashed) and transmission (dotted).

fied. According to this relation, for monochromatic incident light, interference maxima are positioned at the diffraction angles θ_m ($m = 0, \pm1, \pm2, ...$) that fulfill

$$\sin(\theta_\mathrm{m}) = \sin(\theta_\mathrm{in}) + \mathrm{m}\frac{\lambda}{\Lambda}. \tag{2.7}$$

The splitting of the incident beam into various diffraction orders in reflection and transmission is schematically depicted in **Figure 2.5**. Since the diffraction angle is a function of the wavelength λ each wavelength is diffracted at a slightly different angle. Hence, with non monochromatic light each diffraction order (except m=0) exhibits spectral dissection. This is indicated in the first order in reflection in Fig. 2.5.

2.2.3 Photonic Crystals

Photonic crystals are nanostructured materials with a periodic modulation of the refractive index. This periodic modulation can be in one, two, or three dimensions resulting in one, two, and three-dimensional photonic crystals, respectively, as depicted in **Figure 2.6** (illustration based on [85]).

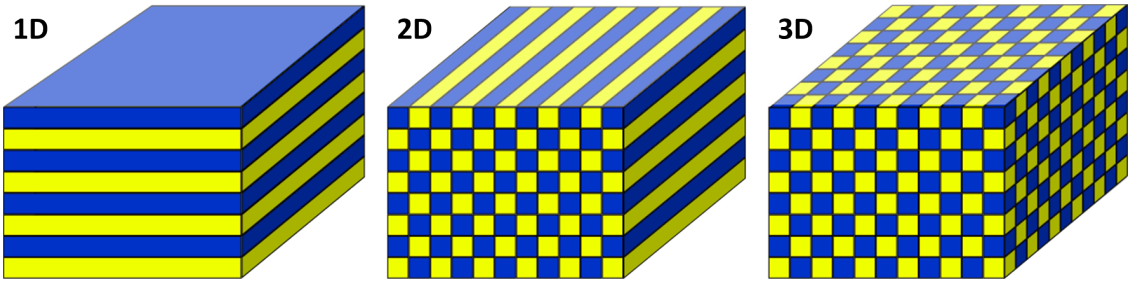

Figure 2.6: **Types of photonic crystals.** One-dimensional, two-dimensional and three-dimensional photonic crystals are characterized by the dimension with periodically modulated refractive index.

The name *photonic crystal* originates from the analogy of photons propagating in this nanostructures like electrons in atom lattices in solids. Similar to semi-conductor materials for electrons, the photonic crystal can show a photonic band-gap for photons with a specific wavelength depending on the feature sizes and refractive indices of the crystal's materials. These photons are completely reflected by the photonic crystal while others propagate unobstructed. The intense color of photonic crystals is due to this phenomenon and occurs, when the band gap is in the range of the visible spectrum.[2,81,83] In natural photonic crystals and also most artificial photonic crystals composed of polymers, the refractive index difference between the materials is not sufficient to cause a complete pho-

tonic band gap. Instead, a stop band or pseudo gap occurs where the forbidden wavelength changes with the orientation of the crystal yielding angle dependent colors.

One-Dimensional Photonic Crystals

The most basic way to form structural colors in the form of iridescence is the interference of light due to reflection at a thin film of a transparent, dielectric medium with n_2 and constant thickness d_2 bound by two "infinite" media. The term "thin film" refers to film thicknesses in the same range as the wavelength of the light. Technically speaking, single thin films are not considered as photonic crystals. Nevertheless, thin film interference is introduced in this chapter due to its one-dimensional character and as basic principle for multilayers. The two mentioned infinite media enclosing the dielectric thin film can exist in two configurations: one where both of the enclosing media have a lower reflective index $n_1 < n_2$ and a second one where one of the framing layers is optically more dense than the film $n_1 < n_2 < n_3$. The first case is the same configuration as in a soap bubble, the latter as in an anti-reflective coating.[2] Both are schematically represented in **Figure 2.7** A and B, respectively. Because reflection at an optically more dense material changes the incident wave's phase by π, the two configurations cause opposite interference conditions for the same wavelength. Part of the incident light is reflected at the upper interface and interferes with the part of the light, that is reflected by the lower interface and subsequently transmitted by the upper interface. Depending on the phase difference of each wavelength, constructive or destructive interference occurs. This phase difference is determined by the possible phase shifts and the optical path length inside the n_2 film

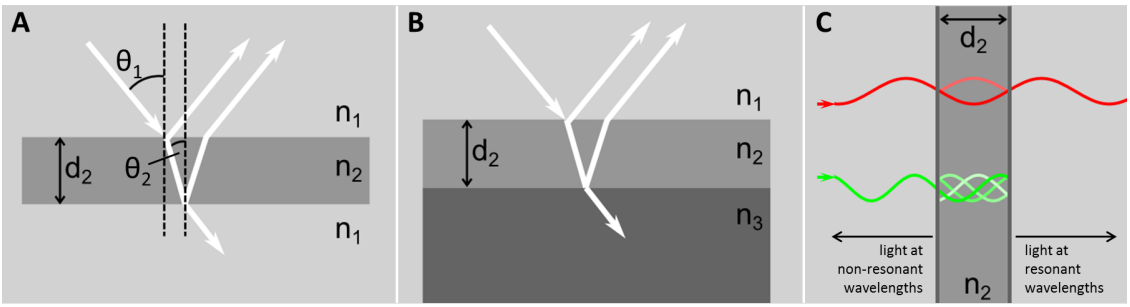

Figure 2.7: **Interference effects at thin films. A** As in a soap bubble the thin film is bound by lower refractive index media. Constructive interference occurs when the optical thickness of the film is $\lambda/4$. **B** The same film attached to a higher refractive index medium yields destructive interference at a thickness of $\lambda/4$ as an anti-reflective coating. **C** If the interfaces framing the film are highly reflective, the dielectric film can be regarded as Fabry-Pérot interferometer with effective wavelength selective transmission.

and therefore by the angle of incidence θ_1, the film thickness d_2, and the refractive indices n_1, n_2, and n_3. Constructive interference in the soap bubble case is given if the condition

$$2 n_2 d_2 \cos(\theta_2) = (\mathrm{m} - 1/2)\,\lambda \tag{2.8}$$

is fulfilled with the wavelength λ, angle of refraction in the film θ_2 and m as an integer. In the anti-reflective coating case, constructive interference occurs for

$$2 n_2 d_2 \cos(\theta_2) = \mathrm{m}\,\lambda. \tag{2.9}$$

If the conditions (2.8) and (2.9) are fulfilled for the other case, respectively, destructive interference is obtained.

Usually, the reflectivity of these interfaces is considered as low and single reflection at each interface is regarded. If the reflectivity is considerably higher multiple reflections at each interface occur. Multiple beam interference amplifies the reflectance for the wavelengths that interfere constructively at the given conditions and suppress the others. Such structures of a thin film framed by plane-parallel, highly reflective materials can be regarded as a kind of Fabry-Pérot interferometers that act as efficient wavelength filters in transmission as well as reflection as illustrated in Fig. 2.7 C (illustration based on[86]). In such a Fabry-Pérot interferometer, wavelengths that resonate between the reflective interfaces, i.e. wavelength that satisfy the relation

$$\lambda = \frac{2 n_2 d_2 \cos\theta_2}{m}, \tag{2.10}$$

are transmitted. Hence, the reflected spectrum of the non-resonant wavelengths exhibits significant dips at those wavelengths.

The concept of thin film interference can be expanded to stacks of a pair of films of two materials with different refractive indices: multilayers or one-dimensional photonic crystals. An exemplary structure of a multilayer is depicted in **Figure 2.8** A (illustration based on[87]). Similar to the thin film, dependent on angle of incidence θ_1, refractive indices $n_2 < n_3$, and thicknesses of N alternating layers of two materials d_2 and d_3, the multilayer reflects highly wavelength selective. If we look at one (3) layer between two (2) layers, the same conditions apply as in the case of the soap bubble. A high refractive index layer is framed by two low refractive index layers and the same relation for constructive interference (Eq. 2.8) is valid. For a (2) layer between two (3) layers, phase shifts at both

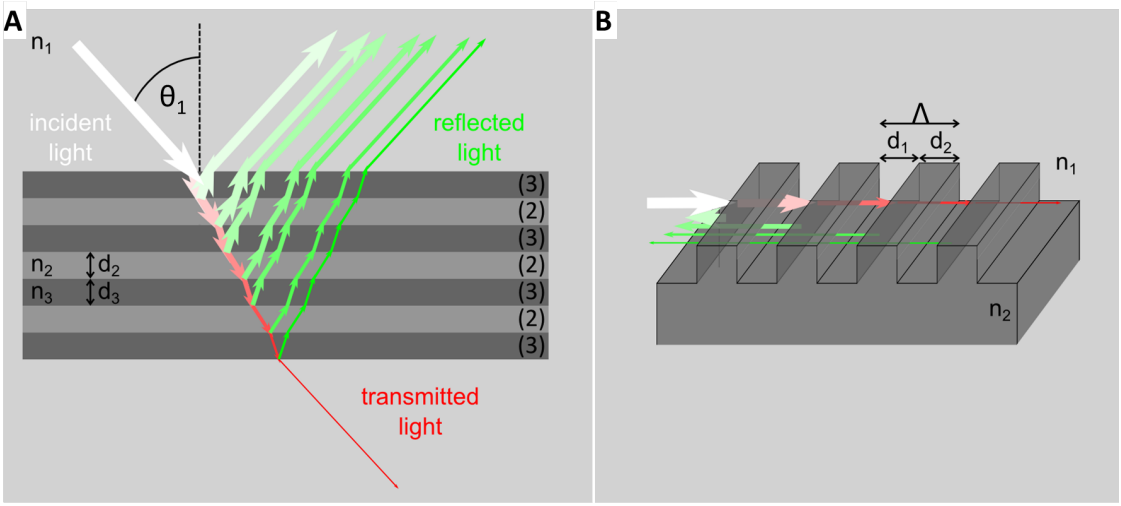

Figure 2.8: **Interference at multilayer structures and Bragg grating. A** Incident white light is reflected at every interface of a mulitlayer structure. Depending on layer thicknesses and refractive indices, different wavelengths interfere constructively when reflected. The structural color of the multilayer originates from this wavelength selection. **B** Periodical modulation of refractive index can also be achieved with a surface grating and light propagating in the direction of the periodicity as in a Bragg grating.

((2)-(3)) interfaces have to be considered. The condition for constructive interference resembles the previously discussed case of the anti-reflection coating:

$$m' \lambda = 2 \left(n_2 d_2 \cos(\theta_2) + \mathrm{n_3\, d_3} \cos(\theta_3) \right). \tag{2.11}$$

An *ideal multilayer* is the particular configuration with $m = m' = 1$, corresponding to the lowest order case where the optical path lengths $n_2 d_2 \theta_2$ and $n_3 d_3 \theta_3$, respectively, are equal. The number of layers influences the effect of a multilayer in that with increasing number the peak reflectivity increases while the bandwidth gradually decreases. However, this discussion of multilayer interference in this simplicity is only applicable for low refractive index contrasts. For higher contrasts, multiple reflections within the respective layers have a stronger impact and the mechanism of interference is significantly complicated. Due to the large differences of the refractive indices of the two layer materials, reflection at the interfaces is drastically increased. In principle, the larger the refractive index difference the less layers are needed to gain high selective reflectivity and the broader the bandwidth and vice versa. Dependent on the thicknesses of those layers, specific wavelengths cannot propagate through the stack and are completely reflected: a band gap in the dispersion curve exists. To those structures it is commonly referred to as photonic crystals. As shown by Fig. 2.8 B, a periodic modulation of refractive index can also be achieved by a structured surface. In contrast to the diffraction gratings introduced

previously, here, light travels in the direction of the periodicity instead of transverse to it. Such a grating or multilayer, where the respective layers fulfill $n_x d_x = \lambda/4$ with $x = 1,2$ in the case of the grating and $x = 2,3$ for the multilayer and λ as the desired resonant wavelength, is known as Bragg grating.[83] The period Λ of such a Bragg grating (or thickness of a layer pair) corresponding to the resonant wavelength λ_{Bragg} is

$$\Lambda = d_1 + d_2 = \frac{\lambda_{\text{Bragg}}}{4}\left(\frac{1}{n_1} + \frac{1}{n_2}\right) = \frac{\lambda_{\text{Bragg}}}{2n_{\text{eff}}} \tag{2.12}$$

with

$$n_{\text{eff}} = 2\left(\frac{1}{n_1} + \frac{1}{n_2}\right)^{-1} \tag{2.13}$$

as the effective index of refraction. Again, the width of the grating features (or thicknesses of the layer) can be an integer multiple m of $n_x d_x$ which results in the Bragg equation:

$$\lambda_{\text{Bragg}} = \frac{2}{m} n_{\text{eff}} \Lambda. \tag{2.14}$$

With a sufficient high number of periods, a Bragg grating is a very effective resonator for specific wavelengths.

Two- and Three-Dimensional Photonic Crystals

The introduced concepts to describe the propagation of electromagnetic waves in one-dimensional, periodic structures can be in general expanded to two- and three-dimensional architectures.[81] Instead of multiple reflections in the stack of a multilayer, more complex architectures yield scattering and interference of waves by various sorts of periodic microstructures. With higher dimension of the structure, the dimensionality of the photonic band gap increases, too. Two-dimensional photonic crystals hinder the propagation of the light in the two directions of their periodic refractive index modulations. Hence, the photonic band gap exists in two directions, too. Complete band gaps for all propagation directions can only occur in three-dimensional photonic crystals. They completely prohibit propagation of the particular wavelengths that correlate with the size of the structure features. For an in depth discussion of the interaction of light with two- and three-dimensional periodic structures it is referred to the respective literature.[81,83,84]

2.3 Materials and Methods

For the fabrication and analysis of the diverse, in this thesis introduced, micro- and nanostructures I used various techniques. Each evaluated regarding their assets and drawbacks, often a combination of several of the in the following section introduced methods is applied to achieve the best possible results.

2.3.1 Materials

This section gives a brief overview on the utilized materials, especially the shape-memory polymer on which all approaches to obtain tunability in this thesis are based.

Tecoflex®EG 72D

The in this thesis utilized SMP is a completely amorphous block-copolymer with a thermally triggered, one-way SME. It is commercially available under the name of Tecoflex®EG 72D (TFX) from Lubrizol. Its two blocks' monomers consist of poly(tetramethylene ether) glycol (PTMEG) and 1,4-butanediol (1,4-BD), respectively, that were each polymerized in a polyaddition with 1-isocyanato-4-[(4-isocyanatocyclo-hexyl)methyl] cyclohexane (H_{12}MDI) to a polyether urethane. **Figure 2.9** illustrates the molecular structure of TFX. The polymer PTMEG is previously synthesized from tetrahydrofuran and is added as precurser to be able to control the molecular mass of the product sufficiently. To build urethane groups, the isocyanate groups of H_{12}MDI react with terminal hydroxy functional groups of PTMEG and 1,4-BD, respectively, by opening of the N-C double bonds. The segments of PTMEG plus H_{12}MDI constitute the switching segments in TFX whereas the hard segments (or netpoints) are composed of 1,4-BD and H_{12}MDI. In its pure form, PTMEG possesses a melting temperature below 30 °C. The polyaddition with H_{12}MDI alters its melting behaviour significantly, nevertheless the phase transition

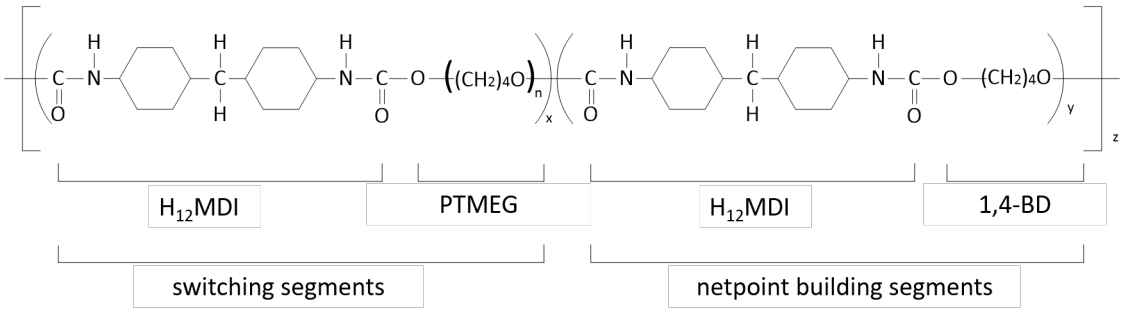

Figure 2.9: **Molecular formula of the repeating unit of Tecoflex®EG 72D.**

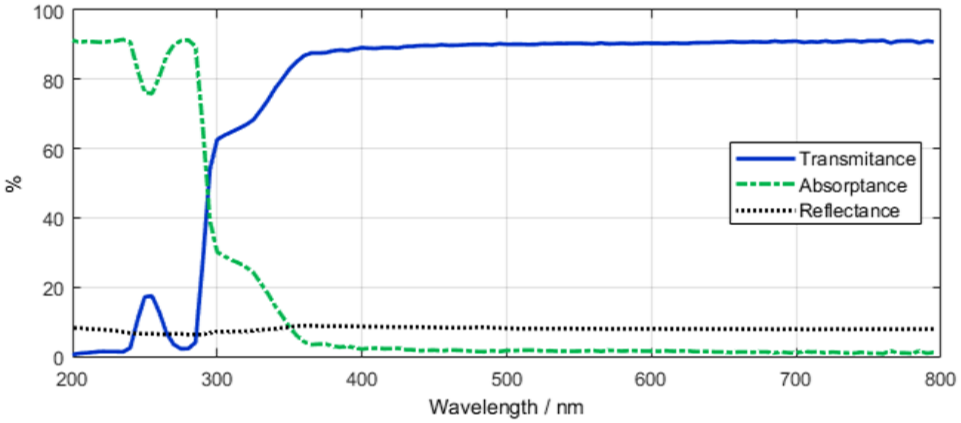

Figure 2.10: **Transmission, absorption, and reflection spectra of Tecoflex®EG 72D.**

regime is still in the low temperature range with $T_{switch} \approx 50 - 80\,°C$. The second type of segments, H_{12}MDI plus 1,4-BD, has a significantly higher transition temperature of $T_{hard} \approx 155\,°C$. The proximate H_{12}MDI parts, linked only by the compared to PTMEG short 1,4-BD parts, build strong hydrogen bonds with neighboring H_{12}MDI parts. The two blocks of the polymer chain are poorly miscible. Hence, they arrange phase segregated in the bulk polymer: the softer PTMEG+H_{12}MDI parts combine to the switching segments and the harder 1,4-BD+H_{12}MDI parts build the netpoints. The exact numbers of the indices *x*, *y*, and *z* are kept secret by Lubrizol and are unknown to us.

As the potential of the SMP TFX is investigated in this work with respect to its applicability for tunable optical components and structural colors, we investigated the optical properties of it. Therefore, we measured reflection and transmission in UV, VIS and NIR of a 60 µm thick TFX foil and calculated its absorptance. The results are given in **Figure 2.10**. In the UV at wavelengths of 200 to 300 nm the polymer's absorptance is high as it is typical for polyurethanes due to their molecular structure. In the complete measured spectral range above 350 nm, the transmission of the polymer is relatively constant at 90 % with a reflection (AOI=8 °, smooth foil surface) as low as 8 %.

PMMA

Besides TFX there is one other polymer that I used frequently to produce structures: poly(methyl methacrylate) (PMMA). More specifically, it is the PLEXIGLAS 8NL22 from Evonik Degussa GmbH. The main criteria to choose PMMA were its molecular structure and therefore mechanical and optical properties. It is an amorphous thermoplastic as well as TFX with a melting temperature of $\approx 105 - 120\,°C$, that is considerably

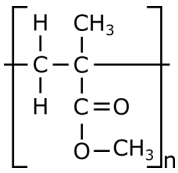

Figure 2.11: **Molecular formula of the repeating unit of PMMA.**

higher than the switching temperature of TFX but still below TFX's melting temperature. Moreover, the thermoplastic property allows easy structuring of PMMA with hot embossing. With a Young's modulus of 3100-3300 N/mm^2 it is sufficiently harder than TFX which is a required property for the fabrication of my wrinkle structures (see Chap. 5).[88] At last, due to its amorphousness it is transparent with absorption below 10 % in the visible regime of light.[89] As PMMA will be applied as a thin coating, its good solubility in organic solvents such as xylene is of use. **Figure 2.11** depicts the molecular formula of the repeating unit of PMMA.

2.3.2 Fabrication Tools and Techniques

Thermoplastic polymers offer the possibility to reshape them again and again from melt after complete synthesis. A multitude of polymer processing techniques has evolved in the last century to satisfy the various requirements of quantity, throughput, dimension, complexity, and many others. In my work, I use several state-of-the-art techniques and combinations thereof, each chosen to achieve the optimal results for the specific demand. The techniques used to fabricate polymer films, structured foils, and material compounds are described in this section.

Hot Embossing

Hot embossing is a versatile technique to structure the surface of thermoplastic polymers and a few other materials. The basic principle is to heat a mold insert to the respective polymer's melting temperature, press it into the surface and sustain the force while cooling until the polymer is solidified again.[90] The attributes that make hot embossing attractive for polymer structuring, include suitability for a very large range of materials, the low cycle times and therefore high throughput, and the large areas with the prospect of even greater scaling by transferring the process to continuous roll-to-roll embossing. As the desired structure is replicated from a master mold into the respective polymer surface, hot embossing is a convenient technique for small and medium size batches rather than prototyping of single samples.

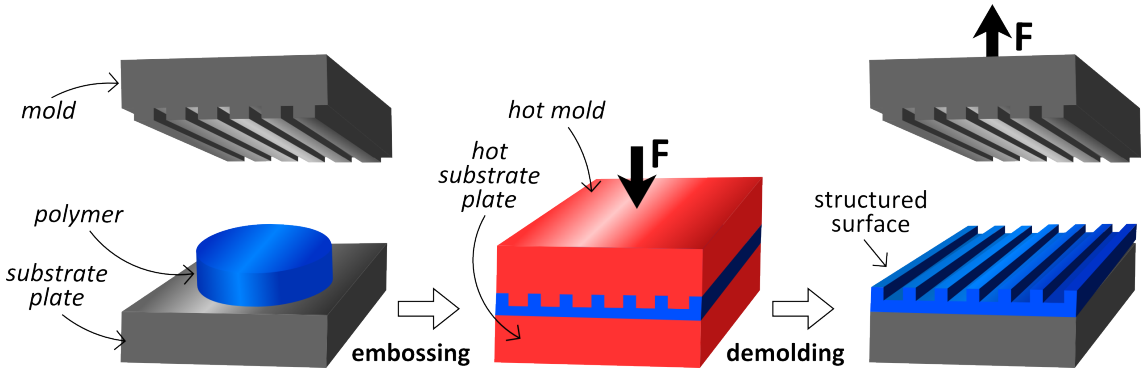

Figure 2.12: **Illustration of the hot embossing process.** A polymer piece is placed between a structured mold and a substrate plate. Subsequently, mold and substrate plate are heated to the melting temperature of the polymer and pressed into its surface. After cooling, demolding results in a structured polymer foil.

In its basic composition a hot embossing machine consists of one fixed and one movable traverse guided by a four tie bar load frame, and a drive mechanism. The bottom traverse possesses a substrate plate and the top traverse exhibits a jig to which the respective tools and molds are mounted. Both traverses are equipped with precisely and individually controllable heating-cooling elements. The embossing procedure can be sectioned into three steps: assembly, embossing, and demolding. **Figure 2.12** describes the procedure schematically. First, prior to insertion of the polymer foil, the favored mold is installed and a suitable substrate plate chosen. The second step, the actual embossing, comprises approaching of the tool plate to the substrate plate either force or position controlled, heating both plates to pertinent temperatures, and building up the required embossing pressure with specified velocity. For each individual experiment, the values as well as the order of those aforementioned individual operations have to be determined and can be altered according to the desired needs. Lastly, after an appropriate wait time at constant embossing temperature and pressure to allow the polymer to flow in the mold's cavities, the substrate's, tool's, and sample's temperatures are decreased to solidify the polymer. If now the sample's adhesion to the substrate plate exceeds its adhesion to the mold due to form closure and friction, automatic demolding takes place when the top traverse withdraws from the bottom one. The adhesion of the polymer to the substrate plate can be significantly boosted by increasing the plate's surface roughness through sandblasting. However, this entails a roughened and therefore scattering, whitish backside of the resulting sample that can, depending on the purposed use of the sample, be a major drawback. This can be avoided with manual demolding, where the substrate plate is smooth and the demolding is executed by hand. In **Figure 2.13** exemplary experimental data for temperature of top and bottom plate and embossing force for embossing of a microstruc-

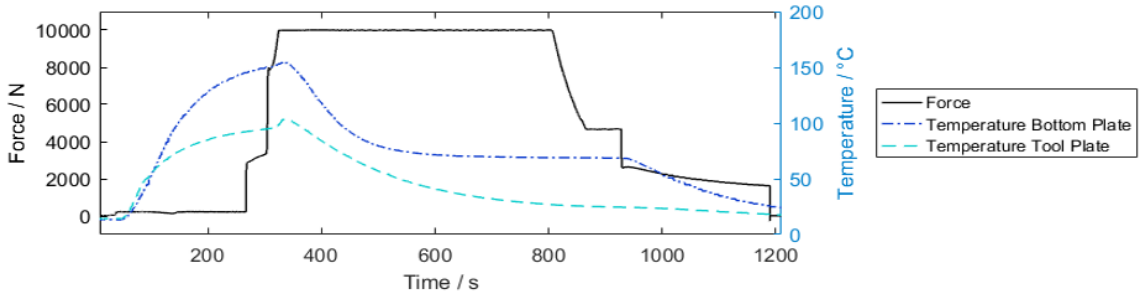

Figure 2.13: **Exemplary force and temperature profiles for hot embossing.**

ture on a SMP substrate as permanent shape are given. In the course of the described hot shaping of the sample, the polymer undergoes several phase transitions.[30,32,90] Thermoplastic polymers exhibit the capacity to convert into a molten state at temperatures above their melting temperature without decomposition. Due to their not cross-linked, largely linear molecule architecture those chains can easily slip at sufficient high temperatures and flow into the by the mold imposed shape. Amorphous and semi-crystalline thermoplastics behave slightly different when their temperature rises. At low temperatures thermoplastics are in their glassy state: they are stiff and brittle due to high intermolecular forces and entanglements. With increasing temperature they enter the glass transition range where the molecular movement is increased and chains start to slide. To that effect the shear modulus decreases significantly. Above its glass transition temperature the polymer becomes viscoelastic, the shear modulus continues to decrease and with further increase of the temperature the polymer reaches the flow range and finally the melt range. Eventually, a further temperature increase will result in irreversible decomposition of the molecules. The shear modulus drop of semi-crystalline polymers is delayed and more confined compared to completely amorphous thermoplastics.[90] A qualitative, graphic depiction of the dependency of the shear modulus to the temperature in **Figure 2.14** A illustrates the response of amorphous polymers to rising temperature (illustration based on[90]). To be able to achieve the for hot embossing necessary pressure, the polymer has to be in a certain viscosity range. This molding window is indicated in blue in the graphic. In Fig. 2.14 B the time resolved response of a polymer sample is qualitatively exemplified in creep curves according to the various aforementioned states (illustration based on[30]). Both of the depictions of the polymer's behavioural response to temperature and time, respectively, clarify the influence and importance of the careful selection of the embossing temperature.

Although thermoplastic polymers are the most straightforward materials for hot embossing, the technique is suitable for other materials, too. Basically, the used material has

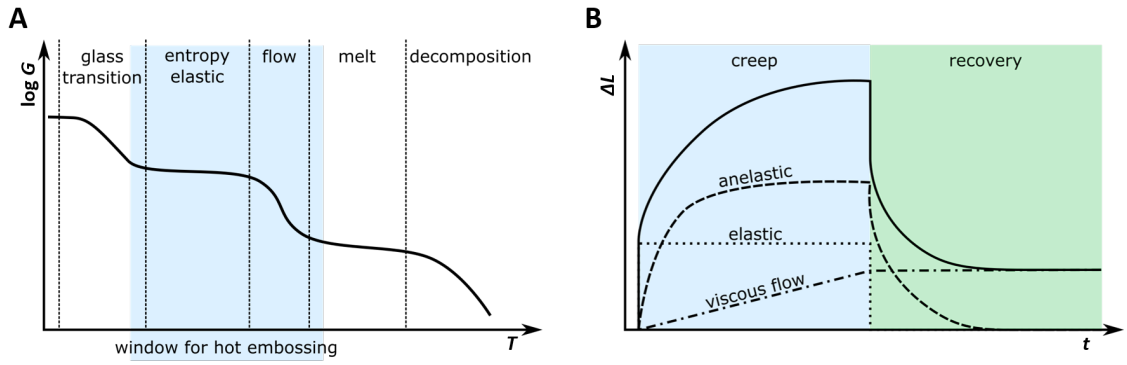

Figure 2.14: **Shear modulus as f(T) and displacement as f(t). A** The rheological behavior of an amorphous thermoplastic is illustrated by the shear modulus G as a function of the temperature T. The viscosity range for high-quality hot embossing is indicated in blue. **B** The creep curve of a polymer sample under tension (blue area) is the superposition (solid line) of the various parts contributing to the polymer's behavior: immediate elastic (dashed), retarded anelastic (dash-dotted), and viscous (dotted) response. After removal of the load (green area) and completion of the recovery process, a remaining elongation is existent.

to be to some extent hot shapeable and the utilized mold has to be harder than the material at the embossing temperature. For instance, bulk metallic glasses have been successfully structured with stainless steel molds in order to develop tissue adhesion reducing, ultrasonic scalpels and liquid wood, a compound of cellulose fibers and lignin that is a by product of paper industry, was embossed to exhibit, e.g., high-aspect microstructures for superhydrophobic microfluidic channels.[91–94]

In terms of replicate-able structure sizes, the limitations to the hot embossing technique are given rather by the mold fabrication than the actual embossing step. Although, the smaller the structure features are, especially in combination with high aspect ratios, the more prone to failure is the demolding step. Above a critical surface area to bulk ratio, the adhesion of the polymer to the mold exceeds its cohesion so that structures rip off and residual polymer clog the mold's cavities.

The major drawback of hot embossing regarding producible structure geometries is the inability to replicate complex, three-dimensional structures that contain undercuts. Therefore, it is often referred to hot embossing as a technique able to fabricate 2.5D structures as in plane geometries can basically be arbitrary but in the third dimension only the height of the structure is partially unrestricted. The actual, at maximum achievable aspect ratio depends on the polymer's stiffness. Vast efforts have been taken to annul those limitation with thermoforming and, to achieve even sub-micron structure features, nanothermoforming.[78] This thesis contains an advancement of another approach to overcome this issue by combining hot embossing with the wrinkling technique in order to fabri-

cate three-dimensional, hierarchically structured surfaces. The results are described in Sec. 5.3. Current state-of-the-art limits regarding the overall area that can be structured in one step are in the range of six inches diameter. However, the replication for many structures can be easily transferred the to continuous roll-to-roll fabrication. Roll-to-roll embossing is in its basic principles very similar to common hot embossing though especially the replication of sub-micron sized structures challenges researchers as regards the fabrication of those master structures on the roll's curved surface. [95]

Throughout my work, I used hot embossing in various ways to produce and tune structures. The machine I used is a partially in our institute (IMT, Worgull group) home-build hot embossing machine based on a Zwick 1488 universal testing machine.

Mold Fabrication

For structure replication with hot embossing a negative of the desired structure in the form of a master mold is required. For the fabrication of those molds one of a few standard lithographic processes such as e-beam lithography, direct laser writing, wet and dry etching, two-photon lithography, milling, and others, is used to fabricate the structure that is then, if necessary, transferred into a metallic mold by electroplating. However, all of those techniques feature some limitations with respect to structured area, shape, resolution, aspect ratio and/or are extremely expensive or time-consuming. For my work I needed a quick solution to fabricate an one-dimensional, triangular grating with an aspect ratio (AR) greater than 0.5 and a period between 5 and 20 µm. While the triangular structure is easily producible with anisotropic etching, the AR>0.5 requirement is challenging. Therefore, I utilized a silicon mold with a low AR and applied a trick to achieve the high AR. I replicated the Si-structure into a 2 mm thick polymer substrate, in this case TFX (though the SME is not necessary here), and stretched it by 200 % in the tensile testing machine. Stretching was carried out in the same direction as the orientation of the 1D grating. By doing so the with stretching accompanied lateral contraction of the polymer decreases the structure period to a greater extent that the structure height since the height of the structure is only a tiny fraction of the overall sample thickness. The decrease in period (but almost constant structure height) results in a remarkably increased AR. The respective steps of the procedure are schematically depicted in **Figure 2.15** A and structure details in various steps are given in Fig. 2.15 B-E.

Since I utilized a SMP, stretching results in an elongated sample in its temporary shape. In this state the polymer is not very resistant to elevated temperatures as it reacts with a shape-change to heat.

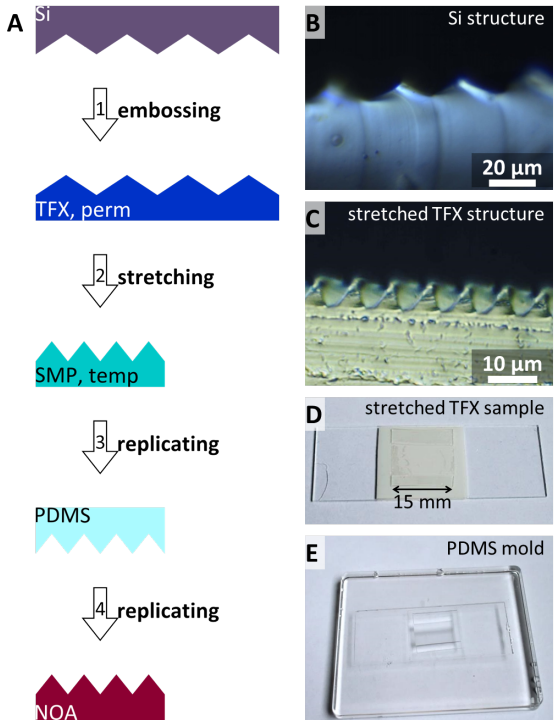

Figure 2.15: **Preparation of the mold negative. A** The schematic depicts the fabrication steps that were improvised to achieve a triangular grating structure with sufficient high aspect ratio. A low AR Si-structure is transferred into the surface of a TFX sample by hot embossing. Subsequent uniaxial stretching of this sample parallel to the grating orientation decreases the grating's period and increases the AR. Because TFX cannot endure the following mold fabrication, the structure is first replicated into PDMS and then into NOA68. **B** The initial silicon structure has a triangular grating structure with a low AR. **C** After replication of the Si mold into a TFX substrate and stretching thereof, the AR of the structure is increased. **D** To gain a flat mold surface the TFX sample is mounted on a glass slide and subsequently PDMS is poured over. **E** After removal of the glass slide and the TFX sample, the PDMS stamp exhibits the negative of the grating structure.

In the subsequent steps of the mold fabrication, e.g. coating and electroplating, the sample is exposed to temperatures close to its switching range. In order to avoid this problem, We replicated the structure into polydimethylsiloxane (PDMS) by pouring a mixture of 5:1 base to curing agent ratio on the structured sample (SYLGARD®184 SILICONE ELASTOMER KIT, Dow Corning). Before this step the sample was glued to a glass slide to keep it flat and was placed into a small plastic container. The resulting PDMS mold is pictured in Fig. 2.15 E. An additional replication step is needed because the actual mold fabrication by electroplating has to be conducted on a structure that is the same as the structure that is required in the embossed polymer samples in the end. However, the PDMS mold exhibits the negative of this structure. Therefore, the UV-curable adhesive NOA68 (Norland Optical Adhesive 68, Norland Products) is poured into the

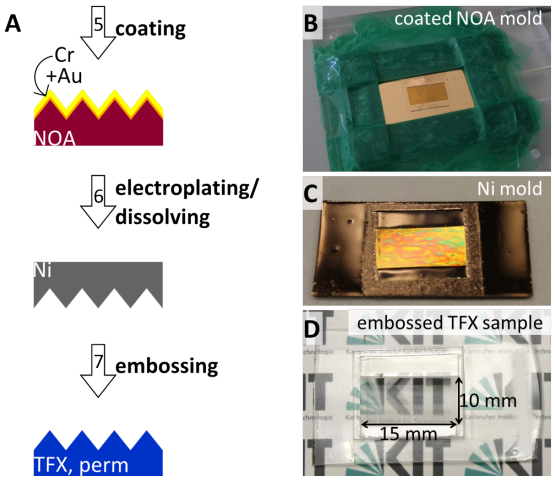

Figure 2.16: **Fabrication of the mold and replication. A** The NOA structure fabricated as described in Fig. 2.15 is coated with Cr and Au as electroplating starting layer. Thereupon a thick Ni layer is electroplated on the NOA structure that is afterwards dissolved. This mold can now be used to emboss its structure into various polymers such as, in this case, TFX. **B** The photograph shows the NOA structure covered with Cr and Au and a taped frame that will determine the thickness of the nickel. **C** The finished Ni-mold is slightly iridescent in the structured area. **D** An example of a with this mold embossed polymer structure demonstrates the prismatic effect of the triangular grating structure.

PDMS structure, covered with a Si-wafer, and exposed to UV-light. On this NOA replication of my structure, adhered on the Si-wafer, the electroplating starting layer of first 7 nm chromium and afterwards 100 nm gold was deposited. To define the size of the resulting mold a frame is created with multiple layer of tape according to the required mold thickness. In the subsequent nickel electroplating procedure the framed section is plated with an approximately 800 µm thick Ni-layer. After completion of this step first the Si-wafer is removed by dissolving it in 30 % KOH solution and then the NOA adhesive is dissolved in M1144. **Figure 2.16** A describes the process schematically and photographs of the mold in different states are given in Fig. 2.16 B-D.

Figure 2.17 reveals the details of the fabricated structure. The finished mold possesses a structured area of $15 \times 10\,\mathrm{mm}^2$ with overall dimensions of approximately $40 \times 25 \times 0.8\,\mathrm{mm}^3$. The 1D, triangular structure has a period of $\approx$7 µm and an AR of 1.0-1.2. Despite of the multiple replication steps in the course of the fabrication of this mold, the structure is largely defect free and homogeneous with only very slight variations in structure height. In conclusion, we could demonstrate a fast alternative to alter structure dimensions in a simple, elegant, and quick fashion. For what purpose I use this mold and how the increased AR is beneficial is described in Sec. 5.3.

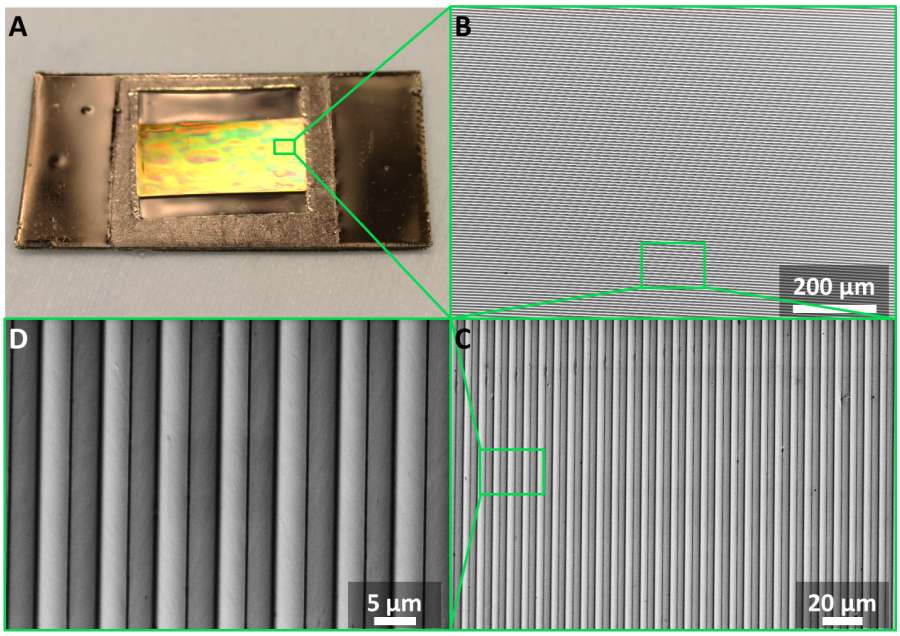

Figure 2.17: **Structure of the finished mold. A** The nickel mold has a structured area of $1.5 \times 1\,\mathrm{cm}^2$. **B-D** SEM images reveal the triangular structure and its accuracy on large scales.

Extrusion

While the previously described hot embossing technique is an ideal polymer processing method to shape polymers into substrates with micro- and nanostructured surfaces, it is less suitable for the fabrication of material composites. The marginal flow of the molten materials to fill the mold's cavities and possibly the volume of a mask is not sufficient to homogeneously combine materials. For the purpose of compounding thermoplastic materials, extrusion is the common procedure. The to be combined materials are fed to the extruder where they are heated until its softened and compressed and sheared between one or more screws and the chamber walls.[96,97] Due to the screw geometry the material is then pushed through a die and cools down in ambient conditions. The principle of an exemplary extruder with two counter-rotating screws is illustrated in **Figure 2.18**.

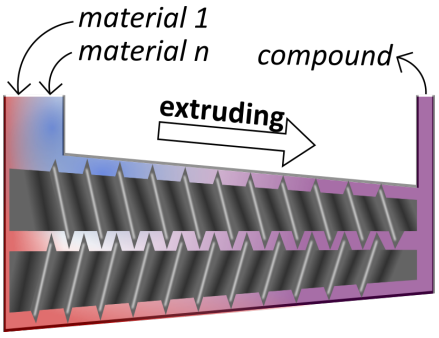

Figure 2.18: **Illustration of the extruding process.** The materials are simultaneously fed to the extruder and mixed, often at elevated temperatures, between the counter-rotating screws of the extruder. The compound exits the extruder through the die.

As in this graphic, the extruder used in this work to fabricate the material composites (see Chapter 6), the HAAKE MiniLab by Thermo Scientific, has conical twin-screws for homogeneous mixing of materials.

Spin Coating

Achieving homogeneous, sub-micrometer thick polymer films as they are required, e.g., for thin film interference or coatings, from melt is very challenging. Fabrication techniques that are based on processing of polymer solutions and subsequent drying of the films are the reasonable, common choice for those purposes.[98] To produce thin polymer films on various substrates throughout my work, the spin coating technique is used. Spin coating generates even films from solutions, liquids, and some dispersions by using the interplay of centrifugal forces, adhesion, and cohesion. A drop of the respective liquid is deposited on a wettable, flat substrate. Rotating the substrate around its vertical axis distributes the liquid evenly and discharges excess liquid. The resulting film thickness and quality is influenced by the liquid's viscosity, the substrates rotation speed and acceleration, the spin time, as well as environmental conditions such as humidity and temperature. For the in the respective chapters introduced fabrication methods of my

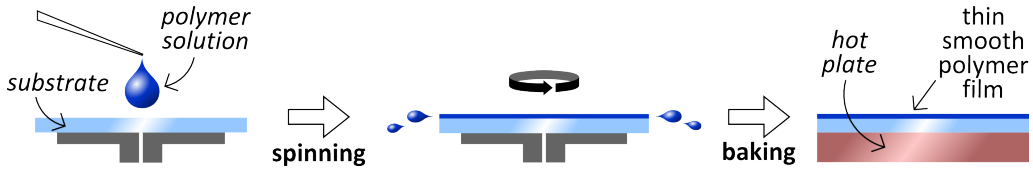

Figure 2.19: **Illustration of the spin coating process.** A polymer solution is deposited onto a smooth substrate. Spinning causes the solution to spread and a thin coating is generated. The solvent evaporates in the baking step and a smooth, solid thin film is formed.

structures the polymer coatings are fabricated from solution. Therefore, the polymers are solved to different ratios in a suitable solvent. After spinning, the samples are heated on a hot plate in a subsequent baking step to evaporate the solvent and obtain solid, uniform polymer films. The spin coating procedure is schematically depicted in **Figure 2.19**. For each series of experiments the acceleration, spin time, humidity, and baking time and temperature are adjusted to achieve the optimal outcome. The solution's concentration, hence its viscosity, and/or the spin velocity are varied to influence the polymer thin film thickness. The herein used spin coater is the WS 650MZ 23NPPB model from Laurell Technologies Corporation.

Sputter Deposition

The metallic coatings applied for the fabrication of various structures in this thesis are produced by magnetron sputter deposition. This technique belongs to the physical vapour deposition methods and generates homogeneous metallic films. By an electric and magnetic field charged and accelerated ions knock off atoms of the target that in turn are accelerated in the direction of the sample and condense its surface. The sputter deposition equipment used in this work is the MED 010 of Balzers Union operated with argon plasma and a silver target.

Universal Testing Machine

An universal testing machine is one of the most important tools for characterization of mechanical material properties. Operated in its tensile testing mode it is used to record stress-strain curves from which critical material characteristics such as the Young's modulus, yield strength, Poisson's ratio, and failure stress are determined. Furthermore, the machine can be used for three point flexural tests, and compression tests. **Figure 2.20** gives an exemplary stress strain curve of a TFX sample of $50 \times 20 \times 2\text{mm}^2$ performed at room temperature. The curve exhibits the for an amorphous thermoplastic polymer characteristic shape. In this work, the universal testing machine is primarily used to impose a mechanical deformation on TFX samples in order to program the temporary shape into the SMP. For this purpose an Instron 4505 was utilized. The precise control of distance and velocity enabled by the machine allowed us to carefully investigate the influence of the extent of the mechanical deformation on the subsequent structure fabrication.

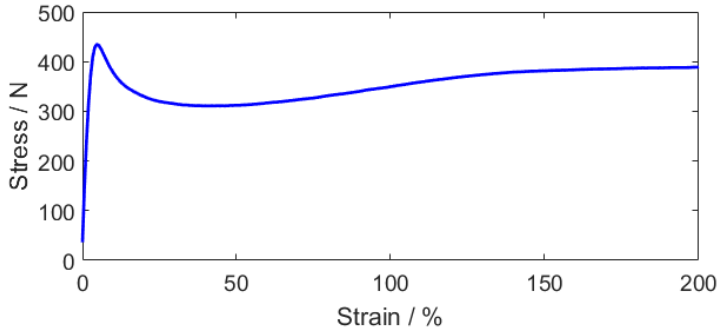

Figure 2.20: **Exemplary stress-strain curve of a TFX sample.**

2.3.3 Dynamic Mechanical Analysis

To measure shape-memory properties of our polymer and polymer compounds in terms of their shape-changing response to a certain treatment of mechanical deformation and temperature cycle, we used dynamic mechanical analysis (DMA). Due to the dynamic mechanical analyzer's highly accurate control and measurement of temperature, strain, displacement, and stress it is a common tool to determine the shape-memory ability of SMPs in cyclic thermomechanical tests.[18,21] In those tests, the SMP is first heated to its switching temperature, then stretched to a certain extend, and afterwards cooled down to room temperature at constant strain in order to program and fix the temporary shape. In the next step, the strain is released that causes the SMP to slightly recover the elastic part of the deformation instantly. Lastly, the temperature is elevated to the switching temperature again and the SMP recovers its original, permanent shape to a certain degree. This process can be repeated several times to gain information on the reproducibility of the shape-recovery behaviour. For the experiments included in this work, the Q800 dynamic mechanical analyzer from TA Instruments was utilized.

2.3.4 Microscopic and Surface Analytic Tools

Depending on the morphology of the surface, the requested information, and the further use of the sample, different analytic tools are used to reveal and depict the structures produced in this work. An optical microscope gives a first impression of the surface structure with limited resolution but the sample's color is visible. Scanning electron microscopy is useful to image surfaces from large scales of several hundreds of microns down to a few nanometers. High aspect structures can be depicted in detail by imaging cross sections. However, depending on the sample material, conductive coatings have to be applied to achieve high resolution pictures which limits the further usability of the sample. Vertical scanning interferometry is a fast and useful tool to gain information about the morphology of structures on large scales but steep and vertical lateral faces of structures are challenging. Atomic force microscopy allows detailed mapping of structures with, depending on the experimental conditions, atomic resolution. Besides information about the topography, atomic force microscopy measurements also can be used to gain information about mechanical properties of the material. As a non-destructive analytic tool, it is the ideal method to map the surface of a sample that shall further be used or processed. Lastly, insight about the surface energy and wetting properties of a material or structure can be obtained through contact angle measurements.

Vertical Scanning Interferometer

For large structures, especially for large heights or aspect ratios, the atomic force microscope approaches its limits. For those structures 3D optical microscopes or vertical scanning interferometers (VSI) are a versatile, non-destructive tool to depict the samples topographies.[99,100] The VSI operates in its basic mode with white light that is directed partly on the sample and partly to a reference. If the sample's surface is in focus, the light forms a pattern of intensity variations that is effected by the surface. Recombination of the two beam parts and analysis of the phase differences gives information on the sample topography. Automatically, the focal point is moved vertically through the sample to get a full 3D image of the sample. For a few measurements in this thesis, where atomic force microscopy and scanning electron microscopy were not able to sufficiently depict my samples' surfaces, I used the ContourGT from Bruker to obtain the necessary information about the respective topographies.

Scanning Electron Microscopy

Scanning electron microscopy (SEM) is an useful tool to obtain topographical images of samples.[101] By the same principles as an optical microscope a beam of electrons is shaped and focused on the sample's surface. Scanning the surface with this beam and detection of the secondary electrons emitted by the surface atoms produces an image. Due to using electrons instead of photons, a much higher resolution (nanometer range) can be achieved with SEM than with optical microscope. However, a conductive sample surface improves the image quality especially at high magnifications significantly. Therefore, samples often are coated resulting in SEM not being a non-destructive measurement method. Additionally, images taken from the surface of a sample from above might lack crucial information of the structure height. The SEM utilized to image the in this thesis produced structures, is a Supra 55P by Zeiss.

Atomic Force Microscopy

The principle of atomic force microscope (AFM), also known as scanning probe microscopy, is in its basic idea the same as a finger gliding over a surface and thereby sensing the topography. In order to transfer this concept to an automated system and adapt it to being able to resolve atomic structures, researchers developed sophisticated methods in the last 30 years.[102–105] At the today's state of this development and optimization process a standard AFM is able to perform measurements gaining plenty of more infor-

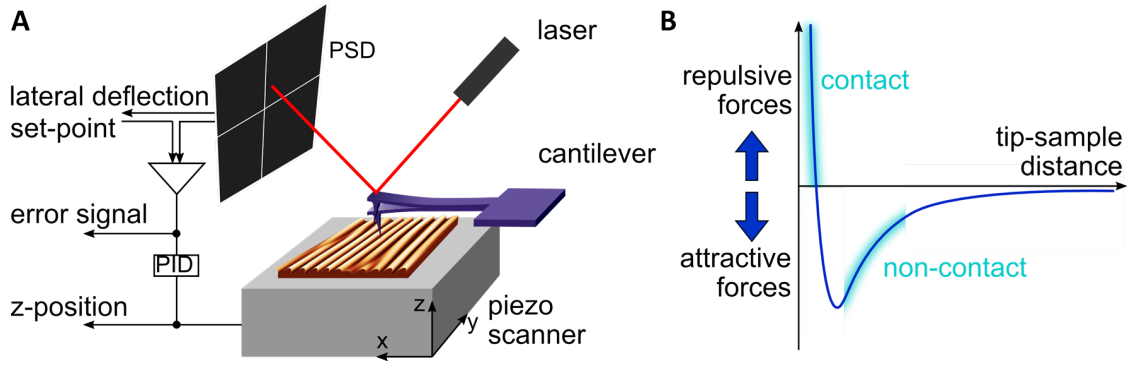

Figure 2.21: **Set-up and force-distance curve for atomic force microscopy. A** The schmeatic illustrates the set-up of sample, cantilever, laser, and detector of an AFM. **B** When the probe approaches the sample surface, first attractive forces determine the probe-sample interactions. With decreasing distance, repulsive forces dominate. The operation ranges for contact and non-contact mode are indicated.

mation than the topography of a surface in various modes. A sample does not require a specific coating to be scanned with an AFM and scanning is usually performed in ambient air and pressure. Water-containing specimen cannot only easily be scanned but also measurements can be performed even in fluids with the respective AFM equipment. In terms of resolvable structures the geometry of the tip is the critical factor. Super sharp tips with radii down to one atom and high aspect ratios of the tip of more than ten enable even scanning of nano- and sub-nanostructures and deep, narrow grooves. Commercially available standard AFMs are usually restricted to maximum scan areas of less than $100 \times 100\,\mu m^2$.

In AFMs, the "finger" is replaced by a probe consisting of a cantilever with a sharp tip mounted to one end. If this probe scans over the surface of a sample, the cantilever deflects according to the topography. This deflection can be measured in various ways with the most established way being a laser that is focused on the cantilever's backside and a position sensitive photo detector (PSD) that senses deflections in the reflected laser beam.[106] This set-up is schematically depicted in **Figure 2.21** A. For non-destructive measurements and to increase the life span of the tip, in some AFM operation modes such as the tapping mode the tip is not actually in contact with the surface. The cantilever is therefore excited to harmonically oscillate in a certain frequency depending on its stiffness. When the tip approaches the sample surface interactions such as electrostatic forces, capillary forces, Van der Waals forces, and Pauli repulsion between tip and sample arise and those forces influence the cantilevers oscillation frequency.[103–105] The effects of the tip-sample forces on the deflection of the cantilever and the distance ranges for the contact and non-contact operation modes are schematically illustrated in Fig. 2.21 B. This change in the cantilever's oscillation is sensed and the system readjusts the z-position of the probe

through a feedback loop. After completed scans of the sample in x- and y-direction, the data put together result in a 3D-image of the topography. Besides the topography, the phase shift between input and output signal of the oscillation gives information about the mechanical stiffness of the sample surface. Furthermore, a material's Young's modulus, adhesion, deformation, and dissipation can be measured directly by approaching the probe without oscillation and retracting it after the peak force was reached. These quantitative material properties can be extracted from force-distance curves. The indentation depth of the tip in the material is proportional to the materials stiffness. Information about this depth is gained from the difference between the cantilever deflection and the scanner move in z-direction. The AFM used to study sample topographies and mechanical properties in this work is the Dimension Icon by Bruker with the NanoScope software. In their system, the mode that allows direct scanning of mechanical properties is called Peak Force QNM (Quantitative Nanomechanical Mapping).

Contact Angle Measurements

Contact angle measurements quantify the wettability of a liquid on a surface. A droplet deposited on a surface will completely spread, remain spherical, or anything in between those two extrema depending on the interaction of liquid and surface. Contact angles of water on a surface below $10\,^{\circ}$ are classified as superhydrophilic and between $10\,^{\circ}$ and $90\,^{\circ}$ as hydrophilic. For angles between $90\,^{\circ}$ and $150\,^{\circ}$ the surface is denoted as hydrophobic and is the contact angle above $150\,^{\circ}$ as superhydrophobic. In this work, the static contact angles of water droplets on various surfaces are disposed with a DataPhysics Instruments OCA 40 system and the corresponding software SCA20 is used to determine the contact angles by Laplace-Young fitting.

2.3.5 Optical Spectroscopic Methods

UV-VIS-NIR spectrophotometry is an useful tool to quantitatively determine the interaction of a sample or structure with light. A calibrated light source of ultraviolet (UV), visible (VIS), or near infrared (NIR) light is guided to the sample where it interacts with the structure and material. Depending on the arrangement of sample and the photodetector, transmission or reflection is measured. By determination of both, also the absorption can be calculted from this measurement. Reflectance spectra reported in this work were recorded using a LAMBDA 1050 UV-VIS-NIR Spectrophotometer from PerkinElmer that offers an operating range of 175 to 3300 nm. Complemented with an integrating sphere, that is a highly reflective hollow sphere, and a center-mounted, rotatable sample holder,

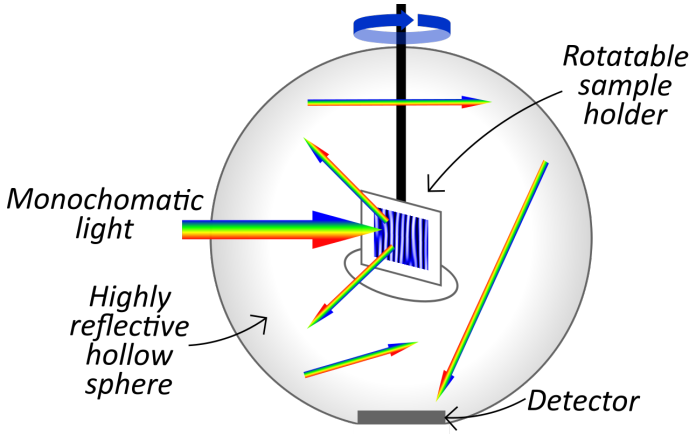

Figure 2.22: **Illustration of the set-up to measure AOI resolved reflection.** The sample is placed on a rotatable holder in the center of a hollow, highly reflective integrating sphere. A blind protects the detector from direct scattering. The sample is successively illuminated by monochromatic light in the range of UV, VIS to IR and the respective integrated reflectance recorded.

it allows measurements of diffuse and total (diffuse and specular) reflected light, angle of incident (AOI) resolved reflectance, as well as transmission.

2.4 State-of-the-Art: SMPs in Optics

The shape-memory ability of SMPs is an interesting feature for many optical applications. The refractive and diffractive properties of optical devices correlate with their shape and structure, respectively. The refractive behavior of a lens, for example, is characterized by its focal length that directly depends on the geometrical shape of the lens. With a lens made of the transparent SMP TFX, this characteristic can easily be tuned over a wide range by addressing the curvature of the lens with the SME as revealed in **Figure 2.23**.[12]

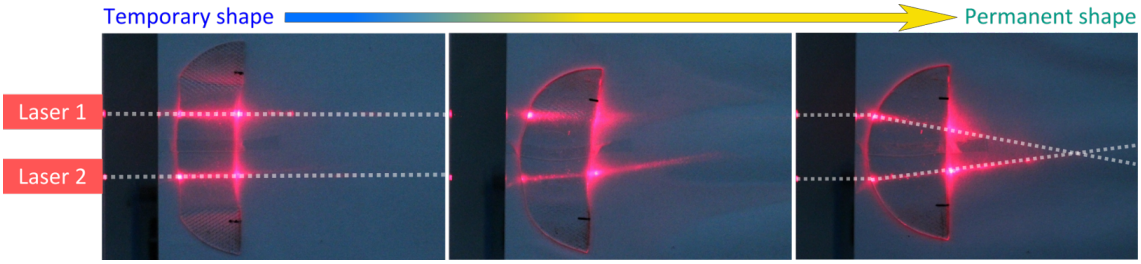

Figure 2.23: **Tuning of the focal point of a convex lens.** A flat semicircle of a transparent SMP is stretched to an almost rectangular, temporary shape. The previous curvature is recovered upon triggering the SME. The refraction at the air-lens interface of at the beginning parallel paths of two red laser pointers, illustrated by white dashed lines, is more and more pronounced with recovering curvature. Reprinted with permission from[12]. Copyright 2016 American Chemical Society.

The shape tunability of microstructured SMPs is especially interesting for optical applications since very small structure changes are sufficient to completely redefine the structures interaction with light.[12] An example of such structures that benefit from an implemented SME are diffracted optical elements (DOEs). DOEs are important components in a variety of optical devices such as holograms, optical tweezers and diffractive mirrors for lasers.[83,107–109] The significant characteristics of a DOE, the spatial period and structure height, are typically in the range of a few microns. Various microstructuring techniques and materials are used to manufacture DOEs, however, in nearly all cases their geometrical shape is set at the end of the fabrication process.[110–113] Hence, tuning of the structures is not possible and if structure changes are required, a completely new structure or mold has to be fabricated. SMP-DOEs can resolve this issue as defined shape changes can be programmed and recalled on demand to actively control the structure features defining the devices' diffractive properties.[12,74,79,114]

Especially interesting for optical applications are transparent SMPs. Using such SMPs, the structure changes by imprinting a temporary structure into a sample that disappears when heated or flattening a temporary structure were reported and the effect of this structure change on the transmission of such samples investigated.[74,79,114] The effect of a change in height of structures or periodicity of microoptical gratings on the diffractive

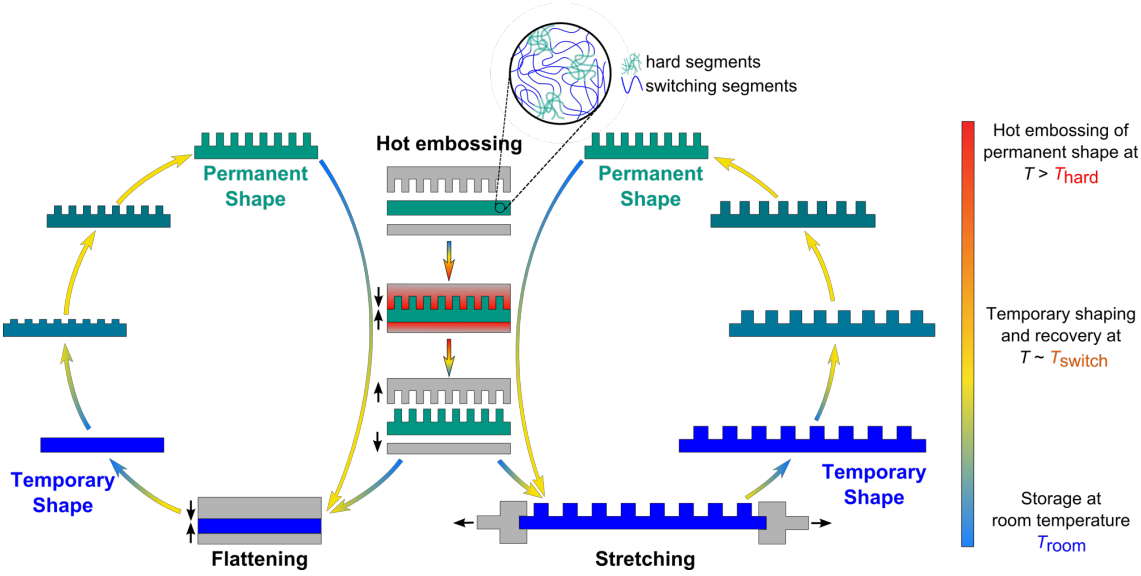

Figure 2.24: **Fabrication of tunable diffractive optical elements made from SMPs.** After hot embossing a diffractive grating structure as permanent shape, the structure features can be temporarily altered either by flattening to change the height (left cycle) or by stretching to influence the period (right cycle). Afterwards, the original shape is recovered upon heating the samples to T_{switch}. Reprinted with permission from[12]. Copyright 2016 American Chemical Society.

effect of an microstructured sample has been investigated in great detail in our research group at the IMT.[12,115] As depicted in **Figure 2.24**, the diffractive structures were embossed as permanent shape into the surface of transparent SMP samples and susequently one of the crucial structure features is temporarily changed by either flattening to affect the height (left cycle) or stretching to address the period (right cycle). **Figure 2.25** displays the results of those experiments. In Fig. 2.25 A the setup for the experiments is given. A sample in its temporary shape is placed in the beam path of a red or green laser pointer that is diffracted to a pattern visible on the screen behind. As the SMP possesses a thermally triggered SME, the sample is heated with a hot air gun to T_{switch} in order to

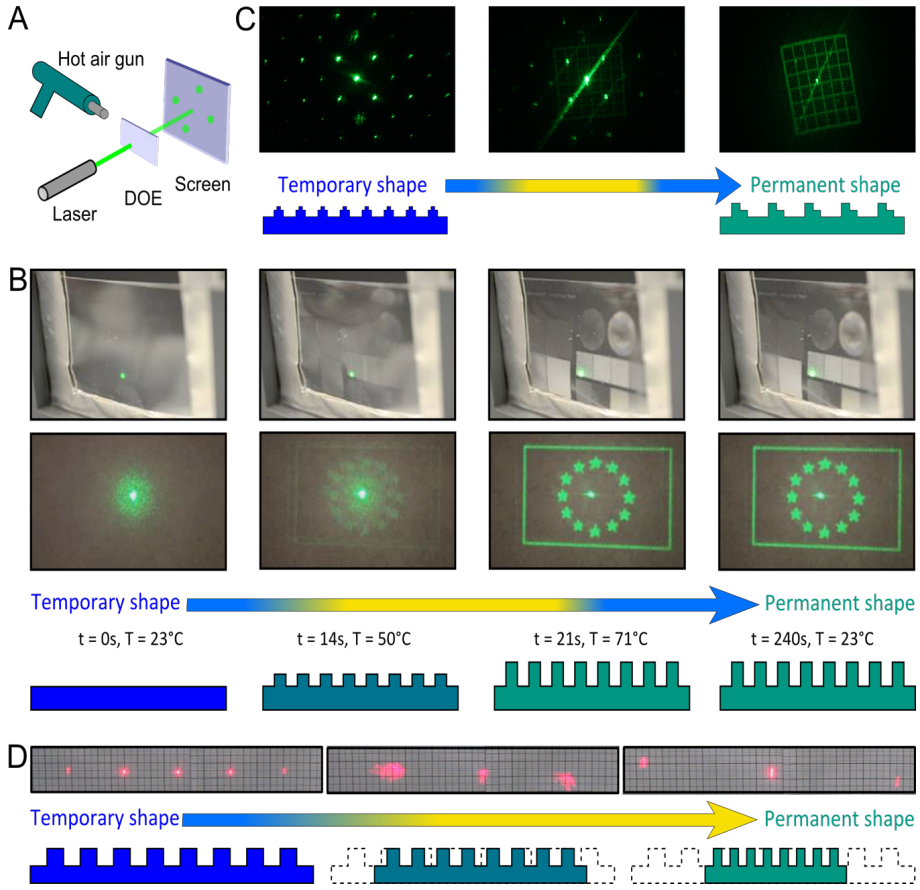

Figure 2.25: **Demonstration of tunable SMP diffractive optical elements. A** The sketch of the experimental set-up illustrates the alignment of laserpointer, sample, and screen as well as the heat gun used to trigger the recovery process. **B** A structure, that generates the European Union flag as diffractive pattern, is temporarily flattened (left photograph) resulting in an undefined scattering of the light. With advancing recovery, the silhouette of the flag reappears. **C** Demonstrated is the diffraction pattern change by morphing from a second, temporarily embossed structure (left) into the original structure. **D** Recovery of the original length (right) of a temporarily stretched sample (left) is visualized by changes of the position of the maxima of the diffraction pattern. Reprinted with permission from[12]. Copyright 2016 American Chemical Society.

trigger the shape change. A temporarily flattened sample recovering the original height of a structure while heated and thereby generating a diffraction pattern in the form of the European Union flag is shown in Fig 2.25 B. Additionally, it is demonstrated, that morphing between two diffractive structures is possible. Instead of flattening a permanently embossed structure, a second microstructure is temporarily embossed in the surface of the same sample. As it is heated, the diffractive pattern correlating to the first structure shown in the left photograph in Fig. 2.25 C, transforms into the pattern exhibited in the right photograph. The enlarged period according to the stretched, temporary shape of a linear grating as illustrated in Fig. 2.25 D diffracts the incident beam to a pattern with little spacing between the maxima. When the period recovers its smaller, original period, the position of those maxima changes accordingly. The applicability of SMPs for optical applications was verified by evaluating the long term stability of a temporary, a partly recovered, a fully recovered, and a sample in its permanent shape. The sample were stored at 4 °C and the structure height and period were measured weekly by AFM. Over a period of three months, none of the mentioned samples showed any structure changes as evidenced by **Figure 2.26** A. Furthermore, we analyzed the time-temperature dependence of the recovery process by capturing the height recovery over time of a previously flattened sample at various recovery temperatures with AFM (Fig. 2.26 B). The graph shows that the higher the temperature the faster the recovery occurs. Moreover, the recovery temperature also strongly influences the extent to which the original, permanent shape is recovered. With only 10 °C lower temperature the structure is almost 20 % less recovered after one hour of heating.

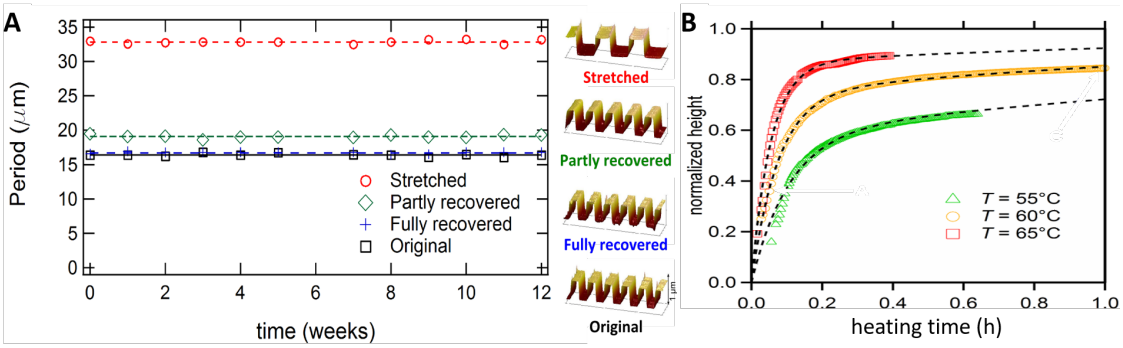

Figure 2.26: **Long term stability and time dependent recovery rate. A** The periodicities of four samples of various stages of the programming/recovery process are recorded over a period of twelve weeks. None of the samples show structure changes in the denoted time frame. **B** The recovery temperature influences the velocity of the recovery process as revealed by the depicted measurements. Reprinted with permission from[12]. Copyright 2016 American Chemical Society.

This study clearly demonstrates the suitability of amorphous SMPs for application in micro-sized, tunable optical devices. Diverse approaches to tune the features of diffractive optical elements, namely height and period, have been presented and the performance of those DOEs in terms of durability and recovery velocity analyzed. Based on this evaluation of the applicability and benefits of SMPs for utilization in optical devices we continued to explore further their potential for tunable light modulating structures as will be introduced in the following chapters.

An extended version of the last section was published as the article "Tunable Diffractive Optical Elements Based on Shape-Memory Polymers Fabricated via Hot Embossing", by Senta Schauer, Tobias Meier, Maximilian Reinhard, Micheal Röhrig, Marc Schneider, Markus Heilig, Alexander Kolew, Matthias Worgull, and Hendrik Hölscher, ACS Appl. Mater. Interfaces 8, 9423-9430 (2016). The majority of the experimental work was performed in the course of my diploma thesis at IMT, KIT in 2013.[115] Additionally, Tobias Meier's work on the time and temperature resolved AFM measurements of the recovery process shown in Fig. 2.26 B is included in the article.

3 Tunable Organic Distributed Feedback Lasers

In the previous chapter, the advantages of SMPs for diffractive optical elements are highlighted. Based on the same tuning principle we downsized the structures to sub-micron features and applied them as a tunable resonator in an organic semiconductor distributed feedback laser. The design of our device as well as its performance are introduced in this chapter. Eventually, we demonstrate the ability of our resonator to tune and adjust the laser's wavelength on demand. Part of this work is based on preliminary tests conducted within the scope of my diploma thesis.[115]

3.1 Motivation and Background

Lasers are pervasive in our daily life as they are used for lightning, in displays, in bar code scanners, in CD and DVD players, and in many other devices.[116] In science, lasers are irreplaceable for material machining, chemical analysis, or distance measurement due their unique properties such as spectrally narrow band emission, low beam divergence, high time and spatial coherence, and high energy and power density. Also, they become more and more important for telecommunication technologies.[116] Here, very specific requirements have to be fulfilled by the applied lasing devices. One of the currently intensively studied issues is the realization of tunable laser sources due to their potential in miniature devices. By now lasers are one of the most important light sources for photonic applications because of the unique properties of the emitted radiation. High power of up to 10^{20} W, pulses of less than 5×10^{-15} s, and emission in the range of few nanometers up to tens of microns wavelength are possible.[117] At the present time, commercially available laser diodes are limited to the visible range of the electromagnetic spectrum and the tunability of a single diode does not exceed a few nanometers. Therefore, diode arrays have to be utilize to cover a broad wavelength range. Opto fluidic dye laser systems are tunable over the whole UV-VIS-NIR spectrum through the dye solution that is exchanged in the system accordingly. Disadvantages of those systems are their potential toxicity and the constant necessary renewal of the dye solution since excitation of the dyes yields quick fading of the color.[117,118] Organic lasers offer new possibilities to tune the emission wavelength because their wavelength can be easily tuned by changing resonator

features.[119] Organic solid-state lasers have attracted attention since the demonstration of an UV tunable organic distributed Bragg reflector as excitation source for biomarker experiments and their benefit for spectroscopic applications is discussed.[120] State of the art, organic solid-state lasers are applied in transmission microscopy, absorption spectroscopy, Raman spectroscopy, and fluorescence excitation.[120–126] In UV and VIS, such lasers can be widely tunable in their emission wavelength. Especially distributed feedback lasers, where the resonator has a structured surface, are suitable for implementing a tunability. In this context, approaches of temperature tuning, chirped gratings, wedge shape films, and stretching of elastic grating substrates to tune DFB lasers have been investigated.[117,119,127–137] However, the mentioned methods have some drawbacks such as the fact that time-consuming lithography is needed to fabricate chirped gratings and elaborate mechanical support is inevitable to tune and adjust elastic gratings. With our approach we overcome all those impairments by using a shape-memory polymer as material for our resonators as will be discussed in the following sections.

Laser

The word “laser” is an acronym meaning “Light Amplification by Stimulated Emission of Radiation”. This stimulated emission occurs after exciting a laser active material. Three components make up the laser: the active material, the pumping mechanism, and the resonator.[118] The laser active material possesses a chemical structure that allows an appropriate pumping energy to effect a population inversion. A state of higher energy occupies more electrons as the ground state. The by the pumping energy excited electrons eventually spontaneously drop back to the ground state emitting thereby photons. Those photons interact with other excited atoms causing them to drop to a lower energy level and thereby creating photons of identical polarization, frequency, phase, and direction of travel.[81]

The function of a laser resonator is to selectively, depending on wavelength and direction of propagation, reflect photons back into the active material. The reflected photons induce stimulated emission of coherent photons with same wavelength and propagation direction. Hence, the resonator is crucial to determine the unique laser properties. In the most simple case the resonator consist of two opposing mirrors where the distance between those mirrors determines the amplified wavelength. More complex resonator architectures are resonators based on Bragg gratings, namely distributed Bragg reflector (DBR) and distributed feedback (DFB) resonators. A Bragg reflector is a stack of alternating layers of two materials with different refractive indices (see Sec. 2.2). This can be accomplished with a multilayer architecture or with a linear, periodic surface structure

building the grating. In the latter case, the resonator is covered with the active material that fills the grating's cavities by what an alternation of layers with different refractive indices is received. The amplification through Bragg gratings is based on constructive interference of at each boundary reflected waves. The refractive index difference of those layers as well as their thickness or the grating period, respectively, determine the reflected and amplified wavelengths. The Bragg equation Eq. (3.1) defines this correlation between the effective refractive index of the resonator n_{eff}, the resonator's period Λ, the Bragg order m and the amplified wavelength λ_{Bragg}.

$$\lambda_{\text{Bragg}} = \frac{2}{m} n_{\text{eff}} \Lambda \tag{3.1}$$

The Bragg order specifies the emission direction with waves exiting the active material perpendicularly to the reflecting boundaries of the alternating materials at $m = 1$ and at $m = 2$ waves are additionally emitted parallel to those material interfaces.[117] Within the range of the wavelengths emitted by the active material, the resonator's period selects the wavelength that is amplified and thereby determines the color of the laser.

The Organic Laser Active Material Alq_3:DCM

Organic solid-state lasers stand out due to their often very low lasing threshold, i.e. the minimal energy needed to achieve stimulated emission in the active material. This low lasing threshold is accomplished by using a guest-host system to avoid self-absorption.[138] The chemical structures of the guest and the host of the system we used to build our tunable DFB-laser is depicted in **Figure 3.1**. The metal chelate complex tris-(8-hydroxyquinoline)aluminium (Alq_3) hosts the guest molecules of 4-(Dicyanomethylen)-2-methyl-6-(p-dimethylamino styryl)-4H-pyran (DCM). Both molecular structures are given in Fig. 3.1. Alq_3 is an organic semiconductor that is used since three decades as green emitter and electron-transport layer in organic devices.[139] As a host it accommodates 2-3 % DCM which is a well-known red laser dye. Implementing DCM as a guest is necessary as it is a strong absorber that in bulk can only be penetrated for a few nanometers by light. A pump laser with a wavelength of 355 nm excites Alq_3 whereupon it emits in the green spectrum, exactly the spectral range that is absorbed by DCM. The by DCM emitted radiation ranges from ≈ 590 nm to ≈ 690 nm and is in the transparent range of Alq_3, hence, self-absorption is avoided. Measured absorption and emission spectra of Alq_3:DCM are given in Ref.[139]. Both molecules are laser active because of their special molecular structure. Organic semiconductors possess at least one double or triple bond

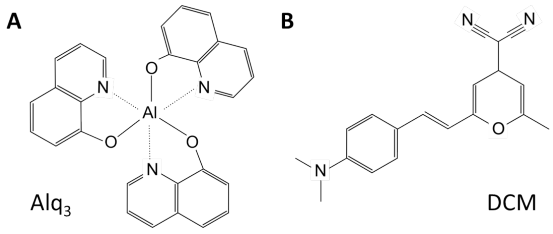

Figure 3.1: **Organic laser active material Alq$_3$:DCM. A** Molecular structure of Alq$_3$. **B** Molecular structure of DCM.

or delocalized electrons in π-orbitals. π-orbitals evolve from overlapping of two or more p-orbitals of neighboring atoms by what the corresponding electrons delocalize and the single energy levels are abolished into bonding π-orbitals and antibonding π-orbitals.[140]

3.2 Fabrication

For the investigation of the applicability of SMPs as tunable laser resonators we designed the device depicted in **Figure 3.2**. A SMP sample exhibiting a prestretched, one-dimensional grating with sub-micron period is covered with a thin layer of the organic laser active material. The device is supported by a thermo-electric module to trigger the recovery on demand by increasing the resonators temperature. Pumping the organic material with UV light results in resonator-period dependent emission.

For fabrication of the resonators a mold featuring the negative of the desired second order Bragg grating with a period of $\Lambda = 400\,\text{nm}$ is embossed on the surface of TFX substrates at $T_{emboss} = 155\,^{\circ}\text{C}$ (see Sec. 2.3.2). **Figure 3.3** A shows an AFM scan of such

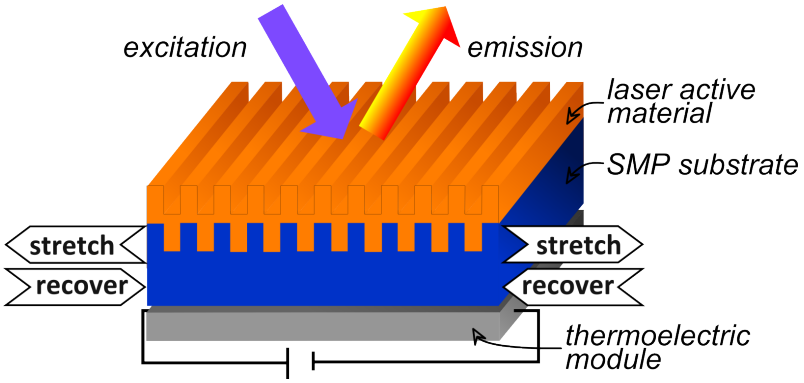

Figure 3.2: **Schematic of the organic DFB laser device based on a tunable SMP resonator.** The organic, laser active layer Alq$_3$:DCM (orange) covers the second order Bragg grating of the SMP substrate (blue). Supported is the device by a thermoelectric element to control the temperature. The by pre-stretching increased grating period reduces as long as the device is heated. Likewise with the period, the emission wavelength is tuned or adjusted.

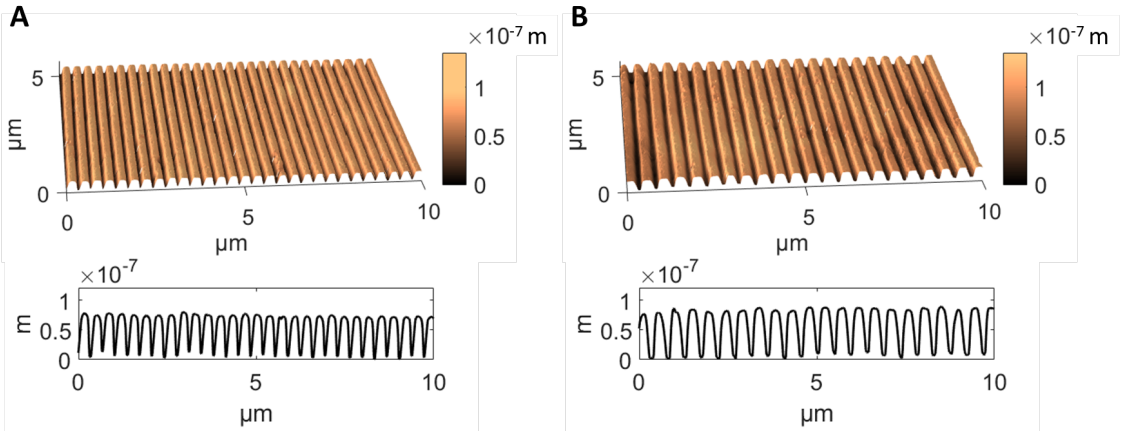

Figure 3.3: **Exemplary permanent and temporary shape. A** The AFM image and cross section show the one-dimensional grating structure of the permanent shape. **B** The temporary shape has a by stretching enlarged period as revealed by the AFM image and the structure's profile.

an embossed grating in the permanent state and the cross section plot reveals the structure's profile. For programming the temporary shape, the substrates were stretched in a tensile testing machine at room temperature to increase the grating's period by 10 % to $\Lambda^* \approx 440$ nm (see Sec. 2.3.2). Topography and profile of a sample in the temporary state are exemplified in Fig. 3.3 B. The structure of the temporary state exhibits a visibly enlarged period compared to the permanent shape while height and duty cycle of the structures are seemingly not effected by the stretching. On top of this temporarily stretched TFX substrate we evaporated a thin layer of the previously introduced organic laser active material Alq_3:DCM in an Lesker Spectros (Kurt J. Lesker Company) chemical vapour deposition (CVD) machine. Since both, Alq_3 and DCM, are small molecules they can be easily evaporated at moderate temperatures without destroying their chemical structure. In this chemical vapour deposition process, the materials are heated to their evaporation temperature and the vapour is directed to the cool sample surface where the molecules condense and build a solid layer. A homogeneous layer is warranted by the high vacuum applied in the process chamber and rotation of the sample. Through an oscillating crystal the deposition rate and layer thickness are controlled *in situ*. **Figure 3.4** A illustrates the CVD process schematically. Alq_3 and DCM are simultaneously evaporated in a high vacuum coating plant at different rates to achieve a concentration of ≈ 2.5 wt.% of DCM in the material. Therefore, we heated Alq_3 to $T_{Alq_3} = 220\,^{\circ}$C resulting in an deposition rate of 0.25 nm/s. At the same time DCM is deposited at a rate of 0.02 nm/s at $T_{DCM} = 120\,^{\circ}$C. After 15 min deposition time at a sample-target distance of about 0.5 m an approximately 235 nm thick layer of Alq_3:DCM covers the TFX substrate. With this CVD coating method, the organic layer possesses a constant thick-

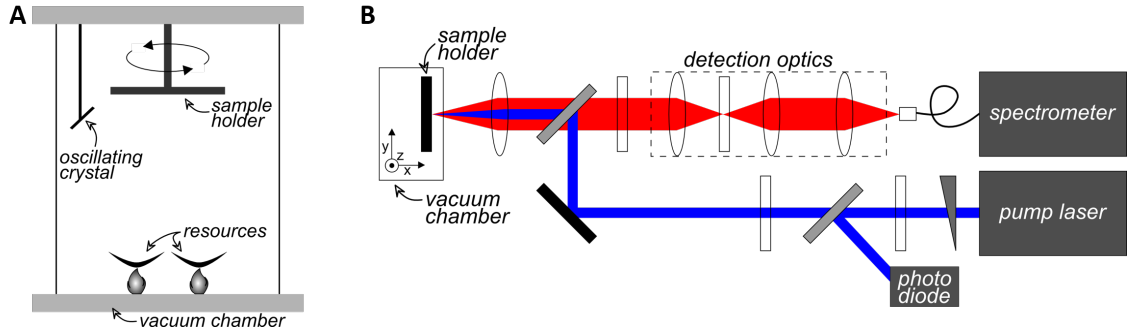

Figure 3.4: **Experimental set-up for device fabrication and optical characterization. A** The schematic illustrates the CVD set-up for coating the SMP substrate with the organic laser active material. **B** The set-up for static and dynamic optical measurements including the beam path of the exciting pump laser beam and the beam path for detection and characterization of the device's emission is shown.

ness so that the layer's surface echoes exactly the morphology of the resonator structure on the substrate. For the optical characterization and measurement of tunability and adjustability we used the set-up depicted in Fig. 3.4 B. As pump laser we used a diode-pumped, actively Q-switched frequency tripled neodymium-doped yttrium orthovanadate (Nd:YVO_4) laser (AOT_YVO_20QSP, Advanced Optical Technologies) with a wavelength of 355 nm and pulse duration of 0.5 ns. To adjust the pump pulse energy we used a variable neutral density filter and for measurements thereof, we applied a calibrated gallium arsenide phosphide (GaAsP) photodiode connected to an oscilloscope. Part of the laser beam is redirected to this photodiode to determine the pulse energy. The main beam is reflected by a dichroic beam splitter and focused with a lens onto the surface of the sample inside the set-up's vacuum chamber. The by the sample emitted beam follows the same optical path at the very beginning but is not redirected by the beam splitter that is transparent above $\lambda = 375$ nm. The beam is then focused on a multimode fiber connected to a spectrometer (grating monochromator: SpectraPro 300i, Acton Research Corporation; ICCD camera: piMax 512, Princeton Instruments). The vacuum chamber is mounted onto a precision stage and, therefore, adjustable in x, y, and z direction in 50 µm increments. For our experiments, it is evacuated to about 10^{-3} Pa in order to protect the organic laser active material from photo oxidation. The thermoelectric element supporting the samples is mounted onto the sample holder inside the vacuum chamber and its temperature is monitored by an added temperature sensor. To allow the sample to contract during the shape recovery process, we fastened it only on one front edge. The back of the sample was covered with heat transfer paste for improved thermal conductivity to the thermoelectric module.

3.3 Results and Discussion

Using the in the previous paragraph described set-up for optical characterization we determined the lasing threshold of our organic DFB laser based on a SMP substrate. The lasing threshold is the minimal needed pump energy input to get beyond fluorescence to stimulated emission. It is therefore an attribute for the quality of the laser. We ascertained it by stepwise increasing the excitation energy fluence until lasing is achieved. For our device we observed the lasing threshold at $\approx 150\,\mu J/cm^{-2}$ as demonstrated in **Figure 3.5** A. The black solid line serves as a guide-to-the-eye. Comparable state-of-the-art Alq_3:DCM laser devices based on PMMA and cyclic-olefin-copolymer substrates as described by Vannahme and coworkers[141,142] exhibit lasing thresholds in the same range. Since the recovery of the SMP resonator's permanent shape is thermally triggered, we

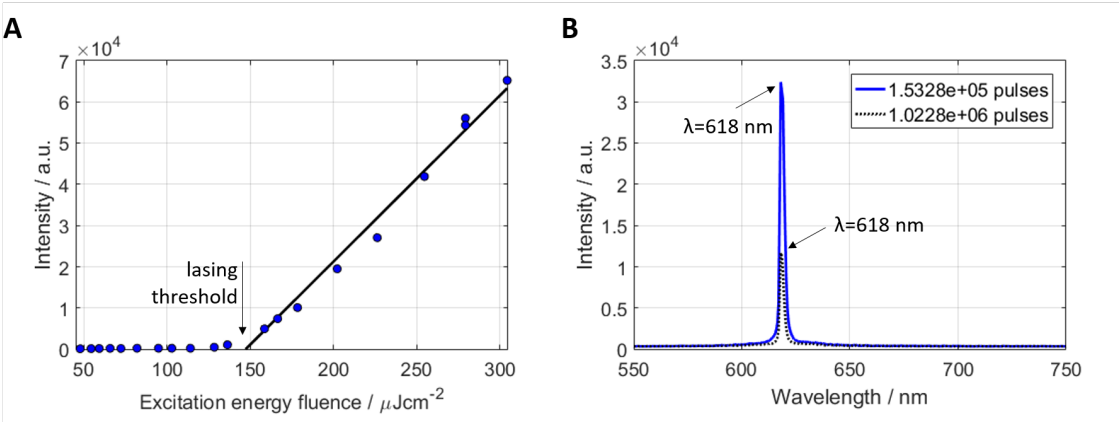

Figure 3.5: **Lasing threshold and life span of the SMP resonator based organic DFB laser. A** The input-output characteristics for evaluation of the lasing threshold shows a clear emission intensity increase at $150\,\mu J/cm^{-2}$. **B** The constant peak wavelength of laser spectra after measured after the denoted number of pulses show that the pump energy cannot trigger the recovery process.

investigated whether the by absorption of the pump energy in the material generated heat is sufficient to trigger the substrate's SME. Therefore, we measured the performance of a stretched device. The result is shown in Fig. 3.5 B. With an excitation energy of 150 nJ per pulse and a repetition rate of 5 kHz the sample is non-stop optically pumped while recording the output intensity. Due to photo-degradation an intensity decrease over the 10^6 applied pulses is noticeable but the peak wavelength remained constant at 618 nm. This proofs that the UV-excitation by the pump laser does not affect the temporary shape. Hence, solely the temperature rise initiated by the mounted thermoelectric module is able to trigger the SME and thereby tune resonator period and emission wavelength.

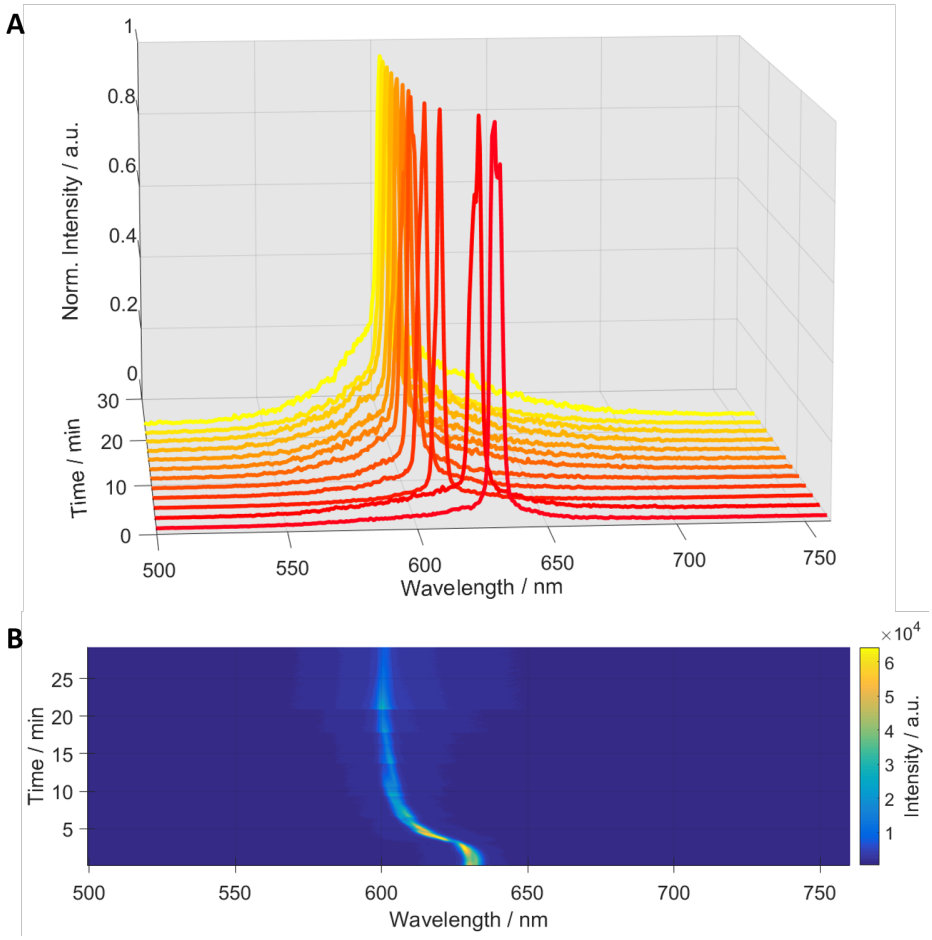

Figure 3.6: **Tuning of the emission wavelength. A** The during the recovery process recorded emission spectra demonstrate the wavelength shift from 630.2 nm to 600.2 nm. The resonator's period was prestretched by 10 %. **B** The false color plot illustrates the wavelength shift, the decreasing intensity with time, and the recovery rate.

In order to demonstrate the dynamic and continuous tunability of our device we heated a by 10 % stretched sample inside the lasing set-up's vacuum chamber to $T_{\text{switch}} \approx 69\,^{\circ}\text{C}$. At the same time the sample was excited and emission spectra were recorded. **Figure 3.6** displays the results of this measurement. The right most curve in Fig. 3.6 A with a peak at $\lambda^* = 630.2\,\text{nm}$ corresponds to the initial period of the stretched sample of $\Lambda^* = 440\,\text{nm}$. The following depicted curves are recorded at equal time intervals of $\Delta t = 2\,\text{min}$ to illustrate the recovery progress. The peak intensities are normalized. Only after the device's temperature exceeds a critical value close to T_{switch} a change in the emission wavelength occurs. The shape recovery rate is highly temperature dependent[12] and therefore accelerates with rising temperature until the maximum temperature of $T_{\text{switch}} = 69^{\circ}\text{C}$ is reached. With approaching the smaller grating period of the resonator's permanent shape of $\Lambda = 400\,\text{nm}$ the recovery process diminishes. Corresponding to that period the emis-

sion wavelength shift ended with a peak at $\lambda = 600.2\,\text{nm}$ (leftmost curve). Hence, we achieve with our devices an overall wavelength shift of $\Delta\lambda = 30\,\text{nm}$.

Additionally, the complete time and wavelength resolved tuning of emission wavelength of this experiment is visualized in the false-color plot in Fig. 3.6 B. By plotting non-normalized values the graph shows the decreasing emission intensity. We consider this to be effected by Alq_3:DCM due to degradation and approaching a spectral range with a lower gain. The recovery rate is strongly dependent on the temperature.[12] Within the range of the switching temperature, lower temperatures yield slow recovery and the higher the temperature is, the faster the SMP samples move back to their permanent shape. Hence, is the sample cooled below the switching range, the recovery is interrupted and the momentary shape is stable until the recovery is triggered again (see Sec. 2.1). We take advantage of this phenomenon to adjust the emission wavelength of our device to any desired wavelength within the tuning range. This range is determined by the emission spectrum of the organic laser active material as well as the resonators permanent and temporary periods. The experimental setup is the same as in the previously described tuning experiment except that at a certain point during the recovery, the sample is cooled by switching

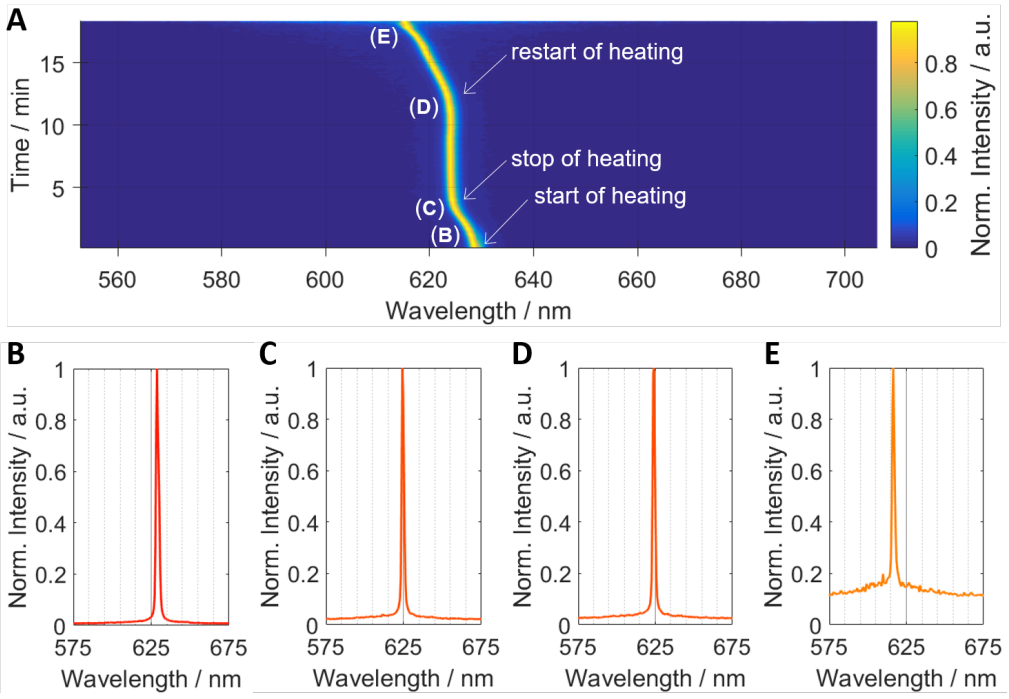

Figure 3.7: **Adjusting of the emission wavelength. A** The recovery process is interrupted and thereby the emission wavelength adjusted to a specific value by using the strong temperature dependence of the recovery velocity. **B-E** Emission spectra shown are recorded at the transition points as denoted in **A**.

off the thermoelectric module. **Figure 3.7** displays the results of this experiment. In the false color plot (Fig. 3.7 A) the device's emission spectra are displayed as a function of time. Figures 3.7 B-E show the normalized emission spectra at the specific experimental steps as denoted in the false color plot. When the thermoelectric module is switched on, the peak wavelength starts to decrease (B). As soon as the temperature decreases below a critical value, the current shape of the resonator is static. Corresponding to this present resonator period, the emission wavelength stays constant (C). After approximately seven minutes the sample is heated again (D) and when the temperature reaches T_{switch} the peak wavelength continues to declines further (E). Between the stop (C) and restart of heating (D) the peak of the emission remains unchanged at about $\lambda = 625\,\text{nm}$. We deduce from this that the grating stays constant in its shape, too. Our experimental data proofs, that by utilizing the temperature dependent recovery rate, we can easily adjust the device's emission wavelength on demand.

3.4 Conclusion and Outlook

By transferring the principles of the fabrication of tunable optical structures that where introduced in Sec. 2.4 to sub-micron structure sizes, we were able to produce tunable Bragg gratings. We successfully applied those gratings as DFB resonators in organic semiconductor lasers with Alq_3:DCM as the organic, laser active material. The experimentally determined excellent performance over time and low lasing threshold of our device proof the suitability of TFX as resonator material in this set-up. Mounted on a thermoelectric module, the SME of the pre-stretched resonator can be heat-triggered on demand to change its resonating characteristics and, therefore, tune the emission wavelength. In addition to the observed tunability over a wavelength range of 30 nm we also demonstrated the possibility to interrupt the continuous tuning at any point as long as demanded. The shape-changing ability of TFX and its transparency offer a multitude of opportunities for the development of optical elements that are tunable without the aid of mechanical framework. This is especially interesting for applications, where the need of reduced volume and cost is more important than the potential of for- and backward tuning of the wavelength. Medical products designed for one-time usage are an example of such devices. Tunable SMP structures might find applications as material for integrated on-chip organic lasers or even complete Lab-on-a-Chip platforms in the course of the development of spectroscopes for biomedical and chemical point-of-care analysis.

A shortened version of this chapter was published as the article "Shape-memory polymers as flexible resonator substrates for continuously tunable organic DFB lasers", by Senta Schauer, Xin Liu, Matthias Worgull, Uli Lemmer, and Hendrik Hölscher, Opt. Mater. Express 5, 576-584 (2015). The study was designed by Xin Liu and me, the tunable resonators were fabricated by myself and the optical measurements were conducted with Xin Liu at the LTI.

4 Tunable Fabry-Pérot Interferometer

Nature offers a vast amount of examples for structural colors and has ever been a source of inspiration for researchers. In this work, I discuss three examples of bio-inspired, light modulating structures that I engineered and fabricated with the aid of shape-memory polymers. This chapter introduces an one-dimensional photonic structure with tunable, wavelength selective reflection that is inspired by the color changing mechanism in some cephalopod species.

4.1 Motivation and Background

The diversity of colors in marine life and mechanisms to produce them are by no means inferior to terrestrial animals and plants, with exception to the deep sea to where little to no light penetrates. In both environments bright and flashy colors are key elements to gain attraction for mating purposes. Likewise, colors are crucial for camouflage to hide from predators or lurk for prey. In terms of camouflage, marine animals face different problems than terrestrial habitants. One of the difficulties is that the shadow cast by an animal makes it clearly visible for potential predators below it.[13,143] Many species of fishes partly solved this issue by light reflecting flanks to match the background illumination. The scales on the fish flanks consist of iridophores. Those are cells that contain highly reflective platelets of an unique family of proteins and cause the typical silvery, shiny appearance of many fish.[144] Depending on the thickness, spacing, and arrangement of the platelets, specific ranges of the electromagnetic spectrum are reflected. Some species even developed mechanisms to influence one of the listed characteristics in their iridophores to tune the reflected color.[13,144–147] This color tuning capability allows the species to perfectly adapt the current surrounding where light conditions might change with depth and time of day. Some of the most fascinating and prominent examples of animals capable of rapid color changes in their skin are cephalopods (e.g. octopus, squid, and cuttlefish). They are perfectionists in matching their color and even texture to their surrounding using specialized skin cells.[13] While most of those color changing cells, the chromatophores, contain pigments that are translocated depending on the to be generated hue, iridophores have been reported, too.[13] Alternating high-refractive index and

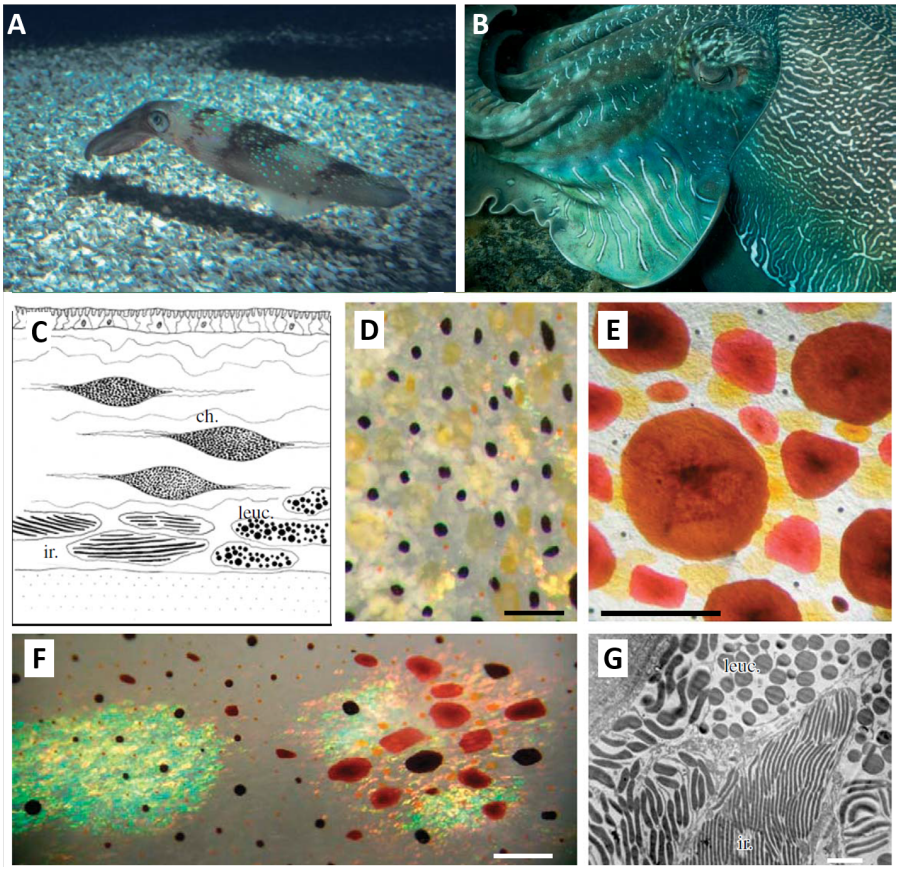

Figure 4.1: **Color production in cephalopods. A** The squid *Logio pealeii* has iridescent spots. **B** Blue-green iridescence and bright white stripes are observable in the cuttlefish *Sepia apama*. **C** The schematic shows the location of chromatophores (ch.), the pigment containing cells, the iridophores (ir.), the iridescence causing cells, and the leucophores (leuc.), the cells that are responsible for white scattering in cephalopods. **D** Chromatophores (yellow/brown/orange) and leucophores (white) of the cuttlefish *Sepia officinalis* and **E** the squid *Logio pealeii* are shown. Scale bars: 1 mm. **F** The photograph shows the iridescence in iridophores in the skin of the squid *Logio pealeii*. Scale bar: 1 mm. **G** An electron micrograph shows the ultrastructure of iridophores and leucophores in *Sepia officinalis* skin. Scale bar: 1 µm.
Adapted from[13].

low-refractive index platelets stacked in those cells build Bragg reflectors causing highly wavelength selective reflection of light.[13,144] For example, the iridocytes of the California market squid (*Doryteuthis opalescens*), the longfin inshore squid (*Loligo pealeii*), the European common cuttlefish (*Sepia officinalis*), and the giant cuttlefish (*Sepia apama*) are able to shift the reflected peak wavelength by 250 nm from red to blue by decreasing the thicknesses of the layers constituting the Bragg stacks by approximately a factor of two.[144] **Figure 4.1** displays the vivid, iridescent colors based on the respective cell ultrastructures in some of the before mentioned examples.

Inspired by the capability of those squids to actively tune the interference conditions in their iridophores and therefore the reflected structural color, I investigated the suitability of SMPs as spacing material between two highly reflective layers that allows tuning of the spacing thickness.

A "sandwich" of a sub-micron thick dielectric spacing between two reflective surfaces is known as a Fabry-Pérot etalon or interferometer (see Sec. 2.2). Incoming light is reflected at both surfaces and in accordance to the distance between those two surfaces specific wavelengths interfere constructively. With varying thickness of the dielectric film, also the reflection spectra changes. The majority of first reported tunable Fabry-Pérot interferometers consist of two microelectromechanically fabricated, anorganic Bragg-mirrors separated by an air gap that shortens due to electrostatic attraction when voltage is applied.[148–150] The fragility of the produced devices as well as the fabrication costs limit the applicability of those interferometers. The eligibility of stimuli responsive materials to function as variable dielectric layers between the two reflective mirrors has been object of inquiry in the last decades. Serpe and his coworkers pioneered in the application of microgels such as poly (N-isopropylacrylamide) (pNIPAm) for Fabry-Pérot interferometers. They demonstrated a temperature-coupled tuning of the thickness of the microgel layer between two Au films.[151–153] The tuning mechanism is based on the characteristic behavior of pNIPAm to switch between a hydrophilic and a hydrophobic state at a temperature of 32 °C. At room temperature it forms a hydrogel that undergoes a phase transition at the mentioned temperature whereupon it repels the adsorbed water and shrinks to its dehydrated state. With this material they reported shifts in the peak wavelength of about 30 nm. With their concept they face the problem that the color change is directly linked to the temperature dependent thickness of the pNIPAm layer. Hence, the temperature has to be held constant at an elevated level to achieve a color change. Furthermore, the absorption/dehydration mechanism might allow continuously tuning of the color in the swelling/repelling process but results in a bi-stable device. Also, a sufficient amount of water (or aqueous solution) has to be provided at all times.

To overcome those drawbacks we developed a concept that allows us to tune the thickness between the two reflective layers through the shape-memory effect of the spacing polymer. The nature of the SME of our polymer Tecoflex®EG 72D (TFX) (see Sec. 2.3.1) enables continuous tuning from one specific shape into a second one with the possibility to stop and restart this morphing at any state between those two distinct shapes. However, the volume of the SMP during this shape transition remains constant. This implicates that the required shape change cannot be as simple as a thin film which is temporarily decreased in thickness while all other dimensions of the film stay the same. Our solution to

this problem and concept for the realization of a Fabry-Pérot interferometer with tunable interference conditions is presented in the following sections.

Our approach is to emboss an array of nanopillars as temporary structure into a sub-micrometer thick TFX film. While embossing, the softened TFX will flow to some extent into the cavities of the mold and form the pillars. At the same time, the area between the pillars will be thinned by the same volume that is consumed by the newly formed pillars. From an one-level thin film framed by the two reflective layers at the beginning, the sample will now be transformed into a temporary two-level structure. Due to using a polymer that possesses a SME, the structuring is reversible. In this concept, the over the sample uniform interference conditions and therefore color of the permanent shape are divided into two sections in the temporary shape. The resulting color stems from the superposition of the pillar-caused interference and the film-caused interference.

4.2 Fabrication

One main question arose in the process of the realization of our concept: How do we fabricate a sub-micrometer thick TFX film that does nevertheless exhibit good shape-memory properties? Common ways to produce homogeneous polymer films with thickness below one micrometer are solution based methods such as spin coating, dip coating, or wire-bar coating.[98] While preparing a solution of TFX is possible with various solvents, the answer to the question whether the solvent or the solution processing affect the arrangement of the segments of the block-copolymer (and therefore the SME) is not trivial and will be discussed in the following. For the realization of the tunable interference conditions in the metal-SMP-metal tri-layer I fabricated a sandwich structure of a TFX thin film between two silver layers and applied a sophisticated programming procedure. In the first step of the fabrication of the tri-layer, sputter coating was used to cover a before with isopropyl alcohol and de-ionized water thoroughly cleaned, square glass slide with a thin silver film as depicted in **Figure 4.2**. With a sample-to-target distance of 50 mm, a current of 50 mA,

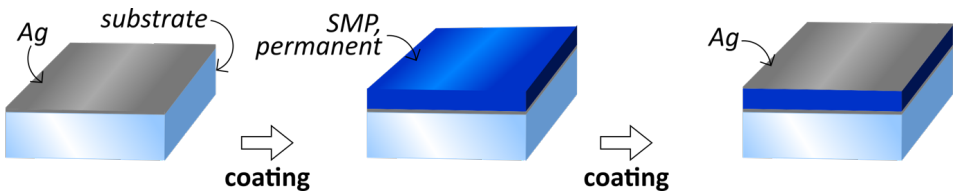

Figure 4.2: **Schematic illustration of the tri-layer fabrication.** A glass substrate is first sputter coated with an Ag layer, then a thin SMP film is applied by spin coating from solution and afterwards a second, thinner Ag layer is sputter coated onto the polymer.

Argon plasma, and a duration of 120 s an Ag thickness of ≈ 71 nm was achieved. The film thickness was determined with ellipsometry. Afterwards, a thin SMP film was produced from solution with spin coating (see Sec. 2.3.2). Therefore, TFX was dissolved in a 1:1 mixture of the solvents dimethylacetamide and methoxybenzene to ensure good solubility and a homogeneous coating. The concentration of TFX in this solution was 3 % by weight and applied spin coating parameters were 30 s duration and an acceleration of 2000 rpm/s in a nitrogen atmosphere. The spin speed was varied between 500 rpm and 4000 rpm to adjust the SMP film thickness. With those parameters, film thicknesses ranging from ≈ 800 nm to ≈ 80 nm could be produced. Those thicknesses were determined by measuring the step height of an inflicted scalpel scratch by AFM. Directly after coating, the samples were tempered on a 100 °C hot plate for 1 h, first to evaporate the solvents and secondly, to temper the film. As mentioned before, we expected the strong centrifu-

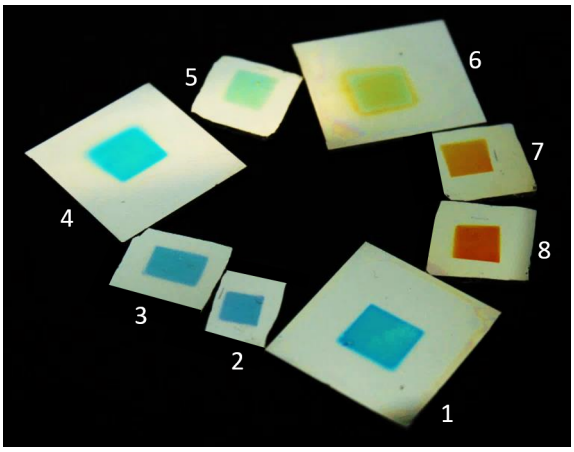

Figure 4.3: **Different TFX layer thicknesses result in different colors.** With increasing TFX layer thickness (from 1 to 8) between identical Ag layers the perceived color shifts from blue over green, yellow, and orange to red.

gal forces while spinning, the substrate-solution interactions, and the rapid evaporation of the solvent to have a heavy influence on the arrangement of the TFX chain blocks in the bulk of the film. In fact, experiments support this assumption. A sample that was dried at only 30 °C for one hour at the hot plate, but otherwise processed identically, did not show any noticeable shape change in the recovery step. The tempering at temperatures as high as 100 °C seems crucial in that it allows the different blocks to arrange phase segregated. Such an arrangement is a prerequisite for the polymer's SME (see Sec. 2.1). After processing from solution and tempering, the TFX film is in its permanent shape ('perm'). Subsequent to tempering, the samples were covered with the top Ag film, again by sputter coating. The sputter time was reduced to 60 s while all other parameters were identical to the process parameters for generating the bottom Ag layer. This reduced time

resulted in a semi-transparent coating with a thickness of ≈ 23 nm. Depending on the spin parameters and therefore the TFX film thickness, the interference conditions change and the resulting colors vary. This influence is demonstrated in **Figure 4.3**. The samples shown in the photograph exhibit a color change from blue to red with increasing TFX film thickness from ≈80 nm (1) to ≈800 nm (8). The top Ag layer was sputtered with a mask to visualize the necessity of multiple reflection between the two silver layers for the generation of intense colors.

Figure 4.4 depicts the major steps that were performed for programming the second, temporary shape into the tri-layer ('temp'). Before the temporary structuring by hot embossing took place (see Sec. 2.3.2), the samples were prepared. In consequence of the spin coating process, the "coffee ring" effect yielded in a thicker film at the edges and corners of the glass substrate. This rim was removed to ensure uniform contact of the mold to the film. Subsequently, the sample was placed between a silicone rubber sheet and the mold on a smooth bottom plate in the hot embossing machine. The silicone rubber sheet compensates small unevenness of the bottom plate to support even force distribution while embossing and prevents from breaking of the glass substrate. Due to the resultant, shallow structures demolding was conducted by hand and the mold was not fixed to the tool plate. Deviating from the in Sec. 2.3.2 described procedure, the mold was pressed on

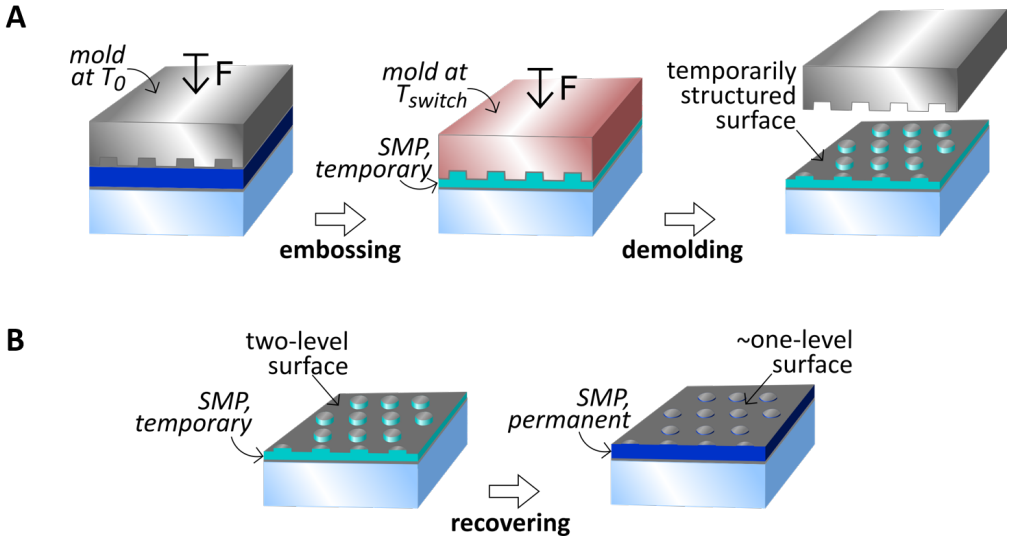

Figure 4.4: **Schematic illustration of the programming and tuning procedure. A** A structured mold is pressed on the surface of the tri-layer and subsequently heated to the SMP's switching temperature to temporarily structure the polymer. After cooling the mold down to room temperature the structure is demolded. **B** Now, the structure consists of a two-level surface with thinned film between small pillars. Heating the sample to the switching temperature leads to recovery of almost the original film thickness and the pillars vanish.

the sample at room temperature in the first step and only afterwards heated to T_{switch}. The intentions of this modulation are first, the mold's and sample's temperatures are increased at the same rate to minimize the risk of cracking of the glass because of thermally induced tension and secondly, to prevent rupturing and flowing of the top Ag layer. While mold and sample were heated to $T_{\text{switch}} = 50\,^{\circ}\text{C}$ the pressure of 4,8 MPa was kept constant resulting in a readjustment of the tool position and thereby thinning of the TFX film between the emerging pillars. After a dwell time of 600 s at constant temperature and pressure, the mold and sample were cooled down to room temperature at constant tool plate position. Thereafter, the mold could easily be removed from the now temporarily structured sample. To recover the original film thickness as depicted in Fig. 4.4 B the sample was heated to 80 °C for 5 min on a hot plate, a temperature at the upper end of the switching range of TFX. As the film thickness increases the pillars' height reduces until they are almost vanished in the recovered shape ('rec').

4.3 Results and Discussion

The in the course of this programming of the temporary shape and recovery of the initial shape achieved change in TFX film thickness between the two Ag layers results in a distinct color change of the samples. **Figure 4.5** reveals this color change of an initially green sample in photographs and microscope images. The permanent shape of the sample is shown in Fig. 4.5 A. The photograph (left) shows the whole sample in ambient light from an angle of $\approx 10\,^{\circ}$ to the surface normal. Slight inhomogeneity in the film thickness effect deviation to red from to otherwise intense green color. The structure change upon temporary embossing results in a color shift to deep red in the structured areas (Fig. 4.5 B). The area, where the microscope and AFM pictures in the following are taken, is marked with the dotted, white rectangle. The microscope pictures reveal the different colors arising from the two levels of the surface. While in the low magnification (middle picture) the colors superpose to one observable, red color, the close-up shows the differentiation of the greenish color of the pillars and orange-red in the interspace. The photograph (left) also shows that the structuring is not uniform in the embossed areas. Smallest variances of the mold might affect the embossing result strongly since the polymer layer thickness is below 1 µm. After recovery, the sample shows again a green color in the considered area as revealed by Fig. 4.5 C. It is evident in the microscope images that a residual structure remained and the recovery of the smooth surface is not complete.

The structure changes corresponding to the color change in the different programming/recovery steps were analyzed with AFM. In **Figure 4.6** A the smooth surface of

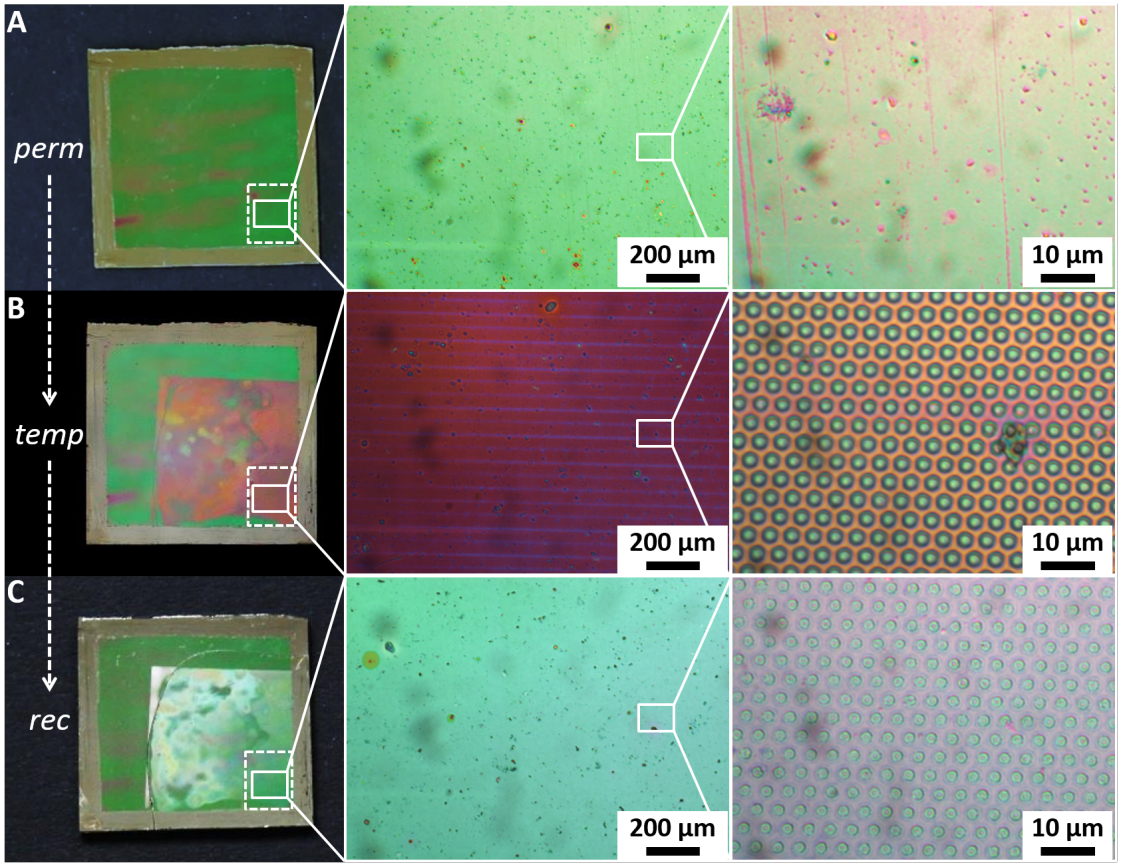

Figure 4.5: **Tunable color in the programming and recovery steps.** One sample is shown in the three steps of the programming/recovery process in photographs (left column) and microscope pictures (middle and right column) with **A** the initial, permanent shape with its intense green color, **B** the embossed, temporary shape exhibiting deep red coloration with by the microscope images revealed color differences between the pillars and the film, and **C** the recovered, again green sample with slight residual pillars.

the permanent shape is displayed. The surface of the tri-layer film possesses a roughness of $R_{rms} = 1.3\,nm$. The measurement of the temporary shape in Fig. 4.6 B depicts the division of the surface in two levels. The smooth surface of the now thinned TFX layer is disrupted by hexagonally arranged pillars. As a result of the shape recovery process those pillars vanish to a great extent as seen in Fig. 4.6 C. The residual structure is due to incomplete recovery of the permanent shape of TFX. Additionally, the top Ag coating is disrupted in the hot embossing step and thus does not return to the initial, smooth surface.

In order to analyze the corresponding height of the pillars and the thickness of the film in between in each sample state, the sample is scratched in each state and the respective step height is measured with AFM. The cross sections of those measurements are displayed in Fig. 4.6 D and show the step heights from the bottom of a scratch to the films' surfaces. Visual examination did not reveal any damage to the bottom Ag layer. There-

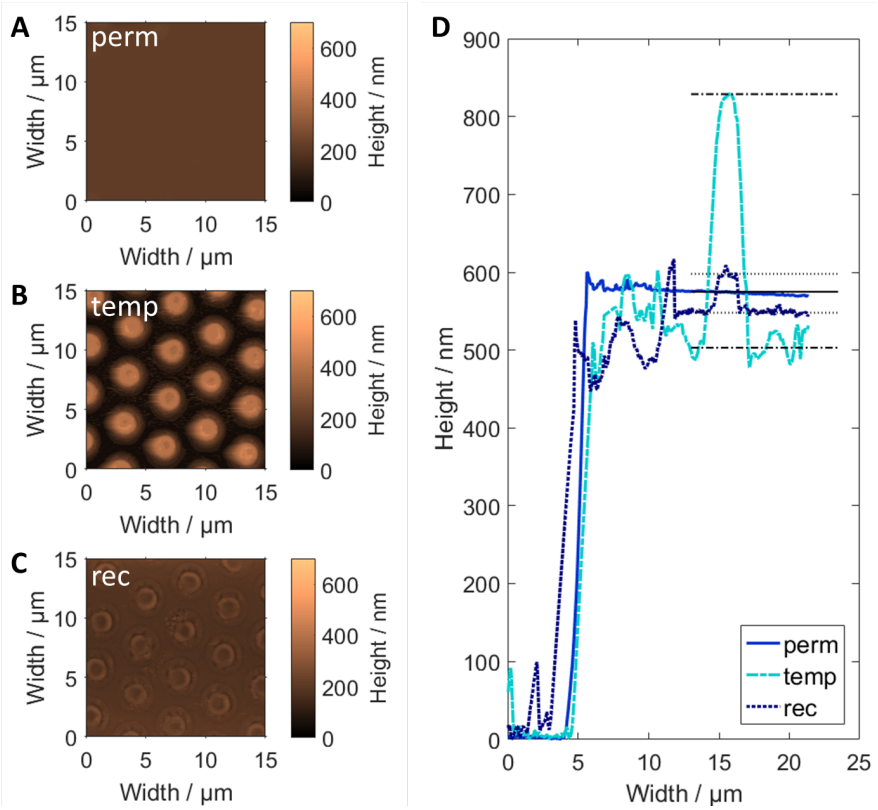

Figure 4.6: **Topography and thickness of the three states of a sample measured with AFM.** The surfaces of **A** the permanent shape, **B** the temporary shape, and **C** the recovered shape show the topography changes resulting from the programming and recovery procedures. **D** Cross sections from measurements at a scratch in the respective sample states demonstrate the film thickness changes.

fore, only the top Ag layer thickness is subtracted from the measurement to determine the TFX layer thickness. The cross section of the permanent shape (blue, solid line) reveals its smooth surface except some irregularities close to the scratch. The pillars and thinned TFX layer between the pillars is clearly visible in the cross section that was measured on the temporary shape (turquoise, dash-dotted line). In the recovered state, the height of the pillars is significantly decreased and the TFX film thickness is increased (dark blue, dotted line). The black lines indicate the

Table 4.1: Height of film and pillars in the three sample states.

	permanent	temporary	recovered
film	570 nm	505 nm	542 nm
pillars	-	824 nm	605 nm

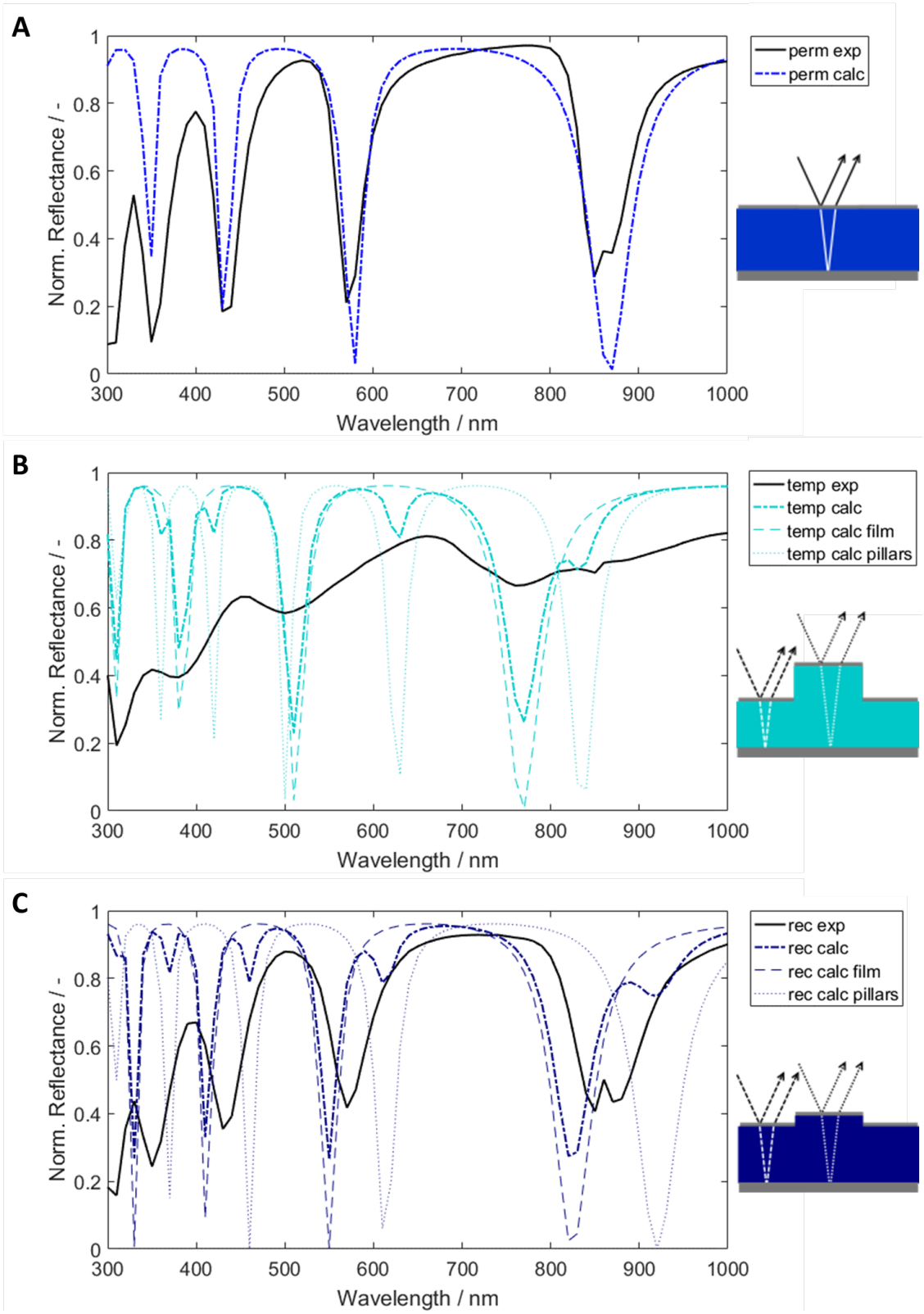

Figure 4.7: **Measured and calculated reflection of the three sample states.** The graphs depict the measured and calculated reflection of one sample in its **A** permanent, **B** temporary, and **C** recovered state.

extracted thicknesses summarized in **Table 4.1**. On the same sample as depicted in the previous two pictures I performed reflection measurements and compared them with the calculated reflection based on the film thicknesses determined with AFM. A reflection measurement was conducted for the permanent shape before embossing, for the temporarily structured sample, and after recovery of the initial shape. The reflectance was determined with an angle of incidence (AOI) of 8 ° for wavelengths from 300 to 1000 nm in a spectrophotometer (see Sec. 2.3.5). **Figure 4.7** depicts the results of those measurements ("exp", black lines) and the according calculation of the reflectance ("calc", blue/turquoise/dark blue lines). For the calculation I considered the same AOI as in the measurements. Under this angle the various optical path lengths of the waves in the TFX film were calculated to determine the phase difference between the reflected waves for each wavelength as discussed in Sec. 2.2. For the permanent shape with the uniform TFX layer between the two reflecting Ag layers, the measurement and calculation show good conformity as demonstrated in Fig. 4.7 A. In the visible regime the peak is in the green range with some contribution in the blue and red ranges. For the calculation of the reflectance of the temporary and recovered structures the contributions of the film areas (dashed) and the pillar areas (dotted) were calculated separately with the according film thicknesses and structure heights, respectively, and finally weighted with the percentage they possess of the total surface area and summed up (dash-dotted). Additionally, interference between beams exiting at the film level and those exiting at the pillar level is considered. The results for the temporary shape is shown in Fig. 4.7 B. The dash-dotted turquoise line marks the superposition of the light reflected at the film level and the pillar level. When compared to the experimentally gained reflectance data (solid black line), vast differences are obvious although the position of the reflectance peaks are similar. Presumably, there is mainly one reason for the strong deviation of experiment and calculation: In the photographs in Fig. 4.5 it is apparent that the structured area is not uniformly structured. Small variances in TFX film thickness combined with the not perfectly flat surface of the mold yielded differences in the embossed pillar height. The AFM images to compare the three structures of the sample in its different states were all taken from within the area marked with the white, dashed line in Fig. 4.5. However, the spot of the spectrophotometer exceeds this area and therefore, film thicknesses contribute to the experimentally gained reflection spectra that are not considered in the calculation. This might also be the reason for the minor differences of experiment and simulation of the sample in its recovered state shown in Fig. 4.7 C. While the peaks of the profiles of the measured reflectance spectra and the superposed, calculated spectra are in similar positions, there is a distinct difference between the shape of the two reflected spectra. Nevertheless, the three graphs

in comparison confirm the in Fig. 4.5 photographically captured color change from the permanent shape to the temporary shape by embossing and from the temporary state to the recovered shape by triggering the polymer's shape-memory effect.

4.4 Conclusion and Outlook

Using our shape-memory polymer as dielectric layer between two highly reflective silver layers allows us to tune the interference conditions of this tri-layer system and, hence, the reflected spectrum. In this chapter, a fabrication route was introduced that facilitates the shape-memory ability even in solution processed, sub-micrometer thick SMP films. Our approach to tunable Fabry-Pérot interferometers comprises the change from an one-level, Ag-framed layer in the SMP's permanent shape to a temporarily embossed two-level structure consisting of a thinned film between emerged pillars. We demonstrated that with our fabrication, programming, and recovery cycle we were able to reversibly tune the perceived color of our device from green to red.

The scope of applications for our method can be immensely widened if the mechanical structuring performed in the hot embossing machine to form the temporary shape is avoided. At this point, an once recovered structure is in need of another embossing step to again achieve a shape change. This, however, can be evaded by connecting the two silver layers to a power supply unit and using electrostatic forces between those two layers to manipulate the SMP layer's thickness. This can be accompanied with a certain temperature treatment for programming and shape fixation. A schematic of this idea is sketched in **Figure 4.8**. After one embossing cycle, the top Ag layer features a pattern of holes that allows the SMP to evolve into pillar structures to enable a thinning of the film in between. For this concept, the utilized polymer should exhibit a sufficient low stiffness at a temperature within its switching range in order to allow for reasonable electrostatic forces to mold the SMP.

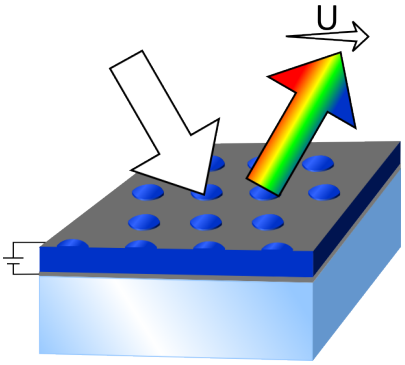

Figure 4.8: **Outlook on advancement of our current device.** Electrostatic forces between the two Ag layers can be used to change the thickness of the SMP layer separating them in order to re-program the temporary shape. A vivid color change comes along with the SMP layer thickness modulation.

Furthermore, it is not necessary to attach the Ag-SMP-Ag tri-layer to a glass substrate. It can be applied to many surfaces, even to, to some extent, flexible substrates. Therefore, large-scale, flexible display offering vivid and intense colors could be realizable based on our approach. The greatest asset of this color producing mechanism is that energy is only needed when a color change is demanded as it is the case for instance in e-reader displays. Between the reimposeable temporary shape and the recovered shape, any intermediate shape can be maintained as long as needed (see Sec. 3.3). Hence, also every color between those two end-states is quasi-statically attainable. Compared to emission based displays such as, e.g. LED displays, every pixel is not limited to one color (red, green, or blue) but is color tunable and therefore, with using the current state-of-the-art contacting framework, a by factor three increased resolution is achievable with color tuning pixels.

5 Surface Wrinkles

The second type of bio-mimicking structures presented in this thesis are inspired by fascinating, complex structures found on the surface of flower petals. Those often hierarchical micro-and nanostructures, i.a., contribute to the exhibited color. In contrast to the previously described concepts, where the shape-memory effect of the SMP is used to tune the respective structures, here, the SME is utilized to generate the structures. Nonetheless, the designed structures are highly adjustable in size and shape by the fabrication parameters. Using the SME for structure production allows us to create otherwise impossible geometries in a (partially) mold free process on large-scales. This chapter presents the development of this surface structuring method based on mechanically directed self-assembly of a polymer film supported by a SMP substrate that creates a highly controllable surface wrinkles. Furthermore, I show the results of the investigation of the effect of all process parameters on the resulting structures that allowed us to tailor the wrinkle sizes over a wide range. Diverse advancements of the basic method to produce hierarchical structures are introduced and their potential for color tuning devices evaluated. For comparison to the biological role models, we investigated the wrinkle's optical properties in terms of diffractive behavior in reflection and transmission.

For the optical characterization of my wrinkle structures, I collaborated with Dr. Guillaume Gomard and Raphael Schmager from IMT, KIT, and Ruben Hünig from the Light Technology Institute (LTI), KIT, and we exploited the benefits of the wrinkles' light incoupling properties for crystalline silicon photovoltaic devices.

5.1 Motivation and Background

Especially plants that rely on cross pollination for fertilization developed amazing solutions to make their blossoms as appealing as possible for insects. Besides scent and nectar offered by the plant to attract pollinators, the petals' coloration plays a major role. Vivid and luscious coloration produced by pigments is in some petals enhanced by structures or structural coloration.[154–156] Structures on petals can, e.g., lower the sunlight's reflection to increase good wide-angle reception of the pigmentary color, act as a diffractive structure and thereby cause iridescence, polarize light to direct insects that have polarization-

sensible vision to their pistil and stamen, efficiently reflect UV radiation, and contribute to the petals' hydrophobicity which provokes a self-cleaning effect.[87,157–163] Self-cleaning of petals assures that the petals' color is always luscious and visible. Water and dirt on petals might also hinder scent dispersal. Furthermore, the structured nature of the surface is discussed to influence potential pollinators' grip.[157,164–166] Among the mentioned diffractive structures, periodic striations caused by wrinkling of the epidermal cell walls are one of the most widespread examples for structural iridescence on petals. These wrinkle structures are particularly pronounced in, for example, many species of the hibiscus family and in multitudinous tulip species.[87,157,163,167,168] Striations causing iridescence are at least one magnitude smaller than typical dimensions of epidermal cells. Therefore, nature has evolved mechanisms to create those small grating structures as part of their epidermis covering the cells. Cell shape and epidermis structure combined generate numerous varieties of hierarchical structures.[169–171] Floral iridescence has been proven to be a beneficial feature for pollinator attraction.[157] The change in petal coloration with different viewing angles is perceived by bees and bumblebees and serves as a cue to guide them to the flower for pollination. With a view on the global thread of declining numbers of pollinators, understanding and mimicking such linear and hierarchical striations as present on petals is of great importance.[157,172,173] **Figure 5.1** gives three examples of hierarchical structures combining linear striations on anisotropic cell structures in different alignments. In the top row photographs of the blossoms taken in ambient light are presented with, in the second row, the respective microscope images of the outer (A) and inner (B and C) side of the petals. The third row shows SEM pictures of the petal surfaces and close-ups thereof are displayed in the bottom row. The cultured tulip species *Queen of the Night* shown in Fig. 5.1 A distinctly exhibits an iridescent sheen on the top parts of the petals' outer side. The deep violet pigmentation emphasizes the angle dependent hue caused by the structures that are revealed by the SEM image. The close-up highlights the structure details. Small grating like structures are aligned in parallel with the large, underlying longitudinal cells.[174] Figure 5.1 B presents the daisy *Bellis perennis*. Its petals feature a mat, white color. The luscious coloration might be linked to possible anti-reflective properties of the hierarchical micro and sub-microstructures on their petals. Sub-micron sized striations are oriented perpendicularly to the corrugated, elongate cells.[174] Lastly, Fig. 5.1 C illustrates the rich red of treasure flower petals (*Gazania rigens*). Here, wrinkle structures are on the side walls of unidirectional, triangularly shaped cells. The wrinkles are orthogonally aligned to those triangle gratings as visible in the SEM picture and its close-up.

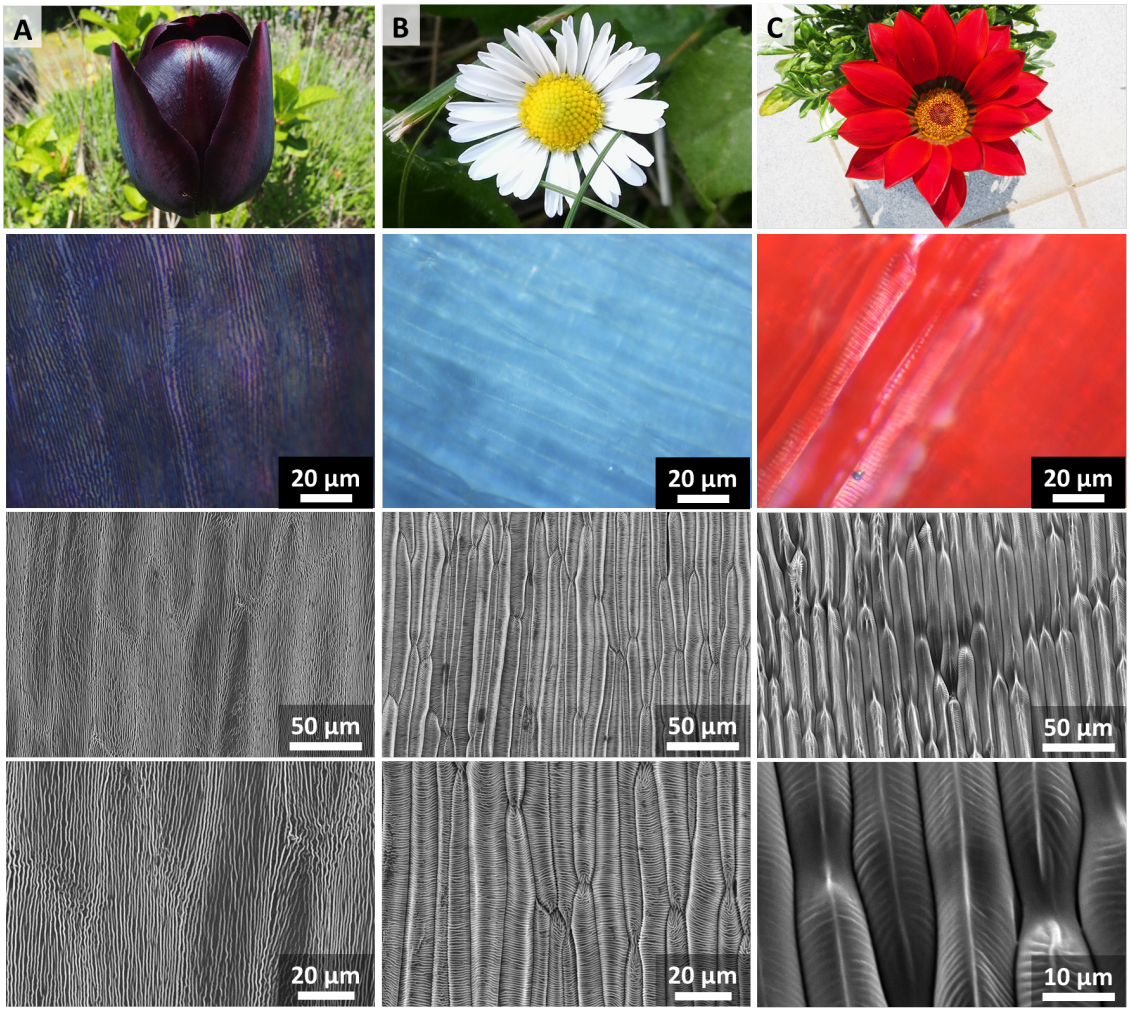

Figure 5.1: **Examples of hierarchically wrinkled flower petals.** A photograph shows the visual appearance of each flower (top row) and microscope (second row) and SEM pictures reveal their hierarchically structured petal surfaces (third row) and the structure details (bottom row). **A** The tulip *Queen of the Night* exhibits slight iridescence and a glossy sheen on its dark violet petals due to micron-sized striations parallel to the orientation of the underlying wavy cells. **B** The petals of the daisy *Bellis perennis* appear in an intense white. Here, the striations are perpendicularly aligned with regard to the undulated cell substructure. **C** Petals of the treasure flower *Gazania rigens* are lusciously red colored. Surface wrinkles are aligned on the lateral faces of almost prism shaped elongate cells.

Slightly irregular structures as exhibited by the petal surfaces displayed in Fig. 5.1 are also of great interest for a wealth of applications in optics and photonics. Such disordered diffraction gratings constitute a class of optical elements that possess controllable optical properties but are not as spectrally and angularly restrictive as their perfectly periodical counterparts.[175–180] Perfectly periodic diffraction gratings are key components for many optical devices where controlled redirection of monochromatic light or spectral separation is needed.[176] However, for some applications this spectral dissociation can

be highly unfavourable. This divergence of light can be abolished by implementing a certain degree of disorder in height and/or period to the grating structure in a way that the individual diffraction angles are significantly broadened. For transmission, broadened diffraction angles of artificial, disordered diffraction gratings have been reported to improve light-extraction and to reduce angle-dependent color effects in organic light-emitting diodes.[175] The applied compound binary gratings yield an angular redistribution of the out-coupled light. Furthermore, it was demonstrated that disordered gratings are efficient in light-trapping over an extended spectral range in thin film solar cells, due to the structure's ability to guide and retain light within the photo-active regions of photovoltaic devices.[181–183] In this context, the hierarchically wrinkled structures of rose petals replicated onto the surface of solar cells have been proven to be highly beneficial for light-harvesting and increase the efficiency of the utilized thin-film solar cells.[184] They have also been shown to be advantageous for redirecting light over a broad angular range in the context of daylighting.[176] The repression of sharp diffraction orders is also beneficial for various applications were the structure is employed as reflective grating.[185] Strong specular reflection as well as intense diffraction orders experienced when sunlight impinges on planar, perfectly periodically structured surfaces is purposely avoided with disordered diffracting structures. Therefore, disability glare, which is a serious safety issue for urban and air traffic, is prevented.[186–188]

Optical Properties of the Tulip Role Model

Due to its iridescence the tulip *Queen of the Night* shown in Fig. 5.1 A was subject of some investigations lately.[163,167,168] Since this tulip served as a role model for our studies, we conducted most of the in the following shown optical measurements on fresh *Queen of the Night* petals or replica thereof for comparative reasons. The replicas were produced according to the process illustrated in Fig. 5.25. The results of those, as reference serving experiments are summarized in **Figure 5.2**.

The reflectivity of a fresh petal and a replica thereof were measured each for various angles of incidence (AOI) ranging from 0 ° to 80 °. The in Fig. 5.2 shown spectra were recorded by altering the AOI perpendicularly to the wrinkle orientation. The spectra of the fresh petal exhibit a slight reflectance increase in the blue range and a vast increase in the red range pursuant to the intense, pigment based, violet color of the tulip's petals. The pigmentary contribution to the color is eliminated in the replica. Thus, the present microstructure results in a low, wavelength-independent reflectance. Up to an AOI of approximately 30 °, the reflectance over the whole VIS spectrum is below 4 % and even

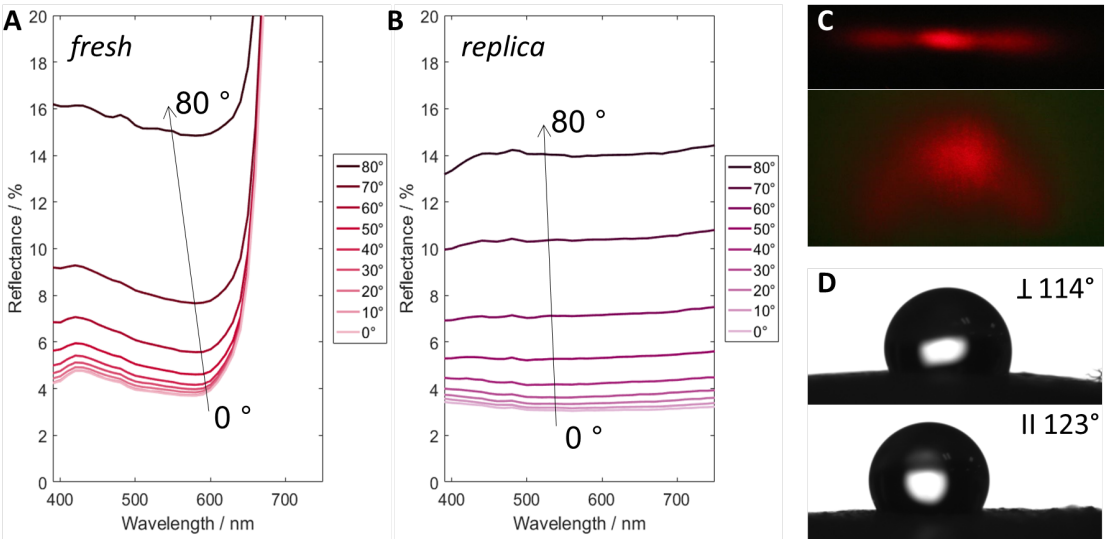

Figure 5.2: **Optical measurements performed on original *Queen of the Night* structures. A** The integrated reflectance of a fresh petal is given for various AOIs measured with perpendicular to the wrinkle orientation altered AOI. **B** The same measurement was performed on a NOA replica of the petal. **C** The photographs display the transmitted (top) and reflected (bottom) diffractive patterns of a NOA replica. **D** The results of contact angle measurements show the wetting anisotropy of the NOA replica.

for 70 ° the reflectance is barely above 11 %. Additionally, I conducted contact angle measurements that revealed the anisotropy on the wetting properties of the tulip petals. The result of the measurement as depicted in Fig. 5.2 and performed on a NOA replica show a difference between the perpendicular and parallel measurements of 9 °.

Buckling in Cells

One of the assumed mechanisms for the formation of periodic striations on the outer surface of epidermal cells is buckling.[167] The cuticle, a continuous cell covering layer composed of cutin, waxes and polysaccharides in a polymer matrix, is produced by epidermal cells.[189] The epidermis cells grow anisotropically whereas the cuticle is generated isotropically, by what compressive stresses in the cuticle might be induced. This can result in buckling and formation of wrinkles in the epidermis due to the different elastic moduli of cell wall and cuticle. If a sufficiently large lateral compression along with tension in perpendicular direction is existent, parallel striations normal to the compression direction are formed.[167]

We avail ourselves of a process based on a similar principle as observed in the flower's structure formation to create artificial striations on large areas. Through wrinkling of a thin polymer film on a shape-memory polymer substrate we generate widely adjustable

periodic surface wrinkles from few hundred nanometers up to several microns with a certain degree of irregularity.

Wrinkling - State of the Art

Wrinkling is a well known phenomenon for the self-organized generation of one or two dimensional patterns based upon mechanical instabilities of a stiff coating on an elastic substrate. The key to fabricate surface wrinkles in a bi-layer heterostructure is to provoke an uni- or bidirectional compressive stress field in the coating that exceeds a critical value. In other words, one induces the attempt of the substrate to reduce its surface area whereby the coating becomes too large for the substrate and compensates this interface area mismatch by wrinkling. This can be achieved for instance by mechanical compression of the elastic substrate or release of an under load strained substrate.[190–192] Additionally, techniques including swelling of the top layer and utilizing the thermal expansion of either only the substrate or the mismatch of the thermal expansion coefficient between substrate and coating have been studied.[193–197] The most commonly reported material combinations for buckling on elastic substrates are thin metal films coating soft elastomers such as polydimethylsiloxane (PDMS) and PDMS substrates with oxygen-plasma treated surfaces by what the uppermost layers are transformed into a hard silica coating.[194,198–203]

However, using metal, PDMS, or both comprises some major drawbacks regarding the sample handling during fabrication, the prospects of up-scaling, and the scope of applications of such wrinkle structures. Elastomeric substrates have to be held under constant tension while their surfaces are treated or coated to effect a stiff top layer. Surface structures created with a metal thin film lack transparency, hence, their applicability for use in optics and photonic devices is limited. Furthermore, due to the marginal elasticity of metals and silica, they tend to form multiple cracks during the buckling process perpendicular to the wrinkle orientation because of the reversion of the lateral contraction during former stretching.[204–206]

To overcome all three impairments, we employ shape-memory polymers as substrate material and cover them with a second thin polymer film, namely poly(methyl methacrylate) (PMMA). Compared to elastomers, SMPs are able to maintain stable in a temporary shape as well as they feature the advantage of being rigid at room temperature, but undergoing a significant Young's modulus drop with rising temperatures.[207] By applying a thermoplastic polymer as coating we also induce the possibility to easily structure this film before wrinkling.

5.2 Linear Wrinkles on Shape-Memory Polymers

The fabrication of surface wrinkles in a bi-layer full-polymer system based on SMP substrates comprises three main steps: stretching of the substrate, applying the polymer coating and using the SME to recover the substrates original shape as illustrated in **Figure 5.3**. The shrinking of the substrate provokes strong compression in the covering PMMA film along and, due to the Poisson's effect, tensile stress orthogonal to the shrinking direction. If the substrate's strain is larger than a critical value and provided that the adhesion between the two layers is sufficient, the coating has to elude the compression by buckling into wrinkles. Since the film forces the substrate to buckle as well, the dimensions of the wrinkles as well as the critical strain are depend strongly on the ratio of Young's modulus of coating and substrate. Taking a closer look at the polymer physics underlying wrinkling

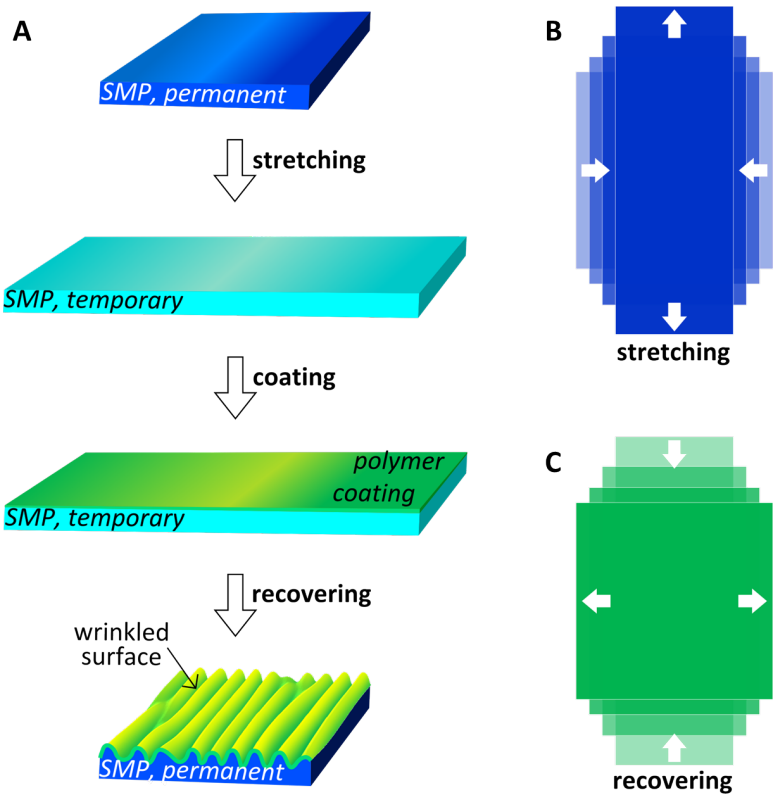

Figure 5.3: **Schematic of the surface wrinkles fabrication process. A** A shape-memory polymer substrate is stretched by an uniaxial load from its permanent shape into an elongated temporary shape. In this state, the substrate is coated with a second polymer from solution by spin coating. After drying, the resulting thin film cover compensates the compression along and strain perpendicularly to the former stretching direction by buckling into surface wrinkles when the recovery of the substrates original, permanent shape is initialized. **B** Stretching causes an elongation of the sample in stretching direction while the sample contracts laterally. **C** During the recovery the sample shrinks to its original length and the width increases to its former size, too.

on polyurethane SMPs, one has to take into consideration that the formation of wrinkling on viscoelastic polymers significantly differs from the evolution of wrinkles on elastic materials.[208] In contrast to an elastic material, viscoelastic properties are characterized by a time-dependent strain response to stress that depends heavily on temperature. However, viscoelasticity is not just superposition of independent elastic and viscous forces, but also a coupling of both known as anelasticity.[30] Chen *et al.*[205] state that an in series combination of a Maxwell model, represented by a Newtonian dashpot in series with a Hookean spring, with a Kelvin model, consisting of dashpot and spring in parallel, is the most adequate approach to describe wrinkling on a thermoplastic, viscoelastic polymer substrate.[205] The Maxwell model describes a material that reacts in two manners to a constant strain. First the deformation is spontaneously executed by the elastic part, the spring, and with time the viscous part, the dashpot, results in gradual relaxation and diminishment of the stress. The formation of wrinkles on thermoplastic, thermally triggered SMPs takes place at the switching temperature where the softer segments of the polymer are close to their melting regime. However, there are some long term phenomena in the

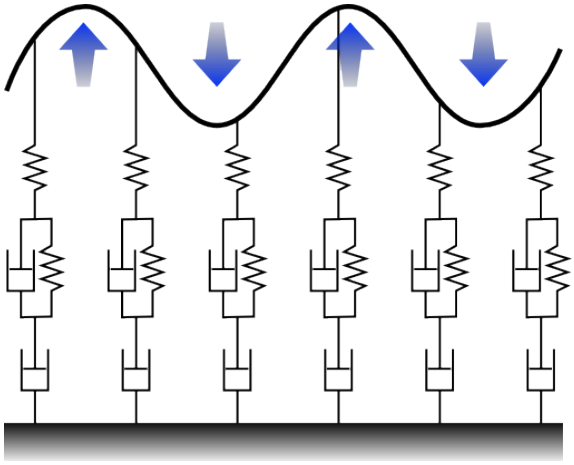

Figure 5.4: **Model to describe wrinkle evolution.** A Maxwell model in series with a Kelvin model describes the viscoelastic behavior of the SMP substrate during and after wrinkle formation.

evolution of wrinkles due to the inherent viscosity of the substrate. After the complete recovery process and at low temperatures ($T << T_{\text{switch}}$), the shape of the substrate is settled, hence, the wrinkle period is unlikely to change but the structure height might be affected by viscoelastic creep. Creep in viscoelastic polymers is described by the Kelvin model. Under constant stress the polymer deforms at a decelerating rate approximating the steady-state strain.[31,205] Both mechanisms described in the Maxwell and the Kelvin model in series combined are depicted in **Figure 5.4**. The wrinkling of the coating induces sudden changes in the interface's topography. In the model, the elastic spring from

the Maxwell element answers this deformation. Right afterwards, the Maxwell element's dashpot begins to compensate some of the stress. The strain inducing creep in the SMP substrate results from the compression followed by wrinkling of the PMMA film. This strain follows the sinusoidal profile of the developed wrinkles and is represented by the blue arrows in Fig. 5.4.[205] To predict the size of the generated wrinkles for a system of an elastic thin film supported by an elastic substrate, that wrinkles upon release of the substrate's pre-strain, Chen and Hutchinson suggest correlations for the wrinkle period Λ and height A and the affecting parameters:[202]

- programming strain ε,
- film thickness h,
- Young's modulus of film E_f, and
- Young's modulus of substrate E_s.

Chen's predictions were advanced by Li *et al.*[207] by taking into account the considerably large Poisson's ratios of film ν_f and substrate ν_s resulting in the following equations:

$$\Lambda = 2\pi h \sqrt[3]{\frac{(1-\nu_\mathrm{s}^2)E_\mathrm{f}}{3(1-\nu_\mathrm{f}^2)E_\mathrm{s}}}, \tag{5.1}$$

$$A = h\sqrt{\frac{\varepsilon}{\varepsilon_\mathrm{c}} - 1}, \text{with} \tag{5.2}$$

$$\varepsilon_\mathrm{c} = \frac{1}{4}\left(\frac{3(1-\nu_\mathrm{f}^2)E_\mathrm{s}}{(1-\nu_\mathrm{s}^2)E_\mathrm{f}}\right)^{2/3}. \tag{5.3}$$

With ε_c as the critical minimum strain necessary to achieve wrinkling. It was already shown by Chen *et al.*,[205] that those correlations describe the wrinkle size dependency of the coating film thickness well for a metal/SMP system. However, they also found a programming strain dependency of the wrinkle period that is not represented in Eq. (5.1). To fabricate surface wrinkles with a wide range of structure sizes, we addressed the listed parameters individually and investigated their correlation on the resulting features dimensions. Thus, we can evaluate whether those equations are legitimate to describe the film thickness and prestrain dependency in our polymer/SMP system.

5.2.1 Adjustable Structure Size

As indicated in the previous section, I aimed to understand the influence of the diverse fabrication parameters to be able to produce a wide range of tailorable structure sizes.

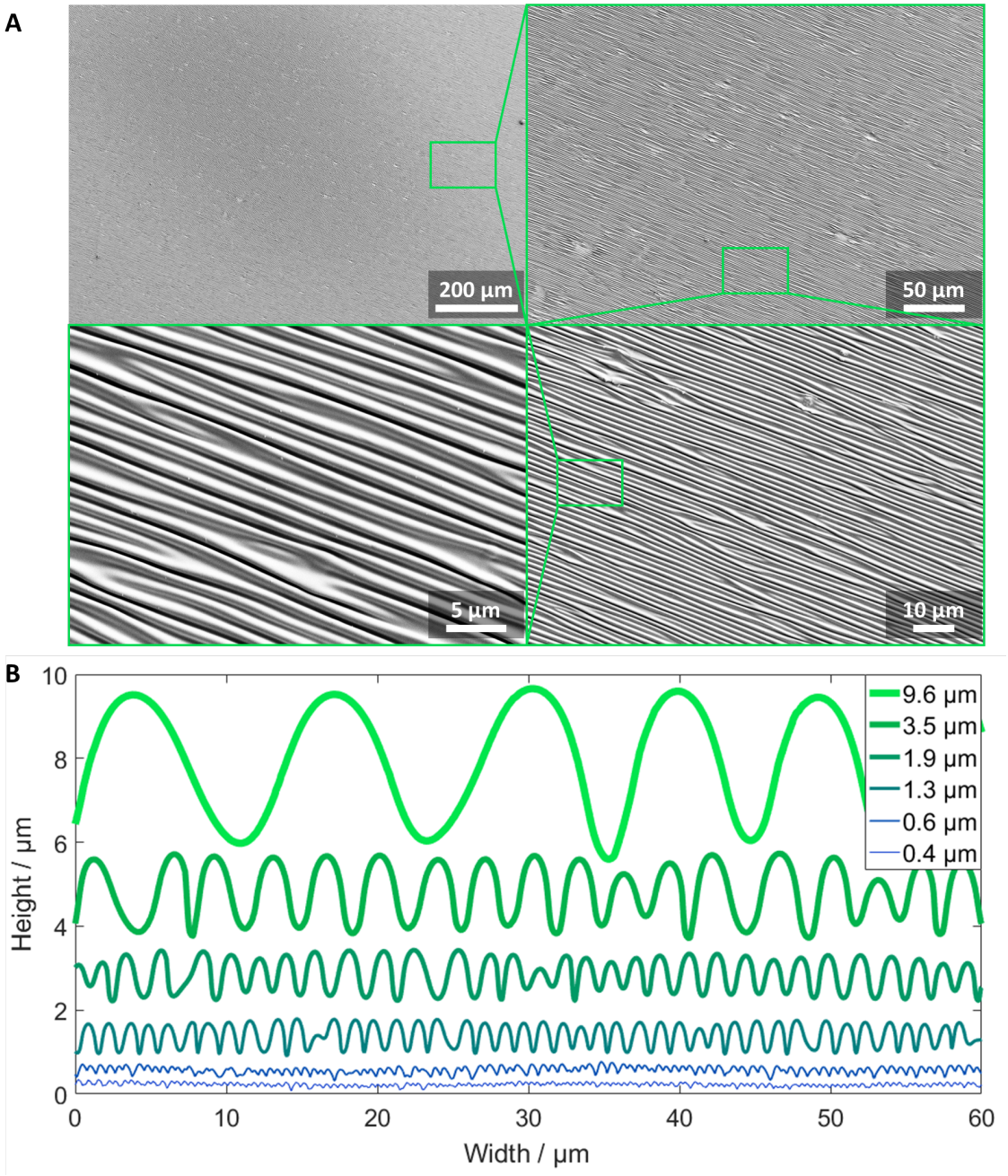

Figure 5.5: **Overview of surface wrinkle structures and their adjustability. A** The SEM pictures in four different magnifications expose the flawless large scale producibility of wrinkles structures generated with our full-polymer system. In higher magnifications the long-range order as well as the short-range randomness become apparent. **B** Cross sections extracted from AFM scans of six different samples demonstrate the broad adjustability in achievable wrinkle sizes from almost ten microns down to less than half a micron. Here, the period is regulated by adjusting the coating thickness *via* the spin coat solution concentration: Thicker solutions yield thicker coatings resulting in larger wrinkles.

Each of the in Fig. 5.3 depicted process steps offers parameters than can influence quality and size of the resulting structures. The roughness of the substrate, as it affects the coating's thickness homogeneity, contributes to the structure's regularity. The extent to which a substrate is stretched and the thickness of the polymer thin film determine the structure size. And the recovery temperature influences the materials' Young's modulus and, thus the formation of the structures.

Before the first, in Fig. 5.3 depicted step the SMP TFX (see Sec. 2.3.1) is shaped into rectangular substrates by hot embossing the polymer above TFX's melting temperature $T_{\text{emboss}} = T_{\text{hard}} = 155\,^{\circ}\text{C}$. The SMP was molded between two Kapton foils to achieve a smooth surface. The surface roughness was determined by an AFM measurement to $R_{\text{rms}} \approx 14\,\text{nm}$. Due to molding at this high temperature, the SMP substrates were in their permanent shape before they were stretched to program the temporary shapes. The stretching was executed in a tensile testing machine at room temperature with 2 mm/min to strains varying from 50 % to 200 %. To provide for a good shape fixity rate in this cold drawing process, the samples were allowed to relax for 30 min under constant load. In the next step, the samples were coated with a PMMA solution by spin coating. To adjust the coating thickness, diverse solution concentrations between 0.75 wt.% and 15 wt.% of PMMA in the solvent xylene were used and spin coated with a spin velocity of 3000 rpm for 1 min with an acceleration of 150 rpm/s. Afterwards, the samples were dried on a hot plate at 30 °C for 2 h. To induce the wrinkling in the last step, the samples were heated in an 80 °C de-ionized water bath by what the substrates' temperatures rose above TFX's switching temperature and they recovered their initial, unstretched, permanent shape within seconds. **Figure 5.5** A shows SEM pictures of one exemplary sample that was produced with this method and parameters within the denoted ranges. The lowest magnification demonstrates the homogeneity of the surface wrinkles on large areas. The close-up views reveal more and more structure details with increasing magnification. The irregularity of the wrinkles becomes apparent and discontinuities similar to typical lattice defects known from crystallography are visible. In the last SEM the short-range randomness and long-range order of the structure is apparent. The mean period of this sample was determined to $\overline{\Lambda} = 1.3\,\mu\text{m}$. Figure 5.5 B compares the various achieved wrinkle periods from almost 10 µm to less than 0.5 µm by displaying cross sections extracted from AFM measurements of the respective samples. All samples shown in this graph were produced with the same programming strain of 120 % and the different structure dimensions were achieved by using a different PMMA solution concentration c_{sol} in each case. The higher the viscosity of the PMMA solution, the thicker is the coating covering the substrate and the larger are the generated wrinkle periods $\overline{\Lambda}$. **Table 5.1** lists the correlations of fabrica-

tion parameters and wrinkle periods. Each coating thickness h was ascertained with AFM by measuring the step height of a scratch in the polymer layer that was spin coated with the respective parameters on a glass substrate.

Table 5.1: Correlation between solution concentration, coating thickness, and wrinkle period.

c_{sol} / wt.%	h / nm	$\overline{\Lambda}$ / µm
0.75	27	0.4
1	37	0.6
2	74	1.3
3	116	1.9
5	222	3.5
12.5	1200	9.6

5.2.2 Parametric Study

To explore the influence of PMMA coating thickness and substrate programming strain separately, I conducted a study containing 25 samples with each combination of five different strains and five different film thicknesses. Each sample's topography was determined accurately by AFM measurements. From those scans period and height of every discrete wrinkle of every scan line were analyzed and expressed in a frequency distribution. From this distribution we extracted a mean value for the sample's wrinkle period Λ and height A with the according standard deviations. As an additional result of those measurements, I found the standard deviations of period and height to be in the order of $\sigma_\Lambda = 30\,\%$ and $\sigma_A = 20\,\%$, respectively, independent of the structure size. The results of the analysis are summarized in **Figure 5.6**. For clarity, the data is divided into four charts to depict the influence of coating thickness h on the wrinkle period Λ (Fig. 5.6 A) and the wrinkle height A (Fig. 5.6 B) for the five different programming strains 43 %, 69 %, 80 %, 93 %, and 113 %. Period Λ and height A in correlation to the programming strain ε are specified for the five PMMA thin film thicknesses 27 nm, 37 nm, 74 nm, 116 nm, and 222 nm in Fig. 5.6 C and Fig. 5.6 D, respectively. The solid lines are guide-to-the-eyes for the individual data sets.

We drew comparisons of the trends proposed by Eq. (5.1) and Eq. (5.2) to each series of our experimental data. The charts show that the experimentally gained data are largely in agreement with the predictions for the dependence of wrinkle size Λ and A to the coating film thickness h (Fig. 5.6 A and B). The formation of the wrinkles is initiated at 80 °C in

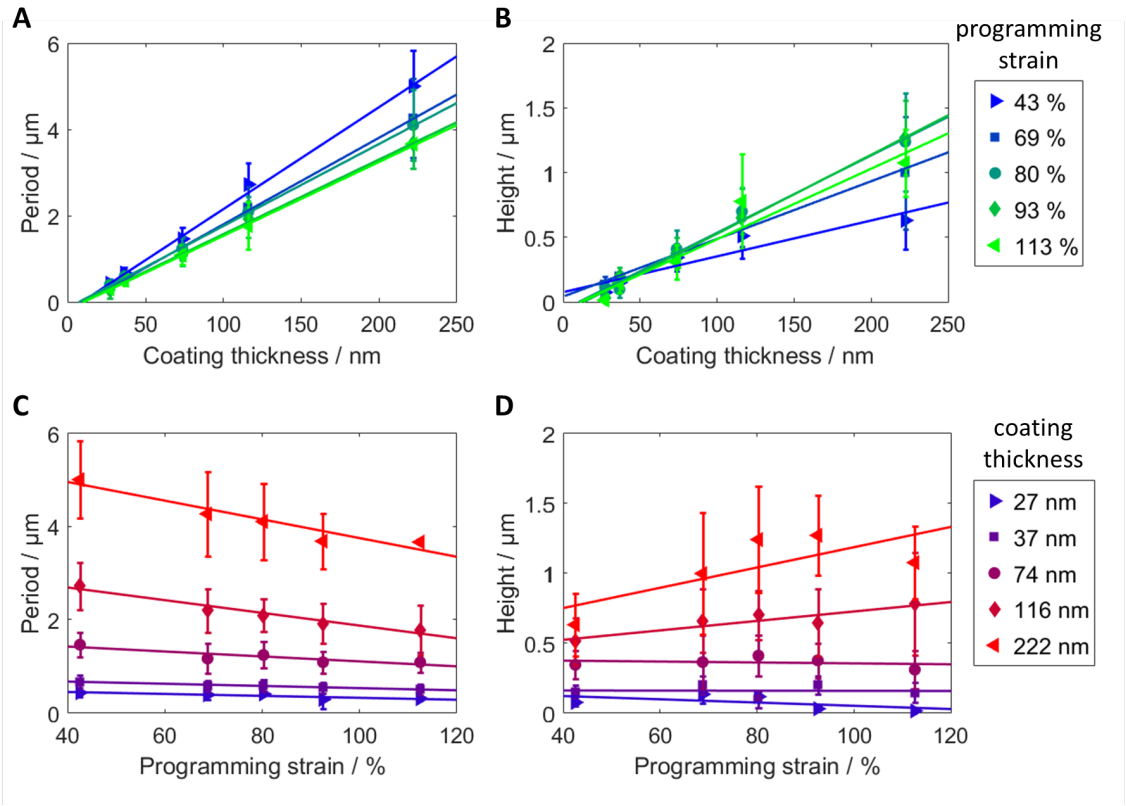

Figure 5.6: **Adjustability of wrinkle size through fabrication parameters. A** The influence of coating thickness on wrinkle period and **B** on wrinkle height is demonstrated for various programming strains. **C** The correlation of wrinkle period and **D** wrinkle height to programming strain of the substrate for various coating thicknesses is illustrated. The solid lines are just guide-to-the-eyes.[174]

our study. Therefore, we cannot refer to literature values for the Young's modulus of TFX at this temperature nor can we state an exact Young's modulus for the coating. For the PMMA film, not only the non-standard temperature is an issue, but also it is known, that for thin films the Young's modulus differs significantly compared to bulk materials.[190] In this context, we compared our data only qualitatively to the trends predicted by Eq. (5.1) and (5.2). The wrinkle period increases virtually linearly with PMMA thin film thickness (Fig. 5.6 A) in accordance with Eq. (5.1) under negligence of the effect of h on E_f. Similarly, the increase of wrinkle height A with thin film thickness h as predicted by Eq. (5.2) is evident in Fig. 5.6 B. Contradictory to Eq. (5.1) but in agreement with Chen *et al.*[205], we find a distinct correlation between Λ and programming strain ε. With increasing strain, the wrinkle period decreases and this trend is even stronger pronounced the thicker the PMMA film is as shown in Fig. 5.6 C. Also, the influence of the programming strain on the wrinkle height A is more distinctive for larger h values (Fig. 5.6 D).

The nature of the shape-memory effect of the herein utilized SMP Tecoflex that is described in detail in Sec. 2.1 and Sec. 2.3.1 allows an adjusting of the wrinkle size by solely varying the recovery temperature. As previously explained, the formation of the surface wrinkles relies to a great extent on the individual stiffness of the applied materials and the ratio thereof. A thermoplastic material's Young's modulus, as it is a measure of the stiffness, experiences a significant decrease when the material converts from being hard and brittle at low temperatures in its energy elastic state to its glass-rubber transition region. As previously explained, TFX has a broad switching temperature range around the glass transition temperature of the soft segments starting at $T_{\mathrm{switch,low}} \approx 50\,^{\circ}\mathrm{C}$. Correlating with this, the polymer's elastic modulus decreases significantly in this region. The glass transition of PMMA is with $T_{\mathrm{g,PMMA}} = 105 - 120\,^{\circ}\mathrm{C}$ to a great extent larger than TFX's T_{switch} and therefore the elastic modulus of PMMA changes assumedly little in the switching region of TFX. Hence, the ratio of the elastic moduli of the two materials $E_{\mathrm{f}}/E_{\mathrm{s}}$ is strongly temperature dependent in the mentioned range. According to Eq. (5.1) the wrinkle period Λ is a function of this ratio and, hence, can be adjusted through the recovery temperature. However, the recovery temperature does not only affect the substrates Young's modulus but also influences the ability of the substrate to fully recover the original length of the substrate. The recovery rate $R_{\mathrm{r}} = \varepsilon_{\mathrm{recovered}}/\varepsilon$ depends on the programming and recovery parameters.[29] As evidenced above, the strain contributes to the wrinkle formation decisively. Due to this presumption, I fabricated one sample that was subsequently cut into four pieces to investigate the influence of the recovery temperature on otherwise identical samples. The sample was stretched by $\varepsilon = 73\,\%$ before it was coated with a 2 % PMMA/xylene solution at a spin speed of 3000 rpm for 1 min with an acceleration of 150 rpm/sec and then dried for 2 h at 30 °C. For the recovery, the four pieces of this sample were submerged in de-ionized water for 1 min at 50 °C, 60 °C, 70 °C, and 80 °C, respectively. The substrate length was documented for each sample before and after the recovery step. **Figure 5.7** A displays the topography of those four samples in AFM pictures.

With the same method as described above the mean period $\overline{\Lambda}$ and mean height $\overline{A}$ of the four samples were determined and the results are summarized in the graph of Fig. 5.7 B. Both the graph and the AFM pictures reveal, that with increasing recovery temperature the wrinkle period and height decrease. For the period (left axis, blue markers), the period changes from 6.44 µm at 50 °C to 5.28 µm at 80 °C, a decrease of approximately 0.6 % per K. The height (right axis, green markers) decreases from 1040 nm at 50 °C to 610 nm at 80 °C, correlating to -2 % per K. The results are summarized in **Table 5.2** However, this trend of decreasing structure sizes with larger recovery temperature is contradictory to our

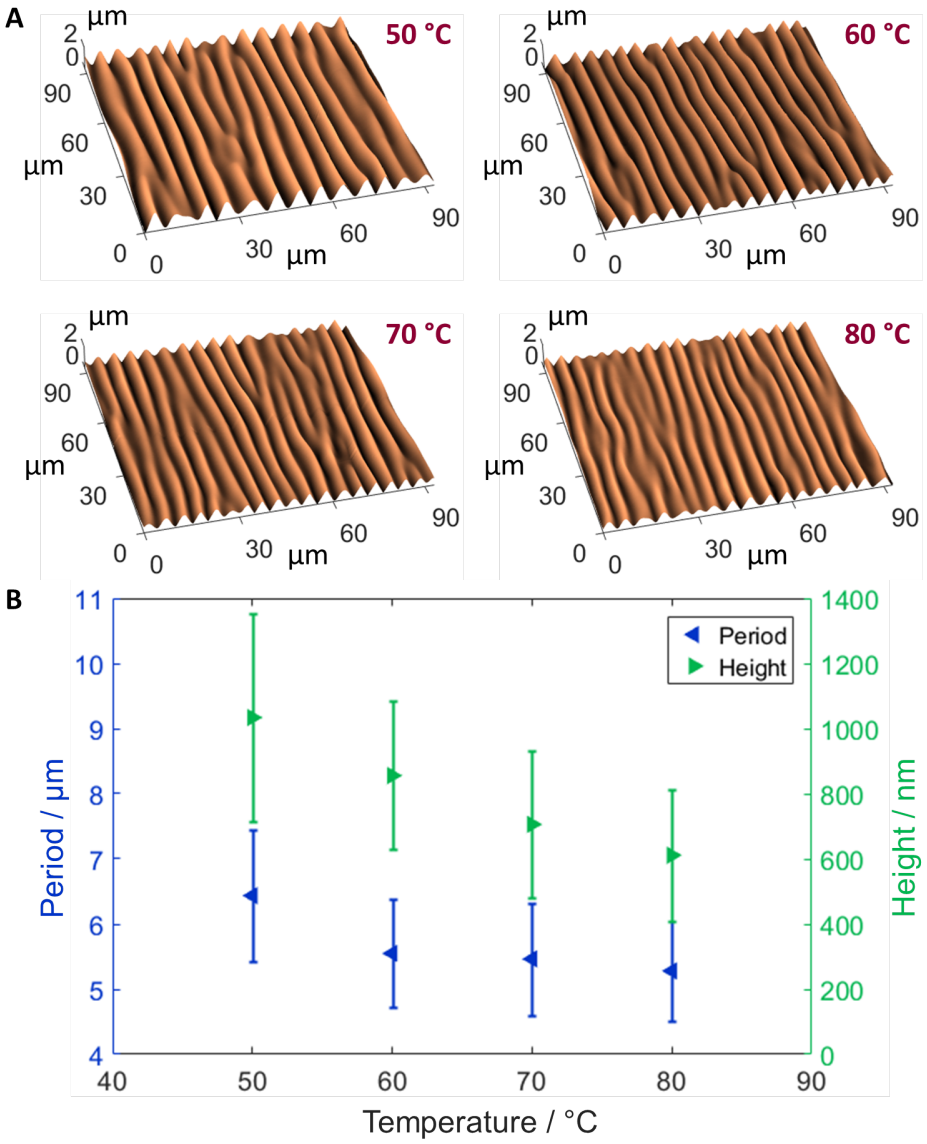

Figure 5.7: **Temperature dependence of the wrinkle formation. A** AFM scans of the at the specified temperatures produced wrinkle structures are displayed. **B** Period Λ and height A of the wrinkle structures are adjusted by applying various recovery temperatures.[174]

expectations as Eq. (5.1) and (5.2) predict the reverse correlation. The herein presented structure-temperature dependency is constantly observed as we repeated the very same experiment several times. Therefore, we conclude, that the recovery temperature dependent wrinkling behaviour of a polymer thin film on a shape-memory polymer substrate cannot be satisfactorily described by the model suggested by Chen *et al.*.[205] The strain dependence of the period, that is observed in Fig. 5.6 C, seems to override the effect of changing Young's modulus ratio. Besides, effects such as thermal expansion, recovery

Table 5.2: Correlation between temperature T, wrinkle period $\overline{\Lambda}$, wrinkle height $\overline{A}$, and recovery rate R_r.

T / °C	$\overline{\Lambda}$ / µm	$\overline{A}$ / nm	R_r / -
50	6.44	1040	0.45
60	5.55	860	0.68
70	5.46	710	0.82
80	5.28	610	0.99

velocity, and changing mechanical behavior for thin film materials might play an important role in this structure formation process. Nevertheless, the results positively show that only by the recovery temperature the structure features of surface wrinkles are notably adjustable over a respectable range. To understand this phenomenon, additional profound investigations and analysis of the SMP and polymer thin film behavior as a function of temperature are inevitable.

5.2.3 Cracking

Many studies on metal/polymer heterogenic bi-layers report wrinkle surfaces with multiple cracks due to the low elasticity of the metal layer.[204–206]. In this study, due to the much lower Young's modulus of polymers and particularly of the here utilized PMMA, no cracks whatsoever could be observed on any of the samples regardless of the programming strain. During stretching of the sample, the positive Poisson's ratio of the SMP substrate causes a contraction transverse to the stretching direction. During the recovery process, the original width of the substrate is restoring and the hereby induced tensile stress might exceed the coating strength.[205] Hence, the coating cracks perpendicular to the wrinkle direction. The formation of cracks and their density is thus dependent on the programming strain and coating material. The Poisson's ratio of TFX was experimentally determined to $\nu_s = 0.5$ and PMMA's Poisson's ratio is in the range of $\nu_f = 0.35 - 0.5$.[209] **Figure 5.8** compares SEM pictures of two samples, each consisting of a TFX substrate stretched to the same programming strain of 120 % but one covered with a 222 nm thick PMMA film (left) and one covered with a 71 nm thick Ag layer (right). Despite the difference in wrinkle sizes, the occurrence of multiple cracks in the silver covered sample and the lack of any cracks in the PMMA covered sample is obvious. The prospect of cracking of the coating limits the range of achievable wrinkle sizes in metal/polymer systems and a surface laced with cracks confines the applicability of those structures immensely, especially in terms of applications that require vast up-scaling of the sample dimensions.

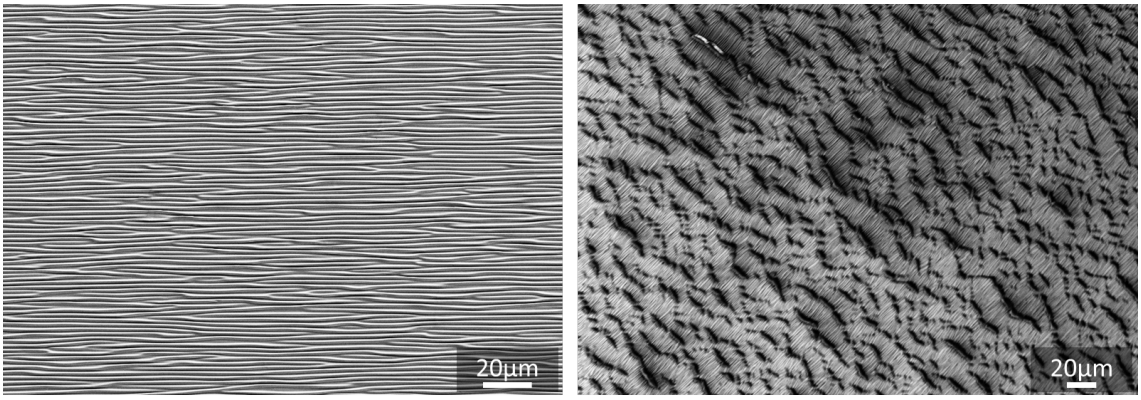

Figure 5.8: **Comparison regarding cracking behavior of polymer (left) and metal (right) wrinkles.**

5.3 Hierarchical Surface Wrinkles

Our role models each exhibit a different kind of hierarchical structures as already shown in Fig. 5.1. Various combinations of the introduced wrinkling method and hot embossing allow us to mimic those petal structures. Here, either the PMMA coating on a temporarily stretched substrate can be structured with a mold and then wrinkled by the recovering SMP or the SMP substrate is first structured by embossing and afterwards programmed into a temporary shape followed by coating and wrinkling.

5.3.1 Wrinkling Combined with Hot Embossing

One path to produce the desired hierarchical wrinkles is to structure the bi-layers top coating. Since this layer consists of PMMA, a thermoplastic polymer, the structuring can easily be accomplished by hot embossing (see Sec. 2.3.2). In consideration of the PMMA film thickness, that is adjustable by the PMMA solution concentration, and the stretching direction, a huge variety of 2.5D patterns can be imprinted to create various hierarchical structures.

The fabrication of such hierarchical wrinkles includes four steps which are illustrated in **Figure 5.9**. Identical to the fabrication already described in Sec. 5.1, at first a smooth SMP substrate is uni-axially stretched in a tensile testing machine and secondly it is covered with a thin PMMA film through spin coating. Subsequently, when the PMMA coating is completely dry, a heated metallic mold featuring the negative of the desired micro- or nano-structure is embossed under high pressure into the PMMA coating. Here, the process temperature is a critical parameter. A temperature is to select, that is the best compromise between good structuring of the PMMA film and not initializing the recovery of the substrate. To guarantee both, the hot embossing machine's tool plate with the

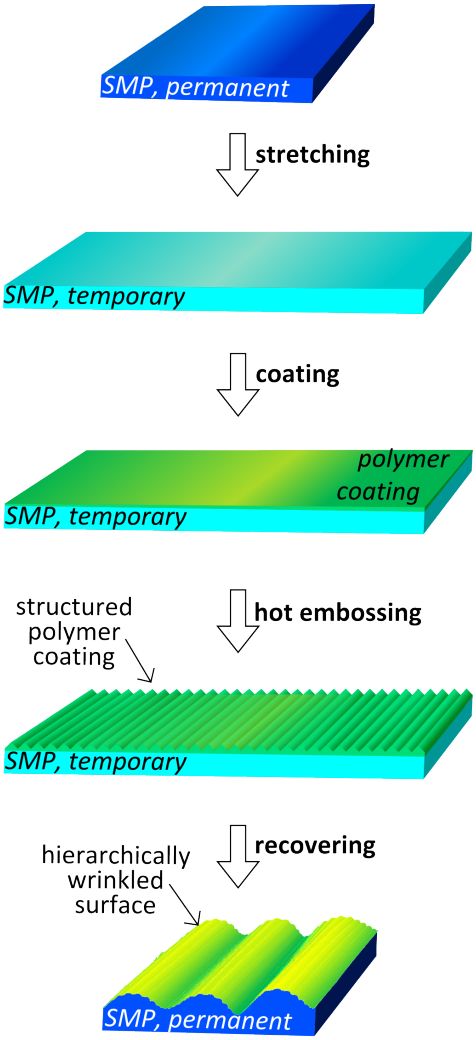

Figure 5.9: **Schematical depiction of wrinkling of structured polymer coatings.** Uniaxial stretching transforms a shape-memory polymer substrate from its permanent shape into a laterally elongated, temporary shape. Subsequently, a spin coating step adds a polymer coating on the stretched substrate. This polymer film is structured by hot embossing where a hot mold is pressed into the sample surface. Heating the sample to the SMP's switching temperature triggers the recovery process and the substrate shrinks back to its original length. The structured coating encounters this interface area mismatch by forming wrinkles.

attached mold is heated to $T_{\text{emboss}} = 55\,^{\circ}\text{C}$ while the machine is still open and tool and substrate plate are several centimeters apart. Meanwhile, the substrate plate at the bottom is cooled down to $T_{\text{substrate}} = 10\,^{\circ}\text{C}$ and kept at this temperature. When the mold reaches T_{emboss} the tool plate approaches the substrate fast with 10 mm/min until a force of 25 kN is reached. Immediately afterwards, the mold is withdrawn to minimize the time where hot mold and cold sample are in contact in order to limit the heat transfer and according heat propagation from mold through PMMA layer to SMP substrate. In the last process step, the substrate's SME is triggered by dipping the sample into an 80 °C hot de-ionized water bath for approximately five seconds whereupon the substrate contracts along the former stretching direction and recovers its original, permanent shape. Thus, the structured PMMA layer is forced to buckle and hierarchical surface wrinkles are formed.

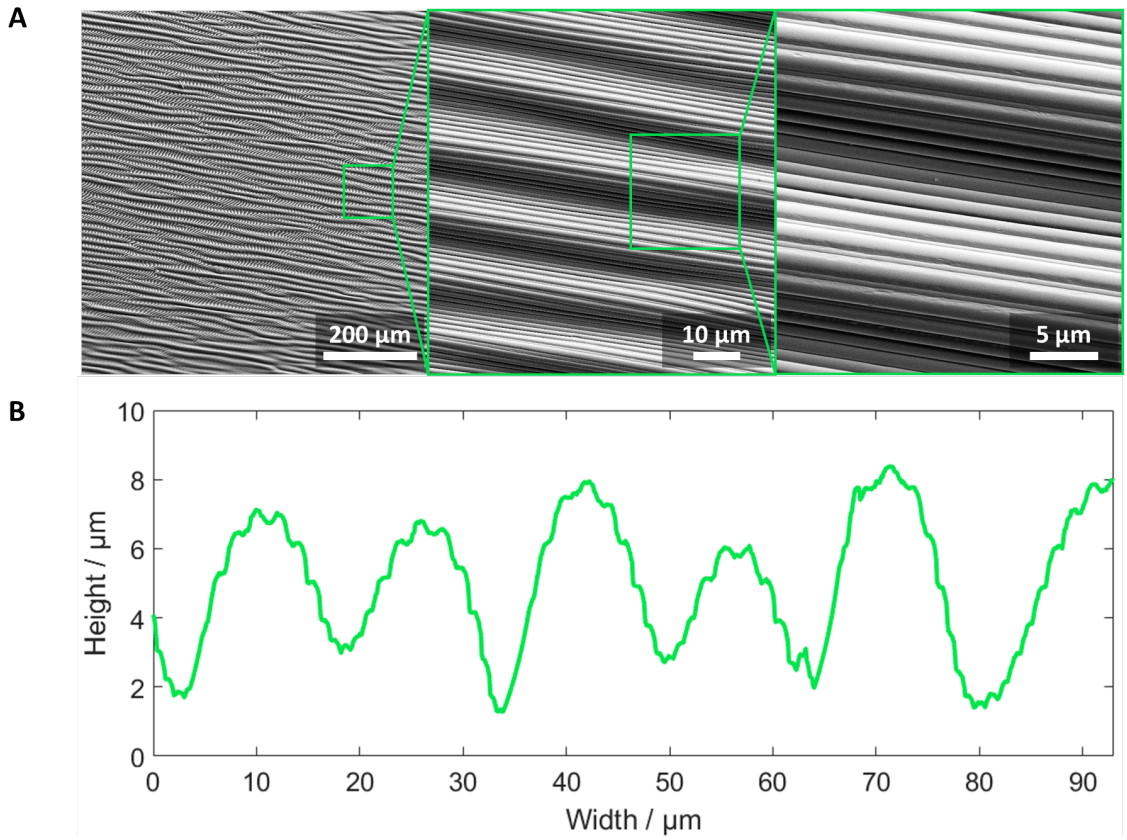

Figure 5.10: **Hierarchical, artificial wrinkles mimicking the tulip structure. A** The SEM pictures show the by combining wrinkling and hot embossing produced hierarchical structures in increasing magnification. Here, the hierarchy is achieved by aligning the hot embossed grating structure parallel to the wrinkle substructure. **B** An AFM cross section of the same structure visualizes the relation between height and period of the small grating compared to the larger wrinkles.

With the knowledge gained from the parametric study presented in Sec. 5.2.2 the hierarchical wrinkles are highly tailorable. The mold's structure dimensions are chosen to be accordingly smaller than the prognosticated wrinkle period in dependency of the desired final structure. For two dimensional structures, the structure orientation can be aligned with the wrinkle formation direction or rotated to any angle. Here, it has to be taken into account, that during the recovery the PMMA layer gets compressed orthogonal to and stretched in wrinkling direction. This might influence the resulting embossed structure dimensions in terms of compression reducing and strain enlarging the period or pitch of the structure features.

The first example of hierarchical surface wrinkles is designed to resemble the tulip structure already presented in Fig. 5.1 A. It exhibits a linear grating with a period of $\approx$ 2 µm and a duty cycle of 0.5. It is embossed into a 1200 nm thick PMMA film on top of

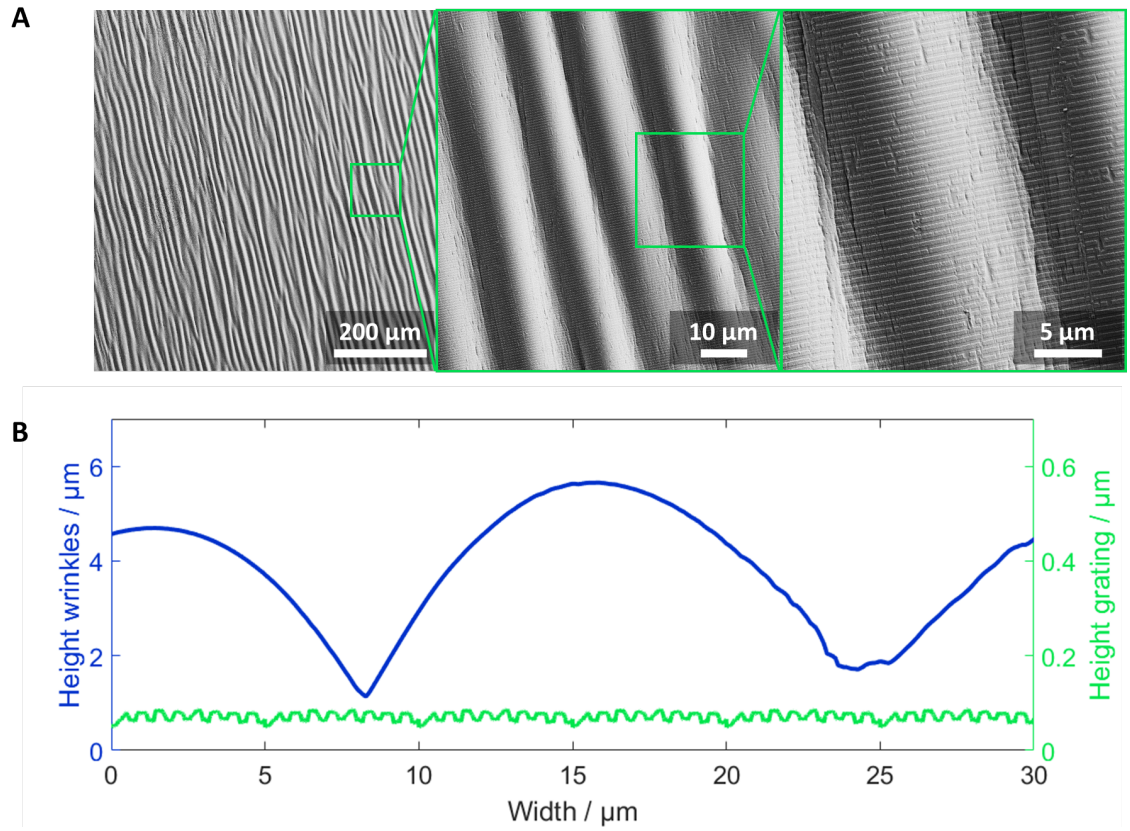

Figure 5.11: **Hierarchical, artificial wrinkles mimicking the daisy structure. A** SEM pictures in three magnifications demonstrate the structure homogeneity on large scales as well as the structure details. To mimic the daisy structure, the polymer coating is structured with an 1D grating oriented perpendicularly to the underlying wrinkle structures. **B** With the AFM cross sections, the big wrinkles (blue line, left axis) exhibiting a period of $\approx 15\,\mu m$ and height of $\approx 4\,\mu m$ are contrasted with the small grating structure (green line, right axis) featuring a period of $\approx 0.65\,\mu m$ and height of $\approx 15\,nm$.

a by 120 % stretched SMP substrate. The mold orientation was selected to yield wrinkles and grating aligned in parallel. **Figure 5.10** A shows the topography of this hierarchically wrinkled structure by SEM pictures in three magnifications and the AFM cross section displayed in B reveals the aspect ratio of the structure.

Both orders of structures are clearly visible in the AFM cross section, although the scan cannot do justice to the full three-dimensionality of the structure since it cannot sample undercuts as they are created by the grating's cavities.

For the second example, mold and PMMA film thickness are chosen to mimic the daisy structure that was introduced in Fig. 5.1 B in Sec. 5.1. In comparison to the tulip mimicking structure, the mold exhibits a linear grating, too, but it is rotated by 90 °. Additionally, a smaller grating period was selected to compensate for the emerging strain perpendicular to the grating orientation at the time when the wrinkles form. The utilized mold pos-

sesses a linear grating with a period of $\approx 600\,\text{nm}$ and a duty cycle of 0.5. It is embossed into a $2\,\mu\text{m}$ thick PMMA layer as described above. The resulting hierarchical structure is displayed in **Figure 5.11**. The SEM picture with the lowest magnification on the left in Fig. 5.11 A reveals the homogeneity of the structure on large scales, whereas the first and second close-ups give information about the structure details such as the dimensions of the underlying wrinkle structure and the dimensions of the covering PMMA nanostructure. Figure 5.11 B shows cross sections extracted from AFM scans. The blue line shows the topography of the wrinkle sub-structure with an average period and height of about $\overline{\Lambda} \approx 15\,\mu\text{m}$ and $\overline{A} \approx 4\,\mu\text{m}$. The second scan, executed in a $90\,^\circ$ angle in reference to the first scan, discloses the linear grating structure in the PMMA film shown in green.

5.3.2 Hot Embossing Combined with Wrinkling

The second approach to create hierarchically wrinkled surfaces combines hot embossing and wrinkling in the reversed order than described in the previous section. More precisely, a wrinkled surface is created on top of an afore structured substrate. I designed this method to resemble the in Sec. 5.1 introduced treasure flower structure. This flower exhibits a structure of very long, almost triangular cells covered with perpendicularly aligned wrinkles on the lateral faces of those triangles. This particular structure is very interesting from the point of designing light in-coupling surfaces. As we will show later in this chapter, small surface wrinkles are effective anti-reflective structures. In combination with the high AR triangular structure, the reflectance is supposedly further decreased. In the first impact of a beam on the face of one triangular ridge, most of the incident light is transmitted due to the anti-reflective surface wrinkles. However, the reflected portion is reflected towards the opposite face of the next triangular ridge and is at this interface, again, mostly transmitted. Hence, reflected light has at least a second chance to be in-coupled to the material. To create a structure that enables this effect, a mold with a sufficient structure AR of ≥ 1 is necessary. Fabrication of this particular geometry and ARs with structure sizes around $10\,\mu\text{m}$ is not trivial. In absence of a suitable mold, I found a quick solution to increase the AR of an existing structure and produced the mold myself as already described in detail in Sec. 2.3.2.

The individual steps of the method to fabricate the hierarchical structures are schematically depicted in **Figure 5.12**. A shape-memory polymer substrate is heated above T_{perm} and pressed into a mold featuring an one-dimensional, prismatic grating structure in a hot embossing step as described in Sec. 2.3.2. Because the sample's temperature in this step is $T_{emboss} > T_{perm}$, the embossing defines the triangular grating as new permanent shape.

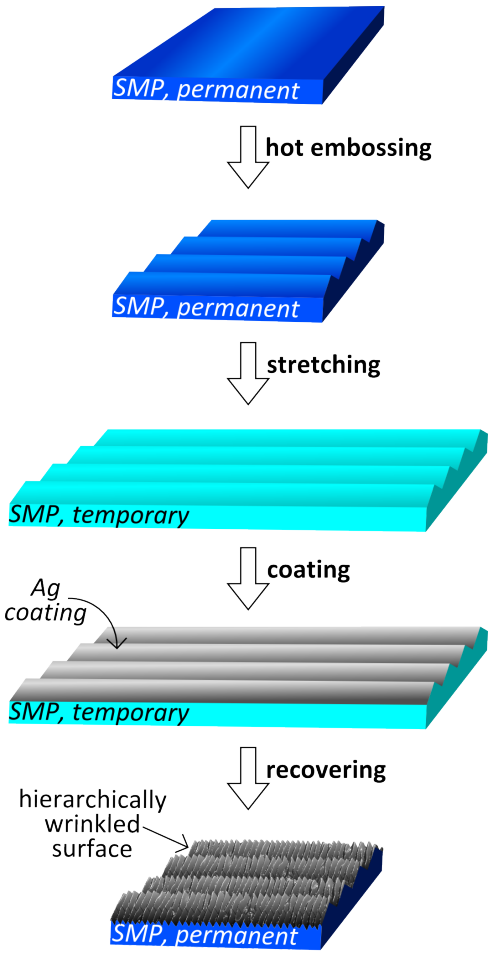

Figure 5.12: **Schematic of wrinkling on structured surfaces.** A smooth shape-memory polymer substrate is structured with a triangular linear grating to set its permanent shape. Stretching lengthens this prisms in longitudinal orientation. Afterwards, the structured substrate is coated with a thin silver layer by sputtering. Shrinking of the substrate in the recovery process yields linear surface wrinkles on the lateral faces of the triangular structure perpendicularly to their orientation.

The mold possesses an one-dimensional grating with triangular profile and a period of 10 µm and an AR of 1.0-1.2. To achieve an increased surface area necessary for later wrinkling, the sample is stretched parallel to the grating orientation in a tensile testing machine. This stretching programs the temporary shape with increased length and transverse contraction into the SMP substrate. In contrast to the previously described wrinkling methods, I did not use a second polymer as a coating. Producing an uniform polymer film atop a structured substrate is difficult with spin or dip coating. On the one side, good wettability is crucial to achieve a coating with the contemplable polymer, on the other side the relatively high structure AR yields filling of the cavities when a solution with good wettability is used. Therefore, in this approach I applied a thin silver layer by sputter coating on the structured substrate as described in Sec. 2.3.2. Sputter coating allows to cover the structure with an uniform layer irrespective of the substrate's topography. As aforementioned, drawback of wrinkling with a bi-layer of SMP and metal is usually the occurrence of multiple cracks in the surface after wrinkling due to the reversion of the transverse contractions in the recovery step. When using a triangularly structured surface

such as in this case, the transverse contraction induced by the stretching of the sample does not directly affect the surface area but is compensated by the structure's geometry. The lateral compression causes the angle between the lateral faces of the triangles to become more acute and increases the structure's AR. The actual surface area of those faces is uninfluenced by the lateral contraction and only increased in stretching direction. Therefore, I am able to generate a crack free surface although using a SMP-metal bilayer for this structuring method. In the last fabrication step, the sample is heated above its switching temperature T_{switch} by submerging it in an 80 °C hot, de-ionized water bath to initialize the recovery of the original shape. In the course of the shrinking of the substrate, wrinkles evolve on the lateral faces of the triangular grating. **Figure 5.13** A shows SEM images of the resulting structure and AFM cross sections are displayed in Fig. 5.13 B. The two cross sections are extracted from two scans conducted perpendicular to each other. It has to be noted, that the cross section extracted from the scan of the triangular structure

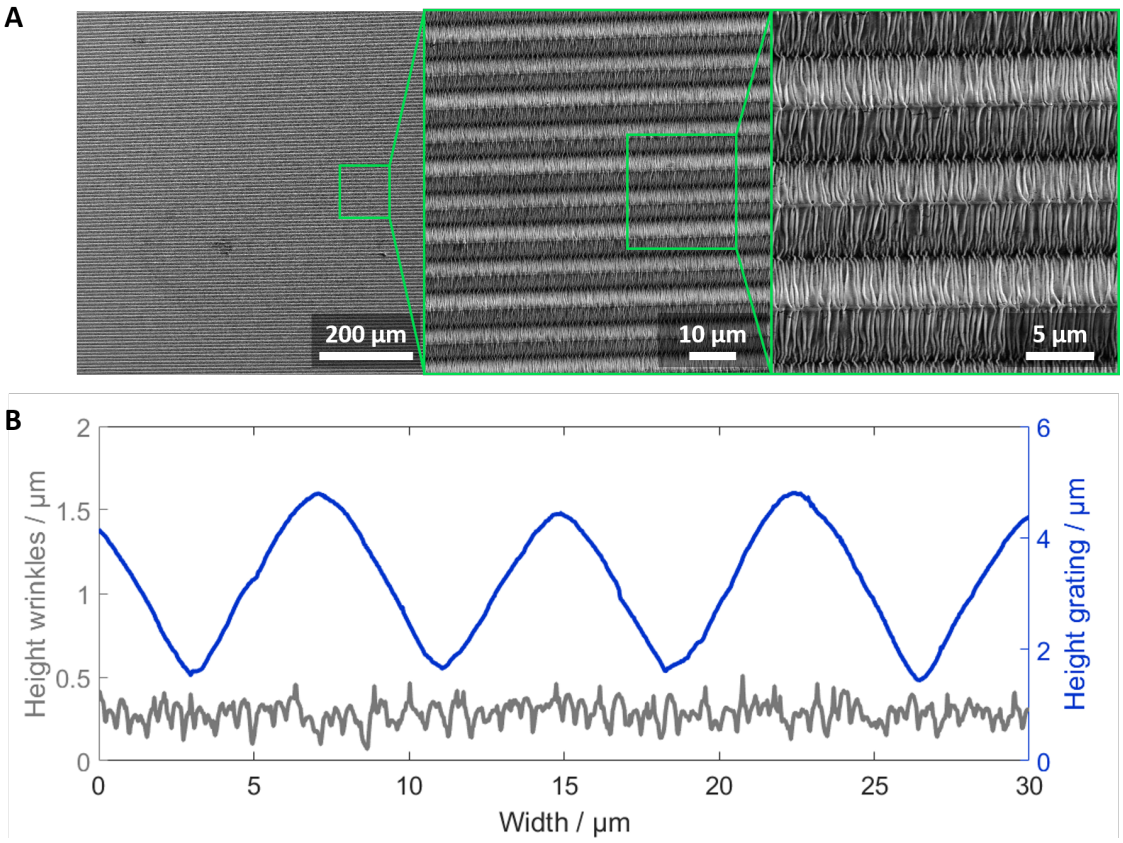

Figure 5.13: **Hierarchical, artificial wrinkles mimicking the treasure flower structure. A** The SEM images show the hierarchical structure created by wrinkling on an embossed grating. The various magnifications reveal the homogeneity on large scales and the structure details. **B** AFM cross sections demonstrate the dimension difference between the underlying grating structure (blue line, right axis) and the on top self-organized wrinkles (gray line, left axis).

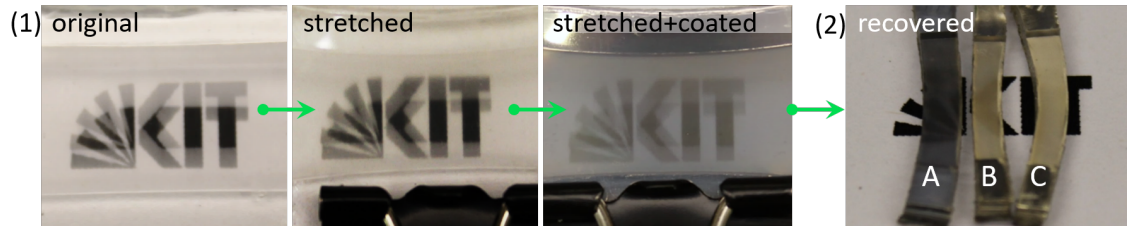

Figure 5.14: **Photographic documentation of the fabrication steps.** The photographs depict one sample in its original shape ((1), left) which was subsequently stretched ((1), middle) and then coated with a thin Ag layer ((1), right). In (2) three examples of in this way processed and afterwards recovered samples possessing three different Ag layer thicknesses ranging from A (thin) to C (thick) are shown. Three different thicknesses result in visibly different appearances.

presumably does not give an exact representation of the actual structure depth due to the high AR of the with wrinkles covered structure. The fabrication process of those hierarchical structures is documented in the photo series shown in **Figure 5.14**. After every in Fig. 5.12 sketched fabrication step a photograph of the sample is taken to capture the with the structure changing visual appearance. Beneath the sample is a printed KIT-logo to visualize the prismatic effect of the embossed grating and the change of transparency over the course of the fabrication process. First, the sample in its permanent, already embossed shape ('original') is transparent and reveals the KIT-logo as it is refracted into two logos due to the triangular, embossed grating. In the second picture ('stretched'), the sample is stretched to approximately 1.5 times its original length. The KIT-logo's visibility is the same as in the first photograph although the two refracted logos are closer together due to the by the transverse contraction changed geometry of the triangular structure. Because of slight bending of the structure the sample is flattened with a clamp. A thin sputter coated Ag film changes the transparency of the sample significantly as shown by the third picture ('stretched+coated'). The coating as shown in this picture results in the recovered structure 'A' in the last photograph ('recovered'). Pieces of sample 'B' and 'C' display the influence of an increasing Ag film thickness on the appearance of the hierarchical structure. While the thinnest Ag layer of 7 nm results in an almost black and semi-opaque structure, the thicker layers of 23 nm of sample 'B' and 71 nm of sample 'C' lead to more opaque and whitish samples. Assumably, the increasing opaqueness is related to the increasing Ag-film thickness and the change from blackish to whitish colors is due to a change of the developed wrinkle shape. Width of each structured area is 1.5 cm.

SEM figures of those three samples and an unwrinkled reference are given in **Figure 5.15**. The schematics on the left refer to the various Ag layer thicknesses. In Fig. 5.15 A the structure of the sample with the thinnest Ag layer is shown. The thin

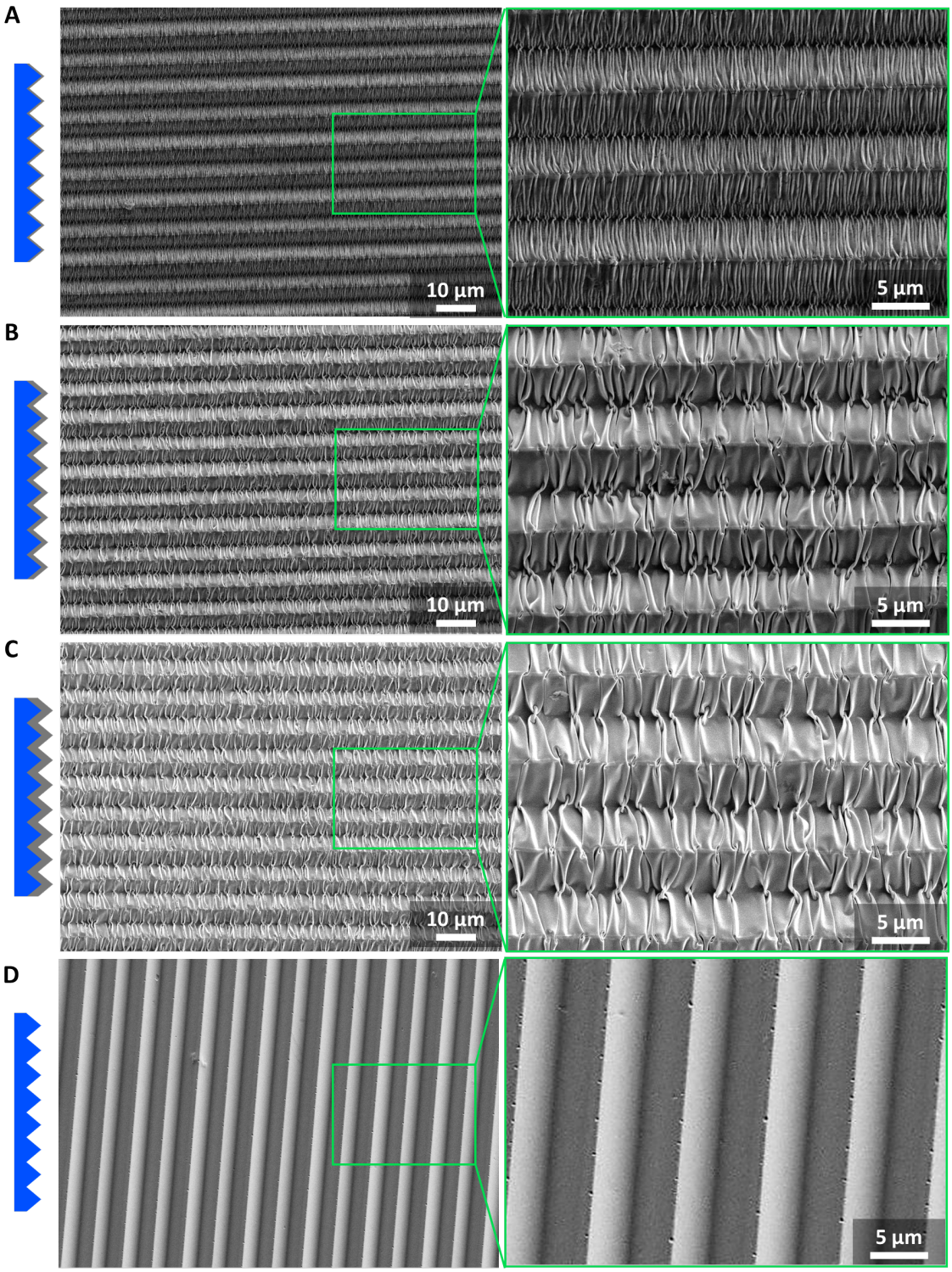

Figure 5.15: **Influence of Ag film thickness on structure topography revealed by SEM pictures.** **A** A thin Ag film yields well aligned small linear wrinkles on the lateral faces of the prism grating. **B** The structure resulting from a medium thick Ag film is less regular with strongly increased wrinkle size. **C** Only occasional folds of the film with further loss of alignment are caused by the thickest Ag layer. **D** The reference of an unwrinkled structure shows the underlying triangular embossed grating.

Ag film wrinkles into well parallel aligned striations on the lateral faces of the embossed triangular grating. This good orientation is lost with thicker Ag films. Number and alignment of the wrinkles is decreased at the sample displayed in Fig. 5.15 B. This trend progresses with the thickest Ag film shown in Fig. 5.15 C. Here, the film is merely folded into irregular wrinkles. This increased randomness of the structure and partial loss of alignment might be responsible for strong scattering and therefore white appearance of the lastly described structure. Figure 5.15 D gives a reference of the structure treated with the same programming and recovering steps except that the Ag film was only applied after recovery to enable high resolution scanning electron microscopy. All samples were treated by the exact same programming and recovery steps.

5.3.3 Hot Pulling Combined with Wrinkling

Motivated by the successful wrinkling on the lateral faces of the prism grating described in the previous subsection, I tested the capability of the wrinkling method to structure vertical side walls. The challenge here is the necessary temporary increase of surface area needed to create the mismatch between coating and substrate later on. The unique ability

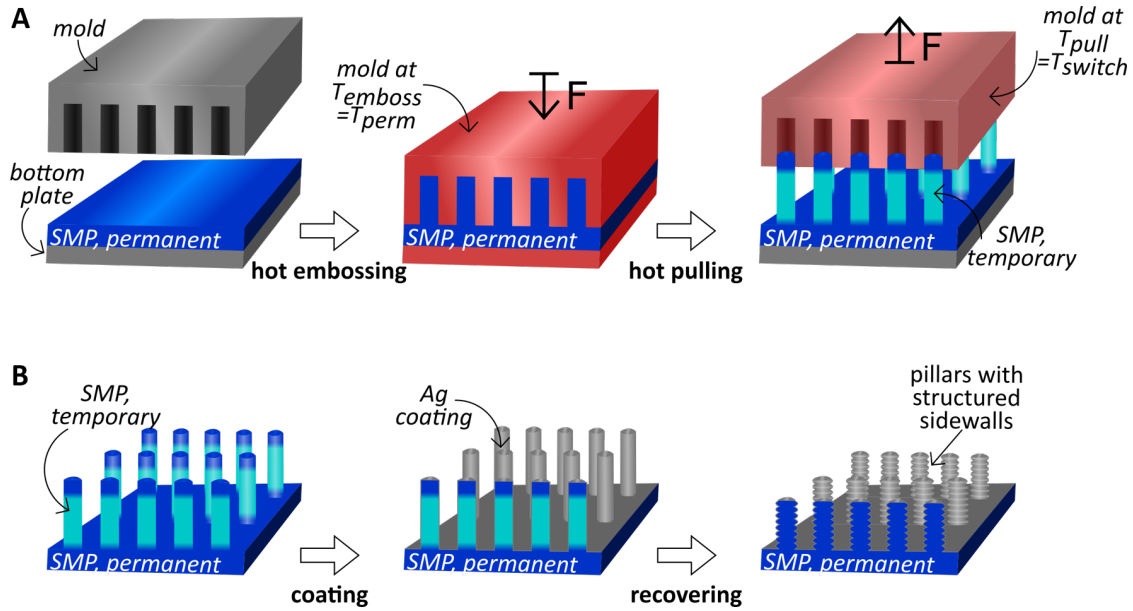

Figure 5.16: **Schematic of the hot pulling process and wrinkling on pillars. A** A mold is pressed into the surface of a SMP substrate at $T_{\text{emboss}} = T_{\text{perm}}$ to define a pillar structure as permanent shape. Subsequently, the mold is cooled to $T_{\text{pull}} = T_{\text{switch}}$ and slowly withdrawn from the sample. Thereby, the pillars are stretched resulting in temporarily elongated structures. **B** Since the stretched parts of the SMP pillars are in the temporary state, coating the structures and subsequent recovery of the permanent shape yields surface wrinkles on the vertical side walls of the pillars.

of our SMP to perform a quasi-plastic, temporary deformation allows us to fulfill this requirement.

To achieve temporarily stretched pillars I modified the standard hot embossing process as it is described in Sec. 2.3.2. The pillar structure is embossed into a SMP sample at a high temperature to define the pillar shape as permanent shape. Instead of cooling the sample down to room temperature to ease demolding, just the bottom plate is cooled to room temperature and the mold is only cooled to the switching temperature of the polymer before it is slowly withdrawn from the sample. Thereby, friction between mold and the still soft polymer causes an elongation of the pillars to the desired temporary shape. The process is depicted in **Figure 5.16** A. When the mold is slowly withdrawn from the surface, the temperature of the now exposed parts of the pillars decreases further and those areas stiffen. This stiffening prevents tearing of the pillars when the mold further withdraws from the sample. Little by little the pillars are pulled out of the mold and are thereby stretched. With precise control of the mold temperature during pulling, the stretched parts of the pillars are in their temporary state. A too high temperature will result in permanently elongated pillars because it affects the SMP's netpoints.The success of this method in terms of height of the structure and whether the pulling results in a temporary or permanent stretching is influenced by the following parameters:

- mold geometry: cavity depth, slope of side walls, ratio volume to surface area of cavities,
- mold roughness,
- temperature of bottom plate and mold during embossing,
- temperature of bottom plate and mold during pulling,
- pulling velocity, and
- pulling distance.

Figure 5.17 gives exemplary relations between the mentioned parameters and the resulting pillar height. The mold geometry, characterized by cavity diameter d, depth z, and roughness are critical because hot pulling relies on adhesion, i.e., friction, of the polymer inside the mold cavities. Friction occurs between the polymer surface and the side walls of the cavities. It has to be high enough to prohibit immediately slipping of the polymer. Simultaneously, the friction cannot be so high, that the adhesion is stronger than the cohesion inside the polymer and the structures tear from the substrate. The diameter and

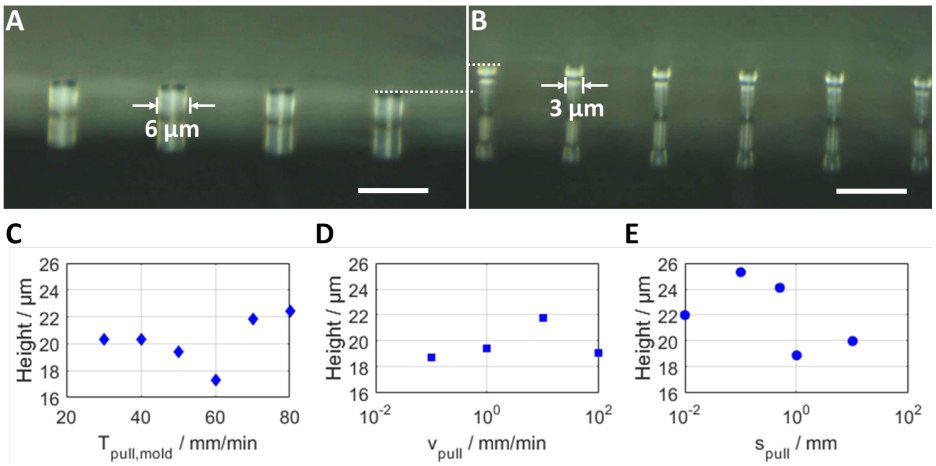

Figure 5.17: **Exemplary influence of process parameters on the hot pulling success. A** The diameter of the mold's cavities influences the achievable strain due to the different volume to surface area ratio. Pillars with 6 µm diameter are barely stretched. **B** The strain of pillars with 3 µm diameter is significantly larger. **C** The results for various pulling temperatures are exemplarily depicted for the switching range of TFX from 30 °C to 80 °C. **D** The withdrawing velocity influences the resulting pillar height. **E** The pillar height is also affected by the pulling distance.

height determine the volume to surface area ratio of such a cavity and therefore influence the adhesion to cohesion ratio as exemplarily depicted in Fig. 5.17 A and B. Here, both structures are from the same sample and embossed and pulled with a mold, that contains a field with 6 µm and field with 3 µm cavity diameter, both featuring the same depth. The in B displayed structures are used for the parameter testing shown in C-E. The temperatures of the embossing step T_{emboss} influence how well the cavities of the mold are filled with polymer and whether this shape is defined as permanent shape. Crucial for the hot pulling success is the bottom and mold temperature, $T_{\text{pull,bottom}}$ and $T_{\text{pull,mold}}$, respectively, during pulling. For the latter a correlation to an exemplary resulting structure height is shown in Fig. 5.17 C. If the temperature is too high, the polymer is very viscous and the structures are teared from the substrate. At a slightly too high temperature, the pulling will result in elongated pillars as their new permanent state. Consequently the structures feature no ability of contraction later on. If the temperature is too low, the friction is very low due to different thermal expansion coefficients of mold material and polymer and the cohesion is high in the stiff structures. Therefore, the structures demold without being pulled. Hence, the temperature range where temporary hot pulling can be achieved is very small and has to be evaluated for every mold geometry and mold/polymer combination. Additionally, another important parameter is the pulling velocity v_{pull}, as exemplarily depicted in Fig. 5.17 D. It determines the time that the polymer is allowed to relax upon the imposed

deformation. The pulling distance s_{pull} can influence the strain of the structures, too, as the example in Fig. 5.17 E demonstrates. Except the in the graphs denoted parameters, all other parameters were kept constant in each experiment.

The possible surface area change due to temporary stretching of the pillars can be used to create surface wrinkles on the side walls of those pillars. As illustrated in Fig. 5.16 B the sample surface was coated with a thin layer of Ag before the pillars were recovered to their original height by increasing the samples temperature above T_{switch}. After careful selection of the mold and evaluation of the relevant process parameters, I determined the optimal parameters for the utilized mold and TFX as SMP as summarized in **Table 5.3**. The surface roughness of the cavity side walls of the utilized mold could not be deter-

Table 5.3: Process parameters for successful, temporary hot pulling.

d_{pillars}	2 µm
z_{pillars}	12 µm
T_{emboss}	155 °C
$T_{\text{pull,mold}}$	70 °C
$T_{\text{pull,bottom}}$	65 °C
v_{pull}	0.1 mm/min
s_{pull}	0.1 mm

mined due to the cavities' high AR. The pillars of the used mold are hexagonally arranged with a pitch double the diameter of the pillars. The pillars stretched with those parameters were in their temporary shape and recovering them at 80 °C resulted in by one third shorter pillars. In contrast to all previously recovery processes described in this chapter, the samples were not submerged in hot water. During drying, capillary forces emerged between the close pillars which resulted in collapsing and clustering of the structures due to their high AR. The shape recovery was instead initialized by placing the samples on an 80 °C hot plate. **Figure 5.18** reveals the topography of a sample before (A,C) and after (B,D) recovery. The topography was measured by VSI, therefore, the approximately vertical side walls of the pillars are gathered badly in the images. Above a certain slope the surface of the structure does not reflect light back to the VSI's detector. The images also show, that not all of the pillars are exactly the same height. Occasionally, pillars are ripped of or teared and variances in strain are apparent. From the cross sections, the height of the temporarily stretched pillars was determined to 18.35 µm and the height after recovery to 12.22 µm. Hence, the tunable strain is $\approx 50\,\%$.

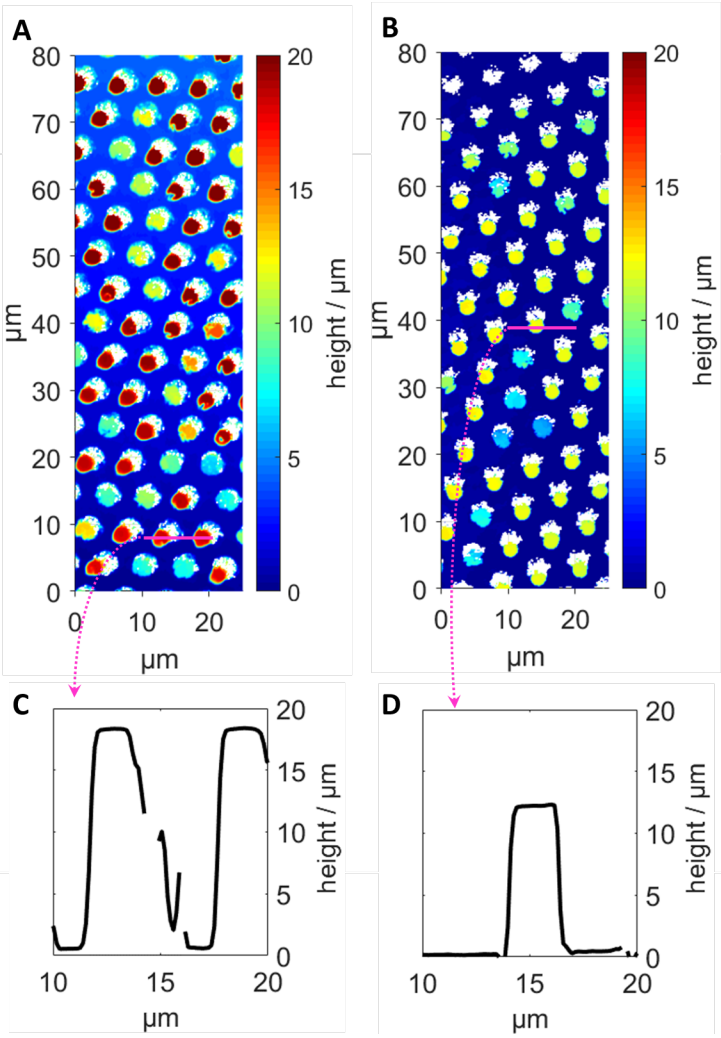

Figure 5.18: **Recoverable strain of temporarily hot pulled pillars.** VSI images demonstrate the homogeneity of **A** temporarily stretched and **B** fully recovered pillars. The pink lines indicate the position of the cross sections that reveal the height difference between **C** temporarily stretched and **D** fully recovered pillars. The approximately vertical side walls of the pillars are only partially captured by the VSI measurement.

For the generation of wrinkles, the structures were coated with a ≈ 7 nm thick Ag layer and recovered as described. Microscope pictures of the structure of one sample after every process step are given in **Figure 5.19** B-D with the permanent, not hot pulled structure as reference in A. The inset in Fig. 5.19 A demonstrates the pillar arrangement. Compared to the reference of the permanently embossed pillars in A, image B shows the in the middle elongated and slightly thinned pillars with the unstretched head. I assume, that this head occurs because at some point the friction between mold and pillars is smaller than the stress caused by stretching so that at this point, the remaining structure ejects at once. The picture in C displays the sample after Ag coating by what the transparency

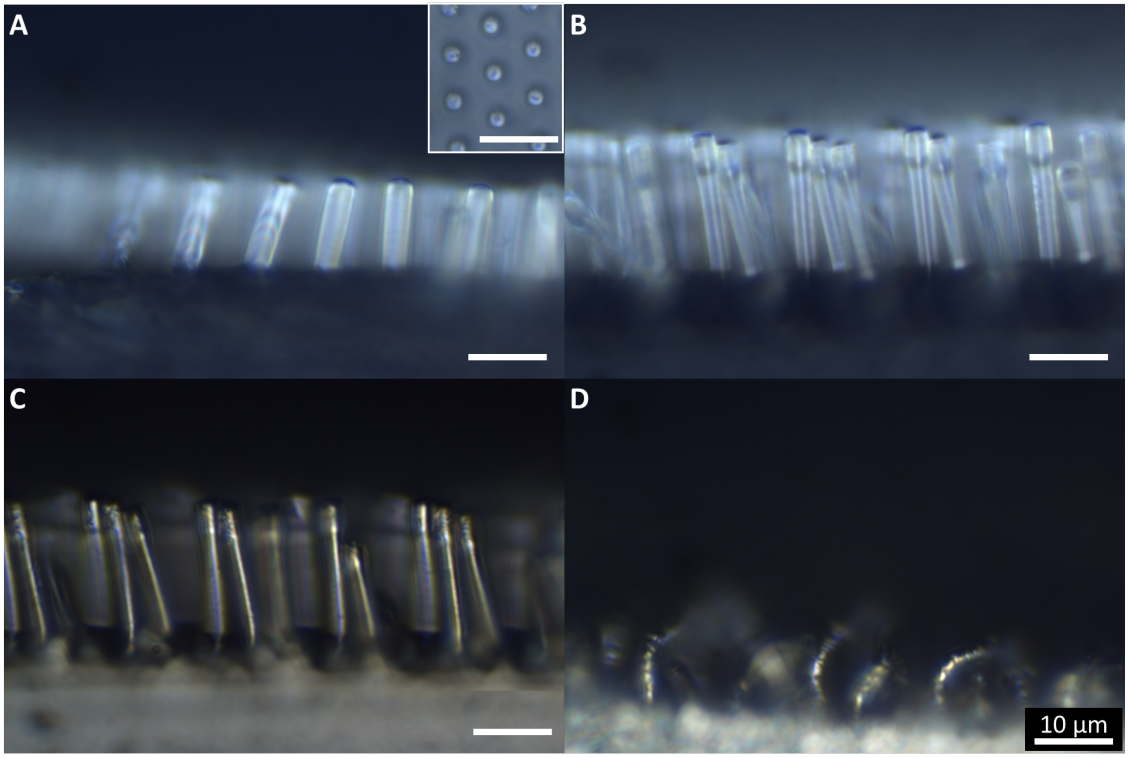

Figure 5.19: **Documentation of the process from stretching to wrinkling. A** The hot embossed, not pulled pillars are shown with an inset that displays their hexagonal arrangement. **B** Hot pulled pillars are clearly elongated compared to the not pulled reference. **C** After coating with Ag, the pillars are still stretched. **D** Recovering of the permanent shape causes the stiff Ag layer to buckle into surface wrinkles on the lateral faces of the pillars. All scale bars are 10 µm.

of the pillars is visibly decreased. At last, the image in Fig. 5.19 D reveals the recovered sample with pillars, that now exhibit wrinkled side walls which scatter the microscope's light as rainbow colors. The resulting pillar structures are exhibited by the SEM shown in **Figure 5.20**. The pillars at the edge of the structured field clearly possess wrinkles side walls. A gradient of the distinctiveness and depth of the wrinkles along the height of the pillars is noticeable. Presumably, this phenomenon correlates to non-uniform stretching of the pillars. It seems that at the bottom of the pillars the temporary shape was stretched to a greater extent. The closer to the to the less temporary stretching occurred. The very tip of the pillars is has not been stretched as was already indicated by the microscope pictures in Fig. 5.19.

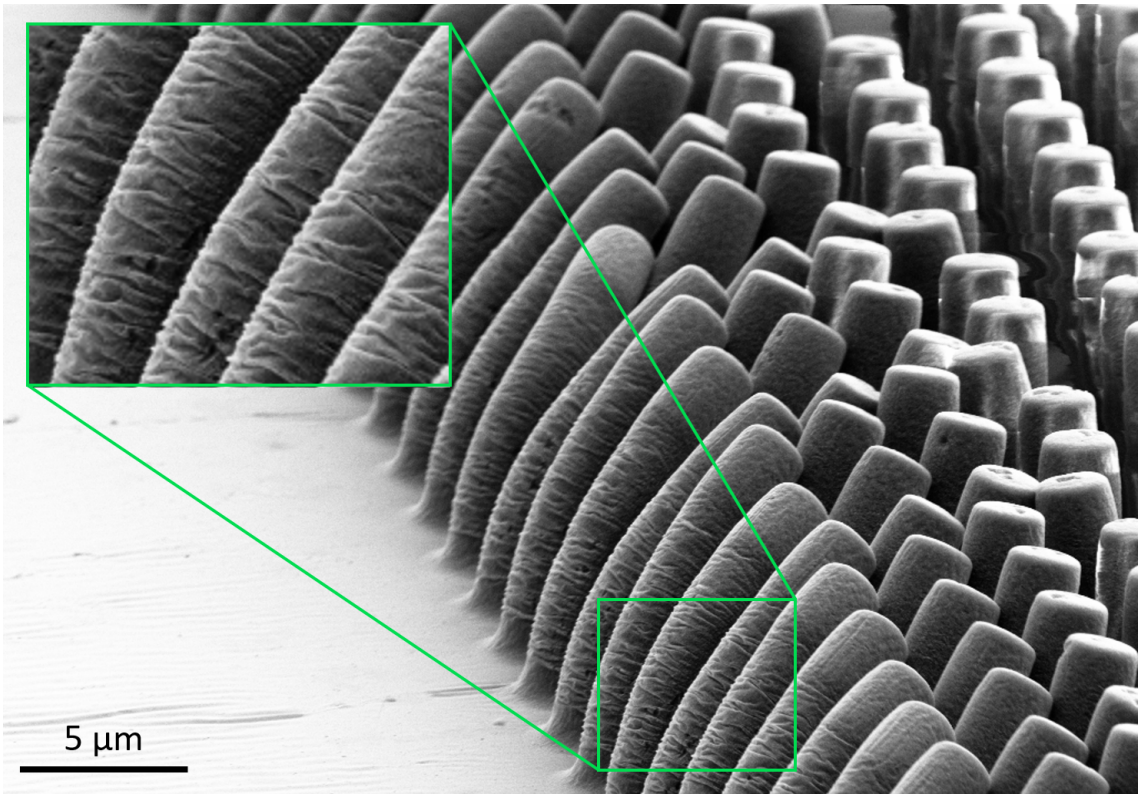

Figure 5.20: **Pillar structures with wrinkled, vertical side walls.** The SEM image demonstrates the successful wrinkling of a thin Ag film on vertical side walls of first by hot pulling temporarily stretched and then recovered SMP pillars.

5.4 Wetting Properties

Besides focusing on optical benefits Sec. 5.1 also emphasized the importance of micro- and nanostructures on petal, leaf and stem surfaces for the plant's water management. Structured epidermal cells play a major role in self-cleaning, fog harvesting, and guidance of the vital water to the roots.[210–212] In this context the wetting properties of our artificial wrinkle structures are analyzed in the following. In consideration of the anisotropy of the wrinkle structures, the contact angle is measured perpendicularly ($CA\perp$, left column) and parallel ($CA\parallel$, right column) to the wrinkle orientation as depicted by the schematic in **Figure 5.21** A. As reference, a 2 µl water drop is disposed on a smooth PMMA surface yielding the slightly hydrophilic contact angle of 73 °C as shown in Fig. 5.21 B. All denoted contact angles are approximated with Laplace-Young fits and determined from the photograph. The contact angles of linearly, non-hierarchically wrinkled samples with

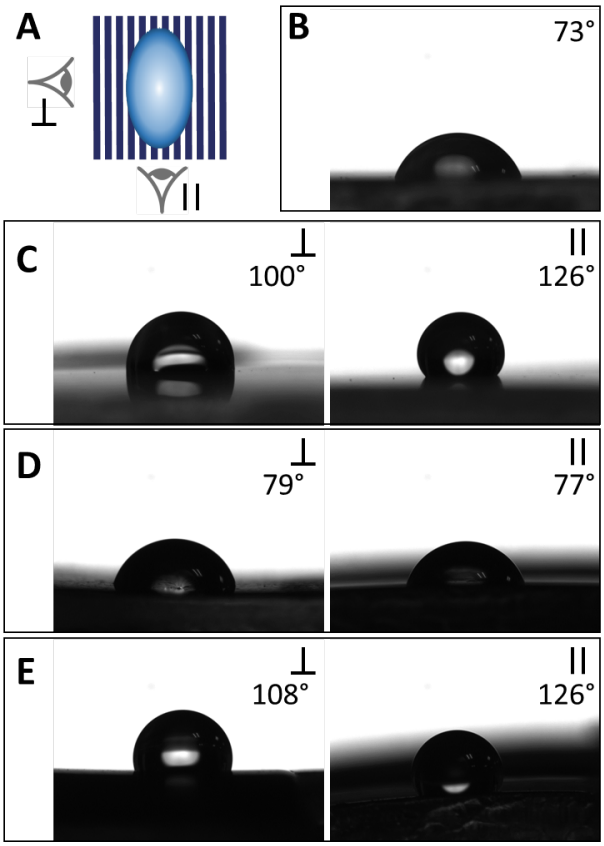

Figure 5.21: **Wetting behavior of non-hierarchical and hierarchical surface wrinkles. A** The schematic illustrates the camera view perpendicularly ($\perp$, left column) or parallel ($\parallel$, right column) to the wrinkle orientation. **B** The water droplet spreads isotropically on a smooth PMMA surface with a slightly hydrophilic contact angle as revealed by the photograph.
C The wetting behavior of a water droplet on a surface with small wrinkles of $\overline{\Lambda} = 1.3\,\mu m$ is distinctly anisotropic and hydrophobic. **D** A water droplet on large wrinkles with $\overline{\Lambda} = 15\,\mu m$ does not exhibit pronounced differences to the smooth PMMA surface. **E** The tulip mimicking, hierarchical structures (see Fig. 5.10) show hydrophobic and anisotropic properties despite the large wrinkle substructure.[174]

$\Lambda \approx 1\,\mu m$ (Fig. 5.21 C) and $\Lambda \approx 15\,\mu m$ (Fig. 5.21 D) are compared with a hierarchically wrinkled sample of the tulip type introduced in Sec. 5.3 and shown here in Fig. 5.21 E. The small wrinkles (C) increase the contact angle compared to the flat PMMA surface drastically to $CA\perp = 100^\circ$ and $CA\parallel = 126^\circ$, respectively, and change the wetting behavior of the surface from slightly hydrophillic to hydrophobic. Additionally, a strong anisotropy of the wetting is visible. Along the wrinkle orientation, the water spreads to a greater extent than normal to it, which results in an ellipsoidal droplet shape. This behavior is not observable for larger wrinkles (D) where neither an increased contact angle compared to the flat surface nor an anisotropy of the spreading water is distinct. For hierarchical wrinkles (E), however, hydrophobicity and anisotropy are as pronounced as for small wrinkles. The wrinkle dimensions resemble here the ones from the structure in D and the on top grating is of similar size than the wrinkles in C. In $\parallel$ direction the droplet experiences the small structure, i.e. roughness, of the surface that strongly influences the wetting behaviour .[213–216] In the perpendicular direction along the large structures the surface appears less textured to the water drop.

5.5 Optical Characterization

As previously mentioned, the herein presented wrinkle structures are producible on large scales in a crack-free manner and feature an intrinsic short-range irregularity in height and period which makes them ideal candidates for applications as disordered diffraction gratings. We measured the reflective properties of some of the hierarchical surface wrinkles and the linear, non-hierarchical structures and examined their diffractive properties in transmission and reflection. As a proof-of-concept, we replicated my wrinkle structures into a transparent resist layer deposited on the front side of crystalline silicon (c-Si) solar cells and determined the cell's external quantum efficiency. The results of these investigations are presented in the following sections.

5.5.1 Diffractive Properties

The light manipulating effect of the surface wrinkles can be easily visualized pointing a light source at the structures as shown in the photographs in **Figure 5.22**. A red laser pointer with a wavelength of 650±20 nm and the collimated beam of a white LED are pointed at the different surfaces depicted by the SEM images in Fig 5.22. The smooth surface of an unwrinkled sample (A) and a perfectly regular grating (B) serve as reference structures. The grating is fabricated by laser interference lithography[217,218] and tailored to match the below shown wrinkle sample in its period of $\Lambda = 1.3\,\mu m$. The grating's height, however, is by approximately a factor two smaller than the height of the wrinkles due to the laser interference lithography being at its utmost capability limits in this size regions. Nevertheless, this grating structure will serve as perfectly ordered counterpart to the disordered wrinkles in various of the following measurements to demonstrate the influence of structure irregularity. The exemplary wrinkle structure (C) used for this measurement is the same as the one shown in Fig. 5.5 A. The wrinkles exhibit a period of $\Lambda = 1.30 \pm 0.39\,\mu m$ and a height of $A = 650 \pm 130\,nm$ accordant to the wrinkle typical size deviations of ±30 % in period and ±20 % in height. Furthermore, as example for hierarchical structures, the tulip type structure (D) introduced in Fig. 5.10 is subject of investigation. For each sample, the diffraction of the monochromatic red and the VIS light source is observed in transmission (T_{red} and T_{VIS}) and in reflection (R_{red} and R_{VIS}). Since the wrinkle structures exhibit excellent anti-reflective properties as demonstrated later, the surfaces of the samples were coated with a thin silver layer for the here shown photographs in order to enhance the intensity of the reflected diffraction patterns. All structure orientations are vertical as in the SEM images.

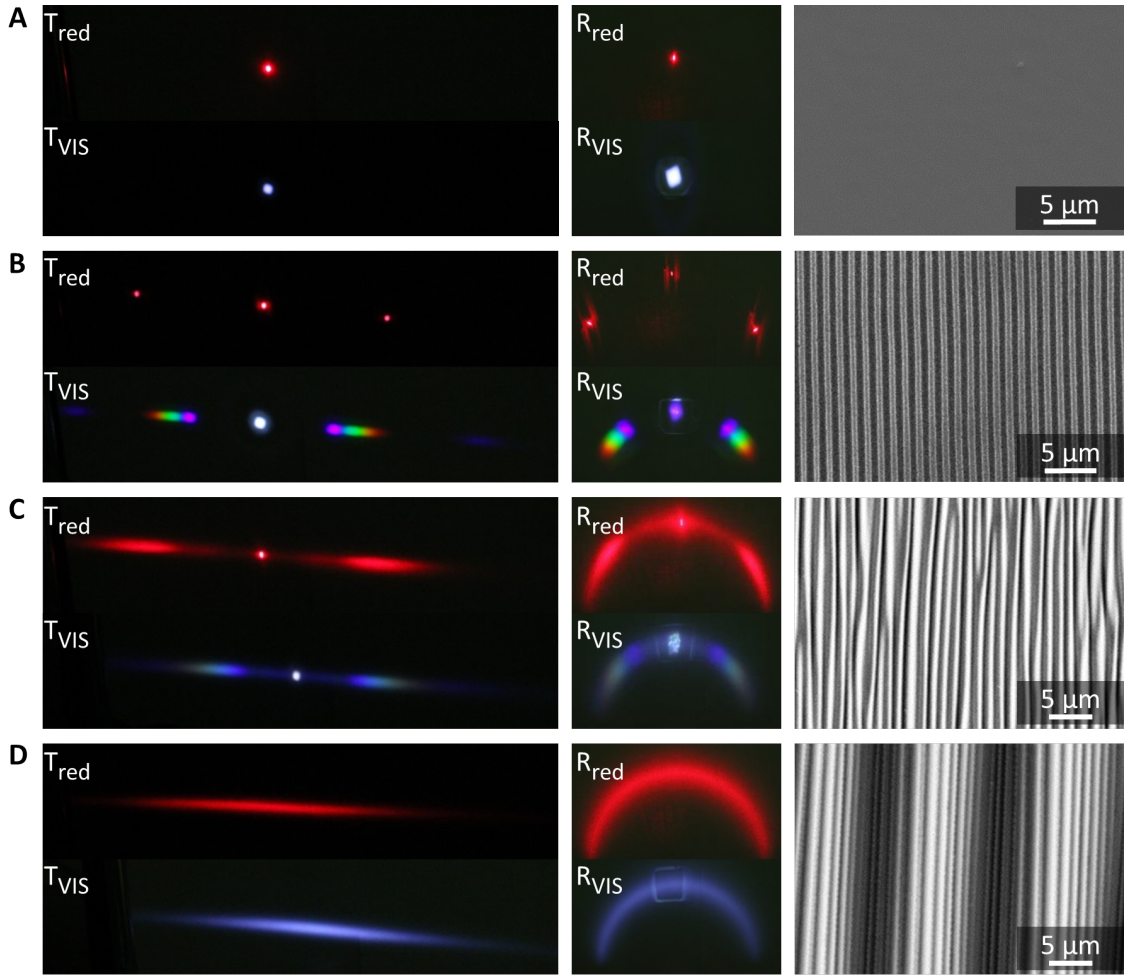

Figure 5.22: **Transmission and reflection on wrinkled samples and references.** The transmission of a red laser pointer (T_{red}) and a white LED (T_{VIS}) are depicted in the photographs of the left column. In the middle column the same light sources were used to visualize the light manipulation of the various structures in reflection (R_{red} and R_{VIS}). The according SEM pictures of the samples' topographies are shown in the right column. **A** Smooth surface. **B** Perfectly ordered grating. **C** Linear surface wrinkles. **D** Tulip mimicking, hierarchical surface wrinkles.

Whereas the smooth sample does diffract the beams of both light sources neither in transmission nor in reflection, in both cases the grating induces a distinct dissociation of zeroth and first order of the red laser pointer and the spectral colors of the white LED, respectively. The wrinkle structure generates a distinction between zeroth and first order of the diffraction of the red laser pointer beam, too. Compared to the grating, the peak of the first order is significantly broadened which is visible in the decreased sharpness of the spot. The same effect occurs for the white light source in transmission and reflection mode. Although a faint spectral divergence between the light source's colors is

discernible, the individual peaks are washed-out. The structural disorder present in the surface wrinkles sample represses sharp diffraction orders partially. The transmission and reflection diffraction patterns created by the hierarchical structure are particularly interesting. Even though the embossed, regular grating presumably diffracts light similarly to the grating shown in (C) albeit to different angles because of the dissimilar structure sizes, the underlying wrinkle structure distributes the positions of the individual peaks homogeneously as a fine line. For the monochromatic light source, no distinction between diffraction orders is distinguishable and the white beam is shaped to a homogeneously white line by the structure. This phenomenon suggests especially hierarchical surface wrinkle structures for applications in beam shaping devices.

The comparison of the here shown diffractive properties with the photographs displayed in Fig. 5.2 C with transmission in the upper and reflection in the lower picture demonstrates, that the pattern generated by the tulip replica resembles more the pattern observed with linear wrinkles than the hierarchical tulip imitation. This is presumably due to the comparably low aspect ratio of the big, underlying wrinkles in the original petal surface structures.

The color dissociation witnessed in the reflected diffraction pattern of the linear surface wrinkles in Fig. 5.22 C is also evident in the iridescence observed on such samples. In **Figure 5.23** A the reflection of a linearly wrinkled, not Ag coated sample with a mean period of $\Lambda = 1.1\,\mu m$ is photographed at various angles. The angle denoted in the pictures is the angle of camera to the perpendicular while the white light source was kept constant at $0\,^\circ$. The camera is oriented orthogonally to the wrinkle direction. With increasing angle starting at $25\,^\circ$, the by the structure reflected light changes from blue to green, yellow, and finally violet at $65\,^\circ$. The ellipsometer measurement of the angular spectral distribution in Fig. 5.23 B verifies the observed iridescence. With an AOI of $20\,^\circ$ of s-polarized light the false color plot reveals the reflectance intensity at relative scatter angles of -5 $^\circ$ to 55 $^\circ$ corrected to the surface normal in dependence of the wavelength in the range of VIS and NIR from 400 nm to 1300 nm. The sample utilized for this measurement has a mean period of $\Lambda = 1.5\,\mu m$. The measured intensity maximum of the diffraction's first order shifts with increasing scatter angle to higher wavelengths. The red, dotted line marks the from the known mean period calcuated position of the first order maximum according to:

$$sin(\theta) = \frac{\lambda}{\Lambda} + sin(\theta_{in}) \tag{5.4}$$

with θ as the scatter angle of the first order, λ is wavelength of light, the wrinkle's mean period is Λ, and the AOI of the light source is denoted as θ_{in}. The measured and calculated

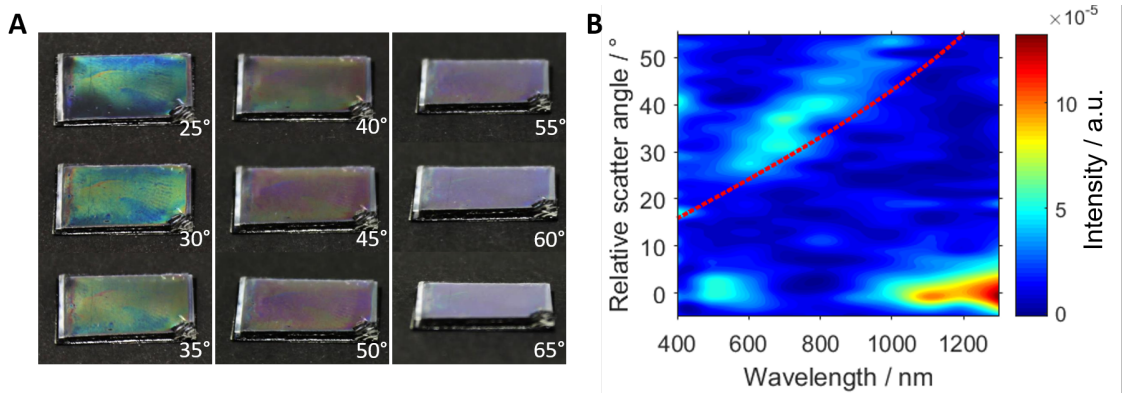

Figure 5.23: **Iridescence on wrinkle structures. A** The photographs show a from above illuminated linearly wrinkled sample ($\overline{\Lambda} = 1.1\,\mu m$) in various viewing angles. Denoted is the angle to the perpendicular. With increasing viewing angle, the perceived color changes from blue over green and orange to violet. **B** The false color plot of an ellipsometer measurement displays the scatter angle resolved reflection intensity in the VIS and NIR range of s-polarized light on a linearly wrinkled sample ($\overline{\Lambda} = 1.5\,\mu m$). The red dotted line indicates the calculated angle of the first order maxima of reflection.[174]

angle of the first maximum of the diffraction pattern are in good conformity. Nevertheless, the disorder of the wrinkle structure is very prominent in the pronounced peak broadness.

To investigate the influence of the period disorder and the height disorder separately, my colleague Raphael Schmager (IMT) performed a finite deformation time domain (FDTD) simulation of the wavelength dependent, angular distribution of transmitted and reflected light based on the structure observed on my surface wrinkle samples. The simulation considered a wrinkle structure with $\Lambda = 1.3\,\mu m$ and an AR of 0.5 for the case of a perfectly ordered sinusodial grating, the case of $\pm 30\,\%$ disorder only in period, the case of $\pm 20\,\%$ disorder only in height, and lastly, the case of both of the denoted disorders combined. To summarize, the results show, that the influence of the wrinkles' period irregularity is the dominating effect that caused peak broadening in reflection as well as in transmission. The height variances yield an overall lower reflectance compared to a structure with no height variances. More details on this numerical results will be published by Schauer and Schmager *et al.*.[217]

5.5.2 Anti-Reflective Behaviour

With a view to the wrinkle's structure irregularity, the structure heights in the order of the wavelength of light for the smaller wrinkle samples, and the sinusodial profile of the linear, non-hierarchical wrinkle structures, not only the relative distribution of the diffracted light but also the overall reflectivity is of interest. Those listed structure features suggest good anti-reflective properties over a wide AOI. Therefore, we quantified the overall re-

flectivity of various samples by measuring the reflection in an integrating sphere from a normal AOI of 0 ° to a glancing AOI of 70 °. For those measurements, the back of all samples were covered with a black foil to minimize any back reflection of in-coupled light and then placed on the rotatable sample holder in the center of the spectrophotometer described in Sec. 2.3.5. As an example, the spectrally resolved reflectivity of a linearly wrinkled sample with a mean period of $\overline{\Lambda} = 1.3\,\mu m$ and mean height of $\overline{A} = 650\,nm$ at various AOIs is given in **Figure 5.24**. In consideration of the anisotropy of the wrinkle structure, two sets of measurements were conducted: one with the AOI altered in orthogonal direction ($\perp$) to the wrinkle orientation and one with parallel ($\parallel$) alteration. The results are shown in Fig. 5.24 A and B, respectively. The smaller the AOI the lower is the sample's reflectance with little dependence of the wavelength whereas the reflectance for the $\parallel$ case consistently exceeds the reflectance of the $\perp$ case. The unsteadiness observed for all AOIs between approximately 490 nm and 570 nm was also present in the same measurement conducted with a not wrinkled sample with the same thickness of PMMA layer on TFX substrate (data not shown) but not on a smooth sample, consisting of only one resist material. Hence, we attribute those variances to thin film effects. Figure 5.24 C depicts a comparison of the reflectances of linearly wrinkled samples (blue triangles), the tulip and daisy type hierarchical wrinkles (green stars), as well as the smooth and grating samples as reference (gray crosses). The in the legend denoted numbers refer to the mean period of the linearly wrinkled samples (see Fig. 5.5). For the sake of clarity, a mean value for the wavelength range of 390 nm to 760 nm for every AOI of every sample was calculated and the reflectance is shown with a logarithmic scale. The integrated reflectances for the linear wrinkle samples show only little dependence to the period below 3 % even up to an AOI of 40 °. For larger AOIs the reflectance increases drastically to $7 - 11\,\%$ percent with clear correlation to the wrinkle period. Whereas in lower AOI regions the small periods excel the anti-reflective properties of larger wrinkles, this trend reverses for larger AOIs. Compared to the smooth and grating references, the wrinkled samples are able to reduce the reflection by almost 50 % irrespective of the AOI. The two hierarchical structures exhibit very different results. The tulip type with the two structures aligned show good anti-reflective properties with around 3 % at 10 ° and even lower reflectance as the smaller linear wrinkle structures at 70 °. Yet, the daisy structure shows no significnt reflectance decrease compared to the smooth reference surface in the whole AOI range.

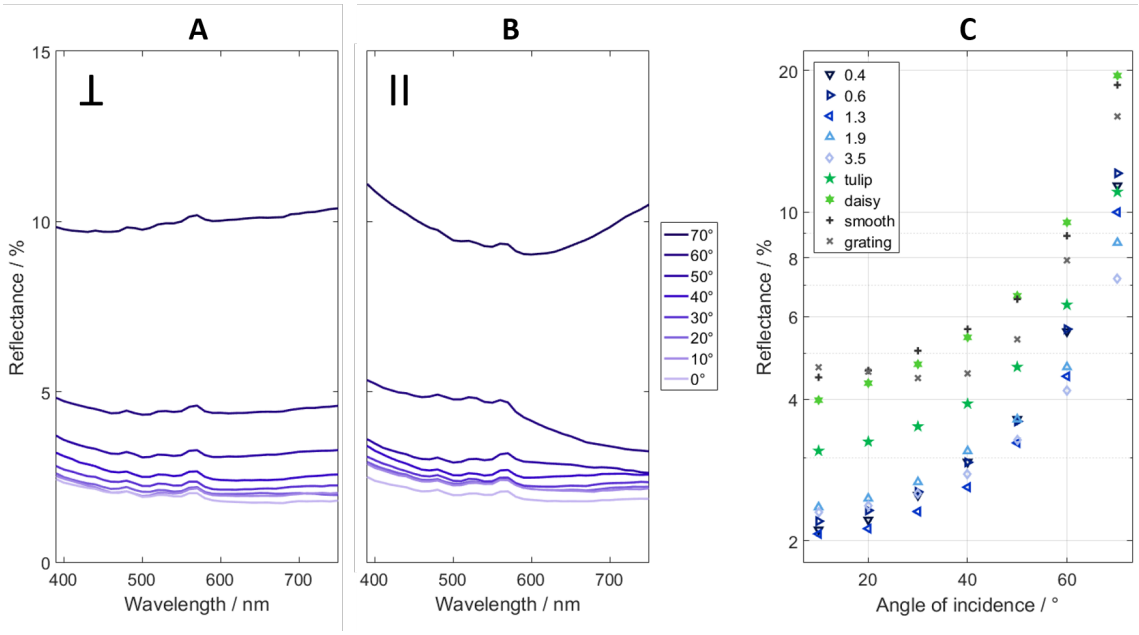

Figure 5.24: **Comparison of the reflectivity of diverse wrinkle structures. A** The reflectance in VIS of an exemplary wrinkles structure with a period of 1.3 µm is determined with an AOI altered perpendicularly to the wrinkle orientation from 0° to 70°. **B** The same measurements are performed with an parallel to the wrinkle orientation increasing AOI from 10° to 70°. **C** Compared are the over VIS integrated reflectance of linear wrinkles of various sizes (notation is period in µm), the tulip type hierarchical wrinkles, the daisy type structure, and as reference a smooth and a perfectly periodic grating surface for various AOIs.

5.5.3 Application on Solar Cells

The anti-reflective properties and beam shaping ability of the wrinkle structures is interesting for applications where homogeneous light in-coupling is required such as in solar cell coatings. Although my wrinkle samples were used, the measurements shown in this section were performed by my colleague Raphael Schmager. Since the explanation of the optical effect of my structures relies partially on this work and for the sake of completeness, the results are summarized in the following. For the applications of the wrinkle structures it is necessary to replicate them into a thin layer of a suitable resist directly on the surface of the cell since a gap between sample and surface would lead to unwanted reflections. The process to replicate structures onto diverse substrates such as in our case the surface of a crystalline silicon solar cell is illustrated in **Figure 5.25**. First, the surface of a wrinkle structure is covered with a thick PDMS layer, that is peeled off of the sample after thoroughly curing. The sample's topography is transferred as negative into the PDMS stamp. This stamp is pressed into a liquid layer of a photo-curable resist directly on the surface of the respective substrate. After curing this resist, the mold is removed and the substrate possesses now the exact same structure than the initial sample.

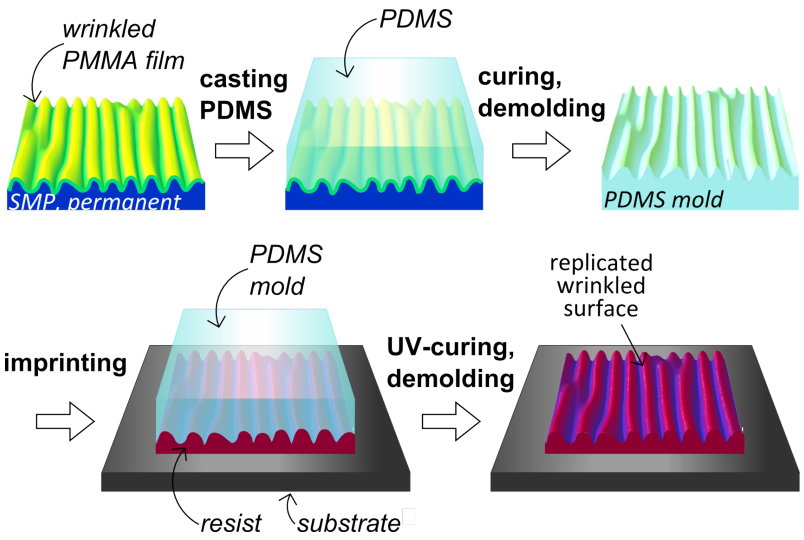

Figure 5.25: **Schematic of the replication process.** To transfer the wrinkle structure onto various substrates, the structure is first copied into PDMS that is afterwards used as a mold to replicate the structure in a photo-curable resist directly on the respective substrate.[217]

Here, a 10:1 weight ratio of the two components Sylgard Silicone Elastomer 184 and Sylgard Curing Agent 184 were mixed and poured on a linearly wrinkled sample with a mean period of 1.3 µm and mean height of 650 nm in an accurate to size aluminum foil container. Air bubbles were removed by placing the mixture in an evacuated desiccator for 20 min before pouring. Afterwards, the PDMS mixture was allowed to cure on the samples for 48 h at room temperature before the container was removed and it was peeled off of the sample. Subsequently, this PDMS mold was pressed into a $\approx 50\,\mu L$ drop of the UV-curing adhesive Norland Optical Adhesive 88 (NOA88) directly on the surface of a c-Si solar cell. After 20 min of exposure to UV-radiation with 1.5 mW/cm^2 surface power density, the PDMS mold was removed leaving a perfect replica of the wrinkle structures as coating on the cell.

The results from our reflection measurements demonstrate, that the wrinkle structures are efficient in diffracting and transmitting incident light as forward propagating light. However, if the wrinkle structures are applied on, e.g., photovoltaic devices, part of transmitted light will experience reflection on the interface of the wrinkle structure to the surface of the device. Hence, for efficient light-harvesting, not only good in-coupling of incident light is important but also effective prevention of out-coupling of on the interface reflected light. While for incident light a low reflectance at the front of the structures is required, the amount of at the back side reflected light is to be high to recapture the light and reflect it back towards the photoactive layer. On account of this we investigated the back reflection of our structures. Therefore, a wrinkle structure with the mean period of

$\overline{\Lambda} = 1.3\,\mu m$ is with the described replication process transferred to a planar glass slide. As a benchmark, the already in Fig. 5.22 B introduced grating is prepared in the same way. For both samples we measured the overall front and back reflectance wavelength resolved under normal incidence. While the reflectances of both samples for at the front incident light are nearly the same, the results differ strongly for the back reflectance. The respective reflection spectra are shown in **Figure 5.26** with the surface wrinkle structure denoted as "SW". An extensive reflection increase is observed that is more pronounced

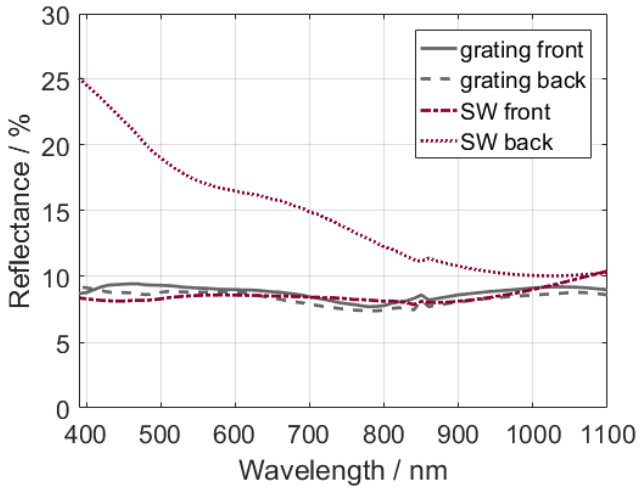

Figure 5.26: **Back side reflection of replicated wrinkle and grating structures.** The reflectance of the wrinkle structures and the grating reference is shown for illumination at normal incidence from the front as well as from the back. The back side reflectance is significantly increased for surface wrinkles.[217]

the shorter the wavelength is. This significant difference originates from the different angular distributions of transmitted light caused by the respective structures as it is visualized in Fig. 5.22 B and C. The diffraction of the light at the wrinkle structure yields a strongly reduced intensity in the zeroth order. More light is diffracted into the first order and reflected back towards the substrate. In this way, out-coupling is averted and the light gets a second chance to be captured. The decline of reflection with higher wavelengths might be caused by total reflection within the glass substrate as this long-wavelength light is scattered into the material at high angles. The cells utilized for this proof-of-concept are heterojunction crystalline silicon solar cells fabricated according to the process described in the work of Ding *et al.*[219] by Kaining Ding at the IEK-5 Photovoltaik, Forschungszentrum Jülich GmbH, Germany. A schematic of this cell is displayed in **Figure 5.27** A. A planar indium tin oxide (ITO) layer serves as transparent and conductive electrodes contacted by a grid of silver rods in the front and continuous silver layer in the back. In

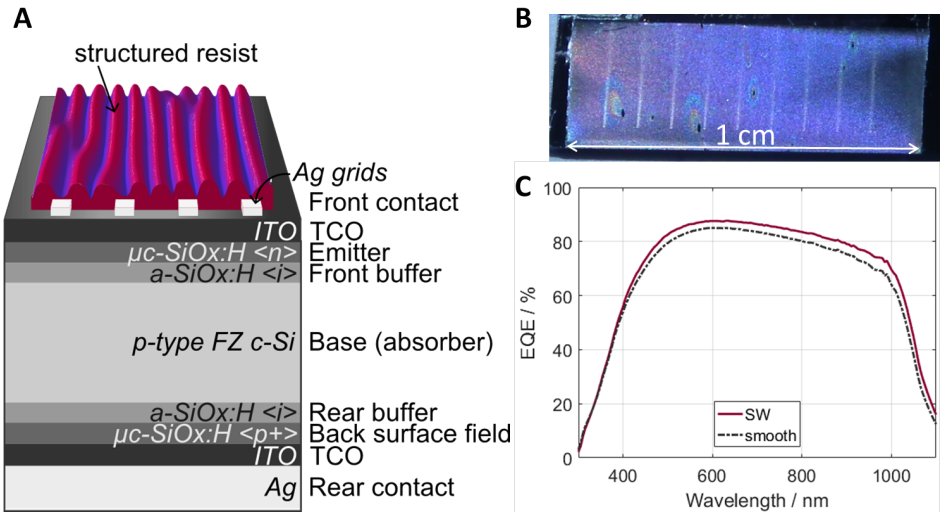

Figure 5.27: **Anti-glaring and light-harvesting properties of wrinkle structures. A** The schematic illustrates the replicated wrinkle structure on the c-Si solar cell stack. **B** In the photographs the low blinding potential of cells coated with wrinkle structures ($\overline{\Lambda}$ =1.3 µm) is evident. **C** The external quantum efficiency of a with wrinkles coated cell is compared to that of an smooth cell and shows the efficiency increase by the wrinkle coating over the whole VIS and NIR spectrum.[217]

between, a 250 µm thick layer of p-type c-Si absorber is framed by thin layers of buffer and emitter/back surface field. In Fig. 5.27 B a photograph of such a cell coated with the wrinkle structure is shown. The picture was taken at a viewing angle of around 50 ° with a white light source. Only half of the utilized c-Si cell was covered with the wrinkle structure and the other half was covered with an unstructured NOA resist film of the approximately the same thickness. In this way, we could directly prove the advantage of the wrinkles. Each of the active areas comprises $10 \times 5\,\mathrm{mm}^2$. For evaluating the impact of the wrinkle coating compared to the smooth coating, we measured the external quantum efficiency (EQE) with a modulated monochromatic light with $\lambda = 300 - 1100\,\mathrm{nm}$. The spot size was restricted to a well defined, rectangular area by a slit aperture in the beam path. The so generated spot covered an area of five Ag grid lines under normal incidence.

A significant increase from 31.4 mA/cm^2 for a smooth cell to 32.9 mA/cm^2 for a wrinkle covered cell in short-circuit current density was measured under normal incidence. This corresponds to an external quantum efficiency increase of 4.78 % due to the application of the wrinkled coating.

5.6 Conclusion and Outlook

Inspired by the structures found on diverse petals, we developed a wrinkling method to produce widely adjustable, linear, and slightly disordered diffraction gratings on large scales. The influence of the programming strain of the SMP substrate and the thickness of the PMMA coating were investigated as they determine the resulting structure size. Thereby, we can tailor the wrinkle structures with periods as small as 400 nm up to 15 µm with aspect ratios of around 0.5. As a parameter unique to SMP wrinkling substrates, solely the recovery temperature can be used to adjust the achieved structure size.

Moreover, our full polymer approach with a SMP as substrate and a PMMA layer as coating allows us to emboss a secondary structure into the coating and therefore, fabricate hierarchical structures. Depending on the combination of wrinkle size and top structure and orientation, a wealth of hierarchical structures can be produced, exemplified here by the tulip-mimcking and the daisy-mimicking structures. A second concept for the realization of hierarchical structures is demonstrated by applying an Ag coating on a pre-structured and pre-stretched SMP substrate. Hereby, depending on the Ag thickness samples with absorbing or scattering properties were produced. Lastly, hot pulling as a method to induce a temporary surface area change was introduced. In an elaborate embossing cycle micropillars can be temporarily stretched by 50 % before being coated with an Ag film that wrinkles upon recovery. In that way I was able to produce wrinkles on vertical side walls of a high aspect ratio microstructure.

On the basis of the remarkable iridescent appearance of the tulip role model, an optical characterization of my wrinkle structures was conducted. The linear wrinkles and hierarchical, tulip-mimicking structures exhibit a distinct broadening of the diffraction peaks in transmission as well as in reflection compared to a smooth and a perfectly periodic grating. This effect is attributed to the wrinkle's short-range disorder of typically $\pm 20\,\%$ in height and $\pm 30\,\%$ in period. Our measurements of the angularly and spectrally resolved reflection demonstrated the low reflectance of the irregular structures. In combination with the examined high back reflection, the effective in-coupling and therefore light-harvesting properties advocate my linear wrinkles for applications on photovoltaic devices. In fact, the measurements of the effective quantum efficiency of a c-Si solar cell revealed an efficiency enhancement of almost 5 %compared to a smooth surface.

Besides the further investigation of the beneficial use of surface wrinkle structures as coatings for photovoltaics, especially the approaches for fabrication of hierarchical structures are promising for optical applications. The treasure flower structure with its submicron wrinkle coating on top of a large aspect ratio prismatic grating might be an ideal

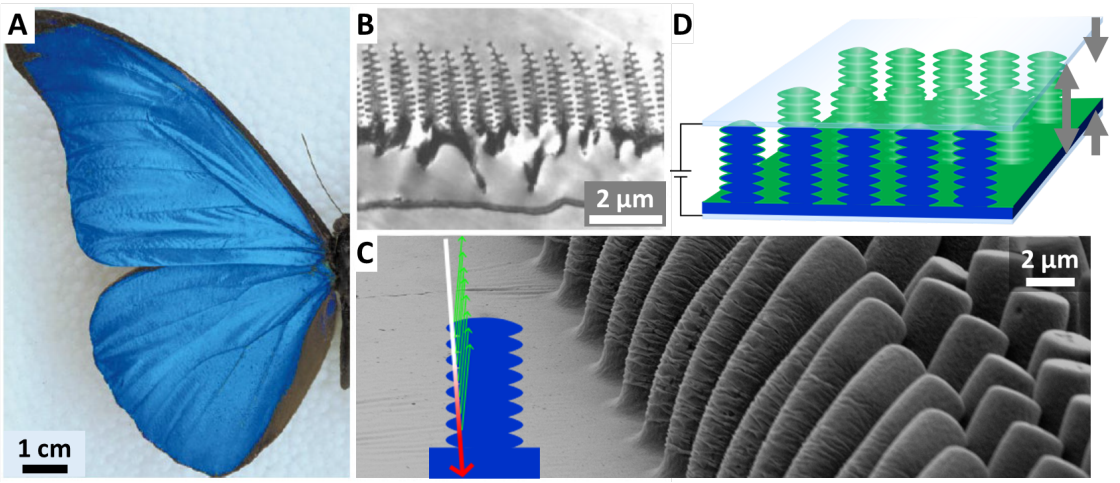

Figure 5.28: **Concept of a *Morpho* inspired color tunable device. A** The photograph shows the wing front side of a *Morpho rhetenor* butterfly. Adapted from [7]. **B** The TEM image reveals the complex nanostructures that are responsible for the striking blue wing color. Adapted from [7]. **C** The *Morpho*'s Christmas tree like structure affects incident light like a multilayer. We want to achieve the same effect with the wrinkled side walls of our pillar structures shown in the SEM picture. **D** The concept of a device that uses electrostatic forces to compress the wrinkles pillars is illustrated. Thereby the wrinkle period is decreased and the interference conditions change which leads to a shift of the reflected wavelength, hence, a color change.

candidate for anti-reflection coatings. Although wrinkling on the vertical walls of SMP pillars is herein demonstrated as an essential proof-of-principle, the structure's morphology resembles the "Christmas-tree" like architecture causing the brilliant blue coloration of the *Morpho rhetenor* butterfly wing that is depicted in **Figure 5.28** A and B. With sensible adjustment of the wrinkle size, further improvement of the homogeneity of the wrinkles, and switch to PMMA/SMP material combination, this concept might be able to produce similar structural colors (Fig. 5.28 C). Furthermore, due to the small pillar size, electrostatic forces between two transparent electrodes, spaced by the pillar structure as sketched in Fig. 5.28 D, could be applied to change the height of the pillars, thereby affect the wrinkle period and, hence, the reflected color.

A shortened version of SMP based wrinkling, the parametric study and formation of hierarchical structures by a combination of wrinkling plus hot embossing was published as the article "Bio-inspired hierarchical micro- and nano-wrinkles obtained via mechanically directed self-assembly on shape-memory polymers", by Senta Schauer, Matthias Worgull, and Hendrik Hölscher, Soft Matter 13, 4328-4334 (2017)

An extended version of the optical analysis and application of wrinkles for solar cells is submitted to Optical Materials Express as the article "Disordered Diffraction Gratings Tailored by Shape-Memory Based Wrinkling and their Application to Photovoltaics", by Senta Schauer, Raphael Schmager*, Ruben Hünig, Kaining Ding, Ulrich W. Paetzold, Uli Lemmer, Matthias Worgull, Hendrik Hölscher, and Guillaume Gomard (September 2017).*

** Authors contributed equally.*

The surface wrinkle samples were produced by me, the optical analysis of the wrinkles structures were performed by Ruben Hünig and me, Raphael Schmager conducted the simulative investigation of the wrinkle structures and performed the solar cell experiments. The solar cells were provided by Kaining Ding.

6 Shape-Memory Polymer Opals

Opals, natural gemstones consisting of three-dimensional periodic arrangements of monodisperse spheres, show intense structural colors. In this chapter, I introduce our approach to artificially recreate a material composite exhibiting this opalescence. Our fabrication method allows us to actively tune the composite's color by changing its shape. Most of the experimental work discussed in this chapter was performed within the scope of my four month research stay at the University of Cambridge in Stoyan Smoukov's group (Active and Intelligent Materials Lab, Department of Material Science and Metallurgy, University of Cambridge, UK) and Prof. Jeremy J. Baumberg's group (Nanophotonics Centre, Cavendish Laboratory, University of Cambridge, UK). Baumberg's group developed an opal composite with hard polymer spheres in a rubber matrix that enables stretch-tuning of the material's color. However, due to the rubbery nature of the matrix, an external load is needed to uphold the desired shape change. In my work, I was able to replace this required external force by an implemented system to impose the necessary constraint by adding a shape-memory polymer to the composite. The characterization and performance of this composite are discussed in the following.

6.1 Motivation and Background

Since ancient times, opals are admired for their viewing angle dependent color, a phenomenon that is named after these gemstones: the *opalescence*. The word "opal" arises from the Sanskrit word "upala" meaning "precious stone" and later adapted by Latin and Greek where "opalus" and "opallios" both translate to "to see a color change".[14] Opals can be found all over the world. Especially Australia and Africa are famous for stunning opals but also in Germany types of opals such as the cat's-eye are common.[220,221] The coloration results from their in three dimensions periodic nanostructure. The fact that diffraction at the ordered spheres of the crystal cause this opalescence was first explained correctly by Sanders *et al.* in the 1960s and is now a well understood mechanism.[222,223] For the discussion of such photonic crystals and their color creating interplay see Sec. 2.2. An example of a natural opal gemstone is depicted in **Figure 6.1** A and the SEM picture in B reveals its microscopic crystal of spheres in a fcc lattice. Opals consist of

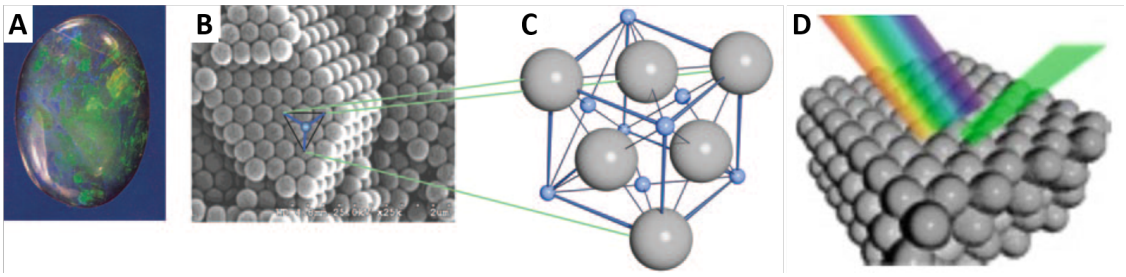

Figure 6.1: **Light modulation by a natural opal. A** The natural, polished opal shows multitudinous facets of blue, green, yellow and red opalescent colors. **B** The SEM picture reveals the reason for this coloration: Small silica spheres build a three dimensional photonic crystal. Sphere diameter is $\approx 200\,\text{nm}$. **C** An arrangement of those spheres in the schematically demonstrated fcc lattice causes the inference based color. **D** Only one, by the sphere diameter determined part of incident white light interferes constructively with the opal structure and is reflected. (A-C Reprinted with permission from[14]. Copyright 2009, Wiley; D Adapted from[224])

amorphous silica spheres of 150 to 400 nm in diameter with hydrated silica $SiO_2 \cdot nH_2O$ filling the spheres' interspaces.[14,225] Impurities such as iron, copper, aluminum or titanium ions can occur and are responsible for the multifarious diversity of colors seen in opals.[14,226,227] The solubility of SiO_2 in water declines drastically with decreasing temperature, therefore, quartz crystals can form in water.[221] In the case that the water evaporates before large crystals are formed, silica precipitates in small spheres. Less pure and barely ordered opals can also evolve from biological materials.[221,228] Many plants contain silica particles and among other marine animals, diatoms produce diverse silica structures.[229,230] Even tunable, on three dimensional photonic crystal based structural coloration exists in nature. One of the most famous example for active color change in response to the surrounding is the fascinating skin of chameleons. This color change relies in large part on dispersion and aggregation of pigments in their color producing cells, the chromatophores.[231–233] However, it was recently reported by Teyssier *et al.*,[231] that structural color is responsible for the colorful appearance of the chameleon skin, too. Besides multilayer nanoreflectors, tuning of three-dimensional nanocrystals in dermal iridophores is a mechanism used by the chameleon to influence its colors.[231]

Artificial Opals

Equally manifold as the potential applications are the types and techniques to produce artificial structures mimicking the opals. The prospects of applications of static and tunable artificial opals range from decorative purposes to anti-counterfeiting structures, strain sensors, chemical sensors, photonic ink, and display devices, to name a few.[14,234–240] Compared to pigments and dyes, the structural coloration of opals does not fade with time due

to UV radiation, hence, they are interesting especially for long-lasting outdoor decorative purposes. Flexible opals are suited for simple strain sensors since even small changes in the crystal lattice by stretching or compression result in a color change.[235,241] Opals and inverse opals, with one of the phases being air, can easily be applied as sensors for chemicals. Are the voids filled with a liquid or gas, the color of the opal will change according to the fluids refractive index.[240] Swelling of the opal matrix in a suitable solvent can also be used to produce photonic ink.[242] Is the liquid applied locally, the spatially resolved color change is visible in only those areas and patterns or letters can be drawn. Especially for display applications, the color tuning ability of opals is of great interest since multiple colors can be generated in a single pixel. If this could be realized with an electrical tuning mechanism, a display with three to four times higher resolution compared to displays relying on red/green/blue sub-pixels is possible

Synthetic opals can be classified by material or mechanism underlying the fabrication process and it is differentiated between opals and inverse opals. All mechanisms have in common that they hold certain requirements:[243,244]

- spheres and matrix material need to differ in refractive index,
- for modulating light in the VIS spectrum, the sphere size is ideally in the range of 200 to 400 nm, and
- the spheres have to possess a very high monodispersity with diameter deviations of less than 5 %.

One of the most used production methods is the fabrication of opal films by convective self-assembly.[14,244–247] Here, the spheres of a colloidal dispersion self-assemble on a substrate when the dispersion dries. The spheres crystallize in a fcc lattice with the most dense layer parallel to the substrate surface.[248–257] Another widespread technique for self-assembly of opals is sedimentation. Similar as in convective self assembly, the spheres concentrate at the bottom and crystallize when a critical concentration is exceeded.[258,259] Predominantly, for artificial opals the used sphere materials are silica, PS, PMMA, or certain block co-polymers and the generated opals can be used as received, infiltrated with a material that replaces air in order to affect optical or mechanical properties, or used as a template to create inverse opals.[260] For the fabrication of inverse opals, an artificial opal structure is infiltrated with a second material and subsequently, the spheres are removed by dissolving, etching, or pyrolysis.[260–262]

A different approach to fabricate opals are polymer spheres composed of a hard polymer core and a soft, gum-like polymer shell, to that I will refer as “polymer opals” in

the following. In contrast to the before described self-assembly methods, here, external forces are necessary to yield crystal order. Opals produced by the described self-assembly methods usually result in solid, substrate supported, and brittle structures. In the case of polymer opals, the spheres are embedded in a quasi-continuous matrix of a soft polymer by what free-standing, visco-elastic solids are formed.[263] Besides the sizes of the spheres the color and color pureness of synthetic opals is determined by the following five factors:[260]

- the spacing between the opal's spheres,
- the filling fraction,
- the refractive index contrast between the two phases,
- the order, and
- the spheres' symmetry.

Each of the listed factors can be addressed to tune the observed color by external physical or chemical stimuli such as temperature changes, mechanical deformation, electric or magnetic fields, swelling, solvent infiltration, light irradiation and many more. **Figure 6.2** summarizes possible mechanisms for color tuning in synthetic opals (illustration based on[235]). A change of refractive index can be easily addressed in opals and inverse opals if one of the phases is air. By infiltration of the interstices or hollow spheres with solvents, the refractive index contrast of the two phases is modified and thereby the color.[260] When utilizing solvents that possess a temperature dependent refractive index even the temperature can be altered to change the color.[264] Swelling is one of the simplest and popular methods to change the sphere spacing. For instance, if the continuous phase of the opal is a hydrogel, exposition to water yields fast and immense volume changes of the matrix.[265] Lattice spacing can also be affect by external magnetic or electric fields, that influences order and arrangement of superparamagnetic spheres in aqueous solutions or actuate biaxial stretching in gum-like opals, respectively.[266–270] Stretch-tunability, the change of color in response to mechanical deformation of the opal, is present in systems, where spheres are embedded in flexible polymers such as elastomers or soft thermoplasts.[235,241] The spacing of the non-close-packed array of spheres in such polymer opals is affected by stretching in a way that the distance between the spheres in stretching direction increases. The effect of the crystal layers moving closer together perpendicularly to the stretching yields a blue shift of the perceived color. For more complete and in depth overviews on opal tunability it is referred to relevant literature.[235,260]

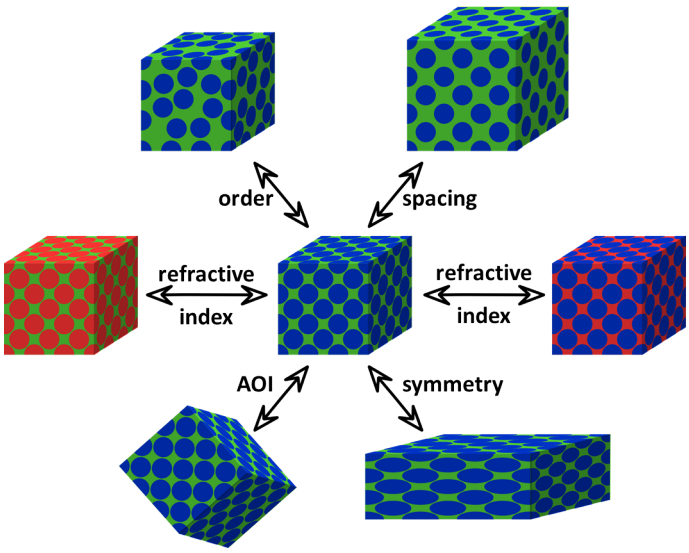

Figure 6.2: **Concepts for color tuning of opals.** The stop band position in colloidal opals is tunable by changing the refractive index of one of the phases, the spacing between the opals spheres e.g. by swelling or variation of the viewing angle, and order and symmetry of the opal spheres.

However, the mentioned approaches have some major drawbacks. Achieving static color change or color switching by swelling comprises several difficulties. While swelling might be fast, the reverse sphere distance change by drying of the composite can be very slow. On the other hand, to keep a constant color after swelling, drying has to be prevented by encapsulation or similar measures. Spatially resolved color changes through local application of the solvent is also temporally constricted due to diffusion of the solvent in the composite. Therefore, neither fast color switching nor static spatially resolved color changes are feasible with by swelling tunable photonic crystals. In general, systems containing liquids might be unsuitable for a range of applications as they require special caution to leaking, diffusion and evaporation. Spheres embedded in a soft, rubbery matrix enable color changes by stretching and compression but they feature the disadvantage of being in need of a constant external load as long as the color change is demanded. This impedes utilization relying on a compression based color change and therefore their range of applications is limited to devices where lateral deformation of the material is realizable. Hence, the material can not be attached to any surfaces and static, load free color change is not possible.

Objective

In our approach to tunable opal structures we use spheres embedded in a rubbery matrix, too, but solve the just described issue of the requirement of an external load to uphold the

for the color change necessary shape change. The constraint, that keeps the composite in the desired shape is implemented by adding our shape-memory polymer TFX to the polymer opals' matrix. The amount and distribution of added SMP is sufficient to impose its own ability to perform controllable shape changes (see Sec. 2.1) to the complete composite. Since changing the shape of the composite by stretching or compression affects the arrangement of the polymer opal spheres, this shape-change is accompanied by a defined color change. Hence, in contrast to state-of-the-art polymer opals, our material composite is, in addition to the stretch tunability, able to maintain a by compression induced shape change as long as it is demanded. Therefore, it can be attached to surfaces and color changes can be imprinted. Based on the by adding SMPs extended properties of the polymer opals, we named our composite "shape-memory polymer opals" (SMPO). As will be discussed in the following sections, the focus on our experimental work was to produce SMPOs and investigate the performance in dependence of the amount of added SMP regarding their shape-memory ability.

Polymer Opals - State-of-the-Art

Since my advancement of the polymer opal development is based on the previous outstanding work of many scientists in and around Jeremy J. Baumberg's group, I want to briefly summarize their achievements.

In the field of polymer opals, the group around of Ruhl, Spahn and Hellmann at the at that time *Deutsches Kunststoff Institut* (DKZ) in Darmstadt, Germany, now part of the Fraunhofer Society (Fraunhofer LBF, Darmstadt, Germany) contributed pathbreak-

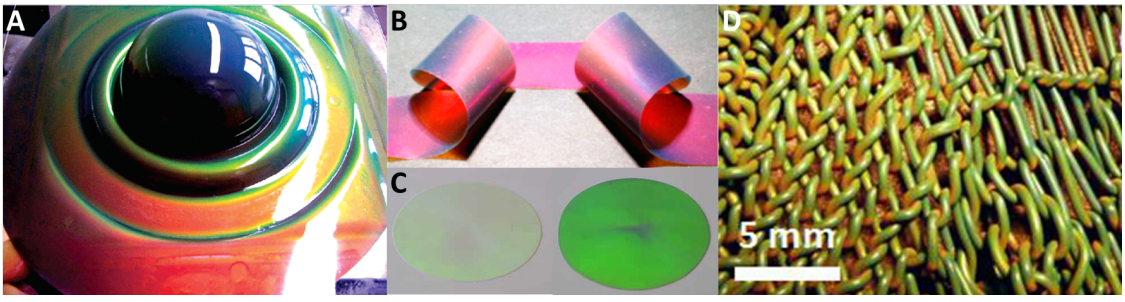

Figure 6.3: **State-of-the-art examples of polymer opals. A** Deep drawing of a polymer opal film reveals the different strain regions by the related stretch-dependent color. Adapted from [271]. **B** The photograph displays a part of a multimeter long film produced by extrusion, rolling, and edge-induced shearing of red polymer opal. The strand is 4 cm in width. Adapted from [272]. **C** The sample on the right is doped with 0.05 wt.% carbon black. It shows a drastically enhanced color intensity compared to the not doped sample on the left. The diameters of the samples are 10 cm. Adapted from [273]. **D** Polymer opal fibers were knitted into a fabric showing the stretch tunability of the perceived color. Adapted from [274].

ing work with their research on the fabrication of core-shell-interlayer (CIS) spheres building rubbery opals by step-wise emulsion polymerization.[275,276] In close collaboration with Prof. Baumberg from the Nanophotonics Centre they pioneered the production of highly monodisperse CIS-spheres, developed effective shearing mechanisms, and, over the years, advanced a great part of their techniques from batch to continuous processes.[241,263,271,273–284] Within the scope of my research stay in the University of Cambridge in 2016 I was able to contribute to the research on those polymer opals and benefit from the experience and knowledge of Prof. Baumberg. His group's work is shortly summarized in the following section because my in this chapter presented work is a direct continuation of their achievements. One of the main research interests of Prof. Baumberg's group is in the development and understanding of techniques to order the opal spheres into regular lattices. Since in polymer opals, the spheres are embedded in a viscoelastic matrix and there is no liquid involved whatsoever, self-assembly of the spheres cannot be witnessed. Snoswell and his colleagues studied the crystallization of polymer opals by dynamic shear ordering extensively and thereby facilitated a deep understanding of the developments of bulk ordering.[263] Based on this knowledge, the scientists around Baumberg and Ruhl successfully developed a shearing technique that uses bending-induced oscillatory shear (BIOS) to order CIS-spheres to intensely colored opals to upscale effective shearing to infinite films. Extruded thick PO films are sandwiched between two poly(ethylene terephthalate) (PET) sheets and bend over several cylinders at elevated temperature. The bending of this laminate around cylinders creates strong shear parallel to the surface which forces the spheres into fcc lattice arrangement.[277,285] Besides the fabrication of thin, ordered PO films, simple extrusion has great potential to produce ordered PO fibers. It was reported, that the extrusion parameters speed, temperature, and die nozzle diameter influence the degree of order in the produced PO strings to a great extent.[280] Generally, the higher and longer the material is subjected to pressure in the die, the better the ordering is. Stretching of polymer opals in the form of films or fibers causes the sphere in the plane parallel to the force vector to move apart whereas the planes' distances perpendicular to the stretching direction decreases due to the Poisson's effect. The latter causes the reflected color to shift to lower wavelengths. Additionally, the reflection peak broadens significantly as a result of a lattice transformation.[274] Typical color shifts in PO fibers have been reported to be in the range of -2.5 nm to -3 nm per 1% of strain as long as the strain does not exceed the elastic limit of approximately 50 %.[280]

6.2 Fabrication

The SMPO composite consist of two materials: the shape-memory polymer TFX and the opal spheres. While we used TFX as received (see Sec. 2.1) the opal spheres were synthesized by our colleagues at die DKZ. This process is summarized briefly in the following. Furthermore, this section describes the procedure of compounding the SMPOs in an extruder.

6.2.1 Emulsion Polymerization of CIS-Spheres

The pure polymer opal spheres for our study were produced in a stepwise emulsion polymerization yielding core-interlayer-shell (CIS) particles with polystyrene (PS) as core, poly(methyl methacrylate) (PMMA) as interlayer and poly(ethyl acrylate) (PEA) as shell. Emulsion polymerization is a variation of radical polymerization where the reaction is confined to the small volumes of micelles.[286,287] Thereby small polymer particles with narrow size distribution can be generated. An emulsifier causes the formation of monomer micelles in mostly aqueous solutions and a water soluble initiator starts subsequently the polymerization within the micelles. The particles grow with further monomers that diffuse through water to the micelles. The size of the resulting polymer particles is tailorable by the emulsifier concentration.

For the fabrication of our SMPOs we received pure polymer particles in various sizes from our cooperation partners from the DKZ. The particles were synthesized according to the process described by Ruhl and his colleagues.[275,276] The PS core was synthesized from styrene monomers, with sodium dodecylsulfate (0.3 wt.%) as emulsifier and ammo-

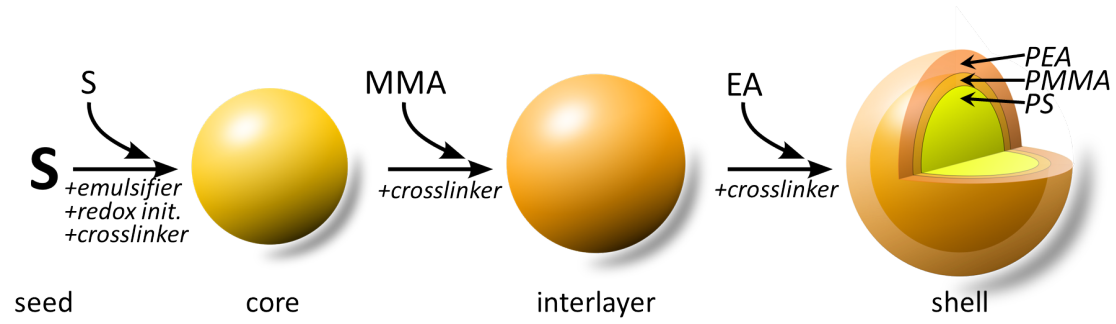

Figure 6.4: **Schematic of the fabrication of CIS-particles by emulsion polymerization.** Styrene monomers polymerize to PS around the seed (S) to the particle's core under addition of emulsifier, redox initiator and crosslinker. Afterwards, MMA crosslinks to the PS surface and polymerizes to build the interlayer. In the last step EA grafts with the help of a crosslinker to the PMMA surface building the soft PEA shell.

nium peroxidsulfate and sodium dithionite as redox initiator system in aqueous solution. Butylenediol diacrylate (10 wt.%) was used as crosslinker. A schematic of the process is given in **Figure 6.4**. The produced particles were coated with a PMMA interlayer by strongly crosslinking methyl methacrylate (MMA) with allyl methacrylate (ALMA, 10 wt.%) on the PS cores. Crosslinking is crucial here for achieving monodispersity as it prevents swelling by monomers in successional process steps. Subsequently, EA grafted to the allyl double bonds in the PMMA interlayer and formed the soft PEA shell. The fabricated CIS-particles range from 150 to 300 nm in diameter depending on the emulsifier concentration, while the composition of PS:PMMA:PEA of 2:1:3 in weight (or in terms of radii 69:10:21) remained constant. A dry, rubbery mass with PEA as continuous matrix resulted from coagulation of the latex. In dynamic light scattering measurements Ruhl *et al.* identified the particle size distribution of with this method produced CIS-spheres as 1.07. The average refractive index was determined to 1.51 by Ruhl *et al.* comprising a net relative refractive index contrast that is typically in the order of 7 %.[263,275] In this polymer opal systems, the soft shell polymer PEA builds a quasicontinuous viscoleastic matrix. In consequence, the spheres have no ability to self-assemble but have to be ordered through external forces.[263]

6.2.2 Extrusion and Ordering

For the generation of the production of functional polymer opals with an additional shape-memory effect we mixed the coagulated CIS spheres with the shape-memory polymer TFX (see Sec. 2.3.1). In order to ascertain a throughout good mixing of the PO mass and the SMP, we fed both materials simultaneously to an extruder. Besides PO and SMP, a small amount of less than 0.05 wt.% carbon black (CB) was added to the compound to absorb the secondary scattering inside the later SMPO material and therefore to intensify the specular, wavelength selective reflection.[241] An additive of CB as absorber is known to be able to increase the transmission contrast by a factor of >100.[241] The CB particles fill in the interstices of the lattice without affecting the lattice disorder due to the large size difference. PEA has a lower refractive index than PS/PMMA, hence, the PO matrix supports the optical modes with shorter wavelengths. However, since the CB is distributed only in this matrix, the short wavelength modes are absorbed therein whereas long wavelengths are considerably less absorbed by CB particles.

Figure 6.5 demonstrates the influence of the PO sphere diameter on the color of our SMPO compounds. While the dry coagulated latex of diverse particle sizes appear white with only a faint hue due to the light scattering at the utterly random arrangement of the

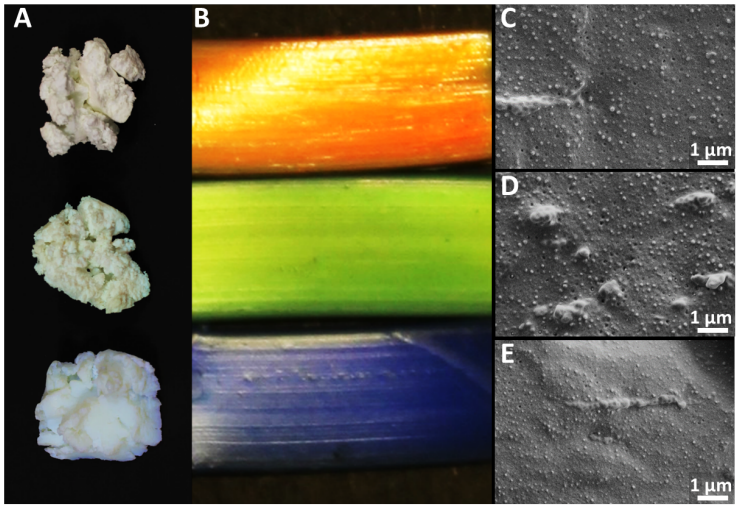

Figure 6.5: **Different PO particle sizes yield different SMPO colors. A** The coagulated latex of PO particles with different diameters shown in the photograph appear almost completely white due to their random arrangement. **B** Extruded strings of those POs with added carbon black and 15 wt% Tecoflex exhibit strong coloration with the decreasing particle sizes yielding a shift from red coloration (top), over green (middle) to blue (bottom). **C-E** SEM images reveal the different particle sizes generating the different colors red (C), green (D), and blue (E).

particles, the extruded and with 15 wt.% TFX and a pinch of CB mixed SMPO compound shows intense coloration as displayed in the photographs. The irregular arrangement of the PO particles in the SMPO compound is revealed by the given SEM pictures.

The extruder utilized for throughout mixing of various SMP to PO ratios consists of two counter rotating steel screws in a heatable chamber (see Sec. 2.3.2). The extruder needs an amount of at least 10 g of feed materials to ensure proper function. The rotation speed of the screws are adjustable from 1 to 250 rpm and the temperature can be elevated up to 250 °C. Granules of TFX and the PO precursor were simultaneously, manually fed to the extruder that was preheated to 170 °C. The screws were set at a rotation speed of 20 rpm . While extruding at the denoted temperature, the rubbery shells of the PO spheres softened to being close to liquid and the TFX granules were molten, too. The extreme shear forces provided by the rotating screws combined the two melts to a composite.[280] To guarantee excellent mixing the produced strings were fed a second and a third time to the extruder. When the SMPO material exits the extruder through the die the sudden pressure drop causes the still hot material to swell. This swelling is related to the viscoelastic nature of polymer melt and driven by entropic and relaxation forces within the polymer chains. Therefore, it can be controlled by the extrusion flow rate as well as temperature profile and length of the land.[96,97] While under compression in land and die the PO spheres align into crystal lattices. This order gets partly lost with the swelling and expansion of

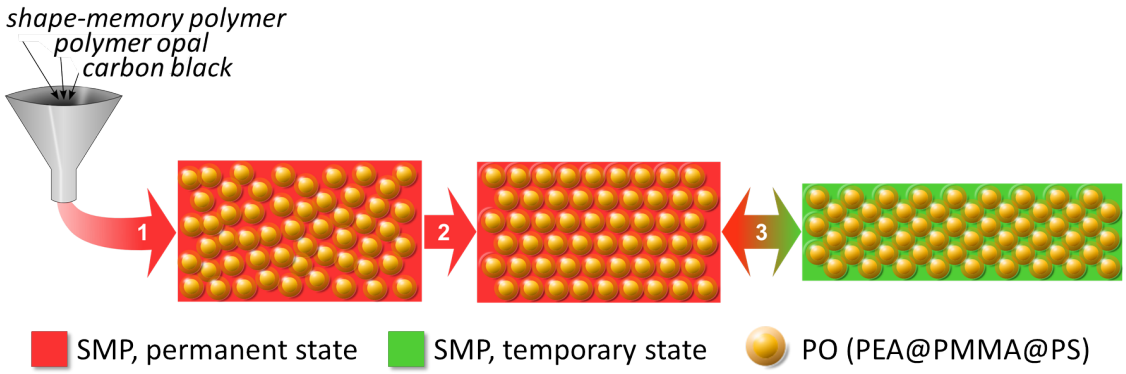

Figure 6.6: **Schematic of the SMPO extrusion process, shearing, and stretch induced color change.** Shape-memory polymer and coagulated polymer opal particles in various weight ratios are fed with a pinch of carbon black to an extruder (*1*) and blend above the SMP's melting temperature. The result is a string with scarcely ordered PO particles in a matrix of SMP in its permanent state. Shearing (*2*) increases the order of PO particles and thereby enhances the color. By stretching (*3*) or compressing the SMP is transferred into its temporary state and the spacing between those ordered particles is influenced yielding a color change. Subsequent heating reverses the shape transformation attended with the shape-coupled color change.

the polymer strand after exiting the die. Especially pronounced is this order loss with high extrusion flow rates as illustrated in process step *(1)* of **Figure 6.6**. To increase the order of the PO beads in the SMP matrix, the extrusion process was followed by an ordering step (Fig. 6.6 *(2)*). Ordering of the PO beads can be accomplished by different methods.[263,277,288] For producing thin ordered films we used the well-proven method of shearing the compound over a hot, sharp edge.[280] Therefore, we placed a SMPO strand between two PET sheets and first spread it between those sheets into a foil under a heavy quartz roller on a hot plate heated to 150 °C. Subsequently, the PET-SMPO-PET sandwich is placed on a hot, sharp brass edge and held in place by two roles adjacent to the brass triangle. The metallic hot-edge features an apex angle of 90 ° and a radius curvature of less then 10 μm. This ordering mechanism is known to yield face centered cubic (fcc)-lattice arrangement of pure POs.[280] Furthermore, an increased degree of order in the PO spheres alignment can also be achieved by compressing the SMPO film between two hot plates, e.g., in a hot embossing machine (see Sec. 2.3.2). In this case, the samples' geometries are not limited to foil dimensions.

Color change of SMPO devices is induced by changing the arrangements and thereby distance between the PO spheres in the SMPO compound, for instance by stretching the devices in a tensile testing machine (see Chap. 2.3.2) as depicted in Fig. 6.6, step *(3)*. **Figure 6.7** shows the feed materials carbon black (A, top), PO coagulation with spheres of according diameter for red opals (A, middle), and Tecoflex granules (A, bottom) and

Figure 6.7: **Materials and products at different stages of the fabrication process. A** A small amount of carbon black (top) is extruded with coagulated PO particles (middle) and TFX granules (bottom) in various weight ratios (here 15 wt%) to colorful strings with a 5×1 mm^2 profile (**B**). The compound is spread between two PET-sheets (**C**) and subsequently sheared over a hot edge to order the PO particles and enhance the color (**D**).

an exemplary extruded SMPO strand (B). Additionally, the photograph shows a SMPO strand spread between two PET sheets before (C) and an identical strand after shearing over the hot edge (D).

6.3 Results and Discussion

In our experimental investigation of the SMPOs we focused primarily on examination of the influence of the percentage of added SMP on the composites' shape-memory ability as well as on the optical appearance, SMP distribution in the PO matrix, and mechanical properties. The results of these experiments are discussed in the following sections. Furthermore, we tested the SMPO's capability to induce a color change by a temporary shape change through stretching and compression.

6.3.1 Analysis of the SMPO Composite Structure

In order to explore the influence of the SMP additive on the POs' mechanical behavior and shape memory ability I produced seven different composites with a percentage of TFX in the SMPO of 0, 5, 10, 15, 20, 25, and 50 %. In the following it is referred to those mixtures as PO, SMPO5, SMPO10, SMPO15, SMPO20, SMPO25, and SMPO50,

respectively. Strings as extruded of all seven composites are depicted in the left column of **Figure 6.8** from 0 % at the top to 50 % at the bottom of the photograph. The PO sample features an intense red/orange color whereas with increasing TFX percentage, the color becomes more dull and shifts from red to more and more brown shades. The seven composites as spread between two PET sheets are shown, too. The middle column of the photograph in Fig. 6.8 demonstrates, that the same relation of color brightness to material ratio applies here. Ordering of the PET-SMPO-PET tri-layer over the hot edge intensified the colors of all seven samples as presented in the figure's right column. Not sheared and sheared films were photographed in one picture. Thus, they are displayed in the ecaxt same viewing angle and the difference between low and high TFX percentages in the composites becomes even more distinct. We conclude, that for SMPO20 and larger TFX/PO ratios the coloration significantly suffers from the additional material in the matrix, whereas SMPOs with less added TFX exhibit sufficient color performance.

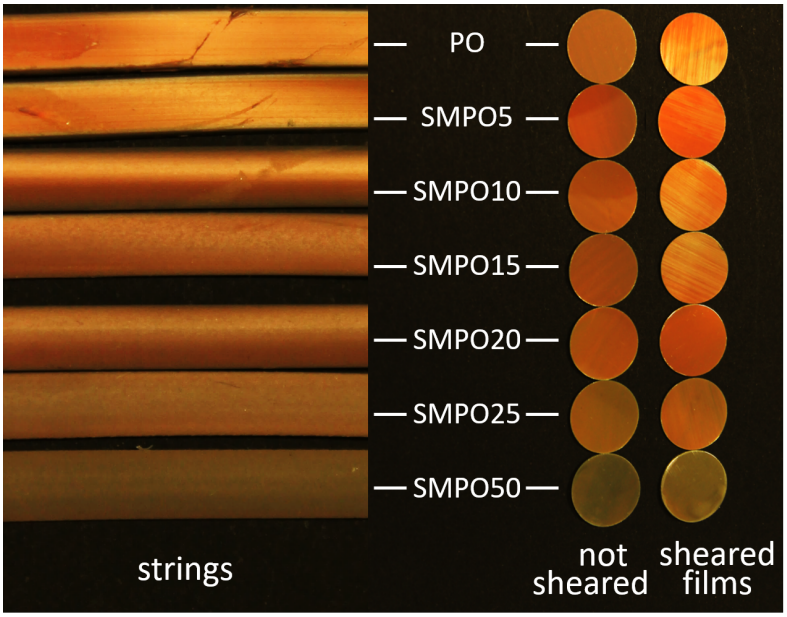

Figure 6.8: **Influence of PO:SMP ratio on optical appearance.** With increasing percentage of SMP in the SMPO compound the color of the extruded string changes from bright red/orange to a dull brownish orange. Although the color is more intense, the same trend is visible in the photograph of cutouts of the strings spread between PET sheets before and after shearing.

In the course of understanding the effect of TFX in the SMPO matrix on the PO sphere arrangement, I used the PeakForce QNM mode of our AFM to map the SMP's distribution. PeakForce QNM allows quantitative characterization of mechanical properties of a sample on nanometer scales (see Sec. 2.3.4). Here, our AFM was not calibrated to measure the actual Young's modulus of the samples quantitatively but we can compare the

adhesion and deformation mappings of our SMPOs as long as we use the same tip and parameters. **Figure 6.9** shows those measurements with the examples of PO, SMPO15 and SMPO50. The scans were performed on $5 \times 5\mu m^2$ areas on the fracture surface of in liquid nitrogen frozen and then broken, not ordered SMPO strings. With 512 samples per line on this area one adhesion and deformation measurement was conducted roughly every 10 nm. In Fig. 6.9 A the topography of the three examples can be seen while B shows the adhesion measurements and in C the sample deformation is displayed. Mea-

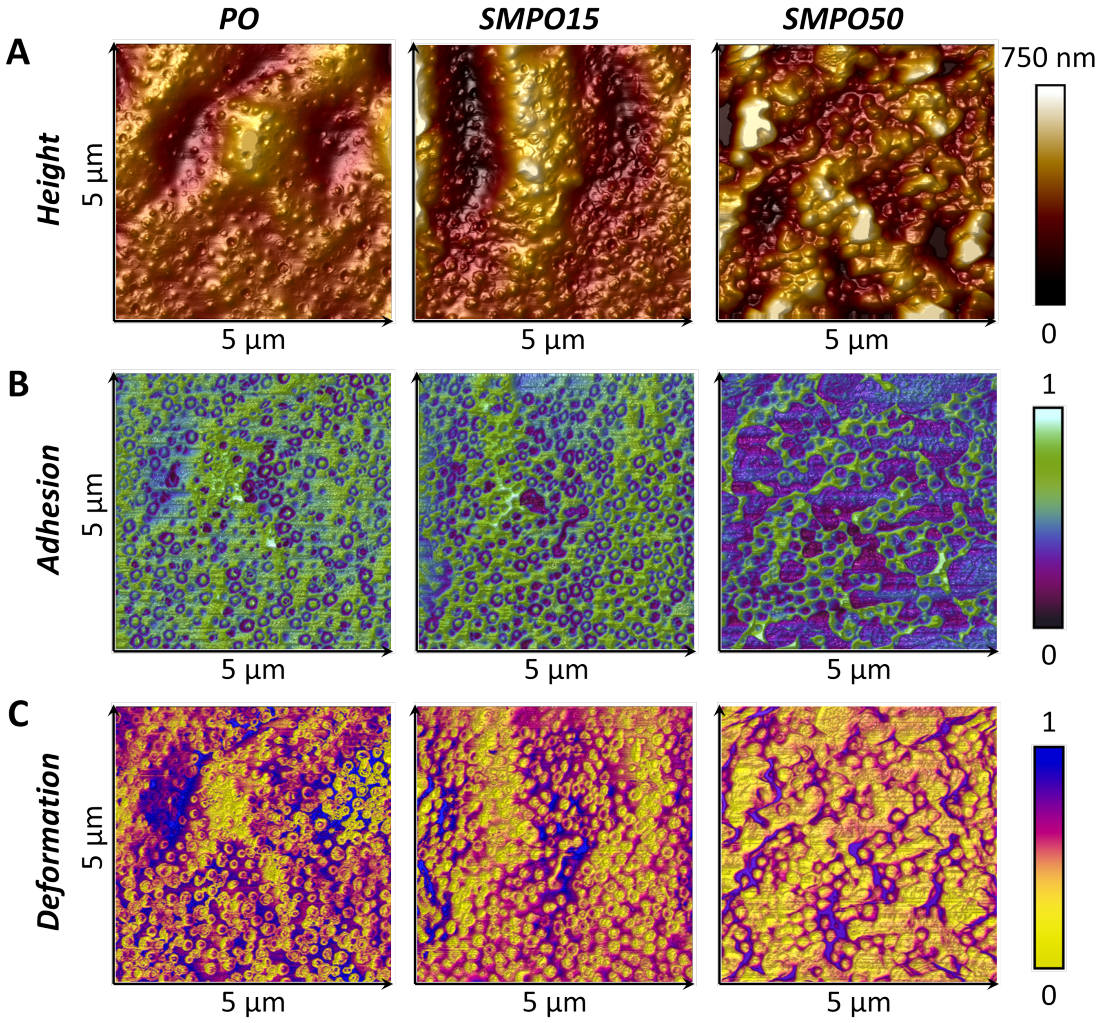

Figure 6.9: **PeakForce QNM of PO and SMPO samples.** The figure shows the results of the nanomechanical properties mapping with AFM of a sample containing only PO in the left column, the graphs in the second column belong to a SMPO15 sample, and the measurements on a SMPO50 sample are shown in the right column. **A** The height profiles show the topographies of the samples. **B** Normalized adhesion measurements reveal the different mechanical properties of the composite materials. **C** The normalized deformation mapping gives spatially resolved information about each composite's hardness.

surement of the PO sample are shown in the left column, the middle column represents the SMPO15 sample and in the right column the results of the SMPO50 sample are included. Since the AFM was not sufficiently calibrated for the QNM mode, all images (except the height graphs) are normalized to maximal and minimal values to get the optimal contrast and comparability. Additionally, it is worth mentioning that the Young's modulus of PS, PMMA and TFX are very similar and we only expect a significant differentiation of those polymers to PEA. Literature values for the Young's moduli are for PS $E_{\mathrm{PS}} = 3.1 - 3.3\,\mathrm{GPa}$, PMMA is characterized with $E_{\mathrm{PMMA}} = 3.1 - 3.3\,\mathrm{GPa}$, and we measured for TFX $E_{\mathrm{TFX}} = 2.8\,\mathrm{GPa}$.[88] While the plots of the sample's height profiles look very similar on all three images displayed in Fig. 6.9 A and cannot reveal the differences of composition and joining of the SMPO, the adhesion measurements reveal more information about the samples' textures. The PO graph shows predominantly high adhesive zones correlating to the PO's soft PEA matrix as indicated by the green color. The low adhesion areas related to the stiffer materials such as TFX become slightly more present in the SMPO15 plot and very dominant in the SMPO50 image. Here, it is very prominent that TFX is not homogeneously distributed within the PEA matrix but rather arrange in segregated islands (blue areas). The exact same trend of increasing dominance of the stiff materials with increasing SMP percentage represented by yellow can be witnessed in the deformations plots in Fig. 6.9. To a very small extent the topography seen in the corresponding height images is reflected by the adhesion and deformation maps due to the topography dependent contact area and angle of AFM tip to surface.

6.3.2 Shape-Memory Ability of SMPOs

The aim of this investigation is to develop a material composite, that enables static change and on demand tuning of structural color through the material's shape-memory ability. Therefore, I determined two representative values that characterize the shape-memory effect for all six SMPO composites: the shape fixity ratio R_{f} and the shape recovery ratio R_{r}. The shape fixity ratio describes the efficiency of a SMP to uphold the programmed deformation when the external force is released. The shape recovery ratio characterizes the performance of the SMP regarding its capability to recover its original, permanent shape after being deformed.[18,21,27,35] The conventional method to determine both values is by conducting at least one complete programming and recovery cycle where a sample strip is stretched, fixed, released, and recovered in a temperature, strain, and stress controlled process. **Figure 6.10** schematically describes this procedure. A sample strip with the initial strain ε_0 is in step (1) stretched with a defined velocity at a constant programming

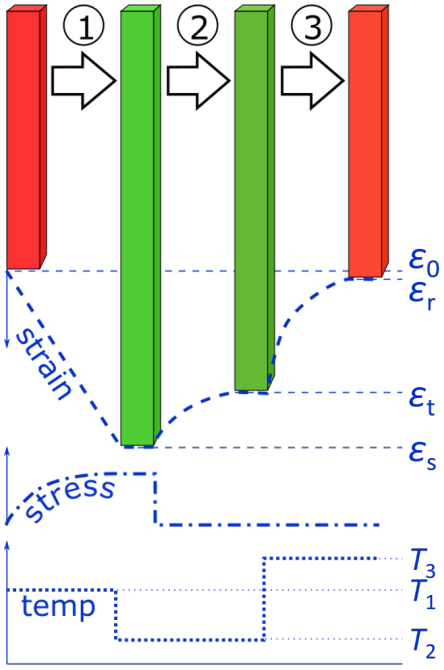

Figure 6.10: **Programming and recovery cycle to determine R_f and R_r.** The strain, stress and temperature profiles describe one cycle of the procedure, including stretching (1), evolving of the temporary shape (2), and recovering (3), that is used to measure the shape fixity rate and the shape recovery rate.

temperature T_1. When the final strain ε_s is attained, the sample is cooled down to T_2 to fix this shape and subsequently the stress, that built up during stretching, is released in step (2). Hereupon the sample contracts due to the elastic part of the imposed deformation to a time dependent value ε_t. The sample is now in its temporary state. To recover the permanent shape in step (3) the sample is heated to its switching temperature T_3 by what it contracts until it reached a final strain value of the recovered shape ε_r. From those values of the strain ε after each process step the shape fixity R_f and recovery ratio R_r of the first programming cycle are calculated according to the following equations:

$$R_f(t,T) = \frac{\varepsilon_t(t,T)}{\varepsilon_s}, \tag{6.1}$$

$$R_r(t,T) = \frac{\varepsilon_s - \varepsilon_r(t,T)}{\varepsilon_s}. \tag{6.2}$$

The color change correlated to SMPO composites undergoing this procedure is exemplified by re-enacting the cycle of stretching and free recovery of a SMPO15 strip documented by the photographs displayed in **Figure 6.11**. The result of the programming is shown in Fig. 6.11 A. A $3 \times 1 \times 40\,\mathrm{mm}^3$ strip of red SMPO15 is gradually stretched to 50 % and after every 10 % of stretching a photograph captures the color change. The original sample (0 % stretching) exhibits an intense coral red color that shifts over orange ($\varepsilon = 10\,\%$) to various shades of green and olive ($> \varepsilon = 20\,\%$). The color brilliance di-

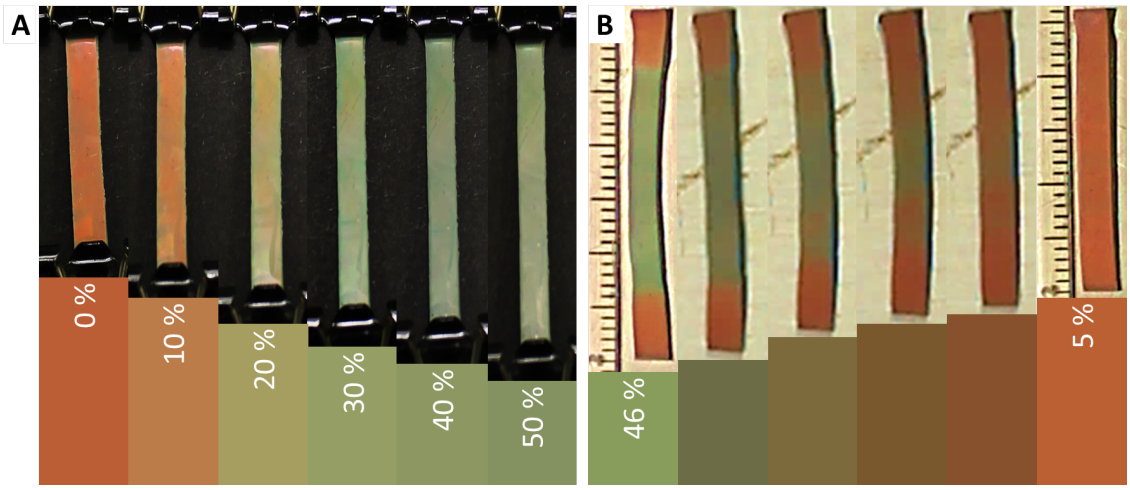

Figure 6.11: **Demonstration of the color change coupled with programming and recovering strain of the SMPO. A** A SMPO15 string is stretched step wise to 50 % whereby its color changed from red to green. **B** After releasing the load the string is stable in the programmed shape and color. When heated above T_{switch} the sample gradually recovers its original shape and color.

minishes with increasing strain due to loss of order of the PO spheres in strain direction. Programming was conducted at room temperature of 21 °C. After releasing the clamps, the sample was put on a 60 °C hot plate. This exposure to heat triggered the recovery of the initial shape as is shown by the photographs shown in Fig. 6.11 B. The photographs document the recovery progress in 5 s intervals. The color of the stretched middle part of the strip is tuned from green back to red as the sample recovers its original length. In order to determine the shape fixity and recovery ratios of all six prepared SMPO composites, I performed in each case a dynamic mechanical analysis (see Sec. 2.3.3). The results of those measurements are shown in the two graphs of **Figure 6.12**. The strain curves (A) and the corresponding stresses (B) of all samples are displayed as a function of time and the temperature profile of the process is given. To program the temporary shape, all samples were stretched with a velocity of 2.5 % per minute until a strain of $\varepsilon_s = 50\,\%$ is achieved. During the stretching process the temperature was kept constant at $T_1 = 40\,°C$ and afterwards decreased to $T_2 = 20\,°C$. Evidently, the SMP:PO ratio strongly influences the stiffness of the individual composites as revealed by the stress curves in Fig 6.12 B. Although those measurements were not conducted at standard conditions, so that the measurement is not valid to determine the Young's modulus of the composites, the stress results offer valuable clues to the differences in the materials' mechanical properties. The force needed to deform the sample increases drastically with increasing SMP percentage. After 5 min at $T_2 = 20\,°C$ and $\varepsilon_s = 50\,\%$ the load was released and regulated to 0.01 MPa

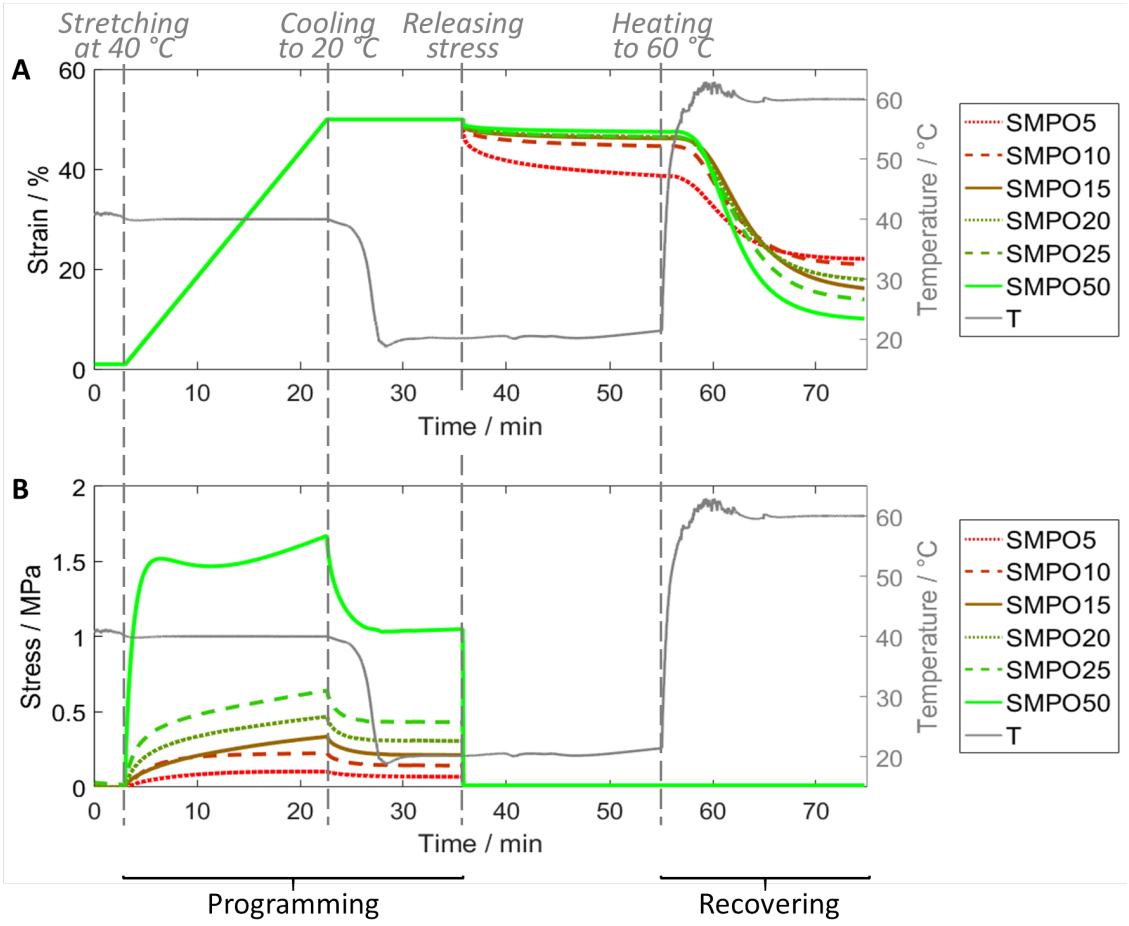

Figure 6.12: **Dynamic mechanical analysis of the shape memory abilities of various SMPO composites.** Strain (**A**) and stress (**B**) as well as the process temperature T during the DMA cycle are shown for seven SMP:PO ratios. At the programming temperature the samples are stretched to 50 % and cooled to room temperature to fix the shape. After a short relaxation time the stress is released and the elastic part of the deformation contracts in dependence of the SMPO mixture. For the recovery, the temperature is risen to the recovery temperature and in correlation to their shape memory ability the samples contract.

and all samples were allowed to relax under these conditions for 20 min. Depending on their SMP content, the samples contracted gradually to their eventual temporary shape due to the polymers viscoelastic nature. Up to 15 % TFX content, the different amounts of SMP in the rubbery PO matrix yield significantly different relaxation behaviors. The higher the SMP percentage, the better the sample was able to maintain in the programmed shape. Above a percentage of 15 % no distinct differentiation of the relaxation behavior is noticeable. In the last step, the temperature was increased to $T_3 = 60\,^{\circ}\mathrm{C}$ to trigger the shape recovery and held isothermal for additional 20 min to allow the samples to fully relax into their recovered shape. As for the fixation of the temporary shape, the amount

of SMP in the composite significantly influences the recovery behavior. The higher the TFX content the more capable the composite is to recover the original sample length. The values for ε_t and ε_r are each extracted at the end of the 20 min relaxation periods and used to calculate the shape fixity and recovery ratios of each composite as summarized by **Table 6.1**.

Table 6.1: Shape fixity ratio and shape recovery ratio for various SMP:PO ratios.

	SMPO5	SMPO10	SMPO15	SMPO20	SMPO25	SMPO50
R_f	0.77	0.89	0.92	0.93	0.93	0.95
R_f	0.56	0.58	0.68	0.64	0.72	0.80

We conclude from the mechanical testing of our six different SMPO ratios, that with 15 % SMP in the SMPO composite we achieve the best combination of color intensity and shape fixity plus recovery ability. Thus, we used the SMPO15 composite for the proof of concept of on demand color- and shape-tunable imprinted structures. For other applications the most suitable color/shape-memory effect trade-off might be different.

6.3.3 Compression Induced Color Change on Demand

As previously described in the introduction to this chapter, we aim to prove the concept of employing SMPOs to enable color tuning on demand by compression on laterally fixed substrates. This compression and the accompanied color change can be achieved by embossing patterns on SMPO foils. Throughout this thesis hot embossing is used to structure the surface of diverse samples. However, for hot embossing of our SMPOs it has to be taken care of some issues. The DMA measurements of the various composites showed, that the shape-fixing ratio of the SMPO15 composite (that will be utilized here, too) is inferior to high SMP percentage SMPOs or pure SMP. Hence, the selected mold needs to have a sufficiently larger structure depth that what is required in structure height of the result. Furthermore, we want to impose the shape change as the temporary shape which defined us the temperature process window to T_switch. On account of this, the composite is fairly viscous and high pressure needs to be applied for proper structuring. Compared to pure SMP the SMPO is much softer, though. Sharp edges of structures easily cut into the material and the shape-memory effect of the added SMP in the matrix is not able to reverse such damages. Regarding the structure size, the sphere size has to be considered and we wanted to observe the color change through compression on definite areas. On these grounds we choose a structure with millimeter sized features

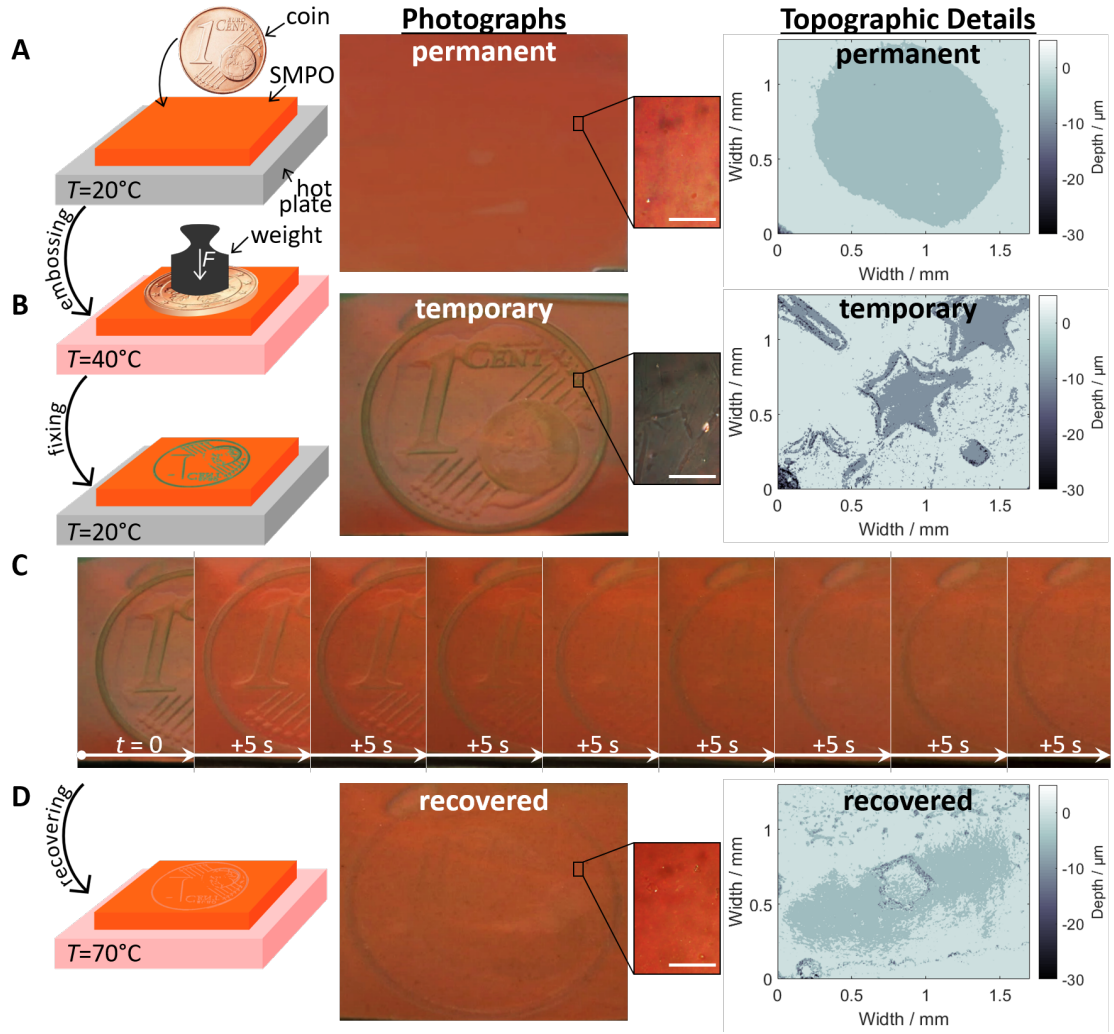

Figure 6.13: **Color change on demand of temporarily imprinted structures.** The left column depicts the procedure schematically, the middle column shows photographs of the respective samples with close ups (scale bars 10 µm), and topographic details of the respective structures are given in the right column. **A** The surface of a SMPO15 sample in its permanent shape shows a smooth surface and uniform red/orange color. **B** The face of an 1 Euro-Cent coin is pressed at elevated temperature into the sample's surface. The topography of the coin is well replicated. Compression of the material result in a color change from red to green. **C** The sample is heated to the SMP's switching temperature whereupon the original shape recovers and the coin's indentation fades as revealed by the color change. **D** The original shape is almost completely recovered with only slight residual marks of the coin structure.

in lateral dimension and a feature height of less than one millimeter with rather round edges that we found in the topography of an one Euro-Cent coin. First, extruded, red SMPO15 strings were molded between PET-sheets into a $25 \times 25 \times 2\,\mathrm{mm}^3$ substrate with a smooth surface. **Figure 6.13** A shows this substrate with a photograph (middle) and a microscope picture (middle), and a vertical scanning interferometer (VSI) image (right). The surface is smooth with an uniform red-orange color. In this substrate, we imprinted the structure of the face of an one Euro-Cent coin at 40 °C substrate and coin temperature as it is illustrated by the schematic depiction on the left. This yielded a color change in the areas where the coin's bulges indented the substrate and therefore compressed the SMPO composite. Figure 6.13 B pictures the generated image of the coin (photograph is mirrored). The microscope picture illustrates the distinct color change from red to green at the structure's cavities and the correlated structure depth is indicated in the VSI plot. Indentations of 10 to 20 µm are responsible for the color change. To tune the color and structure back to the initial, smooth and red surface, we increased the sample's temperature on a hot plate to 70 °C and captured the recovery process in photographs taken every 5 s. The evolution of the recovery is displayed in Fig. 6.13 C. By the series of photographs the gradual disappearance of the coin image is revealed. The green indentations become more shallow with continuing recovery process and the color changes gradually back to red. After exposing the sample for a total of 1 min to the heat, the resulting color and structure are documented in Fig. 6.13 D. Although a faint residual structure and color change is noticeable, the coin image largely vanished. Those results demonstrate, that because of the SME of the composite color changes on large scales can be imprinted by spatially resolved compression.

Those results demonstrate, that the composite's SMP content enables imprinting of color changes due to spatially resolved compression on large scales.

6.4 Conclusion and Outlook

By implementing a certain amount of SMP into the matrix of state-of-the-art polymer opal we successfully disposed of the need of external forces to uphold an imposed deformation that is coupled to a color change. Polymer opal precursors received from our cooperation partners were compound in different ratios to the SMP TFX in an extruder. We found the best compromise of mechanical properties, shape-memory ability and optical impression for our purposes in a mixture of 15 wt.% TFX. Up to 15 % TFX content little deviation to the bright color of pure POs was observable. QNM measurements of three different SMPOs verified the homogeneous distribution of TFX in within the PO's PEA matrix.

To analyze the shape-memory performance in dependence of the added amount of SMP I performed DMA measurements for each composite. Samples above 15 % TFX in the material did not increase the shape fixity ratio significantly. Contents below 15 % TFX exhibited poor recovery ratios below 0.6. The shape-coupled color tuning without the necessity of a constant external load was demonstrated by stretching and subsequent free recovery of a SMPO15 strand. Moreover, compression as a possible method to achieve quasi-stable color changes was confirmed, too. The combination of the optical properties of opals with the thermo-mechanical property of SMPs to remain in a certain shape until triggered externally and then shifting back to an original shape allows a controlled and continuous color tuning. This feature, in turn, leads to numerous potential applications. Previous experiments of our institute showed, that absorption of UV light in a

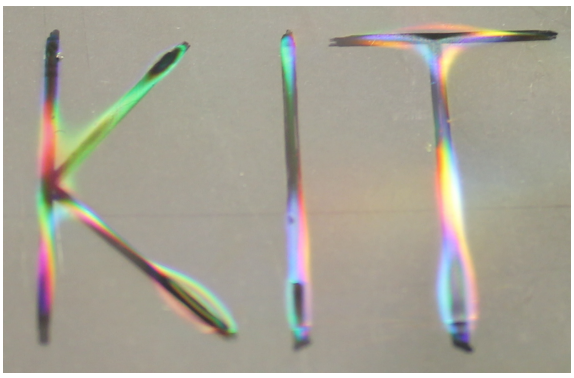

Figure 6.14: **Spatially resolved recovery due to light absorption.** An on TFX embossed periodic grating with micrometer period was first temporarily flattened. Subsequently, the sample was exposed to intense UV radiation whereupon in the black pigment enough heat was produced to trigger the recovery process in those areas. The recovered grating causes the visible rainbow iridescence.

black absorber layer generated enough heat to trigger the shape recovery in a temporarily deformed TFX sample.[115,289] **Figure 6.14** demonstrates spatially resolved recovery by light absorption. Since SMPOs contain a certain amount of highly absorbing carbon black, we think this triggering concept can be transferred to SMPOs. In contrast to the given example, not the pattern absorbing pigments could be the factor for spatially resolved recovery but the incident light. Beforehand compressed SMPO sheets might be attached to a rigid surface and with a laser pointer the desired color change is then triggered to display the favored image or writing.

A shortened version of this chapter is in submission at Advanced Materials as the article "Tuning of Structural Colors like a Chameleon enabled by Shape-Memory Polymers", by Senta Schauer, Jeremy J. Baumberg, Hendrik Hölscher, and Stoyan Smoukov (September 2017). Jeremy J. Baumberg supervised and provided me with the opal materials and lab equipment for the fabrication of the composites. I conducted the mechanical analysis of the materials in Stoyan Smoukov's lab facilities at University of Cambridge.

7 Summary and Outlook

In compliance with the aim of this work diverse tunable photonic structures made of shape-memory polymers were developed and fabrication routes investigated. Besides examining classical applications of micro- and nano-structures in optics such as diffractive optical elements and laser resonators, I mimicked diverse principles found in nature to produce structural colors. For this purpose three concepts to apply the shape-memory effect of the utilized polymer either to tune or to produce optical structures have been devised and realized. Potential applications of structural colors reach far beyond biomimicry. For each of my approaches the main findings are summarized in the following paragraphs.

Tunable Organic Distributed Feedback Lasers. After successful utilization of the shape-memory polymer to develop tunable refractive and diffractive optical elements on the macro and micro scale, respectively, we advanced this approach to sub-micron structures. A Bragg grating was embossed into a shape-memory polymer substrate which then served as a tunable and adjustable resonator for a distributed feedback laser with Alq_3:DCM as the organic, laser active material. Wide tunability of the emission spectrum is enabled by heating the pre-stretched resonator by what the grating's period decreases to its original value. The suitability of the used shape-memory polymer TFX for this application was experimentally verified by measuring an over time in peak wavelength stable performance and a low lasing threshold of 150 µJ/cm^2 with our device. We were able to achieve a continuous tuning of our laser's emission wavelength by 30 nm and additionally demonstrated, how the shape-memory effect of our polymer allows us to interrupt the wavelength shift at will at any point as long as demanded. The fact that no mechanical framework is needed for tuning reduces the device's dimensions considerably which is especially interesting for applications in medical products designed for one-time usage where the need of reduced volume and cost is more important than the potential of for- and backward tuning of the wavelength. Hence, implementation of our tunable laser for, e.g., lab-on-chip spectrometers is suggested.

Tunable Fabry-Pérot Interferometer. The first example of the presented bioinspired mechanisms is designed to realize tunable structural colors based on thin film interference such as those found in some cephalopod species. Therefore, a shape-memory polymer was processed in a way that allows tuning of the interference conditions of the developed Fabry-Pérot interferometer. A fabrication procedure was developed to generate polymer thin films with shape-memory effect from solution that are framed by two silver layers. From the smooth surface of the permanent shapes the devices were transferred into nanostructured, two-level, temporary states by imprinting pillar structures. By increasing the temperature of the temporary structures the devices recover their original, one-level structures. This shape transformation entailed a change in the reflected spectra and, hence, in the perceived color of the device from red in the temporary state to green in the permanent state. Further development of the device might comprise the utilization of electrostatic forces to restructure the temporary shape and, therefore, allow for two-way shape and color change. With applying my color changing principle to individual pixels and implementing this reversible tuning mechanism, I invented a new route to full-color, passive displays that only consume energy for switching.

Surface Wrinkles. In order to mimic formation and architecture of sophisticated, often hierarchical structures found on various petals I developed a versatile fabrication process based on wrinkling of a polymer film supported by a shape-memory polymer substrate. The method allows to produce diffractive gratings with a specific irregularity that is crucial for efficient light-harvesting as it lowers front and back reflection and redirects the propagation of light. In-depth investigation of the correlation between fabrication parameters and result of this simple yet elegant technique enables adjusting of the structures' periods from 400 nm up to 15 µm with aspect ratios up to 0.5. By applying a thermoplastic as coating I can further tailor the created structure to various hierarchical architectures through hot embossing. Moreover, the shape-memory polymer substrate provides the possibility to induce wrinkling of a coating on top of a predefined structure. Three exemplary combinations of wrinkling and embossing demonstrate the versatility of this advancement. Wrinkling of an embossed periodic grating to mimic tulip topographies yields hierarchical structures with effective beam shaping properties. Wrinkling of a metallic coating on the side walls of acute-angled triangular gratings produce promising architectures for highly anti-reflective structures as seen on treasure flower petals. Finally, temporary hot pulling of high aspect-ratio pillars allows wrinkling on vertical faces which might be an auspicious, innovative technique to achieve *Morpho*-mimicking structural coloration in a highly scalable, cost-effective fabrication. In the optical characterization

of the plain wrinkle structures we proved that, besides displaying vivid iridescence, the structure's irregularity benefits the light in-coupling on c-Si solar cells immensely as they significantly decrease reflectance by roughly 50 % over the whole investigated angle of incidence range compared to a perfectly periodic grating. Together with low back reflection this leads to an increase in the cell's efficiency by almost 5 %. Besides the further investigation of the beneficial use of surface wrinkles for photovoltaics, especially the hierarchical structures are promising for optical applications. Efficient light redistribution properties observed with the tulip type structure has potential for various beam shaping applications and the treasure flower structure with its sub-micron wrinkle coating on top of a large aspect ratio prismatic grating might be an ideal candidate for anti-reflective, light-harvesting coatings. Further development on the wrinkled pillar structures might advance them to color producing structures such as found on butterfly wings.

Shape-Memory Polymer Opals. The third approach to bioinspired photonic structures addresses the color tunability by changing the sphere spacing in a three-dimensional photonic crystal. Hard polymer spheres embedded in a soft elastomer matrix arranged in an opal structure required up to now external forces to achieve a color change by stretch-tuning. We overcame this detriment by adding a shape-memory polymer to this composite that is able to support the imposed deformation. An experimental study of the mechanical properties in dependence of the shape-memory polymer content revealed that a proportion as little as 15 % shape-memory polymer in the matrix is sufficient to stabilize the temporary shape and gain good recovery performance. The advanced functionality of the shape-memory polymer opals allows now tuning of the color not only by stretching but also by compression which enables us to emboss shape-coupled color changes. Further advancements can be achieved by using spatially resolved absorption of high energy radiation to initialize the recovery process in a temporarily deformed sample locally and inscribe a desired image.

Acknowledgement

Writing this thesis would not have been possible for me without the continuous, substantial support and contribution of numerous people. Without their encouragement I would not have been able to start let alone finish my PhD journey.

First of all, I would like to express my gratitude to my supervisor PD Dr. Hendrik Hölscher, who first gave me the opportunity to start my PhD project and then guided me with open mind and helping hands through those exciting years. He managed to subtly direct me while giving me plenty of room to grow and develop and taught me way more than it is captured on the pages of this thesis. With patience and courtesy he endured my excited, nervous, defiant, and distressed moments and motivated me to go beyond my limits.

Furthermore, I want to thank Prof. Dr. Manfred Kohl for his scientific and personal support and advice during this time. In addition, I thank Prof. Dr. Aránzazu del Campo Bécares for taking the effort to be my co-referee.

In the course of the last three years I also experienced continuous support from Prof. Dr. Uli Lemmer, who played an essential role in enabling me to start my PhD project, and PD Dr. Matthias Worgull, who always had an open door for scientific questions and all other sorts of concerns. A big thank-you to both of them.

Special thanks is due to the Karlsruhe House of Young Scientists (KHYS) that allowed me to experience two research stays abroad that yielded invaluable, amazing adventures. From the University of Cambridge, UK, I want to thank Dr. Stoyan Smoukov for welcoming me in his group as well as Prof. Dr. Jeremy J. Baumberg for facilitating my research. Special thanks also to I-Ting Lin and David Snoswell and all other members of both groups for helping me in any possible way and making my time in Cambridge extraordinarily rememberable. Secondly, I thank Prof. Dr. Diana Skigin from the University of Buenos Aires, Argentina, for her support of a promising start of future collaborations.

I owe a very big thank-you to my students Johanna Wolf, Marius Schmidt, and Qihao Jin who contributed with their experimental results, creative input, and stimulating discussions to the success of my work. Special thanks also to my colleagues from the LTI, mainly Xin Liu, Raphael Schmager and Dr. Guillaume Gomard and his team for the joyful collaborations. Additionally, I would like to thank the whole IMT staff. Just to name a few: Markus Guttmann, Andreas Bacher, and Stefan Hengsbach for the fabrication of my molds, Alexandra Moritz and her team for the help in the workshop, Marc Schneider and Alexander Kolew for their endless, hands-on support for hot embossing and many other techniques, Holger Moritz, Dieter Maas, Siegfried Roth, Uschi Rothweiler, Herr and Frau Klein, and Nina Giraud for helping me with all the non-scientific hassles that come with the job, and all that I might have forgotten to mention.

It is a very special pleasure for me to thank the many ~~colleagues~~ friends who, everyone in his very own way, made my time at the IMT an unforgettable, enjoyable experience: Norbert Schneider, who became much more than the best dress shopping companion because of synergy. Felix Vüllers, who nevertheless was the best ally in our everyday struggles, many during work and fewer afterwards. Radwanul H. Siddique, who taught me how to catch butterflies. Andreas Striegel, who still tries to make our mob somehow more classy. Richard Thelen, who had my back in every possible way and showed me that age is no valid reason to grow up. An additional huge thank-you to these guys for proof-reading my thesis over and over again. Many thanks also to Maryna Kavalenka for her enduring heartiness, Michael Röhrig for sparking the idea of doing a PhD at IMT, and Tobias Meier for giving me the last necessary push to actually do it. Lastly, I would like to thank all my fellow PhD students/post docs for their fruitful discussions, professional and unprofessional support, and extracurricular company: Randy, Frederik, Bastian, Tobias, Hinnerk, Marcel, Tobias, Frieder, Sebastian, Clemens, Julia, Christian, Sebastian, Ruben, Benjamin, and many more.

Finally, I cannot express with words my gratitude to my friends and family, especially my mother and my father: For believing in me, for their unlimited, loving support, for encouraging me to shoot for the stars.

List of Publications

Articles

- **Senta Schauer**, Xin Liu, Matthias Worgull, Uli Lemmer, Hendrik Hölscher. *Shape-Memory Polymers as Flexible Substrates for Continuously Tunable Organic DFB Lasers*, Optical Materials Express, **5**, 576-584 (2015)

- **Senta Schauer**, Tobias Meier, Maximilian Reinhard, Michael Röhrig, Marc Schneider, Markus Heilig, Alexander Kolew, Matthias Worgull, and Hendrik Hölscher. *Tunable Diffractive Optical Elements Based on Shape-Memory Polymers Fabricated via Hot Embossing*, ACS Applied Materials & Interfaces, **8**, 9423-9430 (2016)

- **Senta Schauer**, Matthias Worgull, and Hendrik Hölscher. *Bio-inspired hierarchical micro-and nano-wrinkles obtained via mechanically directed self-assembly on shape-memory polymers*, Soft Matter, **13**, 4328 - 4334 (2017)

- **Senta Schauer**[*], Raphael Schmager[*], Ruben Hünig, Kaining Ding, Ulrich W. Paetzold, Uli Lemmer, Matthias Worgull, Hendrik Hölscher, and Guillaume Gomard. *Disordered Diffraction Gratings Tailored by Shape-Memory Based Wrinkling and their Application to Photovoltaics*, in submission at Optical Materials Express
([*] authors contributed equally)

- **Senta Schauer**, Jeremy J. Baumberg, Hendrik Hölscher, and Stoyan K. Smoukov. *Tuning of Structural Colors like a Chameleon enabled by Shape-Memory Polymers*, in submission at Advanced Materials

Book Contributions

- Andreas Lendlein, Steffen Kelch, Karl Kratz, Jürgen Schulte, and **Senta Schauer**. *Shape-Memory Polymers*, Reference Module in Materials Science and Materials Engineering, Saleem Hashmi (editor-in-chief), Elsevier (2016)

Conference Contributions

Oral

- **Senta Schauer**, Xin Liu, Tobias Meier, Marc Schneider, Matthias Worgull, Uli Lemmer, and Hendrik Hölscher, *Tunable Distributed Feedback (DFB) Lasers built from Shape-Memory Polymers*. DPG spring meeting, April 2014, Dresden, Germany

- **Senta Schauer**, Xin Liu, Norbert Schneider, Matthias Worgull, Uli Lemmer, and Hendrik Hölscher. *Using Shape-Memory Polymer Resonators for building Continuously Tunable Organic Distributed Feedback Lasers*, February 2015, SPIE Photonics West San Francisco, USA

- Norbert Schneider, **Senta Schauer**, Radwanul H. Siddique, Hendrik Hölscher, Jürg Leuthold, and Matthias Worgull. *Large-scale fabrication of 3D photonic nanostructures*, February 2015, SPIE Photonics West, San Francisco, USA

- Norbert Schneider, **Senta Schauer**, Radwanul H. Siddique, Hendrik Hölscher, and Matthias Worgull. *Large-scale replication of the blue Morpho's hierarchical photonic nanostructures utilizing shape memory polymers*, March 2015, SPIE Smart Structures, San Diego, USA

- **Senta Schauer**, Xin Liu, Norbert Schneider, Matthias Worgull, Uli Lemmer, Hendrik Hölscher. *Shape-Memory Polymers for Active Optical Devices: Continuously Tunable Organic Semiconductor Distributed Feedback Lasers*, SPIE Smart Structures/NDE, March 2015, San Diego, USA

Poster

- **Senta Schauer**, Xin Liu, Tobias Meier, Marc Schneider, Matthias Worgull, Uli Lemmer, and Hendrik Hölscher. *Variable Iridescent Surface Gratings Built from Shape-Memory Polymers*, Living Light: Uniting Biology and Photonics, April 2014, Namur, Belgium

- **Senta Schauer**, Xin Liu, Matthias Worgull, Uli Lemmer, and Hendrik Hölscher. *Shape-Memory Polymers as Flexible Reosnators for Continuously Tunable Organic DFB Lasers*, 2^{nd} Prize Poster Award, Statusworkshop Kompetenznetz "Funktionelle Nanostrukturen", September 2014, Bad Herrenalb, Germany

- **Senta Schauer**, Xin Liu, Matthias Worgull, Uli Lemmer, and Hendrik Hölscher. *Shape-memory polymer resonators for novel continuously tunable organic distributed feedback lasers*, SPIE Optics and Photonics, August 2015, San Diego, USA

- **Senta Schauer**, Matthias Worgull, and Hendrik Hölscher. *Shape-Memory Polymers for Tunable Structural Colors*, 1st Prize Poster Award, 644. Heraeus-Seminar: Bio-inspired, Nano- and Microstructured Surfaces: New Functionality by Material and Structure, May 2017, Bad Honnef, Germany

Scientific Talks at Other Institutions

- **Senta Schauer**, Xin Liu, Tobias Meier, Matthias Worgull, Uli Lemmer, and Hendrik Hölscher. *Shape-Memory Polymers for Novel Tunable Organic Distributed Feedback (DFB)-Laser and Space-Resolved Recovery*, July 2014, ETH Zürich, Switzerland

Bibliography

[1] S. Kinoshita, S. Yoshioka, *Structural colors in nature: The role of regularity and irregularity in the structure*. ChemPhysChem (2005), ***6*** 1442–1459.

[2] S. Kinoshita, S. Yoshioka, J. Miyazaki, *Physics of structural colors*. Reports on Progress in Physics (2008), ***71*** 076401.

[3] C. Neinhuis, W. Barthlott, *Characterization and distribution of water-repellent, self-cleaning plant surfaces*. Annals of Botany (1997), ***79*** 667–677.

[4] K. Autumn, M. Sitti, Y. A. Liang, A. M. Peattie, W. R. Hansen, S. Sponberg, T. W. Kenny, R. Fearing, J. N. Israelachvili, R. J. Full, *Evidence for Van der Waals adhesion in gecko setae*. Proceedings of the National Academy of Sciences (2002), ***99*** 12252–12256.

[5] J. Zi, X. Yu, Y. Li, X. Hu, C. Xu, X. Wang, X. Liu, R. Fu, *Coloration strategies in peacock feathers*. Proceedings of the National Academy of Sciences (2003), ***100*** 12576–12578.

[6] T. Tan, D. Wong, P. Lee, *Iridescence of a shell of mollusk Haliotis Glabra*. Optics Express (2004), ***12*** 4847–4854.

[7] P. Vukusic, J. R. Sambles, *Photonic structures in biology*. Nature (2003), ***424*** 852–855.

[8] T. Lenau, M. Barfoed, *Colours and metallic sheen in beetle shells—a biomimetic search for material structuring principles causing light interference*. Advanced Engineering Materials (2008), ***10*** 299–314.

[9] H. Zollinger. *Color chemistry: Syntheses, properties, and applications of organic dyes and pigments*. John Wiley & Sons (2003).

[10] E. F. Schubert, T. Gessmann, J. K. Kim. *Light emitting diodes*. Wiley Online Library (2005).

[11] K. Kakinuma, *Technology of wide color gamut backlight with light-emitting diode for liquid crystal display television*. Japanese Journal of Applied Physics (2006), ***45*** 4330.

[12] S. Schauer, T. Meier, M. Reinhard, M. Röehrig, M. Schneider, M. Heilig, A. Kolew, M. Worgull, H. Hölscher, *Tunable Diffractive Optical Elements based on Shape-Memory Polymers Fabricated via Hot Embossing*. ACS Applied Materials & Interfaces (2016), ***8*** 9423-9430.

[13] L. M. Mäthger, E. J. Denton, N. J. Marshall, R. T. Hanlon, *Mechanisms and behavioural functions of structural coloration in cephalopods*. Journal of the Royal Society Interface (2009), ***6*** S149–S163.

[14] F. Marlow, P. Sharifi, R. Brinkmann, C. Mendive, *Opale: Status und Perspektiven*. Angewandte Chemie (2009), ***121*** 6328–6351.

[15] A. Lendlein, S. Kelch, *Shape memory polymers*. Angewandte Chemie (2002), ***41*** 2034 - 2057.

[16] C. Liu, H. Qin, P. T. Mather, *Review of progress in shape-memory polymers*. Journal of Materials Chemistry (2007), ***17*** 1543-1558.

[17] P. T. Mather, X. Luo, I. A. Rousseau, *Shape Memory Polymer Research*. Annual Review of Materials Research (2009), ***39*** 445–471.

[18] A. Lendlein. *Shape-memory polymers*. Springer, Berlin (2010).

[19] Q. Zhao, H. J. Qi, T. Xie, *Recent progress in shape memory polymer: New behavior, enabling materials, and mechanistic understanding*. Progress in Polymer Science (2015) 1–42.

[20] M. D. Hager, S. Bode, C. Weber, U. S. Schubert, *Shape memory polymers: Past, present and future developments*. Progress in Polymer Science (2015) 1–31.

[21] A. Lendlein, S. Kelch, K. Kratz, J. Schulte, S. Schauer. *Shape-memory polymers, In Reference Module in Materials Science and Materials Engineering*. Elsevier (2016).

[22] J. A. Shaw, C. B. Churchill, M. Iadicola, *Tips and tricks for characterizing shape memory alloy wire: Part 1 — differential scanning calorimetry and basic phenomena*. Experimental Techniques (2008), ***32*** 55–62.

[23] A. Lendlein, R. Langer, *Biodegradable, elastic shape-memory polymers for potential biomedical applications*. Science (2002), ***296*** 1673-1676.

[24] W. Voit, T. Ware, R. R. Dasari, P. Smith, L. Danz, D. Simon, S. Barlow, S. R. Marder, K. Gall, *High-strain shape-memory polymers*. Advanced Functional Materials (2010), ***20*** 162–171.

[25] B. Heuwers, A. Beckel, A. Krieger, F. Katzenberg, J. C. Tiller, *Shape-memory natural rubber: An exceptional material for strain and energy storage*. Macromolecular Chemistry and Physics (2013), ***214*** 912923.

[26] R. Hoeher, T. Raidt, C. Krumm, M. Meuris, F. Katzenberg, J. C. Tiller, *Tunable multiple-shape memory polyethylene blends*. Macromolecular Chemistry and Physics (2013), ***214*** 27252732.

[27] T. Xie, *Recent Advances in Polymer Shape Memory*. Polymer (2011), ***52*** 4985-5000.

[28] K. Yu, T. Xie, J. Leng, Y. Dinga, H. J. Qi, *Mechanisms of multi-shape memory effects and associated energy release in shape memory polymers*. Soft Matter (2012), ***8*** 5687.

[29] K. Yu, Q. Ge, H. J. Qi, *Reduced time as a unified parameter determining fixity and free recovery of shape memory polymers*. Nature Communications (2014), ***5***.

[30] G. R. Strobl. *The Physics of Polymers*. Springer (2007).

[31] H. F. Brinson, L. C. Brinson. *Polymer Engineering Science and Viscoelasticity*. Springer (2008).

[32] M. Rubinstein, R. H. Colby. *Polymer Physics*. NEW YORK: Oxford University (2003).

[33] M. Behl, M. Y. Razzaq, A. Lendlein, *Multifunctional Shape-Memory Polymers*. Advanced Materials (2010), ***22*** 3388–3410.

[34] J. Hu, Y. Zhu, H. Huang, J. Lu, *Recent advances in shape–memory polymers: Structure, mechanism, functionality, modeling and applications*. Progress in Polymer Science (2012), ***37*** 1720–1763.

[35] D. Ratna, J. Karger-Kocsis, *Recent advances in shape memory polymers and composites: A review*. Journal of Materials Science (2008), ***43*** 254-269.

[36] L. Sun, W. M. Huang, Z. Ding, Y. Zhao, C. C. Wang, H. Purnawali, C. Tang, *Stimulus-responsive shape memory materials: A review*. Materials & Design (2012), ***33*** 577–640.

[37] C. M. Yakacki, *Shape-Memory and Shape-Changing Polymers*. Polymer Reviews (2013), ***53*** 1-5.

[38] I. Bellin, S. Kelch, R. Langer, A. Lendlein, *Polymeric triple-shape materials*. Proceedings of the National Academy of Sciences (2006), ***48*** 18043-18047.

[39] J. Li, T. Xie, *Significant impact of thermo-mechanical conditions on polymer triple-shape memory effect*. Macromolecules (2011), ***44*** 175–180.

[40] T. Pretsch, *Triple-shape properties of a thermoresponsive poly(ester urethane)*. Smart Materials and Structures (2010), ***19*** 015006.

[41] T. Ware, K. Hearon, A. Lonnecker, K. L. Wooley, D. J. Maitland, W. Voit, *Triple-shape memory polymers based on self-complementary hydrogen bonding*. Macromolecules (2012), ***45*** 10621069.

[42] T. Xie, X. Xiao, Y. T. Cheng, *Revealing triple-shape memory effect by polymer bilayers*. Macromolecular Rapid Communications (2009), ***30*** 1823–1827.

[43] S. V. Ahir, A. R. Tajbakhsh, E. M. Terentjev, *Self-assembled shape-memory fibers of triblock liquid-crystal polymers*. Advanced Functional Materials (2006), ***16*** 556–560.

[44] F. Brömmel, D. Kramer, H. Finkelmann, *Preparation of liquid crystalline elastomers*. In *Liquid Crystal Elastomers: Materials and Applications*, 1–48. Springer (2012).

[45] H. Finkelmann, H.-J. Kock, G. Rehage, *Investigations on liquid crystalline polysiloxanes 3. Liquid crystalline elastomers — a new type of liquid crystalline material*. Die Makromolekulare Chemie, Rapid Communications (1981), ***2*** 317–322.

[46] T. Ikeda, J. Mamiya, Y. L. Yu, *Photomechanics of liquid-crystalline elastomers and other polymers*. Angewandte Chemie International Edition (2007), ***46*** 506–528.

[47] S. Krause, F. Zander, G. Bergmann, H. Brandt, H. Wertmer, H. Finkelmann, *Nematic main-chain elastomers: Coupling and orientational behavior*. Comptes Rendus Chimie (2009), ***12*** 85–104.

[48] J. Küpfer, H. Finkelmann, *Nematic liquid single crystal elastomers*. Die Makromolekulare Chemie, Rapid Communications (1991), ***12*** 717–726.

[49] C. Ohm, M. Brehmer, R. Zentel, *Liquid crystalline elastomers as actuators and sensors*. Advanced Materials (2010), ***22*** 3366-3387.

[50] T. Chung, A. Rorno-Uribe, P. T. Mather, *Two-way reversible shape memory in a semicrystalline network*. Macromolecules (2008), ***41*** 184–192.

[51] J. Li, W. R. Rodgers, T. Xie, *Semi-crystalline two-way shape memory elastomer*. Polymer (2011), ***52*** 5320–5325.

[52] M. Behl, K. Kratz, J. Zotamann, U. Nöchel, A. Lendlein, *Reversible bi-directional shape-memory polymers*. Advanced Materials (2013), ***25*** 4466-4469.

[53] M. Ebara, K. Uto, N. Idota, J. M. Hoffman, T. Aoyagi, *Shape-memory surface with dynamically tunable nanogeometry activated by bodyheat*. Advanced Materials (2012), ***24*** 273–278.

[54] T. Pretsch, M. Ecker, M. Schildhauer, M. Maskos, *Switchable information carriers based on shape memory polymer*. Journal of Materials Chemistry (2012), ***22*** 7757–7766.

[55] H. Yabu, R. Jia, Y. Matsuo, K. Ijiro, S.-a. Yamamoto, F. Nishino, T. Takaki, M. Kuwahara, M. Shimomura, *Preparation of highly oriented nano-pit arrays by thermal shrinking of honeycomb-patterned polymer films*. Advanced Materials (2008), ***20*** 4200–4204.

[56] A. Charlesby. *Atomic Radiation and Polymers*. Pergamon Press Oxford (1960).

[57] W. Chen, K. Xing, L. Sun, *The heat shrinking mechanism of polyethylene film*. Radiation Physics and Chemistry (1983), ***22*** 593-601.

[58] S. Machi, *New trends of radiation processing applications*. Radiation Physics and Chemistry (1996), ***47*** 333-336.

[59] S. Ota, *Current status of irradiated heat-shrinkable tubing in Japan*. Radiation Physics and Chemistry (1981), ***18*** 81-87.

[60] H. Tobushi, H. Hara, E. Yamada, S. Hayashi, *Thermomechanical properties in a thin film of shape memory polymer of polyurethane series*. Smart Materials and Structures (1996), ***5*** 483.

[61] J. Hu, X. Ding, X. Tao, J. Yu, *Shape-memory polymers and their applications to smart textile products*. Journal of Dong Hua University (English Edition) (2002), ***19***.

[62] I. K. Kuder, A. F. Arrieta, W. E. Raither, P. Ermanni, *Variable stiffness material and structural concepts for morphing applications*. Progress in Aerospace Sciences (2013), ***63*** 33–55.

[63] Y. J. Liu, H. Y. Du, L. W. Liu, J. S. Leng, *Shape memory polymers and their composites in aerospace applications: A review*. Smart Materials and Structures (2014), ***23*** 023001.

[64] W. M. Sokolowski, A. B. Chmielewski, S. Hayashi, T. Yamada, *Cold hibernated elastic memory (CHEM) self-deployable structures*. Proc SPIE (1999), ***3669*** 179-185.

[65] Y. Yu, X. Li, W. Zhang, J. Leng, *Investigation on adaptive wing structure based on shape memory polymer composite hinge*. In *Proc SPIE* (2007) 64231D–5.

[66] D. Zhang, O. J. George, K. M. Petersen, A. C. Jimenez-Vergara, M. S. Hahn, M. A. Grunlan, *A bioactive "self-fitting" shape memory polymer scaffold with potential to treat cranio-maxillo facial bone defects*. Acta Biomaterialia (2014), ***10*** 4597–4605.

[67] M. Wache, J. Tartakowska, A. Hentrich, M. Wagner, *Development of a polymer stent with shape-memory effect as a drug delivery system*. Journal of Materials Science: Materials in Medicine (2003), ***14*** 109-112.

[68] D. J. Maitland, T. Wilson, D. Schumann, G. Baer, *Laser-activated shape memory polymer microactuators for treating stroke*. In *Lasers and Electro-Optics Society, 2002. LEOS 2002. The 15th Annual Meeting of the IEEE*. IEEE (2002) 359–360.

[69] F. El Feninat, G. Laroche, M. Fiset, D. Mantovani, *Shape memory materials for biomedical applications*. Advanced Engineering Materials (2002), ***4*** 91–104.

[70] A. Nakasima, J. Hu, M. Ichinosa, H. Shimada, *Potential application of shape-memory plastic as elastic material in clinical orthodontics*. European Journal of Orthodontics (1991), ***13*** 179-186.

[71] A. Lendlein, A. M. Schmidt, R. Langer, *AB-polymer networks based on oligo(ε-caprolactone) segments showing shape-memory properties*. Proceedings of the National Academy of Sciences (2001), ***98*** 842-847.

[72] C. M. Chen, S. Yang, *Directed water shedding on high-aspect-ratio shape memory polymer micropillar arrays*. Advanced Materials (2014), ***26*** 1283-1288.

[73] J. D. Eisenhaure, T. Xie, S. Varghese, S. Kim, *Microstructured shape memory polymer surfaces with reversible dry adhesion*. ACS Applied Materials & Interfaces (2013), ***5*** 7714-7717.

[74] A. Espinha, M. C. Serrano, Á. Blanco, C. López, *Thermoresponsive shape-memory photonic nanostructures*. Advanced Optical Materials (2014), ***2*** 516–521.

[75] T. Meier, J. Bur, M. Reinhard, M. Schneider, A. Kolew, M. Worgull, H. Hölscher, *Programmable and self-demolding microstructured molds fabricated from shape-memory polymers*. Journal of Micromechanics and Microengineering (2015), ***25*** 065017.

[76] S. Reddy, E. Arzt, A. D. Campo, *Bioinspired surfaces with switchable adhesion*. Advanced Materials (2007), ***19*** 3833-3837.

[77] P. Sarwate, A. Chakraborty, V. Garg, C. Luo, *Controllable strain recovery of shape memory polystyrene to achieve superhydrophobicity with tunable adhesion*. Journal of Micromechanics and Microengineering (2014), ***24*** 115006.

[78] N. Schneider, C. Zeiger, A. Kolew, M. Schneider, J. Leuthold, H. Hölscher, M. Worgull, *Nanothermoforming of hierarchical optical components utilizing shape memory polymers as active molds*. Optical Materials Express (2014), ***4*** 1895.

[79] H. Xu, C. Yu, S. Wang, V. Malyarchuk, T. Xie, J. A. Rogers, *Deformable, programmable, and shape-memorizing micro-optics*. Advanced Functional Materials (2013), ***23*** 3299–3306.

[80] D. Halliday, R. Resnick, J. Walker. *Halliday Physik, Bachelor Edition*. Wiley (2007).

[81] B. E. A. Saleh, M. C. Teich. *Fundamentals of Photonics*. John Wiley and Sons, Hoboken, NJ (2007).

[82] W. Demtröder. *Experimentalphysik 2: Elektrizität und Optik*. Springer-Verlag (2006).

[83] J. Jahns, S. Helfert. *Introduction to Micro- and Nanooptics*. Wiley-VCH, Weinheim (2012).

[84] Q. Gong, X. Hu. *Photonic Crystals: Principles and Applications*. Pan Stanford Publishing (2014).

[85] J. D. Joannopoulos, S. G. Johnson, J. N. Winn, R. D. Meade. *Photonic Crystals: Molding the Flow of Light*. Princeton University Press (2011).

[86] *http://www.photonics.byu.edu/Fabry_Perot.phtml* (21.4.2017).

[87] M. Kolle. *Photonic Structures Inspired by Nature*. Springer Science & Business Media (2011).

[88] G. W. Ehrenstein. *Polymer-Werkstoffe*. Carl Hanser Verlag GmbH & Co. KG (2011).

[89] H. Zidan, M. Abu-Elnader, *Structural and optical properties of pure PMMA and metal chloride-doped PMMA films*. Physica B: Condensed Matter (2005), ***355*** 308–317.

[90] M. Worgull. *Hot Embossing - Theory and Technology of Microreplication*. Micro and Nano Technologies, Elsevier Science, William Andrew, Norwich, NY (2009).

[91] R. Ezzat. Master's thesis, Karlsruhe Institute of Technology (2013).

[92] J. Schroers, Q. Pham, A. Desai, *Thermoplastic forming of bulk metallic glass—a technology for MEMS and microstructure fabrication*. Journal of Microelectromechanical Systems (2007), ***16*** 240–247.

[93] M. Worgull, M. Schneider, M. Röhrig, T. Meier, M. Heilig, A. Kolew, K. Feit, H. Hölscher, J. Leuthold, *Hot embossing and thermoforming of biodegradable three-dimensional wood structures*. RSC Advances (2013), ***3*** 20060–20064.

[94] M. Kavalenka, A. Hopf, M. Schneider, M. Worgull, H. Hölscher, *Wood-based microhaired superhydrophobic and underwater superoleophobic surfaces for oil/water separation*. RSC Advances (2014), ***4*** 31079–31083.

[95] N. Kooy, K. Mohamed, L. T. Pin, O. S. Guan, *A review of roll-to-roll nanoimprint lithography*. Nanoscale Research Letters (2014), ***9*** 320-320.

[96] C. Rauwendaal. *Polymer Extrusion*. Carl Hanser Verlag GmbH Co KG (2014).

[97] R. J. Koopmans. *Die Swell or Extrudate Swell*, 158–162. Springer Netherlands, Dordrecht. ISBN 978-94-011-4421-6 (1999).

[98] M. J. Madou. *Fundamentals of Microfabrication: The science of Miniaturization*. CRC press (2002).

[99] S. Wang, C. Tay, *Application of an optical interferometer for measuring the surface contour of micro-components*. Measurement Science and Technology (2006), ***17*** 617.

[100] I. Koyuncu, J. Brant, A. Lüttge, M. R. Wiesner, *A comparison of vertical scanning interferometry (VSI) and atomic force microscopy (AFM) for characterizing membrane surface topography*. Journal of Membrane Science (2006), ***278*** 410–417.

[101] L. Reimer. *Scanning Electron Microscopy: Physics of Image Formation and Microanalysis*. Springer (2013).

[102] L. Gross, F. Mohn, N. Moll, P. Liljeroth, G. Meyer, *The chemical structure of a molecule resolved by atomic force microscopy*. Science (2009), ***325*** 1110–1114.

[103] W. R. Bowen, N. Hilal. *Atomic Force Microscopy in Process Engineering: An Introduction to AFM for Improved Processes and Products*. Butterworth-Heinemann (2009).

[104] B. Cappella, G. Dietler, *Force-distance curves by atomic force microscopy*. Surface Science Reports (1999), ***34*** 15–3104.

[105] H.-J. Butt, B. Cappella, M. Kappl, *Force measurements with the atomic force microscope: Technique, interpretation and applications*. Surface Science Reports (2005), ***59*** 1–152.

[106] T. Meier. *Magnetoresistive and Thermoresistive Scanning Probe Microscopy with Applications in Micro-and Nanotechnology*. KIT Scientific Publishing (2014).

[107] A. W. Lohmann, D. P. Paris, *Binary Fraunhofer holograms, generated by computer*. Applied Optics (1967), ***6*** 1739–1748.

[108] J. R. Leger, D. Chen, Z. Wang, *Diffractive Optical Element for Mode Shaping of a Nd:YAG Laser*. Optics Letters (1994), ***19*** 108-110.

[109] E. R. Dufresne, D. G. Grier, *Optical tweezer arrays and optical substrates created with diffractive optics*. Review of Scientific Instruments (1998), ***69*** 1974–1977.

[110] M. Pitchumani, H. Hockel, W. Mohammed, E. G. Johnson, *Additive lithography for fabrication of diffractive optics.* Applied Optics (2002), ***41*** 6176–6181.

[111] M. T. Gale, *Replication techniques for diffractive optical elements*. Microelectronic Engineering (1997), ***34*** 321–339.

[112] M. T. Gale, C. Gimkiewicz, S. Obi, M. Schnieper, J. Söchtig, H. Thiele, S. Westenhöfer, *Replication technology for optical microsystems*. Optics and Lasers in Engineering (2005), ***43*** 373–386.

[113] A. J. Waddie, M. R. Taghizadeh, J. Mohr, V. Piotter, C. Mehne, A. Stuck, E. Stijns, H. Thienpont, *Design, Fabrication, and Replication of Micro-Optical Components for Educational Purposes within the Network of Excellence in Micro-Optics (NEMO)*. In *Proc SPIE* (2006) 61850B.

[114] Z. Wang, C. Hansen, Q. Ge, S. H. Maruf, D. U. Ahn, H. J. Qi, Y. Ding, *Programmable, pattern-memorizing polymer surface*. Advanced Materials (2011), ***23*** 3669–3673.

[115] S. Schauer. Master's thesis, Karlsruhe Institute of Technology (2013).

[116] H. J. Eichler, J. Eichler. *Laser: Bauformen, Strahlführung, Anwendungen*. Springer-Verlag (2015).

[117] S. B. Klinkhammer. *Durchstimmbare Organische Halbleiterlaser*. KIT Scientific Publishing (2014).

[118] R. Menzel. *Photonics: Linear and Nonlinear Interactions of Laser Light and Matter*. Springer Science & Business Media (2013).

[119] S. Klinkhammer, X. Liu, K. Huska, Y. Shen, S. Vanderheiden, S. Valouch, C. Vannahme, S. Bräse, T. Mappes, U. Lemmer, *Continuously tunable solution-processed*

organic semiconductor DFB lasers pumped by laser diode. Optics Express (2012), ***20*** 6357-6364.

[120] D. Schneider, T. Rabe, T. Riedl, T. Dobbertin, M. Kröger, E. Becker, H.-H. Johannes, W. Kowalsky, T. Weimann, J. Wang, P. Hinze, A. Gerhard, P. Stössel, H. Vestweber, *An ultraviolet organic thin-film solid-state laser for biomarker applications*. Advanced Materials (2005), ***17*** 31–34.

[121] Y. Oki, S. Miyamoto, M. Maeda, N. Vasa, *Multiwavelength distributed-feedback dye laser array and its application to spectroscopy*. Optics Letters (2002), ***27*** 1220-1222.

[122] T. Woggon, S. Klinkhammer, U. Lemmer, *Compact spectroscopy system based on tunable organic semiconductor lasers*. Applied Physics B: Lasers and Optics (2010), ***99*** 47-51.

[123] S. Klinkhammer, T. Woggon, C.Vannahme, U. Geyer, T. Mappes, U. Lemmer, *Optical spectroscopy with organic semiconductor lasers*. Applied Physics B: Lasers and Optics (2010), ***99*** 47-51.

[124] X. Liu, P. Stefanou, B. Wang, T. Woggon, T. Mappes, U. Lemmer, *Organic semiconductor distributed feedback (DFB) laser as excitation source in Raman spectroscopy*. Optics Express (2013), ***21*** 28941-28947.

[125] X. Liu, S. Klinkhammer, Z. Wang, T. Wienhold, C. Vannahme, P.-J. Jakobs, A. Bacher, A. Muslija, T. Mappes, U. Lemmer, *Pump spot size dependent lasing threshold in organic semiconductor DFB lasers fabricated via nanograting transfer*. Optics Express (2013), ***21*** 27697–27706.

[126] X. Liu, S. Lebedkin, T. Mappes, S. Köber, C. Koos, M. Kappe, U. Lemmer, *Organic semiconductor distributed feedback laser as excitation source in Raman spectroscopy using free-beam and fibre coupling*. Optics Express (2013), ***21*** 28941-28947.

[127] T. Voss, D. Scheel, W. Schade, *A microchip-laser-pumped DFB-polymer-dye laser*. Applied Physics B: Lasers and Optics (2001), ***73*** 105-109.

[128] K. Suzuki, K. Takahashi, Y. Seida, K. Shimizu, M. Kumagai, Y. Taniguchi, *A continuously tunable organic solid-state laser based on a flexible distributed-feedback resonator*. Japanese Journal of Applied Physics (2003), ***42*** L249.

[129] M. R. Weinberger, G. Langer, A. Pogantsch, A. Haase, E. Zojer, W. Kern, *Continuously color tunable rubber laser*. Advanced Materials (2004), ***16*** 130-133.

[130] B. Wenger, N. Tétreault, M. E. Welland, R. H. Friend, *Mechanically tunable conjugated polymer distributed feedback lasers*. Applied Physics Letters. (2010), ***19*** 193303.

[131] P. Görrn, M. Lehnhardt, W. Kowalsky, T. Riedl, S. Wagner, *Elastically tunable self-organized organic lasers*. Advanced Materials (2011), ***23*** 869-872.

[132] S. Döring, M. Kollosche, T. Rabe, J. Stumpe, G. Kofod, *Electrically tunable polymer DFB laser*. Advanced Materials (2011), ***23*** 4265-4269.

[133] J. Wang, T. Weimann, P. Hinze, G. Ade, D. Schneider, T. Rabe, T. Riedel, W. Kowalsky, *A continuously tunable organic DFB laser*. Microelectronic Engineering (2005), ***78-79*** 364–368.

[134] Z. Li, Z. Zhang, A. Scherer, D. Psaltis, *Mechanically tunable optofluidic distributed feedback dye laser*. Optics Express (2006), ***14*** 10494-10499.

[135] F. B. Arango, M. B. Christiansen, M. Gersborg-Hansen, A. Kristensen, *Optofluidic tuning of photonic crystal band edge lasers*. Applied Physics Letters. (2007), ***91*** 223503.

[136] S. Klinkhammer, T. Woggon, U. Greyer, C. Vannahme, T. Mappes, S. Dehm, U. Lemmer, *A continuously tunable low-threshold organic semiconductor distributed feedback laser fabricated by rotating shadow mask evaporation*. Applied Physics B: Lasers and Optics (2009), ***97*** 787-791.

[137] R. Ozaki, T. Shinpo, K. Yoshino, M. Ozaki, H. Moritake, *Tunable liquid crystal laser using distributed feedback cavity fabricated by nanoimprint lithography*. Applied Physics Express (2008), ***1*** 012003.

[138] K. Müllen, U. Scherf. *Organic Light-Emitting Devices*. Ed. Wiley-VCH, Germany (2006).

[139] S. Riechel. *Organic Semiconductor Lasers with Two-Dimensional Distributed Feedback*. Ludwig-Maximilians-Universitüt München (2002).

[140] Y. Wang. *Low Threshold Organic Semiconductor Lasers: Hybrid Optoelectronics and Applications as Explosive Sensors*. Springer Science & Business Media (2013).

[141] C. Vannahme, S. Klinkhammer, A. Kolew, P.-J. Jakobs, M. Guttmann, S. Dehm, U. Lemmer, T. Mappes, *Integration of organic semiconductor lasers and single-mode passive waveguides into a PMMA substrate*. Microelectronic Engineering (2010), ***87*** 693-695.

[142] C. Vannahme, S. Klinkhammer, U. Lemmer, T. Mappes, *Plastic lab-on-a-chip for fluorescence excitation with integrated organic semiconductor lasers*. Optics Express (2011), ***19*** 8179-8186.

[143] J. M. Arnold, R. E. Young, M. V. King, *Ultrastructure of a cephalopod photophore. II. Iridophores as reflectors and transmitters*. The Biological Bulletin (1974), ***147*** 522–534.

[144] A. Ghoshal, D. G. DeMartini, E. Eck, D. E. Morse, *Optical parameters of the tunable Bragg reflectors in squid*. Journal of The Royal Society Interface (2013), ***10*** 20130386.

[145] S. Yoshioka, B. Matsuhana, S. Tanaka, Y. Inouye, N. Oshima, S. Kinoshita, *Mechanism of variable structural colour in the neon tetra: Quantitative evaluation of the Venetian blind model*. Journal of The Royal Society Interface (2011), ***8*** 56-66.

[146] K. M. Cooper, R. T. Hanlon, B. U. Budelmann, *Physiological color change in squid iridophores*. Cell and Tissue Research (1990), ***259*** 15–24.

[147] L. Mäthger, M. Land, U. Siebeck, N. Marshall, *Rapid colour changes in multilayer reflecting stripes in the paradise whiptail, Pentapodus paradiseus*. Journal of Experimental Biology (2003), ***206*** 3607–3613.

[148] P. Tayebati, P. Wang, D. Vakhshoori, R. N. Sacks, *Widely tunable Fabry-Pérot filter using Ga (Al) As-AlO x deformable mirrors*. IEEE Photonics Technology Letters (1998), ***10*** 394–396.

[149] C. A. Barrios, V. Almeida, R. Panepucci, B. Schmidt, M. Lipson, *Compact silicon tunable Fabry-Pérot resonator with low power consumption*. IEEE Photonics Technology Letters (2004), ***16*** 506–508.

[150] S. Irmer, J. Daleiden, V. Rangelov, C. Prott, F. Romer, M. Strassner, A. Tarraf, H. Hillmer, *Ultralow biased widely continuously tunable Fabry-Pérot filter*. IEEE Photonics Technology Letters (2003), ***15*** 434–436.

[151] C. D. Sorrell, M. C. Carter, M. J. Serpe, *A "paint-on" protocol for the facile assembly of uniform microgel coatings for color tunable etalon fabrication*. ACS Applied Materials & Interfaces (2011), ***3*** 1140–1147.

[152] C. D. Sorrell, M. J. Serpe, *Reflection order selectivity of color-tunable poly (N-isopropylacrylamide) microgel based etalons*. Advanced Materials (2011), ***23*** 4088–4092.

[153] C. D. Sorrell, M. C. Carter, M. J. Serpe, *Color tunable poly (N-isopropylacrylamide)-co-acrylic acid microgel-Au hybrid assemblies*. Advanced Functional Materials (2011), ***21*** 425–433.

[154] D. Lee. *Nature's Palette: The Science of Plant Color*. University of Chicago Press, Chicago, IL (2007).

[155] B. J. Glover, C. Martin, *The role of petal cell shape and pigmentation in pollination success in Antirrhinum majus*. Heredity (1998), ***80*** 778–784.

[156] S.-M. Lee, J. Upping, A. Bielawny, M. Knez, *Structure-based color of natural petals discriminated by polymer replication*. ACS Applied Materials & Interfaces (2011), ***3*** 30–34.

[157] H. M. Whitney, M. Kolle, P. Andrew, L. Chittka, U. Steiner, B. J. Glover, *Floral iridescence, produced by diffractive optics, acts as a cue for animal pollinators.* Science (2009), ***323*** 130–133.

[158] B. J. Glover, H. M. Whitney, *Structural colour and iridescence in plants: The poorly studied relations of pigment colour*. Annals of Botany (2010), ***105*** 505–511.

[159] C. E. Jones, S. L. Buchmann, *Ultraviolet floral patterns as functional orientation cues in hymenopterous pollination systems*. Animal Behaviour (1974), ***22*** 481–485.

[160] H. M. Whitney, A. Dyer, L. Chittka, S. A. Rands, B. J. Glover, *The interaction of temperature and sucrose concentration on foraging preferences in bumblebees*. Naturwissenschaften (2008), ***95*** 845–850.

[161] P. G. Kevan, L. Chittka, A. G. Dyer, *Limits to the salience of ultraviolet: Lessons from colour vision in bees and birds*. Journal of Experimental Biology (2001), ***204*** 2571–2580.

[162] H. M. Whitney, K. V. Bennett, M. Dorling, L. Sandbach, D. Prince, L. Chittka, B. J. Glover, *Why do so many petals have conical epidermal cells?* Annals of Botany (2011), ***108*** 609–616.

[163] S. Vignolini, E. Moyroud, B. J. Glover, U. Steiner, *Analysing Photonic Structures in Plants*. Journal of The Royal Society Interface (2013), ***10*** 20130394.

[164] H. Whitney, W. Federle, B. Glover, *Grip and slip*. Communicative & Integrative Biology (2009), ***2*** 505-508.

[165] H. M. Whitney, R. Poetes, U. Steiner, L. Chittka, B. J. Glover, *Determining the contribution of epidermal cell shape to petal wettability using isogenic Antirrhinum lines*. PLoS One (2011), ***6*** e17576.

[166] L. Feng, Y. Zhang, J. Xi, Y. Zhu, N. Wang, F. Xia, L. Jiang, *Petal effect: A superhydrophobic state with high adhesive force*. Langmuir (2008), ***24*** 4114–4119.

[167] R. L. A. Kourounioti, L. R. Band, J. A. Fozard, A. Hampstead, A. Lovrics, E. Moyroud, S. Vignolini, J. R. King, O. E. Jensen, B. J. Glover, *Buckling as an origin of ordered cuticular patterns in flower petals*. Journal of The Royal Society Interface (2012), ***10*** 20120847.

[168] S. N. Fernandes, Y. Geng, S. Vignolini, B. J. Glover, A. C. Trindade, J. P. Canejo, P. L. Almeida, P. Brogueira, M. H. Godinho, *Structural color and iridescence in transparent sheared cellulosic films*. Macromolecular Chemistry and Physics (2013), ***214*** 25–32.

[169] P. G. Kevan, *Insects as flower visitors and pollinators*. Annual Review of Entomology (1983), ***28*** 407-453.

[170] K. Koch, B. Bhushan, W. Barthlott, *Multifunctional surface structures of plants: An inspiration for biomimetics*. Progress in Materials Science (2009), ***54*** 137–178.

[171] K. Koch, H. F. Bohn, W. Barthlott, *Hierarchically sculptured plant surfaces and superhydrophobicity*. Langmuir (2009), ***25*** 14116–14120.

[172] S. G. Potts, J. C. Biesmeijer, C. Kremen, P. Neumann, O. Schweiger, W. E. Kunin, *Global pollinator declines: Trends, impacts and drivers*. Trends in Ecology Evolution (2010), ***25*** 345-353.

[173] N. Gallai, J.-M. Salles, J. Settele, B. E. Vaissiere, *Economic valuation of the vulnerability of world agriculture confronted with pollinator decline*. Ecological Economics (2009), ***68*** 810-821.

[174] S. Schauer, M. Worgull, H. Hölscher, *Bio-inspired hierarchical micro-and nanowrinkles obtained via mechanically directed self-assembly on shape-memory polymers*. Soft Matter (2017), ***13*** 4328-4334.

[175] C. Kluge, M. Rädler, A. Pradana, M. Bremer, P.-J. Jakobs, N. Barié, M. Guttmann, M. Gerken, *Extraction of guided modes from organic emission layers by compound binary gratings*. Optics Letters (2012), ***37*** 2646–2648.

[176] T. Buß, J. Teisseire, S. Mazoyer, C. L. Smith, M. B. Mikkelsen, A. Kristensen, E. Søndergård, *Controlled angular redirection of light via nanoimprinted disordered gratings*. Applied Optics (2013), ***52*** 709–716.

[177] S. M. Mahpeykar, Q. Xiong, J. Wei, L. Meng, B. K. Russell, P. Hermansen, A. V. Singhal, X. Wang, *Stretchable hexagonal diffraction gratings as optical diffusers for in situ tunable broadband photon management*. Advanced Optical Materials (2016), ***4*** 1106–1114.

[178] P. Kim, Y. Hu, J. Alvarenga, M. Kolle, Z. Suo, J. Aizenberg, *Rational design of mechano-responsive optical materials by fine tuning the evolution of strain-dependent wrinkling patterns*. Advanced Optical Materials (2013), ***1*** 381–388.

[179] A. Bozzola, M. Liscidini, L. C. Andreani, *Broadband light trapping with disordered photonic structures in thin-film silicon solar cells*. Progress in Photovoltaics: Research and Applications (2014), ***22*** 1237–1245.

[180] Y.-C. Tsao, T. Søndergaard, E. Skovsen, L. Gurevich, K. Pedersen, T. G. Pedersen, *Pore size dependence of diffuse light scattering from anodized aluminum solar cell backside reflectors*. Optics Express (2013), ***21*** A84–A95.

[181] J. B. Kim, P. Kim, N. C. Pégard, S. J. Oh, C. R. Kagan, J. W. Fleischer, H. A. Stone, Y.-L. Loo, *Wrinkles and deep folds as photonic structures in photovoltaics*. Nature Photonics (2012), ***6*** 327–332.

[182] S. K. Ram, D. Desta, R. Rizzoli, B. P. Falcão, E. H. Eriksen, M. Bellettato, B. R. Jeppesen, P. B. Jensen, C. Summonte, R. N. Pereira, et al., *Efficient light-trapping with quasi-periodic uniaxial nanowrinkles for thin-film silicon solar cells*. Nano Energy (2017).

[183] S. Y. Ryu, J. H. Seo, H. Hafeez, M. Song, J. Y. Shin, D. H. Kim, Y. C. Jung, C. S. Kim, *Effects of the wrinkle structure and flat structure formed during static low-temperature annealing of ZnO on the performance of inverted polymer solar cells*. The Journal of Physical Chemistry C (2017).

[184] R. Hünig, A. Mertens, M. Stephan, A. Schulz, B. Richter, M. Hetterich, M. Powalla, U. Lemmer, A. Colsmann, G. Gomard, *Flower power: Exploiting plants' epidermal structures for enhanced light harvesting in thin-film solar cells*. Advanced Optical Materials (2016), ***4*** 1487–1493.

[185] A. Deinega, I. Valuev, B. Potapkin, Y. Lozovik, *Minimizing light reflection from dielectric textured surfaces*. Journal of the Optical Society of America A (2011), ***28*** 770-777.

[186] J. Jakubiec, C. Reinhart, *Assessing disability glare potential of reflections from new construction: Case study analysis and recommendations for the future*. Transportation Research Record: Journal of the Transportation Research Board (2014) 114–122.

[187] T. Rose, A. Wollert, *The dark side of photovoltaic—3D simulation of glare assessing risk and discomfort*. Environmental Impact Assessment Review (2015), ***52*** 24–30.

[188] F. Ruesch, A. Bohren, M. Battaglia, S. Brunold, *Quantification of glare from reflected sunlight of solar installations*. Energy Procedia (2016), ***91*** 997–1004.

[189] E. Dominguez, J. Cuartero, A. Heredia, *An overview on plant cuticle biomechanics*. Plant Science (2011), ***181*** 77-84.

[190] C. M. Stafford, C. Harrison, K. L. Beers, A. Karim, E. J. Amis, M. R. Vanlandingham, H.-C. Kim, W. Volksen, R. D. Miller, E. E. Simonyi, *A buckling-based metrology for measuring the elastic moduli of polymeric thin films*. Nature Materials (2004), ***3*** 545-550.

[191] C. Harrison, C. M. Stafford, W. Zhang, A. Karim, *Sinusodial phase grating created by a tunably buckled surface*. Applied Physics Letters (2004), ***85*** 4016.

[192] C. M. Stafford, B. D. Vogt, C. Harrsion, D. Julthongpiput, R. Huang, *Elastic moduli of ultrathin amorphous polymer films*. Macromolecules (2006), ***39*** 5095-5099.

[193] E. P. Chan, E. J. Smith, R. C. Hayward, A. J. Crosby, *Surface wrinkles for smart adhesion*. Advanced Materials (2008), ***20*** 711-716.

[194] N. Bowden, S. Brittain, A. G. Evans, J. W. Hutchinson, G. M. Whitesides, *Spontaneous formation of ordered structures in thin films of metals supported on an elastomeric polymer*. Nature (1998), ***393*** 146.149.

[195] T. Okayasu, H.-L. Zhang, D. G. Bucknall, G. A. D. Briggs, *Spontaneous formation of ordered lateral patterns in polymer thin-film structures*. Advanced Functional Materials (2004), ***14*** 1081–1088.

[196] Y. Y. Kim, Q. Huang, S. Krishnaswamy, *Selective growth and ordering of self-assembly on metal/polymer thin-film heterostructures via photothermal modulation*. Applied Physics Letters (2010), ***96*** 123116.

[197] N. Bowden, W. T. Huck, K. E. Paul, G. M. Whitesides, *The controlled formation of ordered, sinusoidal structures by plasma oxidation of an elastomeric polymer*. Applied Physics Letters (1999), ***75*** 2557–2559.

[198] D. B. Chua, H. Ng, S. F. Li, *Spontaneous formation of complex and ordered structures on oxygen-plasma-treated elastomeric polydimethylsiloxane*. Applied Physics Letters. (2000), ***76*** 721.

[199] K. Efimenko, W. E. Wallace, J. Genzer, *Surface modification of Sylgard-184 poly(dimethyl siloxane) networks by ultraviolet and ultraviolet/ozone treatment*. Journal of Colloid and Interface Science (2002), ***254*** 306-315.

[200] M. Ouyang, C. Yuan, R. J. Muisener, A. Boulares, J. T. Koberstein, *Conversion of some siloxane polymers to silicon oxide by UV/ozone photochemical processes*. Chemistry of Materials (2000), ***12*** 1591-1596.

[201] W. T. S. Huck, N. Bowden, P. Onck, T. Pardoen, J. W. Hutchinson, G. M. Whitesides, *Ordering of spontaneously formed buckles on planar surfaces*. Langmuir (2000), ***16*** 3497-3501.

[202] X. Chen, J. W. Hutchinson, *Herringbone buckling patterns of compressed thin films on compliant substrates*. Journal of Applied Mechanics (2004), ***71*** 597-603.

[203] J. Genzer, J. Groenewold, *Soft matter with hard skin: From skin wrinkles to templating and material characterization*. Soft Matter (2006), ***2*** 310-323.

[204] T. Xie, X. Xioa, J. Li, R. Wang, *Encoding localized strain history through wrinkle based structural colors*. Advanced Materials (2010), ***22*** 4390-4394.

[205] Z. Chen, Y. Y. Kim, S. Krishnaswamy, *Anisotropic wrinkle formation on shape-memory polymer substrates*. Journal of Applied Physics (2012), ***112*** 124319.

[206] A. Schweikart, A. Fery, *Controlled wrinkling as a novel method for the fabrication of patterned surfaces*. Microchim Acta (2009), ***165*** 249-263.

[207] J. Li, Y. An, R. Huang, H. Jiang, T. Xie, *Unique aspects of a shape memory polymer as the substrate for surface wrinkling*. ACS Applied Materials & Interfaces (2012), ***4*** 598-603.

[208] V. Nayyar, K. Ravi-Chandar, R. Huang, *Stretch-induced wrinkling of polyethylene thin sheets: Experiments and modeling*. International Journal of Solids and Structures (2014), ***51*** 1847–1858.

[209] G. N. Greaves, A. Greer, R. Lakes, T. Rouxel, *Poisson's ratio and modern materials*. Nature materials (2011), ***10*** 823–837.

[210] K. Koch, B. Bhushan, W. Barthlott, *Diversity of structure, morphology and wetting of plant surfaces*. Soft Matter (2008), ***4*** 1943-1963.

[211] T. Nørgaard, M. Ebner, M. Dacke, *Animal or plant: Which is the better fog water collector?* PloS one (2012), ***7*** e34603.

[212] M. Azad, W. Barthlott, K. Koch, *Hierarchical surface architecture of plants as an inspiration for biomimetic fog collectors*. Langmuir (2015), ***31*** 13172–13179.

[213] R. N. Wenzel, *Resistance of solid surfaces to wetting by water*. Industrial & Engineering Chemistry (1936), ***28*** 988–994.

[214] J. Y. Chung, J. P. Youngblood, C. M. Stafford, *Anisotropic wetting on tunable micro-wrinkled surfaces*. Soft Matter (2007), ***3*** 1163–1169.

[215] Y. Han, Y. Liu, W. Wang, J. Leng, P. Jin, *Controlled wettability based on reversible micro-cracking on a shape memory polymer surface*. Soft Matter (2016), ***12*** 2708–2714.

[216] K. Kubiak, T. Mathia, *Anisotropic wetting of hydrophobic and hydrophilic surfaces–modelling by Lattice Boltzmann method*. Procedia Engineering (2014), ***79*** 45–48.

[217] S. Schauer, R. Schmager, R. Hünig, K. Ding, U. W. Paetzold, M. Worgull, H. Hölscher, G. Gomard, *Disordered diffraction gratings tailored by shape-memory based wrinkling and applied to photovoltaics*. in submission at Advanced Optical Materials (June 2017).

[218] R. H. Siddique, R. Hünig, A. Faisal, U. Lemmer, H. Hölscher, *Fabrication of hierarchical photonic nanostructures inspired by Morpho butterflies utilizing laser interference lithography*. Optical Materials Express (2015), ***5*** 996–1005.

[219] K. Ding, U. Aeberhard, F. Finger, U. Rau, *Silicon heterojunction solar cell with amorphous silicon oxide buffer and microcrystalline silicon oxide contact layers*. Physica Status Solidi (RRL)-Rapid Research Letters (2012), ***6*** 193–195.

[220] B. Rondeau, B. Cenki-Tok, E. Fritsch, F. Mazzero, J.-P. Gauthier, Y. Bodeur, E. Bekele, E. Gaillou, D. Ayalew, *Geochemical and petrological characterization of gem opals from Wegel Tena, Wollo, Ethiopia: Opal formation in an Oligocene soil*. Geochemistry: Exploration, Environment, Analysis (2012), ***12*** 93–104.

[221] F. Neukirchen, *Nicht ganz so heiß gekocht: Amethyst, Achat und Opal*. In *Edelsteine*, 161–178. Springer (2012).

[222] J. Sanders, *Colour of precious opal*. Nature (1964), ***204*** 1151–1153.

[223] J. Sanders, *Diffraction of light by opals*. Acta Crystallographica Section A: Crystal Physics, Diffraction, Theoretical and General Crystallography (1968), ***24*** 427–434.

[224] H. Fudouzi, *Colloidal Photonic Crystal Films: Fabrication and Tunable Structural Color and Applications*. In *Nanomaterials and Nanoarchitectures*, 1–19. Springer (2015).

[225] A. W. Eckert. *The World of Opals*. John Wiley & Sons (1997).

[226] M. S. Kalceff, M. Phillips, A. Moon, A. Smallwood, *Cathodoluminescence microanalysis of natural hydrated amorphous SiO2 opal*. Physics and Chemistry of Minerals (1997), ***24*** 131–138.

[227] E. Gaillou, A. Delaunay, B. Rondeau, M. Bouhnik-le Coz, E. Fritsch, G. Cornen, C. Monnier, *The geochemistry of gem opals as evidence of their origin*. Ore Geology Reviews (2008), ***34*** 113–126.

[228] J. Clarke, *The occurrence and significance of biogenic opal in the regolith*. Earth-Science Reviews (2003), ***60*** 175–194.

[229] M. Sumper, E. Brunner, *Learning from diatoms: Nature's tools for the production of nanostructured silica*. Advanced Functional Materials (2006), ***16*** 17–26.

[230] G. Strout, S. D. Russell, D. P. Pulsifer, S. Erten, A. Lakhtakia, D. W. Lee, *Silica nanoparticles aid in structural leaf coloration in the malaysian tropical rainforest understorey herb Mapania caudata*. Annals of Botany (2013), ***112*** 1141-1148.

[231] J. Teyssier, S. V. Saenko, D. Van Der Marel, M. C. Milinkovitch, *Photonic crystals cause active colour change in chameleons*. Nature Communications (2015), ***6***.

[232] H. Nilsson Sköld, S. Aspengren, M. Wallin, *Rapid color change in fish and amphibians–function, regulation, and emerging applications*. Pigment Cell & Melanoma Research (2013), ***26*** 29–38.

[233] J. D. Taylor, M. E. Hadley, *Chromatophores and color change in the lizard, Anolis carolinensis*. Cell and Tissue Research (1970), ***104*** 282–294.

[234] M. Egen, L. Braun, R. Zentel, K. Tännert, P. Frese, O. Reis, M. Wulf, *Artificial opals as effect pigments in clear-coatings*. Macromolecular Materials and Engineering (2004), ***289*** 158–163.

[235] J. Ge, Y. Yin, *Responsive photonische Kristalle*. Angewandte Chemie (2011), ***123*** 1530–1561.

[236] A. C. Arsenault, D. P. Puzzo, I. Manners, G. A. Ozin, *Photonic-crystal full-colour displays*. Nature Photonics (2007), ***1*** 468–472.

[237] A. C. Arsenault, D. P. Puzzo, A. Ghoussoub, I. Manners, G. A. Ozin, *Development of photonic crystal composites for display applications*. Journal of the Society for Information Display (2007), ***15*** 1095–1098.

[238] S. H. Foulger, P. Jiang, A. Lattam, D. W. Smith, J. Ballato, D. E. Dausch, S. Grego, B. R. Stoner, *Photonic crystal composites with reversible high-frequency stop band shifts*. Advanced Materials (2003), ***15*** 685–689.

[239] A. C. Arsenault, H. Míguez, V. Kitaev, G. A. Ozin, I. Manners, *A polychromic, fast response metallopolymer gel photonic crystal with solvent and redox tunability: A step towards photonic ink (P-Ink)*. Advanced Materials (2003), ***15*** 503–507.

[240] D. Nakayama, Y. Takeoka, M. Watanabe, K. Kataoka, *Simple and precise preparation of a porous gel for a colorimetric glucose sensor by a templating technique*. Angewandte Chemie (2003), ***115*** 4329–4332.

[241] O. L. Pursiainen, J. J. Baumberg, K. Ryan, J. Bauer, H. Winkler, B. Viel, T. Ruhl, *Compact strain-sensitive flexible photonic crystals for sensors*. Applied Physics Letters (2005), ***87*** 101902.

[242] J. Ge, J. Goebl, L. He, Z. Lu, Y. Yin, *Rewritable photonic paper with hygroscopic salt solution as ink*. Advanced Materials (2009), ***21*** 4259–4264.

[243] L. González-Urbina, K. Baert, B. Kolaric, J. Pérez-Moreno, K. Clays, *Linear and nonlinear optical properties of colloidal photonic crystals*. Chemical Reviews (2011), ***112*** 2268–2285.

[244] G. von Freymann, V. Kitaev, B. V. Lotsch, G. A. Ozin, *Bottom-up assembly of photonic crystals*. Chemical Society Reviews (2013), ***42*** 2528–2554.

[245] J. F. Galisteo-López, M. Ibisate, R. Sapienza, L. S. Froufe-Pérez, Á. Blanco, C. López, *Self-assembled photonic structures*. Advanced Materials (2011), ***23*** 30–69.

[246] Y. Xia, B. Gates, Y. Yin, Y. Lu, *Monodispersed colloidal spheres: Old materials with new applications*. Advanced Materials (2000), ***12*** 693–713.

[247] F. Li, D. P. Josephson, A. Stein, *Colloidal assembly: The road from particles to colloidal molecules and crystals*. Angewandte Chemie International Edition (2011), ***50*** 360–388.

[248] C. Dushkin, G. Lazarov, S. Kotsev, H. Yoshimura, K. Nagayama, *Effect of growth conditions on the structure of two-dimensional latex crystals: Experiment*. Colloid & Polymer Science (1999), ***277*** 914–930.

[249] A. S. Dimitrov, K. Nagayama, *Continuous convective assembling of fine particles into two-dimensional arrays on solid surfaces*. Langmuir (1996), ***12*** 1303–1311.

[250] Q. Yan, Z. Zhou, X. Zhao, *Inward-growing self-assembly of colloidal crystal films on horizontal substrates*. Langmuir (2005), ***21*** 3158–3164.

[251] B. Griesebock, M. Egen, R. Zentel, *Large photonic films by crystallization on fluid substrates*. Chemistry of Materials (2002), ***14*** 4023–4025.

[252] P. Ferrand, M. Egen, B. Griesebock, J. Ahopelto, M. Müller, R. Zentel, S. Romanov, C. Sotomayor Torres, *Self-assembly of three-dimensional photonic crystals on structured silicon wafers*. Applied Physics Letters (2002), ***81*** 2689–2691.

[253] J. Zhang, A. Alsayed, K. Lin, S. Sanyal, F. Zhang, W.-J. Pao, V. Balagurusamy, P. Heiney, A. Yodh, *Template-directed convective assembly of three-dimensional face-centered-cubic colloidal crystals*. Applied Physics Letters (2002), ***81*** 3176–3178.

[254] Q. Guo, C. Arnoux, R. Palmer, *Guided assembly of colloidal particles on patterned substrates*. Langmuir (2001), ***17*** 7150–7155.

[255] P. Ferrand, M. Minty, M. Egen, J. Ahopelto, R. Zentel, S. Romanov, C. S. Torres, *Micromoulding of three-dimensional photonic crystals on silicon substrates*. Nanotechnology (2003), ***14*** 323.

[256] J. Ye, R. Zentel, S. Arpiainen, J. Ahopelto, F. Jonsson, S. G. Romanov, C. M. Sotomayor Torres, *Integration of self-assembled three-dimensional photonic crystals onto structured silicon wafers*. Langmuir (2006), ***22*** 7378–7383.

[257] S. H. Im, O. O. Park, *Effect of evaporation temperature on the quality of colloidal crystals at the water-air interface*. Langmuir (2002), ***18*** 9642–9646.

[258] R. Iler, *Formation of precious opal*. Nature (1965), ***207*** 472–473.

[259] K. Davis, W. Russel, W. Glantschnig, *Settling suspensions of colloidal silica: Observations and X-ray measurements*. Journal of the Chemical Society, Faraday Transactions (1991), ***87*** 411–424.

[260] C. I. Aguirre, E. Reguera, A. Stein, *Tunable colors in opals and inverse opal photonic crystals*. Advanced Functional Materials (2010), ***20*** 2565–2578.

[261] D. Wang, F. Caruso, *Fabrication of polyaniline inverse opals via templating ordered colloidal assemblies*. Advanced Materials (2001), ***13*** 350–354.

[262] G. I. Waterhouse, M. R. Waterland, *Opal and inverse opal photonic crystals: Fabrication and characterization*. Polyhedron (2007), ***26*** 356–368.

[263] D. R. Snoswell, C. E. Finlayson, Q. Zhao, J. J. Baumberg, *Real-time measurements of crystallization processes in viscoelastic polymeric photonic crystals*. Physical Review E (2015), ***92*** 052315.

[264] J. Ballato, A. James, *A ceramic photonic crystal temperature sensor*. Journal of the American Ceramic Society (1999), ***82*** 2273–2275.

[265] J. M. Weissman, H. B. Sunkara, A. S. Tse, S. A. Asher, *Thermally switchable periodicities and diffraction from mesoscopically ordered materials*. Science (1996), ***274*** 959–963.

[266] X. Xu, G. Friedman, K. D. Humfeld, S. A. Majetich, S. A. Asher, et al., *Superparamagnetic photonic crystals*. Advanced Materials (2001), ***13*** 1681.

[267] X. Xu, S. A. Majetich, S. A. Asher, *Mesoscopic monodisperse ferromagnetic colloids enable magnetically controlled photonic crystals*. Journal of the American Chemical Society (2002), ***124*** 13864–13868.

[268] X. Xu, G. Friedman, K. D. Humfeld, S. A. Majetich, S. A. Asher, *Synthesis and utilization of monodisperse superparamagnetic colloidal particles for magnetically controllable photonic crystals*. Chemistry of Materials (2002), ***14*** 1249–1256.

[269] Q. Zhao, A. Haines, D. Snoswell, C. Keplinger, R. Kaltseis, S. Bauer, I. Graz, R. Denk, P. Spahn, G. Hellmann, et al., *Electric-field-tuned color in photonic crystal elastomers*. Applied Physics Letters (2012), ***100*** 101902.

[270] B. Michaelis, D. R. Snoswell, N. A. Bell, P. Spahn, G. P. Hellmann, C. E. Finlayson, J. J. Baumberg, *Generating lithographically-defined tunable printed structural color*. Advanced Engineering Materials (2013), ***15*** 948–953.

[271] B. Viel, T. Ruhl, G. P. Hellmann, *Reversible deformation of opal elastomers*. Chemistry of Materials (2007), ***19*** 5673–5679.

[272] C. G. Schäfer, D. A. Smolin, G. P. Hellmann, M. Gallei, *Fully reversible shape transition of soft spheres in elastomeric polymer opal films*. Langmuir (2013), ***29*** 11275–11283.

[273] O. L. Pursiainen, J. J. Baumberg, H. Winkler, B. Viel, P. Spahn, T. Ruhl, *Nanoparticle-tuned structural color from polymer opals*. Optics Express (2007), ***15*** 9553–9561.

[274] C. E. Finlayson, C. Goddard, E. Papachristodoulou, D. R. Snoswell, A. Kontogeorgos, P. Spahn, G. Hellmann, O. Hess, J. J. Baumberg, *Ordering in stretch-tunable polymeric opal fibers*. Optics Express (2011), ***19*** 3144–3154.

[275] T. Ruhl, G. P. Hellmann, *Colloidal crystals in latex films: Rubbery opals*. Macromolecular Chemistry and Physics (2001), ***202*** 3502–3505.

[276] T. Ruhl, P. Spahn, G. Hellmann, *Artificial opals prepared by melt compression*. Polymer (2003), ***44*** 7625–7634.

[277] O. L. Pursiainen, J. J. Baumberg, H. Winkler, B. Viel, P. Spahn, T. Ruhl, *Shear-Induced Organization in Flexible Polymer Opals*. Advanced Materials (2008), ***20*** 1484–1487.

[278] A. Kontogeorgos, D. R. Snoswell, C. E. Finlayson, J. J. Baumberg, P. Spahn, G. Hellmann, *Inducing symmetry breaking in nanostructures: Anisotropic stretch-tuning photonic crystals*. Physical Review Letters (2010), ***105*** 233909.

[279] A. I. Haines, C. E. Finlayson, D. R. Snoswell, P. Spahn, G. P. Hellmann, J. J. Baumberg, *Anisotropic resonant scattering from polymer photonic crystals*. Advanced Materials (2012), ***24***.

[280] C. E. Finlayson, P. Spahn, D. R. Snoswell, G. Yates, A. Kontogeorgos, A. I. Haines, G. P. Hellmann, J. J. Baumberg, *3D bulk ordering in macroscopic solid opaline films by edge-induced rotational shearing*. Advanced Materials (2011), ***23*** 1540–1544.

[281] C. E. Finlayson, A. I. Haines, D. R. Snoswell, A. Kontogeorgos, S. Vignolini, J. J. Baumberg, P. Spahn, G. Peter Hellmann, *Interplay of index contrast with periodicity in polymer photonic crystals*. Applied Physics Letters (2011), ***99*** 261913.

[282] C. E. Finlayson, J. J. Baumberg, *Polymer opals as novel photonic materials*. Polymer International (2013), ***62*** 1403–1407.

[283] D. R. Snoswell, A. Kontogeorgos, J. J. Baumberg, T. D. Lord, M. R. Mackley, P. Spahn, G. P. Hellmann, *Shear ordering in polymer photonic crystals*. Physical Review E (2010), ***81*** 020401.

[284] H. S. Wong, M. Mackley, S. Butler, J. Baumberg, D. Snoswell, C. Finlayson, Q. Zhao, *The rheology and processing of "edge sheared" colloidal polymer opals*. Journal of Rheology (2014), ***58*** 397–409.

[285] Q. Zhao, C. E. Finlayson, D. R. Snoswell, A. Haines, C. Schäfer, P. Spahn, G. P. Hellmann, A. V. Petukhov, L. Herrmann, P. Burdet, et al., *Large-scale ordering of nanoparticles using viscoelastic shear processing*. Nature Communications (2016), ***7***.

[286] R. Arshady, *Suspension, emulsion, and dispersion polymerization: A methodological survey*. Colloid & Polymer Science (1992), ***270*** 717–732.

[287] J. Ugelstad, M. El-Aasser, J. Vanderhoff, *Emulsion polymerization: Initiation of polymerization in monomer droplets*. Journal of Polymer Science Part C: Polymer Letters (1973), ***11*** 503–513.

[288] P. Spahn, C. Finlayson, W. M. Etah, D. Snoswell, J. Baumberg, G. Hellmann, *Modification of the refractive-index contrast in polymer opal films*. Journal of Materials Chemistry (2011), ***21*** 8893–8897.

[289] N. Schneider. *Scalable Fabrication of Three Dimensional Photonic Nanostructures with Shape Memory Polymers*. Karlsruhe Institute of Technology (2016).